Zeitschrift: IABSE publications = Mémoires AIPC = IVBH Abhandlungen
Band: 30 (1970)

Teilband: IABSE Publications = Mémoires AIPC = IVBH Abhandlungen

Nutzungsbedingungen
Die ETH-Bibliothek ist die Anbieterin der digitalisierten Zeitschriften auf E-Periodica. Sie besitzt keine Urheberrechte an den Zeitschriften und ist nicht verantwortlich für deren Inhalte. Die Rechte liegen in der Regel bei den Herausgebern beziehungsweise den externen Rechteinhabern. Das Veröffentlichen von Bildern in Print- und Online-Publikationen sowie auf Social Media-Kanälen oder Webseiten ist nur mit vorheriger Genehmigung der Rechteinhaber erlaubt. Mehr erfahren

Conditions d'utilisation
L'ETH Library est le fournisseur des revues numérisées. Elle ne détient aucun droit d'auteur sur les revues et n'est pas responsable de leur contenu. En règle générale, les droits sont détenus par les éditeurs ou les détenteurs de droits externes. La reproduction d'images dans des publications imprimées ou en ligne ainsi que sur des canaux de médias sociaux ou des sites web n'est autorisée qu'avec l'accord préalable des détenteurs des droits. En savoir plus

Terms of use
The ETH Library is the provider of the digitised journals. It does not own any copyrights to the journals and is not responsible for their content. The rights usually lie with the publishers or the external rights holders. Publishing images in print and online publications, as well as on social media channels or websites, is only permitted with the prior consent of the rights holders. Find out more

Download PDF: 04.04.2026

ETH-Bibliothek Zürich, E-Periodica, https://www.e-periodica.ch

ASSOCIATION INTERNATIONALE DES PONTS ET CHARPENTES
INTERNATIONALE VEREINIGUNG FÜR BRÜCKENBAU UND HOCHBAU
INTERNATIONAL ASSOCIATION FOR BRIDGE AND STRUCTURAL ENGINEERING

MÉMOIRES
ABHANDLUNGEN
PUBLICATIONS

30-II

1970

PUBLIÉS PAR LE SECRÉTARIAT GÉNÉRAL À ZURICH
HERAUSGEGEBEN VOM GENERALSEKRETARIAT IN ZÜRICH
PUBLISHED BY THE GENERAL SECRETARIAT IN ZURICH

Editeur - Verleger - Publisher

Association Internationale des Ponts et Charpentes
Ecole Polytechnique Fédérale, Zurich

Internationale Vereinigung für Brückenbau und Hochbau
Eidgenössische Technische Hochschule in Zürich

International Association for Bridge and Structural Engineering
Swiss Federal Institute of Technology, Zurich

En commission pour la vente en librairie
Kommissionsverlag für den Buchhandel - Copies for sale at

Verlag Leemann Zürich

Printed in Switzerland

Préface

Onze auteurs rapportent dans le présent volume au sujet de leurs recherches et études les plus récentes.

Cette fois également la majorité des contributions est en langue anglaise, tandis que deux sont rédigées en langue allemande. Les thèmes se répartissent également entre les domaines des constructions en béton et des structures en acier, lesquels gagnent de nouveaux aspects grâce au développement technique ininterrompu et aux exigences constamment accrues.

Nous nous permettons de lancer un appel, comme nous l'avons déjà fait dans la préface du volume 30-I, à nos amis d'expression française pour qu'ils accroissent leur collaboration à nos Mémoires, convaincus que nous sommes de la valeur de leurs travaux, comme cela a été démontré dans le passé.

C'est un agréable devoir de constater que les contributions à ce volume vont permettre de poursuivre l'échange d'idées entre les membres de notre Association. Nous remercions très sincèrement tous les auteurs pour leur engagement positif au service d'une cause qui nous est chère.

Zurich, avril 1971

Le Président de l'AIPC:

Prof. Maurice Cosandey
Directeur de l'Ecole Polytechnique Fédérale de Lausanne

Les Secrétaires Généraux:

Dr sc. techn. Hans von Gunten
Professeur à l'Ecole Polytechnique Fédérale, Zurich

Dr sc. techn. Pierre Dubas
Professeur à l'Ecole Polytechnique Fédérale, Zurich

Angelo Pozzi
Ecole Polytechnique Fédérale, Zurich

Vorwort

Elf Autoren berichten im vorliegenden Band über ihre neuesten Studien und Untersuchungen.

Auch diesmal ist die Mehrzahl der Beiträge in englischer Sprache abgefaßt, und nur zwei sind in deutscher Sprache geschrieben. Der Themenkreis umschließt gleichermaßen die Gebiete von Beton- und Stahlbauten, welche – dank der ununterbrochenen technischen Entwicklung und auf Grund der stets wachsenden Anforderungen – stets neue Aspekte gewinnen.

Wir erlauben uns, wie wir es schon im Vorwort zu Band 30-I getan haben, unsere Kollegen französischer Zunge zu intensiverer Zusammenarbeit an unseren Publikationen aufzurufen. Wir sind überzeugt, daß, wie die Erfahrung bereits gezeigt hat, ihre Arbeiten für uns von hohem Wert sind.

Es ist uns eine angenehme Pflicht, festzustellen, daß die Aufsätze im vorliegenden Band dazu beitragen werden, den Gedankenaustausch unter den Mitgliedern unserer Vereinigung zu fördern. Wir danken aufrichtig allen Verfassern für ihren Einsatz zum Wohle einer Sache, die uns sehr am Herzen liegt.

Zürich, April 1971

Der Präsident der IVBH:

Prof. Maurice Cosandey
Direktor der Eidgenössischen Technischen Hochschule Lausanne

Die Generalsekretäre:

Dr. sc. techn. Hans von Gunten
Professor an der Eidgenössischen Technischen Hochschule in Zürich

Dr. sc. techn. Pierre Dubas
Professor an der Eidgenössischen Technischen Hochschule in Zürich

Angelo Pozzi
Eidgenössische Technische Hochschule, Zürich

Preface

In this volume, eleven authors report about their newest studies and investigations.

Again, the majority of the contributions is written in English, and only two of them are in German.

The themes include likewise the fields of concrete structures and steel structures which are showing new features, due to the never-ending technical development and the continuously increasing requirements.

We invite our francophone collegues – as we did already in the preface of vol. 30-I – to collaborate more intensively. We are firmly convinced that, as experiences have shown it repeatedly, their works are very valuable for us.

We are sure that the contributions in this volume will help the interchange of ideas between the members of the IABSE.

Finally, we sincerely thank the authors for their initiative for the benefit of a real serious matter.

Zurich, April 1971

The President of IABSE:

Prof. MAURICE COSANDEY
Director of the Swiss Federal Institute of Technology, Lausanne

The General Secretaries:

Dr. sc. techn. HANS VON GUNTEN
Professor at the Swiss Federal Institute of Technology, Zurich

Dr. sc. techn. PIERRE DUBAS
Professor at the Swiss Federal Institute of Technology, Zurich

ANGELO POZZI
Swiss Federal Institute of Technology, Zurich

Leere Seite
Blank page
Page vide

Table des matières - Inhaltsverzeichnis - Table of Contents

"Working Group on Information on Earthquake Engineering" . . . . . English 1
J. Ferry Borges, J. Despeyroux, Y. Maeda, P. Mazilu, J. R. Robinson

Bref exposé du génie sismique moderne
Kurze Darstellung des heutigen Erdbebeningenieurwesens
Brief Review of Modern Earthquake Engineering

Hugo Bachmann, Switzerland . . . . . English 11

L'influence de la sollicitation de cisaillement et de l'adhérence des armatures sur la capacité de rotation des poutres en béton armé
Der Einfluß von Schubbeanspruchung und Verbund auf die Rotationsfähigkeit plastischer Stahlbeton-Gelenke
Influence of Shear and Bond on Rotational Capacity of Reinforced Concrete Beams

Amin Ghali, K. J. Bathe, Canada . . . . . English 29

Calcul des plaques fléchies à l'aide d'éléments finis de grandes dimensions
Berechnung der Biegung von Platten mittels großer endlicher Elemente
Analysis of Plates in Bending Using Large Finite Elements

A. Hrennikoff, Canada. . . . . English 41

Importance de la symétrie des éléments finis pour le calcul des plaques
Bedeutung der Symmetrie der endlichen Elemente für die Plattenbiegung
Importance of Cell Symmetry in Flexural Finite Element Method

K. T. Sundara Raja Iyengar, K. S. Jagadish, India . . . . . English 57

Comportement dynamique des ponts-routes sous les surcharges mobiles
Dynamisches Verhalten von Straßenbrücken unter bewegter Last
Dynamic Response of Highway Bridges to Moving Loads

Jayme Mason, Brazil . . . . . English 77

Problèmes des perturbations aux bords dans les coupoles à treillis
Zum Randstörungsproblem in Gitterkuppeln
On the Problem of Edge Disturbances in Lattice Domes

Robert P. McBean, William Weaver, USA . . . . . English 95

Calcul des systèmes de plaques par la méthode des substructures
Berechnung von Plattensystemen mittels Substrukturen
Substructures Analysis of Plate Systems

Toshie Okumura, Naruo Ishizawa, Japan . . . . . English 105

Le calcul des contraintes dans l'assemblage d'angle de portiques en acier à nœuds rigides et parois minces et son application
Spannungsberechnung der dünnwandigen, steifknotigen Rahmenecke und deren Anwendung
Calculation of Stress in Knee Joints of Rigid Steel Frames of Thin Walled Section and its Application

Jürgen Pläbn, Indien . . . . . Deutsch 153

Solution rigoureuse pour l'analyse de la résistance à la rupture en flexion d'une poutre isolée en béton précontraint et de section rectangulaire
Eine strenge Lösung des Biegebruchsicherheitsnachweises für den rechteckigen Spannbetonbalken ohne Verbund
A Rigorous Solution for the Moment Carrying Capacity of an Unbonded Prestressed Concrete Beam

J. C. Robertson, R. P. Pama, A. R. Cusens, Scotland . . . . . English 169

Déformations latérales dues au cisaillement des poutres en caisson multicellulaire
Schubverformung in Querrichtung von mehrzelligen Kastenträger-Brücken
Transverse Shear Deformation in Multicell Box Beam Bridges

R. G. Sisodiya, Y. K. Cheung, A. Ghali, Canada . . . . . English 191

Calcul à l'aide des éléments finis des ponts courbes, biais à section en caisson
Berechnung von schiefen, gekrümmten Brücken mit Kastenquerschnitt mittels der Methode der endlichen Elemente
Finite Element Analysis of Skew, Curved Box-Girder Bridge

Brief Review of Modern Earthquake Engineering

Bref exposé du génie sismique moderne

Kurze Darstellung des heutigen Erdbebeningenieurwesens

"Working Group on Information on Earthquake Engineering"

J. FERRY BORGES J. DESPEYROUX Y. MAEDA
P. MAZILU J. R. ROBINSON

1. Introduction

This review is a brief survey of the present status of Earthquake Engineering. It contains information on earthquake hazards, main Earthquake Engineering problems, safety of structures under the action of earthquakes, Earthquake Engineering research and education, and international collaboration.

The review is prepared in accordance with a decision by the International Assocation for Bridge and Structural Engineering to set up a working group for dealing with "Information on Earthquake Engineering". The decision to create this working group was supported by the "Comité de Liaison", which coordinates the activity of several international associations dealing with Structural Engineering, such as the International Association for Bridge and Structural Engineering, the European Committee for Concrete, the International Federation for Prestressing, the International Council for Building Research Studies and Documentation, the European Convention of the Association for Steel Construction, and the International Association for Shell Structures.

2. Earthquake Hazards

Earthquake hazards are among the most serious dangers that mankind has to face. In fact, referring only to the second quarter of this century,

between 1926 and 1950, over 350 000 people were killed and the damage to buildings and public works is estimated in nearly 10 000 million U.S. dollars [1].

The number of casualties due to a large earthquake may be tremendous. It has ranged, for the most severe ones, from 100 000 to 200 000. In the future, if no special precautions were taken, an earthquake hitting a large town could kill millions. On the other hand owing to the increasing density of construction, a single earthquake could result in a tremendous loss of property. Avoiding such catastrophes is the task of Earthquake Engineering.

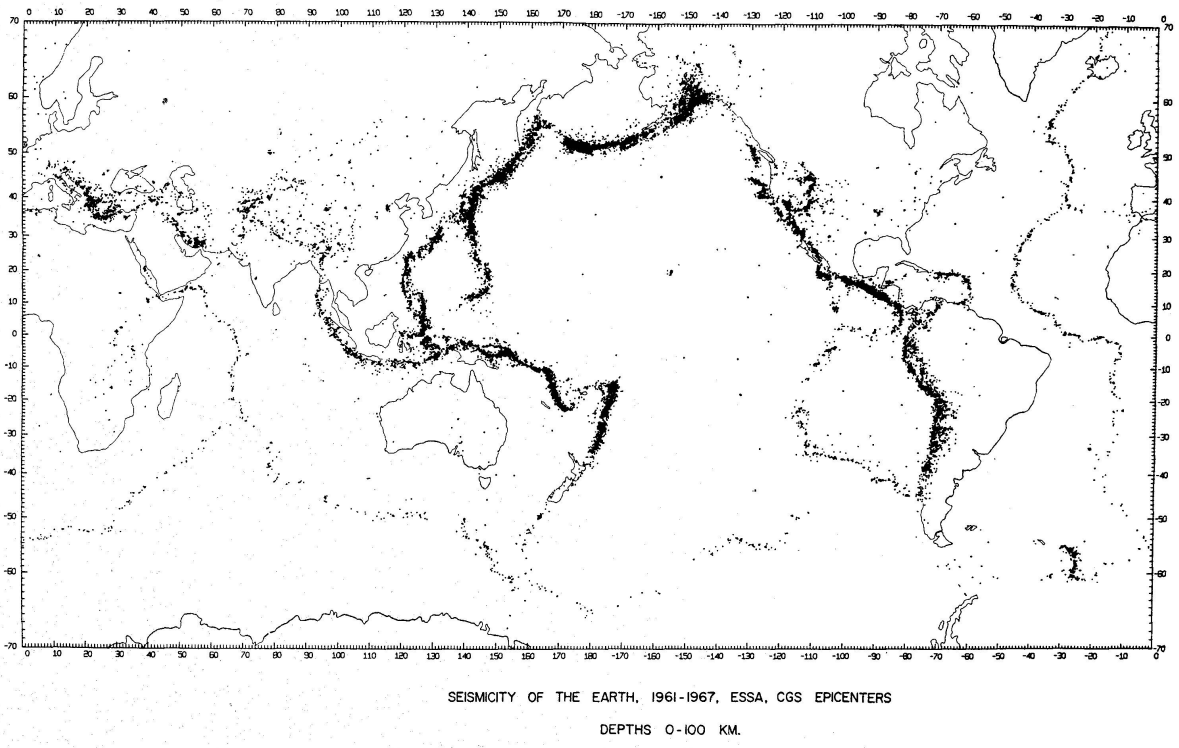


Fig. 1. Seismicity of the earth compiled by the Unites States Coast and Geodetic Survey [2].

Fig. 1 shows a map of world seismicity compiled by the Unites States Coast and Geodetic Survey [2]. This map refers to the period 1961–1967 and includes earthquakes having depths between 0 and 100 km. Owing to the modern seismographic networks and to the modern data processing techniques the definition of hypocenter data is now much more accurate that it was years ago. This accuracy will increase in the near future, so that very reliable data will be available for studying the mechanisms of earthquake generation and defining regional seismicity.

Recently the direct forecast of earthquakes has aroused much interest among researchers [3]. It must be noted however that such a forecast may help to reduce casualties but not substantially to reduce the amount of damage.

Anyhow the information provided by such studies is of foremost interest for a better understanding of earthquake generation, even allowing us to dream of avoiding strong earthquakes by a man-controlled release of energy along

fault zones. In fact, by slowly releasing the stresses that produce the rupture of the crust, the cause of some types of earthquakes might be eliminated. This however is a very remote possibility only potentially applicable in a small number of cases.

The real challenge within our present possibilities is to design and to build earthquake-resistant constructions. This has to be done in economic terms, which implies an accurate estimate of the seismic risk.

3. Earthquake Engineering Problems

There is a large variety of problems to be studied in Earthquake Engineering. Some of the most important ones are:

— Frequency of earthquake occurrences on the whole earth and at localized sites.
— Measurement of strong earthquakes including engineering definition of earthquake ground motion.
— Dynamic soil mechanics; study of earthquake disasters due to soil conditions.
— Application of the stochastic method in Earthquake Engineering, including the simultaneous consideration of physical, economic, and social phenomena in engineering.
— Experimental studies and theoretical analysis of safety of members and structures.
— Survey of earthquake damages, particularly in relation with soils and foundations.
— Prevention of earthquake disasters including installations, plannings, shelters, relief, temporary repairs, rehabilitation.
— Prevention of disasters due to tidal waves.

These problems are being studied all over the world as indicated below. The present review particularly emphasizes structural safety problems.

4. Safety of Structures

Structural safety under earthquake loads has to be dealt with according to the general safety principles used for other types of loads [4]. According to simple economical criteria, one engineering objective is to minimize the total long-term cost of providing earthquake resistance and repairing damage, both resistance and damage being considered in a very broad sense. Achieving this goal and expressing it in statistical terms involves a statistical estimate of seismic loads and a statistical estimate of the behaviour of the different types of structures when subjected to seismic vibrations [5]. The modern principles

of structural safety cannot be applied without accurate information of these two types.

The statistical estimate of seismic loads requires a quantitative definition of the seismicity of the regions. For this purpose, information on the historical occurrence of earthquakes has to be combined with the information gathered in studies on geophysics, geology, rock mechanics and soil mechanics.

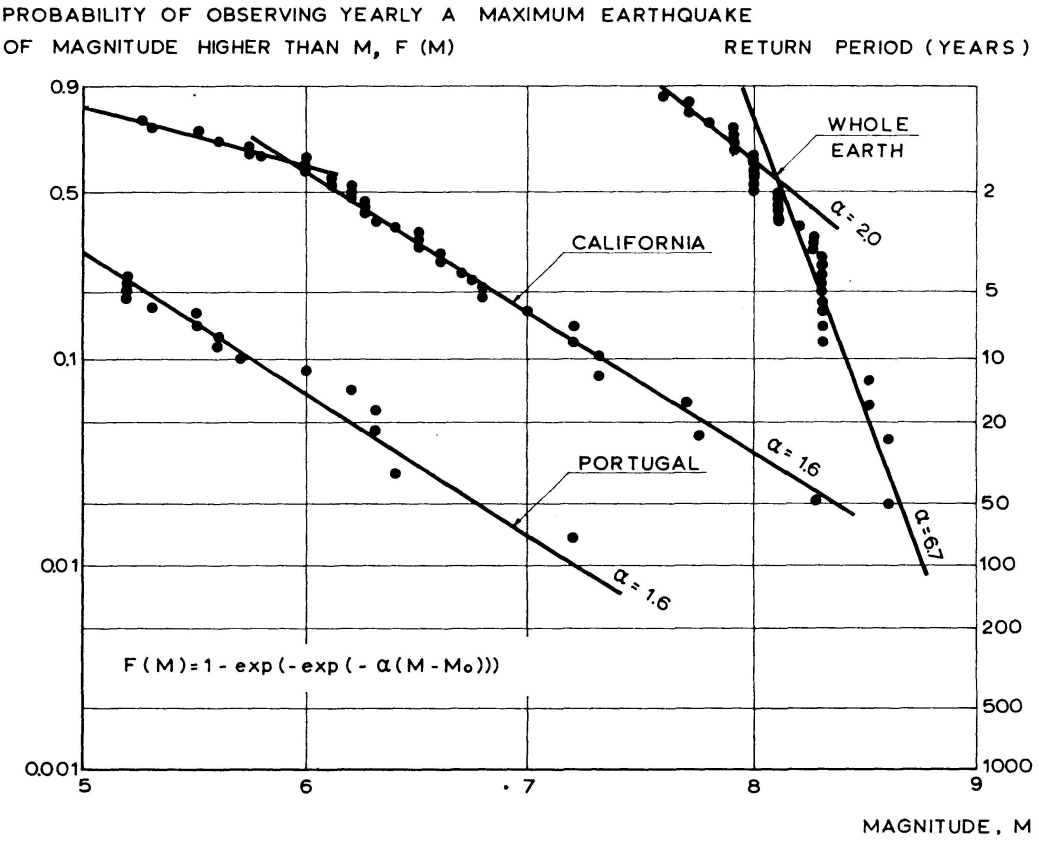


Fig. 2. Relations between probability and magnitude.

Fig. 2 shows the probability of yearly observing an earthquake with a magnitude higher than M in the whole earth, in California, and in Portugal. Within the range of interest the observed data fit double exponential extreme distributions, which are represented by straight lines in the diagrams.

On the other hand, for quantifying earthquake loads, seismic vibrations have to be duly idealized and defined by a convenient number of parameters. The theory of stochastic processes provides the most powerful means for obtaining this idealization.

The statistical distribution of the intensity of the earthquakes in a given region being thus defined, it has to be combined with the statistical distribution of the response of the structures to allow the definition of the statistical distribution of seismic loads. This last distribution is the one to be used in the design.

In general, the statistical distribution of the response of the structure depends on several parameters. For the simple case of linear one degree-of-freedom oscillators these parameters are the natural frequency and the damping factor.

This very brief survey of the tasks necessary for a satisfactory definition of seismic loads could lead to the erroneous conclusion that these are simple problems. In fact much work has already been done along these lines and much is still required to obtain the desired results. However, the general policy being established, sufficiently accurate pratical results are at present obtainable from the existing data.

On the other hand, final results on structural safety can only be reached if the ultimate strength is also statistically expressed. This strength may be defined in terms of ultimate forces or of ultimate displacements. The correspondance between these two concepts can be established using the notion of ductility factor.

The information at present available on structural behaviour allows a more accurate definition of ultimate forces than of ultimate displacements. On the other hand, seismic loads are naturally expressed in terms of maximum displacements. Thus an important research task is the statistical definition of the ultimate displacements in the different types of structures when acted by seismic loads. As indicated, the results of these studies can be expressed either directly in terms of displacements or indirectly in terms of ductility factors.

It is amazing how little information of the above type can be obtained from the very large volume of structural research performed till now. It is expected that this situation will improve in a near future, allowing the safety of structures in seismic regions to be completely defined on a quantitative statistical basis.

5. Earthquake Engineering Research and Education

It is not easy to present a survey of Earthquake Engineering research owing to the lack of centralized information and also to the inter-relation of Earthquake Engineering with many other scientific and technical fields. A very important contribution to this survey is due to the "International Association for Earthquake Engineering, IAEE", that publishes world directories of universities, institutions and personnel engaged in Earthquake Engineering research. The last directory (6), revised in 1968, contains 136 institutes and 539 researchers. Although covering an important part of this activity in the world, this directory refers to 14 countries only. The number of countries where regulations dealing with earthquake loads are at present in force is considerably larger. The world list of earthquake resistant regulations published by IAEE [7] refers to 26 countries.

The majority of research results in this field is published in the proceedings of the world conferences: U.S.A. (1956) [8], Japan (1960) [9], New Zealand (1964) [10] and Chile (1969) [11], which include altogether about 500 papers. Although more than 400 papers were submitted to the last conference only 160 could be accepted.

In addition to the world conferences referred to several regional and national conferences [12 to 15] were recently organized and others have already been announced [16 to 18]. Furthermore several journals specialized in Earthquake Engineering and many others publish papers on this subject. A recent report published by the American Committee on Earthquake Engineering Research [19] gives a broad up-to-date view of the main problems in this field.

All this activity shows that Earthquake Engineering is an attractive field of research. It is in fact so, particularly if on one hand the potential damage of earthquakes is considered and, on the other, if it is recognized that the scientific and technical tools that can avoid such damage already exist.

Specifically as concerns education and training, several international and national institutes and schools were created during the last ten years to improve the specialization in Earthquake Engineering. Among the international institutes special reference is due to the following:

— International Institute of Seismology and Earthquake Engineering, Tokyo, Japan [20].
— International Center of Earthquake Engineering "Arturo Danusso", Milan and Bergamo, Italy.
— Institute of Seismology, Earthquake Engineering and Town Planning, Skopje, Yugoslavia.

Furthermore, special courses on Earthquake Engineering are organized at several universities and national research institutes.

Nevertheless it has to be recognized that education and training in Earthquake Engineering is not yet sufficiently spread even in countries with a high seismicity. Changing the present state of things is surely the most effective way to increase the rate of progress in this field and to put in pratical use the results available.

6. International Collaboration

As indicated, the International Association for Earthquake Engineering, IAEE, is particularly effective in securing international collaboration in its field. Recognizing the importance of Earthquake Engineering other international associations have set up special committees on this problem. Thus a close relation of these associations and their committees with the IAEE seems necessary to obtain the best coordination of efforts. Unhappily exchange of information and collaboration among international associations is sometimes

difficult. Anyhow it seems that further increasing the number of committees on Earthquake Engineering is going to render this coordination even more difficult. It cannot be forgotten that in addition to the IAEE there also exist several other regional and national organizations, more or less interrelated with it.

A practical way to improve the present collaboration among international associations in Earthquake Engineering would be to include IAEE in the "Comité de Liaison" that co-ordinates the major structural engineering associations. Anyhow there is no reason to substitute IAEE in its leading position in Earthquake Engineering. Just on the contrary it seems advisable that the different international associations coordinate their activities in direct collaboration with the IAEE. On the other hand, information on the aims of IAEE should be made known more widely and possible adjustments in the activities of the IAEE so as to satisfy the needs of other associations should be considered.

The UNESCO, United Nations Educational, Scientific and Cultural Organization, plays a very prominent rôle in the field of international collaboration and its activities in Earthquake Engineering have been very important. In fact, in addition to its wide activity in Geophysics and particularly in Seismology, special reference is due to the following actions in Earthquake Engineering: survey missions to the principal seismic zones of the world, field studies of earthquakes, technical assistance missions, working groups on special subjects such as seismic maps, principles of earthquake resistant design and measurement of strong motions, organization of intergovernmental meetings and support of international institutes and of special researches. The activity of the "Joint Committee in Seismology and Earthquake Engineering" formed under its patronage must also being mentioned.

Recently, some other international organizations – for instance NATO, North Atlantic Treaty Organization – have also decided to include in their activities the protection against natural calamities, such as earthquakes [21].

On the other hand, collaboration at associative and governmental levels between USA and Japan, both in the research field through the USA-Japan Science Council, and in the disaster prevention field through the USA-Japan Government Conference for the Natural Resources Utilization, is also yielding good results for the progress of Earthquake Engineering.

References

1. E. M. Fournier D'Albe: Earthquakes – avoidable disasters, Impact, Vol. XVI, No. 3, 1966.
2. M. Barazangi and J. Dorman: World seismicity maps compiled from ESSA, Coast and Geodetic Survey, Epicenter data, 1961–1967, Bulletin of the Seismological Society of America, Volume 59, No. 1, February, 1969.

3. Premointory Phenomena Associated with Several Recent Earthquakes and Related Problems, Joint US. Japan Conference, American Geophysical Union, May, 1969.
4. J. FERRY BORGES and M. CASTANHETA: Structural Safety Course 101, Laboratório Nacional de Engenharia Civil, 2nd Edition, Lisbon, March, 1971.
5. J. FERRY BORGES and M. CASTANHETA: General Recommendations Derived from Basic Studies on Structural Safety, Symposium on Concepts of Safety of Structures and Methods of Design, International Association for Bridge and Structural Engineering, London, September, 1969.
6. International Directory of Universities, Institutions Engaged in Earthquake Engineering Research. International Association for Earthquake Engineering, Tokyo, March, 1970.
7. Earthquake Resistant Regulations. A world list, International Association for Earthquake Engineering, Tokyo, 1966.
8. I World Conference on Earthquake Engineering. Earthquake Engineering Research Institute, Berkeley, California, June, 1965.
9. II World Conference on Earthquake Engineering. Science Council of Japan, Tokyo and Kyoto, 1960.
10. III World Conference on Earthquake Engineering. International Association for Earthquake Engineering, New Zealand, January, 1965.
11. IV Conference on Earthquake Engineering. International Association for Earthquake Engineering, Chile, January, 1969.
12. NSF-UCEER Conference on Earthquake Engineering Research. University Council for Earthquake Engineering Reseach. University of California, Berkeley, California, March, 1969.
13. I Congreso Nacional de Sismologia e Ingenieria Antisismica, Lima, Peru, Setiembre, 1969.
14. Testing Methodology and Technique of Full-Scale and Model Structures Under Static and Dynamic Loads, Bucharest, September, 1969.
15. ECEE/AEIS Joint Symposium on Earthquake Engineering Topics. European Commission for Earthquake Engineering, Madrid, September, 1969.
16. Conference on Earthquake Analysis of Structures, Experimental Methods and Techniques for Dynamic Characteristics and Seismic Response of Structures, Iasi, Rumania, September, 1970.
17. III European Symposium on Earthquake Engineering. European Commission for Earthquake Engineering, Sofia, Bulgaria, September, 1970.
18. Third Japan Earthquake Engineering Symposium. Japanese Society of Soil Mechanics and Foundation Engineering, Tokyo, November, 1970.
19. Earthquake Engineering Research. A report prepared by the Committee on Earthquake Engineering Research, National Academy of Sciences, Washington, D.C., 1969.
20. International Institute of Seismology and Earthquake Engineering. UNESCO/UNDP, Special Fund Component, Report Series, 19, Paris, 1969.
21. Committee on the Challenges of Modern Society. Disaster Assistance Project, NATO Unclassified Document, AC/274-D/3, March, 1970.

Summary

Earthquake resistant constructions are the great challenge of Earthquake Engineering. The scientific and technological knowledge already available

makes it possible to reach this aim safely and economically. It is to be expected that basic and applied research carried out in a well balanced condition will improve this knowledge, notably the rational bases of design, further increasing the efficiency and the economy of constructions. In particular, patterns of earthquake damages should be analysed and understood through actual investigations of the damages.

The present high rate of progress has not been accompanied by a parallel dissemination of knowledge which would enable mankind to take full advantage of the benefits that could derive from this knowledge. Consequently, education and training actions are highly profitable and are strongly recommended.

Special attention must be paid to securing the efficiency of international collaboration, as in fact this collaboration is one of the most effective ways of accelerating progress and disseminating knowledge.

Résumé

Les constructions résistant aux tremblements de terre représentent le grand défi du génie sismique. Ce défi peut être surmonté actuellement grâce aux connaissances scientifiques et techniques déjà acquises. Des recherches appliquées, bien appuyées sur des recherches de base, permettront de rationaliser davantage le projet des constructions, avec des conséquences directes sur l'efficacité et l'économie. En particulier, on doit faire des études quantitatives des dégâts dûs aux tremblements de terre.

Le rapide progrès actuel n'a pas été accompagné d'une diffusion des connaissances permettant de profiter des avantages qui en découlent. En conséquence il est vivement recommandé d'augmenter les actions d'enseignement et d'information.

Il est tout spécialement important d'assurer une collaboration internationale efficace, car cette collaboration est un des meilleurs moyens d'accélérer le progrès et de diffuser les connaissances.

Zusammenfassung

Der Entwurf und Bau von erdbebenbeständigen Bauwerken stellen die große Herausforderung an das Erdbebeningenieurwesen dar. Die bereits vorhandenen wissenschaftlichen und technischen Kenntnisse erlauben dieses Ziel auf sichere und wirtschaftliche Weise zu erreichen. Durch eine ausgewogen durchgeführte Grundlagen- und angewandte Forschung kann das vorhandene Wissen erweitert werden, insbesondere die Grundlagen der Bemessung, so daß ein verbesserter Nutzen und eine erhöhte Wirtschaftlichkeit zu erwarten sind. Vor allem sollten typische Erdbebenschäden untersucht und im Lichte der heutigen Schadensforschung betrachtet werden.

Der derzeitige, rasche Fortschritt wurde allerdings nicht von einer gleichzeitigen Verbreitung der Kenntnisse begleitet, welche der Menschheit erlauben würde, vollen Nutzen aus diesen Kenntnissen zu ziehen. Demzufolge ist eine sorgfältige Ausbildung und Fortbildung von großem Nutzen und besonders zu empfehlen.

Besondere Beachtung verdient die Aufrechterhaltung einer intensiven internationalen Zusammenarbeit, stellt doch eine solche eines der besten Mittel dar, um die Verbreitung der Kenntnisse und den Fortschritt zu beschleunigen.

Influence of Shear and Bond on Rotational Capacity of Reinforced Concrete Beams

L'influence de la sollicitation de cisaillement et de l'adhérence des armatures sur la capacité de rotation des poutres en béton armé

Der Einfluß von Schubbeanspruchung und Verbund auf die Rotationsfähigkeit plastischer Stahlbeton-Gelenke

HUGO BACHMANN

Dr. sc. techn., Assistant Professor of Civil Engineering, Swiss Federal Institute of Technology, Zurich, Switzerland

Introduction

A considerable amount of experimental and theoretical research into the plastic behaviour of statically indeterminate structures has been carried out during the last 20 years. The application of the simple plastic analysis to steel structures has been shown to be valid. In statically indeterminate reinforced concrete structures, however, the rotational capacity of plastic hinges may be very small and as a result theoretical ultimate load can not be reached.

Since 1963 a research programme to study the influence of shear and bond on the general development and the rotational capacity of reinforced concrete plastic hinges has been carried out at the Institute of Structural Engineering of the Swiss Federal Institute of Technology (ETH), Zurich, Switzerland.

Test Specimens

The test series consisted of two groups of 5 symmetrical two-span beams, Series A of a rectangular cross section and Series B of an I-shaped cross section. The load arrangement and dimensions are shown in Fig. 1. The two end reactions were measured with dynamometers at every load step. Thus the value of the moment and shear at every cross section of the beams could be calculated from the equilibrium conditions.

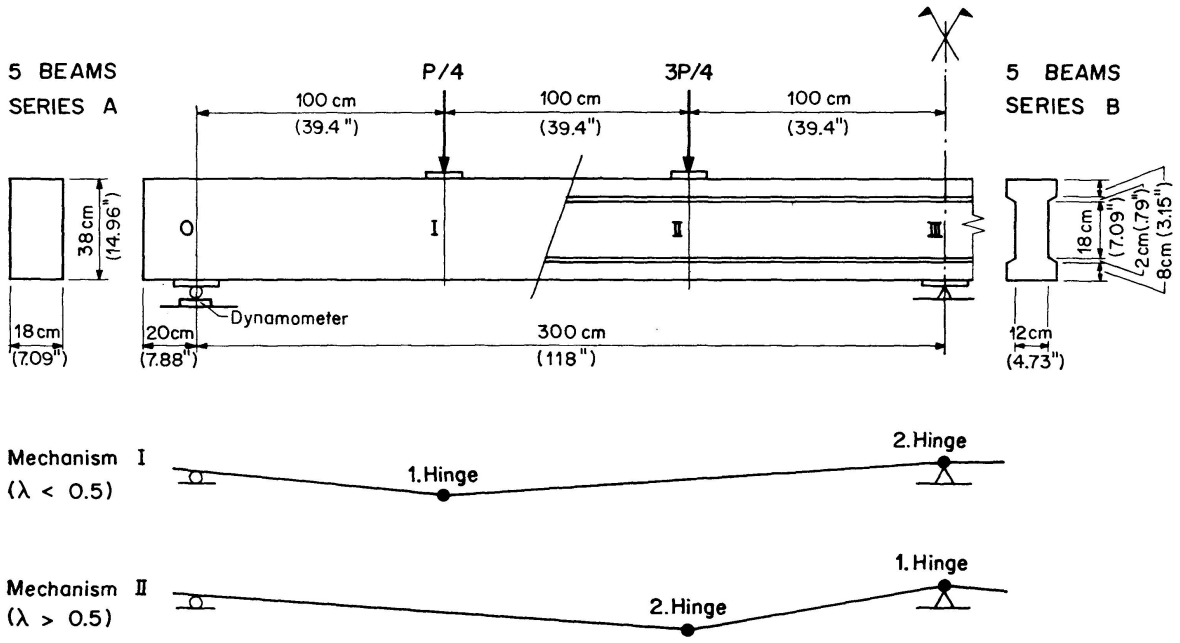


Fig. 1. Loading arrangement and dimensions of test specimens; mechanisms arrived at by plastic analysis.

The test beams were designed on a simple plastic analysis theory as given for instance in [1]. The ratio of the calculated ultimate moments in the spans and over the central support is denoted by λ. The value of λ determines where the first hinge is formed. The corresponding mechanisms are shown in Fig. 1. If $\lambda < 0.5$, Mechanisms I occurs, and if $\lambda > 0.5$, Mechanism II. $\lambda_e = 0.456$ corresponds to the elastic moment distribution. The plastic rotation necessary to allow the calculated ultimate load to be reached increases with the difference between λ and λ_e.

The values of λ for the 10 beams varied from 0.17 to 2.32. The longitudinal tensile reinforcement p varied from 0.34 to 2.04 percent in span and from 0.78 to 2.04 percent over the central support.

For the design of the shear reinforcement it was assumed that

$$V_c = v_c b' d \text{ with } v_c = 4 + 0.025 f'_c \text{ (kg/cm}^2\text{)} \quad (1)$$
$$(v_c = 57 + 0.025 f'_c \text{ [psi]})$$

is carried by the concrete compression zone. The stirrup reinforcement was calculated according to the truss analogy with a shear force of $V_u - V_c$ and a steel stress of f_y. The ultimate shear force V_u was calculated by the simple plastic analysis method.

An example of the stress-strain curve for the longitudinal and stirrup reinforcement (Torstahl) is shown in Fig. 2. The elastic limit stress f_e varied from 3200 to 3800 kg/cm^2 (nom. 46 to 54 ksi), the yield strength f_y (0.2 percent proof stress) from 3600 to 4800 kg/cm^2 (nom. 63 to 87 ksi). Good bond conditions were provided by a combination of spiral and non-continuous ribs. The

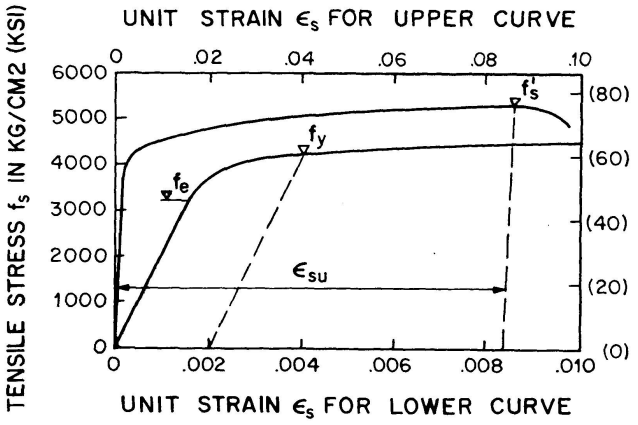


Fig. 2. Example of stress-strain curve of reinforcement.

average compressive strength of the concrete f'_c was 356 kg/cm² (nom. 5000 psi).

Tests to study rotational capacity are often carried out on simply supported one-span beams. However, with this test arrangement the following conditions could be investigated:

— At hinges in the spans: A small shear stress (but no pure bending!).
— At hinges over the central support: A high shear stress and a small moment-shear ratio ($M/Vd = 1.0 + 2.8$ due to contraflexure).
— At hinges in the spans and over the central support: A variation of the shear stress during rotation.

Test Results

In particular curvatures, rotations and the extensions of the stirrups were measured with dials and mechanical extensometers placed along the length of the beams.

General Behavior and Failure

In all the beams the mechanisms developed as predicted by the simple plastic analysis. In the beams A 1 and A 2 the first plastic hinge was formed in span, corresponding to Mechanism I, and in the other beams the first plastic hinge occured over the central support, corresponding to Mechanism II.

In 8 beams the collapse load reached or exceeded the ultimate load computed by the plastic analysis using a bilinear moment-curvature relationship. In 2 beams, however, the rotational capacity of the support hinge was not sufficient to enable the theoretical ultimate load to be reached.

3 beams (A 1, A 2, A 3) failed in span due to bending. The tensile reinforcement was elongated until the steel was ruptured. In the other 7 beams a shear failure occurred at the support hinge during plastic rotation. As the

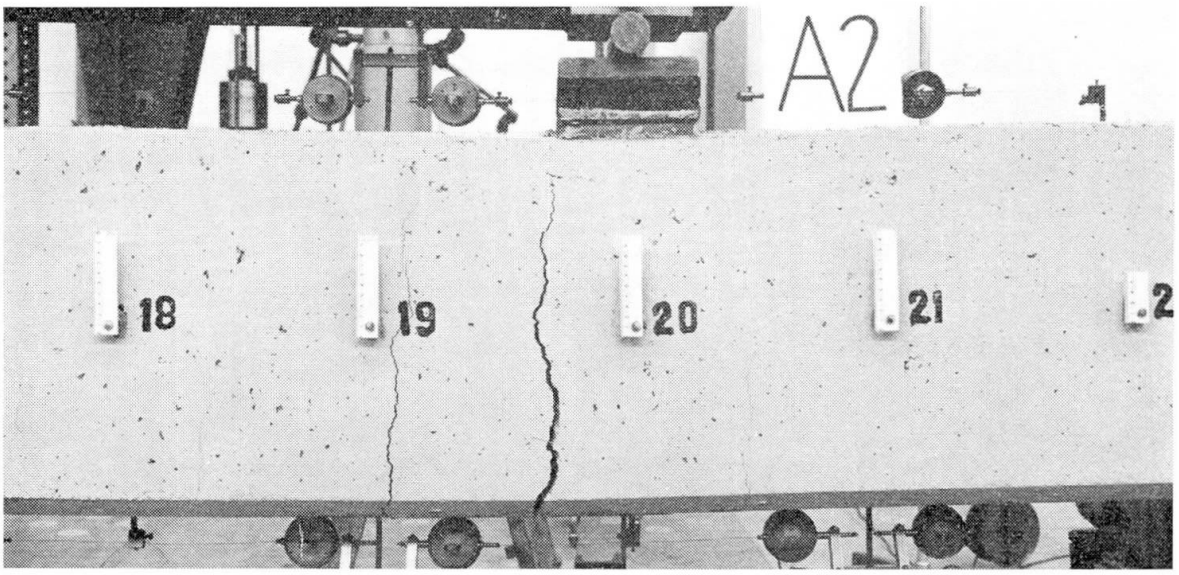


Fig. 3. Typical "flexural crack hinge", beam A 2.

stirrups deformed plastically, that is as their stress exceeded the elastic limit stress f_e, greater shear deformations in the web could be observed. These deformations caused high local stresses in the concrete of the web and the compression zone. Mainly as a result of these stirrup deformations the concrete in the web and the compression zone finally was crushed.

Plastic Hinges

Two entirely different types of plastic hinges were observed. They are described as

"flexural crack hinges", and
"shear crack hinges".

A typical flexural crack hinge is shown in Fig. 3. This type of hinge develops in a beam zone in which the bending moment is predominant. The shear stress is small and therefore only vertical flexural cracks occur. As seen in Fig. 3 plastic deformations were concentrated mainly to one crack. For this reason, the rotational capacity of such a flexural crack hinge may be very small.

A typical shear crack hinge behaves in another way (see Fig. 3). Diagonal flexural-shear cracks are produced through the influence of a relatively large shear stress in addition to the bending moment. This improves the behaviour of the hinge. The tests have shown that the plastic deformations in a shear crack hinge occur over a much wider zone than with flexural crack hinges, and this allows a much greater rotational capacity.

Rotational Behaviour

Plots of the moment ratio against the total rotation of the two types of plastic hinges as shown in Fig. 3 and 4 are given as examples in Fig. 5. The

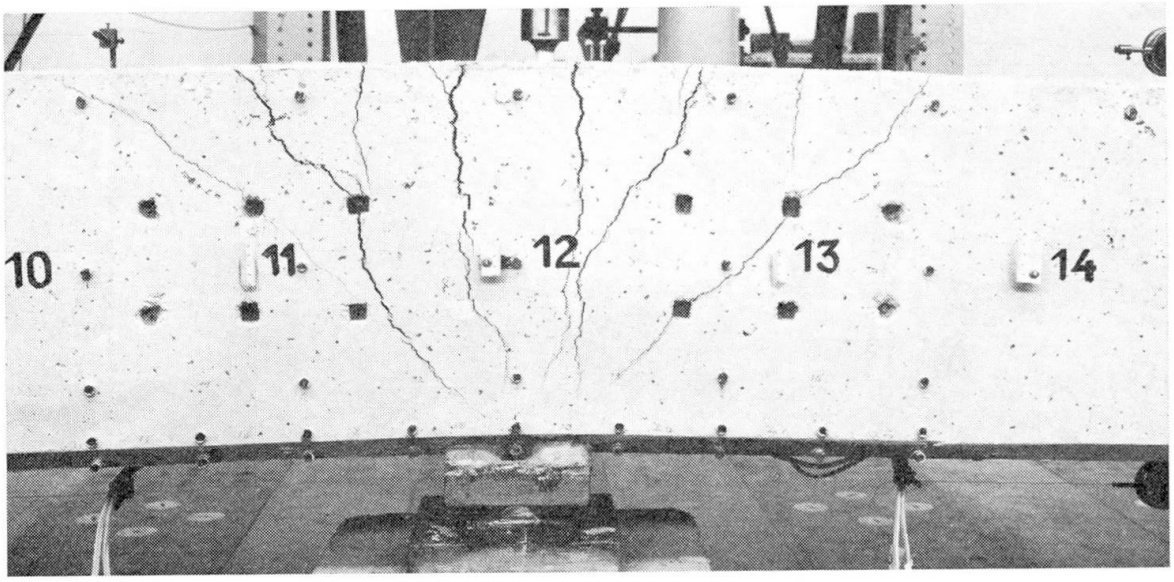


Fig. 4. Typical "shear crack hinge", beam A 5.

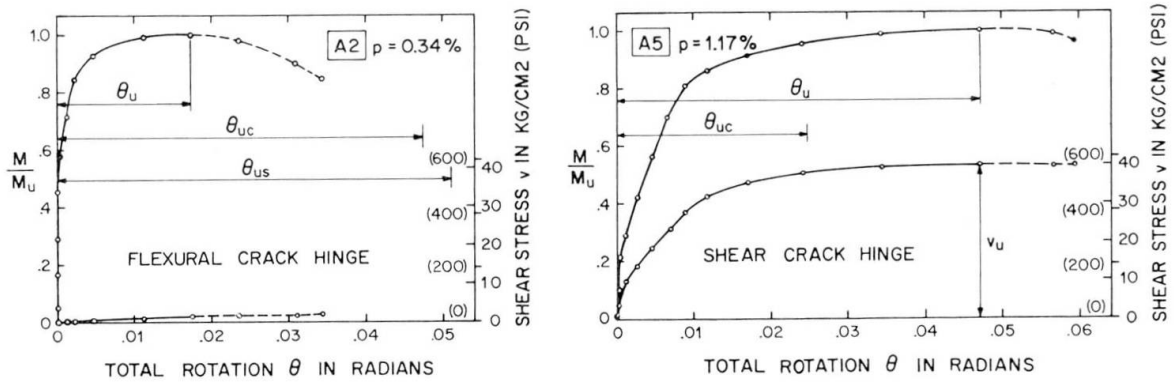


Fig. 5. Moment-rotation and shear stress-rotation relationship of a flexural crack hinge and of a shear crack hinge.

deformation of the hinges was considered to occur in the zone of plastic extension of the tensile reinforcement. This "plastic length L_p" was observed to be 25 cm (nom. 10 in.) at the flexural crack hinge of beam A 2 and 80 cm (nom. 31 in.) at the shear crack hinge of beam A 5. Also the nominal shear stress $v = V/b' d$ in the hinge is plotted against the total rotation in Fig. 5.

The rotational capacity can be characterized by the rotation θ_u which is reached at the ultimate moment M_u. Fig. 5 shows that the rotational capacity θ_u of the shear crack hinge is considerably greater than that of the flexural crack hinge. This result and the rupture of the tension steel in the span hinges of the beams A 1, A 2 and A 3 are incompatible with the usual view and theories as stated in [2] and [3] for instance.

Table 1 lists the values of the amount of the tensile reinforcement as a percentage p, the nominal shear stress v_u at M_u, and the corresponding moment-shear ratio $M_u/V_u d$ at the flexural crack hinge of the beams A 1, A 2, and A 3.

Table 1. Details, Measured and Calculated Values of Test Beams

Beam No.	p percent	v_u kg/cm² (psi)	$\frac{M_u}{V_u d}$	θ_u radians	θ_{uc} radians	$\frac{\theta_u}{\theta_{uc}}$	θ_{us} radians	$\frac{\theta_u}{\theta_{us}}$	θ_{ut} radians	$\frac{\theta_u}{\theta_{ut}}$
A 1	0.34	2.86 (41)	4.4	0.0100	0.0506	0.20	0.0477	0.21	0.0074	1.35
A 2	0.34	1.51 (21)	9.6	0.0173	0.0474	0.36	0.0509	0.34	0.0094	1.84
A 3	0.51	0.27 (4)	83	0.0188	0.0316	0.59	0.0525	0.36	0.0131	1.43

In addition, the rotations θ_u measured over a gauge length of 25 cm (nom. 10 in.) which included the zone of the steel rupture, are listed in Table 1. In beam A 2 plastic deformations of the steel were only produced within this gauge length. Plastic deformations could also be observed outside this gauge length in beam A 1 to a small extent and in beam A 3 to a greater extent. For this reason, the values of θ_u for A 1 and A 3 are only representative of the rotational capacity of the gauge length.

The values of θ_{uc} listed in Table 1 were calculated by the method given in [2] and [3]. θ_{uc} is computed by multiplying a "curvature of rupture" by the plastic length:

$$\theta_{uc} = \frac{\epsilon_{cu}}{c_0} L_p . \tag{2}$$

Taking into account the effect of the binding of the concrete compression zone by stirrups and compression steel as given in [3] the maximum concrete compressive strain ϵ_{cu} was found to be 0.0038. The depth of the neutral axis c_0 was computed neglecting the compression steel as given in ACI 318-63. The plastic length L_p was taken as the gauge length of θ_u, i. e. $L_p = 25$ cm (nom. 10 in.). Comparing θ_u and θ_{uc} in Table 1 it is found that the measured values reach to only 20 to 59 percent of the calculated values.

In analogy to Eq. (2) the total rotation θ_{us} for failure due to rupture of the tension steel is usually calculated by the following formula:

$$\theta_{us} = \frac{\epsilon_{s\,max}}{d - c_0} L_p , \tag{3}$$

in which ϵ_{max} means the maximum steel strain at rupture, viz:

$$\epsilon_{s\,max} = \epsilon_{su} + \frac{f'_s}{E_s} . \tag{4}$$

ϵ_{su} denotes the permanent steel strain measured on a gauge length not including the rupture zone (see Fig. 2). E_s is the modulus of elasticity of the steel.

For the calculation of θ_{us}, L_p was taken again as 25 cm (nom. 10 in.). The results listed in Table 1 show that θ_{us}, as well as θ_{uc}, considerably overrates the measured rotation θ_u. If θ_u, θ_{uc}, and θ_{us} were to be calculated with respect to the observed plastic length and the theoretical plastic length as given in [2] and [3], still greater differences would be obtained.

The situation is quite different with shear crack hinges. As an example the calculated rotation θ_{uc} of the beam A 5 is given in Fig. 5. It demonstrates that for shear crack hinges, θ_{uc} considerably underrates the measured rotation θ_u.

Shear Behaviour

In the cracked sections of flexural crack hinges the shear is almost exclusively carried by the concrete compression zone. If the stress in the tensile reinforcement exceeds the yield strength, any possible shear carrying capacity by interlocking of the aggregates is lost; nor is the dowel action of the tensile reinforcement usually significant.

It was of great interest to realize that in shear crack hinges the stirrup stress is not influenced by the hinge rotation. As an example the shear force V_c in the beam B 4 is plotted against the rotation θ in Fig. 6. V_c denotes here that part of the total shear force V which was not carried by the stirrup rein-

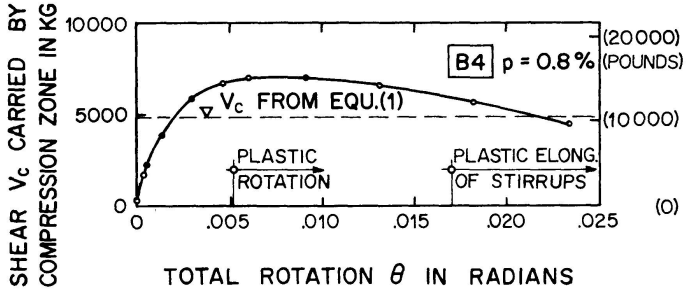


Fig. 6. Shear force V_c carried by compression zone versus total rotation θ at shear crack hinge beam B 4.

forcement according to the truss analogy; hence it was mainly carried by the concrete compression zone. In all the shear crack hinges of the described investigation a significant reduction of V_c could only be observed after some of the stirrups sustained plastic deformations. For this reason, the stress in stirrups of a shear crack hinge is essentially a function of the acting shear force. The stirrup stress does not depend primarily on the deformations produced by progressive rotation.

Further details of the test results are given in a earlier report [4].

Theoretical Investigation

The following approaches try to describe the behaviour of reinforced concrete plastic hinges by means of models which are chosen as close to reality as possible.

Flexural Crack Hinges

The model of a flexural crack hinge is shown in Fig. 7. The spacing of cracks measured along the tension reinforcement is denoted by z. All the

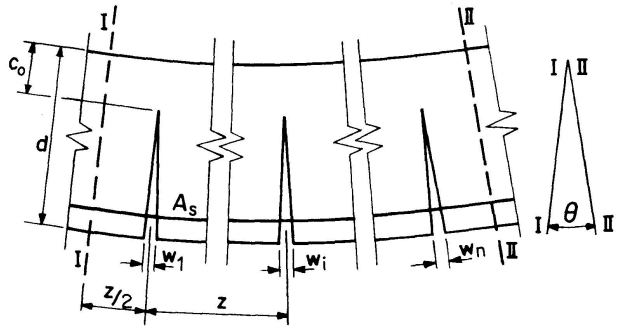


Fig. 7. Model of the flexural crack hinge.

cracks belong to the hinge in which plastic deformations of the steel occured. Neglecting the unimportant elongation of the concrete between the cracks the total rotation θ is given by Eq. (5):

$$\theta = \sum_{i=1}^{n} \frac{w_i}{d - c_0} = \frac{1}{d - c_0} \sum_{i=1}^{n} w_i . \tag{5}$$

w is the width of the crack at the level of the tensile reinforcement.

A "flexural crack element" is shown in Fig. 8. First we assume that this element is affected only by a bending moment M. For this assumption the variation of the following quantities is plotted along the tensile reinforcement:

— The steel strain ϵ_s.
— The steel stress f_s.
— The nominal bond stress u between the surface of reinforcement and the concrete.
— The slip s between the reinforcement surface and the concrete.

To calculate the values of these variables the following fundamental relationships are needed:

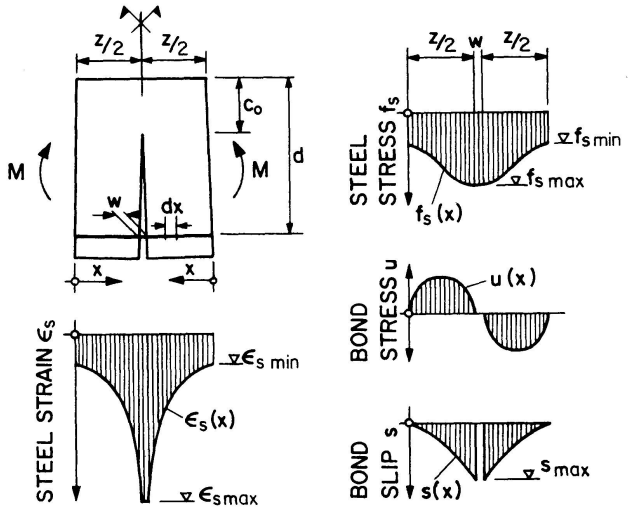


Fig. 8. "Flexural crack element" with variation of several variables.

— The bond-slip curve $u(s)$.
— The stress-strain curve $\epsilon_s(f_s)$ of the steel.

The bond-slip curve of the bar element dx can be found experimentally as shown in [5]. Typical curves for vertically embedded bars are given in Fig. 9. The bond stresses u of horizontally embedded bars are much smaller in most cases.

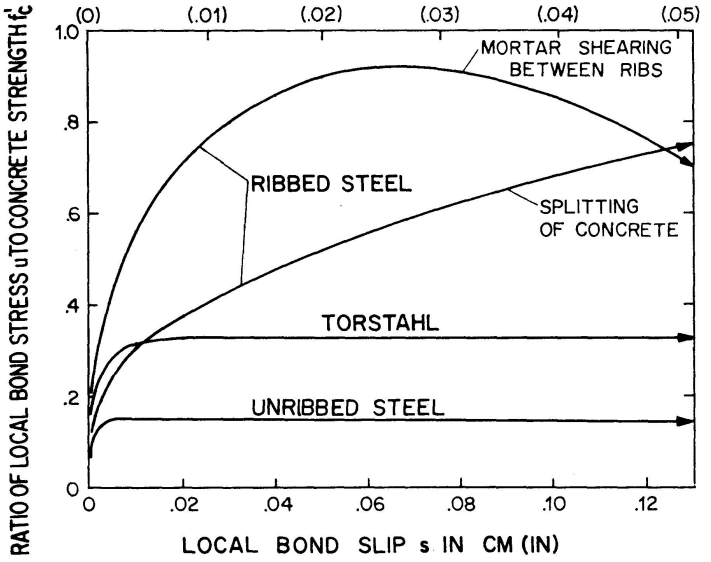


Fig. 9. Typical bond-slip curves of finite elements of vertically embedded bars.

The following relationships between the variables listed above are applic able:

$$df_s \frac{\pi D^2}{4} = u(s)\, D\, \pi\, dx; \qquad \frac{df_s}{dx} = \frac{4}{D} u(s), \tag{6}$$

$$ds = \epsilon_s(x)\, dx; \qquad \frac{ds}{dx} = \epsilon_s(f_s). \tag{7}$$

D is the diameter of the tension steel bars. A general solution of the problem for any functions $u(s)$ and $\epsilon_s(f_s)$ is given in [6]. This approach only investigates the case of steel rupture. The bond-slip curve of "Torstahl" used in the test beams is assumed to be a straight line parallel to the abscissa, hence $u(s) =$ constant $= u^*$ (compare with Fig. 9). For that reason, the function $\epsilon_s(x)$ is a part of the stress-strain curve of the steel. The Eqs. (6) and (7), respectively, lead to the following expressions for the length $z/2$ from the centre of a crack:

$$\Delta f_s = f_{s\,max} - f_{s\,min} = u^* \frac{4}{D} \frac{z}{2}, \tag{8}$$

$$s_{max} = \int_0^{z/2} \epsilon_s(x)\, dx = \frac{D}{4\, u^*} \int_{f_{s\,min}}^{f_{s\,max}} \epsilon_s(f_s)\, df_s. \tag{9}$$

If $f_{s\,max}$ and $\epsilon_{s\,max}$ are given and Δf_s is calculated from (8), the integral expression of (9) can be evaluated from the stress-strain curve of the steel.

The width of the crack is given by

$$w = 2 s_{max} (1 + \epsilon_{s\,max}). \tag{10}$$

The relationship of the average steel strain ϵ_{sa} within the flexural crack element to the maximum steel strain $\epsilon_{s\,max}$ in the crack is characterized by the bond factor κ:

$$\kappa = \frac{\epsilon_{sa}}{\epsilon_{s\,max}} = \frac{2 (1 + \epsilon_{s\,max}) \int_0^{z/2} \epsilon_s (x)\, dx}{z\, \epsilon_{s\,max}}. \tag{11}$$

The value of κ varies from 0.10 to 1.0. κ depends on $\epsilon_{s\,max}$, the shape of the stress-strain curve of the steel (especially the strain-hardening characteristic) and on the quality of the bond.

If the rupture of the steel occurs in a certain flexural crack element, No 1 say, $\epsilon_{s\,max}$ is given by Eq. (4). Then the steel stress in the crack of the neighbour element No 2 is computed by

$$f^2_{s\,max} = f^1_{s\,max} - \frac{\Delta M^{1,2}}{(d - a/2)\, A_s}, \tag{12}$$

where $\Delta M^{1,2}$ is the moment difference between the crack cross sections No 1 and No 2 of the beam at failure, a the depth of the equivalent rectangular stress block in the compression zone, and A_s is the area of the tensile steel. If M varies linearly, Eq. (12) becomes:

$$f^2_{s\,max} = f^1_{s\,max} - \frac{V z}{(d - a/2)\, A_s}. \tag{13}$$

Computing the total ultimate rotation of the hinge θ_u from Eq. (5), each flexural crack element in which plastic steel deformations are present must be taken in account.

This method neglects that the points of zero slip, $s = 0$, is not exactly midway between two adjacent cracks. This point is located slightly closer to the crack with the smaller strain $\epsilon_{s\,max}$. However, as shown in [6], the resulting error is not significant and can be neglected.

The theoretical ultimate rotations θ_{ut} of the gauge length of 25 cm (nom. 10 in.) of the test beams A 1, A 2 and A 3 were computed with this method of calculation using the material properties and the observed crack spacing of the test beams and listed in Table 1. The constant bond stress u^* was assumed to be 50 kg/cm² (nom. 700 psi). To determine ΔM, the theoretical ultimate moment distribution according to the simple plastic analysis was used, and not the measured values.

The comparison of θ_u and θ_{ut} in Table 1 shows that the measured values are 35 to 84 percent greater than the theoretical values. The value of θ_{ut} is

always on the safe side, because several effects not introduced in the theory increase the ultimate rotation. For instance the bond between the steel bars and the concrete at the border of the cracks may become loose over a certain length producing a steel strain $\epsilon_{e\,max}$ on both sides of the cracks. For this reason, it can be concluded that the developed method alwasy gives safe values of the ultimate rotation.

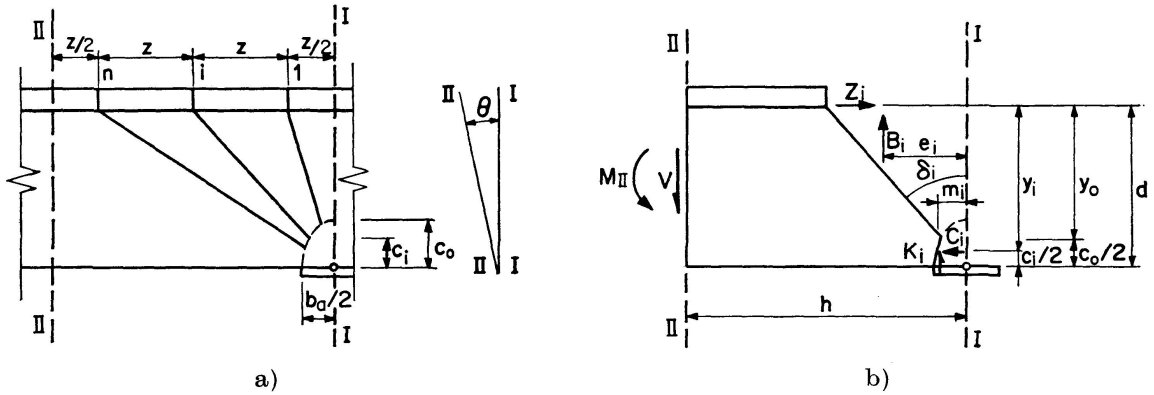
Considering the influence of the important variables, the ultimate rotations θ_u and θ_{ut} as determined by the rupture of the steel are found to decrease with:

— Better bond properties.
— Smaller bar diameters.
— Less strain-hardening.
— Smaller permanent steel strain.
— Greater crack spacing.
— Greater shear force.

Comparing the values of θ_{ut} listed in Table 1 with respect to the shear force it is found that the method of calculation correctly takes into account the influence of the shear force.

Shear Crack Hinges

It was found that in shear crack hinges the rotational capacity is mostly much greater than calculated by the usual methods. It will be shown here why plastic deformations can occur over a wide zone.



a) b)

Fig. 10. Model and internal forces of a shear crack hinge.

The model of a shear crack hinge is shown in Fig. 10a. This model corresponds to the often observed crack pattern shown in Fig. 4. The maximum inclination of the flexural-shear cracks of the hinge is characterised by tan $\delta_n = 1.3$. It is assumed that the tensile reinforcement has good bond properties (ribbed steel bars). Furthermore it is supposed that the shear reinforcement only consists of closely spaced vertical stirrups.

The part of the beam on the left of the flexural-shear crack i of Fig. 10a is shown in Fig. 10b. All the free body forces are shown. It is assumed that no

external loads exist between the cross sections I and II. Cross section II is affected by the bending moment M_{II} and the shear force V. The force in the tensile steel is denoted by Z_i. B_i is the resultant of the stirrup forces crossing the flexural-shear crack i on the left of the support. C_i and K_i denote the forces acting in the flexural compression zone parallel and perpendicular respectively to the beam axis. Any possible fixed end moment between two neighbouring cracks and dowel action of the tensile reinforcement are neglected. Furthermore, due to the large cracks widths, the shear transfer across cracks by the interlocking of aggregate particles must not be considered. The positions of the lines of action of the forces are shown in Fig. 10 also. As a simplification the distance of C_i from the extreme compression fiber is taken as $c_i/2$. c is the distance from the extreme compression fibre to the end of a flexural-shear crack (elliptical form), and b_a the support width.

With $M_I = M_{II} + V h$ the force Z_i in the tensile reinforcement is given by equilibrium conditions:

$$Z_i = \frac{M_I}{Y_i} - B_i \frac{e_i}{y_i} - K_i \frac{m_i}{y_i}. \tag{14}$$

With some transformations Eq. (14) becomes more appropriate for plotting and discussion in the following form:

$$Z_i = V \left[\frac{M_I}{V y_i} - \frac{B_i}{V} \left(\frac{e_i}{y_i} - \frac{m_i}{y_i} \right) - \frac{m_i}{y_i} \right]. \tag{15}$$

B_i/V can be expressed for $\tan \delta_i \geqq b_a/2$ as follows:

$$\frac{B_i}{V} = \frac{B_{45}}{V} \left[\frac{\tan \delta_i - b_a/2d}{1 - b_a/2d} \right]. \tag{16}$$

B_{45} is the resultant of the stirrup forces crossing a 45° crack. Furthermore, if c_0/d and b_a/d are given, the distances e_i, m_i, and y_i are a function of the angle δ_i alone. When using Eq. (16) care must be taken that the condition $B_i/V \geqq 1.0$ is always satisfied.

For flexural cracks perpendicular to the beam axis instead of inclined flexural-shear cracks, the tensile force Z_i would be given by

$$Z_i = V \left[\frac{M_I}{V y_0} - \frac{d}{y_0} \tan \delta_i \right]. \tag{17}$$

In this formula $\tan \delta_i$ characterises the distance from the considered flexural crack to the point of maximum moment (cross section I). Eq. (17) also gives the tensile force corresponding to the usual bending theory of reinforced concrete beams with y_0 as the lever arm of the internal bending forces: $Z_i = M_i/y_0$.

When discussing the derived formulas the following values are usually assumed:

$$\frac{c_0}{d} = 0.2; \qquad \frac{b_a}{d} = 0.3.$$

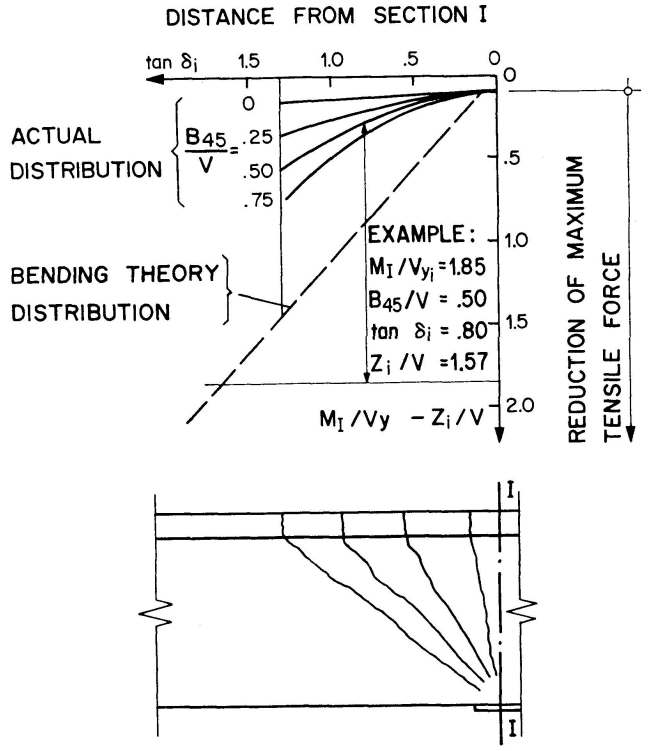


Fig. 11. Distribution of the tensile force in a shear crack hinge.

A dimensionless diagram of the distribution of the tensile force for several assumptions is given in Fig. 11. On the abscissa the distance from the cross section under consideration to cross section I is characterised by tan δ_i. On the ordinate the values of $(M_I/V\,y - Z_i/V)$, which are calculated by Eqs. (15) and (17) are plotted. Therefore, the ordinate values correspond to the reduction of the maximum amount of the tensile force over the support.

For several values of the ratio B_{45}/V the actual force distribution in a zone of flexural-shear cracks is given in the upper part of Fig. 11. B_{45}/V characterises the stress and efficiency of the shear reinforcement. The portion K_{45} of the shear force V which is not transferred by the shear reinforcement is carried by the compression zone. Since the values of M_{45} are always greater than or equal to $V_C = v_c b' d$, the value of B_{45}/V essentially depends on the shear force $V = v b' d$. As a result, B_{45}/V is often very low. But if a very high shear stress v exists, B_{45}/V increases to a maximum value of about 0.75. Furthermore, the distribution of the tensile force, assuming flexural cracks or calculated by the usual bending theory, is shown in Fig. 11. The tensile force is proportional to the bending moment.

In Fig. 11 it can be seen that in a zone of flexural-shear cracks the reduction of the maximum tensile force is relatively low. This explains the wide spread of plastic deformations in shear crack hinges. Since the small force reduction can be compensated by strain hardening of the steel the plastic length of the hinge on both sides of the support often is equal to or greater than the effective depth of the beam.

Dependence of Rotational Capacity on Shear Stress

The dependence of the ultimate rotation θ_u on the shear stress v is shown only generally and qualitatively in Fig. 12. If $v < v_k$ flexural cracks only occur. If $v > v_k$ flexural-shear cracks are developed. Corresponding to these crack

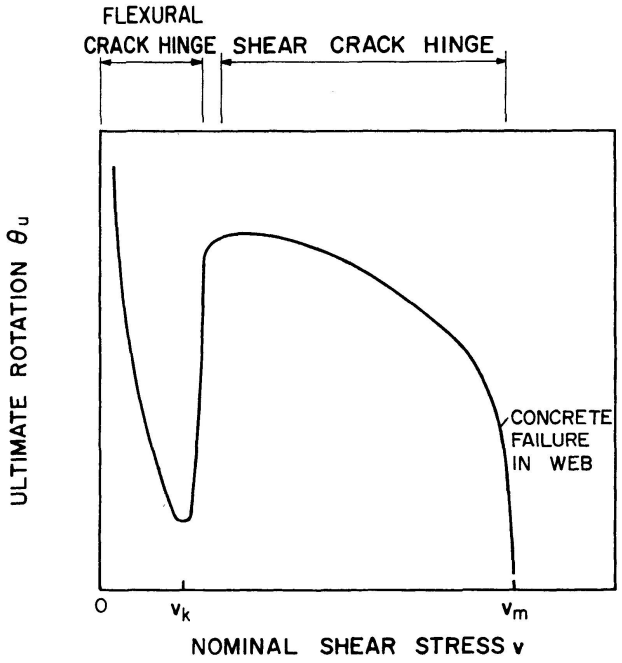


Fig. 12. General dependence of ultimate rotation θ_u on the nominal shear stress v.

patterns a flexural crack hinge or a shear crack hinge develops. In a flexural crack hinge the plastic deformations are concentrated into a smaller zone the greater v is. The value of the ultimate rotation θ_u accordingly decreases. Assuming that a rupture of the steel occurs, the reduction of θ_u is very high. In the case of a concrete fracture a reduction is also confirmed. If the shear stress is enough to produce flexural-shear cracks, the rotation θ_u considerably increases since plastic deformations occur on a much wider zone. With increasing shear stress v the ultimate rotation θ_u decreases again. But if sufficient shear reinforcement exists, a drastic reduction of θ_u only occurs as $v \to v_m$ through crushing of the concrete in the web due to shearing deformations and inclined compression forces. Depending on several conditions the values of v_k and v_m can vary considerably. From tests it can be concluded that v_k and v_m reach approximately the value of v_c and $(4-5)\,v_c$, respectively.

Conclusions

As a result of this experimental and theoretical investigation the following conclusions can be made:

1. According to the amount of shear stress two quite different types of plastic hinges are produced:

— "Flexural crack hinges" which occur in the beam zone mainly affected by a bending moment, and only producing flexural cracks perpendicular to the beam axis (Fig. 3), and

— "Shear crack hinges" which occur in the beam zones which are, in addition to a bending moment, affected by a considerable shear force, and exhibit inclined flexure-shear cracks (Fig. 4).

2. In a flexural crack hinge plastic deformations may be concentrated to a single or only a few flexural cracks. For this reason the rotational capacity may be very small.

3. The danger of a steel rupture can follow from good bond properties of the tensile reinforcement in a flexural crack hinge, since the steel strain only increases in the cracks, while between the cracks the steel strain is still in the elastic range.

4. The usual method of calculating the rotational capacity by integrating a "curvature of rupture" over a "plastic length" may lead to severe errors. The values of ultimate rotation in the case of a steel rupture measured in the described tests reach only 20 to 59 percent of the values calculated by the usual method mentioned above.

5. Therefore, the rotational capacity of flexural crack hinges, particularly in case of a steel rupture, should be investigated with the corresponding crack model (Fig. 7). This method correctly takes into account the influence of bond, bar diameter, strain and strain-hardening properties of tensile reinforcement, as well as the influence of shear force. Thus, this theory gives safe lower limit values of the ultimate rotation.

6. On the other hand plastic deformations in shear crack hinges usually extend over a relatively wide zone. For this reason, the rotational capacity is correspondingly high.

7. This observation can be explained with the aid of the crack model for the shear crack hinge (Fig. 10). The tensile force in the steel is considerably greater than in the case of flexural cracks only or calculated by the usual bending theory.

8. In shear crack hinges the stress of vertical stirrups is mainly a function of the value of the shear force. The stirrup forces do not depend on the deformations in the hinge caused by progressive rotation.

9. In a zone of flexural cracks the shear stress may considerably decrease the rotational capacity. However, if the shear stress is high enough to produce inclined flexural-shear cracks, the rotational capacity is significantly increased.

Notation

A_s area of tensile reinforcement
a depth of the equivalent rectangular stress block in compression zone
B resultant of stirrup forces crossing a flexure-shear crack
b width of compression face
b' width of web
b_a support width
C compression force in bending compression zone
c distance from extreme compression fibre to the end of a flexure-shear crack
c_0 distance from extreme compression fibre to neutral axis and to the end of flexural crack
D bar diameter
d distance from extreme compression fibre to centroid of tensile reinforcement
E_s modulus of elasticity of steel
e distance of the line of action of B from the support in a shear crack hinge
f'_c compressive strength of concrete
f_e elastic limit stress of reinforcement (0.005 percent proof stress)
f_s tensile stress in steel
f'_s tensile strength of reinforcement
f_y yield strength of reinforcement (0.2 percent proof stress)
h distance of the line of action of V from the support in a shear crack hinge
K shear force in bending compression zone of a shear crack hinge
L_p plastic length of hinge
M bending moment
M_u ultimate bending moment
m distance fixing the acting line of K in a shear crack hinge
p tensile steel ratio A/bd
s slip between reinforcement surface and concrete
u nominal bond stress between reinforcement surface and concrete
V shearing force
V_c shear force carried by the concrete compression zone
V_u shear force at ultimate moment
v nominal shear stress $v = V/b'd$
v_u nominal shear stress at (ultimate moment) M_u
v_k nominal shear stress at which flexure-shear cracks are developed
v_m nominal shear stress at failure due to crushing of the concrete
v_c nominal shear stress in concrete compression zone
w width of a crack at tensile reinforcement
y distance determining the line of action of Z in a shear crack hinge
Z force in tensile reinforcement
z spacing of cracks measured along tensile reinforcement

δ angle between a flexure-shear crack and a line perpendicular to the beam axis
ϵ_{cu} maximum concrete compressive strain at M_u
ϵ_s tensile strain in steel
ϵ_{sa} average steel strain
ϵ_{su} permanent steel elongation as a percentage measured on test bars outside of rupture
θ total rotation occurring within the plastic length L_p
θ_u total rotation at ultimate moment M_u
θ_{uc} total rotation calculated by the method as given in [2] and [3] (failure due to failure of concrete)
θ_{us} total rotation calculated by Eq. (3) (failure due to rupture of steel)
λ ratio of calculated ultimate moment in span and over the central support

Acknowledgement

The beam tests were made possible by a research grant from the Von Moossche Eisenwerke at Lucerne (Switzerland) which is gratefully acknowledged. Furthermore the author wishes to thank Prof. Dr. B. Thürlimann and Prof. E. Amstutz from the Swiss Federal Institute of Technology (ETH), Zurich, under whose guidance and with whose help this research programme has been carried out.

References

[1] B. Thürlimann, H. Ziegler: Plastische Berechnungsmethoden (Plastic Design Method). Autographie der Vorlesungen vom Fortbildungskurs für Bau- und Maschineningenieure, ETH, Zürich, 1963.

[2] ACI-ASCE Committee 428: Progress Report on Code Clauses for Limit Design. ACI Journal, Proceedings V. 65, No. 9, September 1968, p. 713–720.

[3] W. G. Corley: Rotational Capacity of Reinforced Concrete Beams. Proceedings, ASCE, V. 92, No. ST 5, October 1966, p. 121–146; also PCA Development Bulletin D-108.

[4] H. Bachmann, B. Thürlimann: Versuche über das plastische Verhalten von zweifeldrigen Stahlbetonbalken (Tests on the Plastic Behavior of Two-Span Reinforced Concrete Beams). Berichte Nr. 6203-1 und 6203-2 des Instituts für Baustatik an der Eidgenössischen Technischen Hochschule (ETH), Zürich, 1965.

[5] G. Rehm: Über die Grundlagen des Verbundes zwischen Stahl und Beton (On the Bond between Steel and Concrete). Deutscher Ausschuß für Stahlbeton, Heft Nr. 136, Berlin 1961.

[6] H. Bachmann: Zur plastizitätstheoretischen Berechnung statisch unbestimmter Stahlbetonbalken (On the Plastic Design of Statically Indeterminate Reinforced Concrete Beams). Bericht Nr. 13 des Instituts für Baustatik an der Eidgenössischen Technischen Hochschule (ETH), Zürich, Juli 1967.

Summary

10 two-span reinforced concrete beams were tested to study the influence of shear and bond on the rotational capacity of reinforced concrete plastic hinges.

The shear stress determines whether a "flexural crack hinge" or a "shear crack hinge" occurs. In flexural crack hinges the rotational capacity can be considered smaller than the values calculated by usual methods. Therefore a new method of calculation giving safe values has been developed. On the other hand in shear crack hinges plastic deformations occur within a wide zone allowing a larger rotational capacity.

Résumé

On a fait des essais avec dix poutres en béton armé à deux travées pour étudier l'influence de la sollicitation de cisaillement et de l'adhérence des armatures sur la capacité de rotation des rotules plastiques en béton armé.

Suivant la valeur de la sollicitation de cisaillement, il résulte une „rotule due à une fissure de flexion" ou une „rotule due à une fissure de cisaillement". Dans des rotules dues à la flexion, la capacité de rotation peut être très inférieure à celle calculée d'après les méthodes usuelles. Par conséquent, il est nécessaire de développer une nouvelle méthode de calcul qui donne des résultats sûrs. Au contraire, dans des rotules dues au cisaillement, les déformations qui s'étendent sur un large domaine provoquent une grande capacité de rotation.

Zusammenfassung

Es wurden Versuche an 10 zweifeldrigen Stahlbetonbalken gemacht zwecks Studium des Einflusses von Schubbeanspruchung und Verbund auf die Rotationsfähigkeit plastischer Stahlbeton-Gelenke.

Je nach Höhe der Schubbeanspruchung entsteht ein „Biegeriß-Gelenk" oder ein „Schubriß-Gelenk". In Biegeriß-Gelenken kann die Rotationsfähigkeit wesentlich kleiner sein als sie sich nach üblichen Methoden berechnen läßt. Daher wird eine neuartige Berechnungsmethode entwickelt, die sichere Resultate liefert. Demgegenüber entstehen in Schubriß-Gelenken plastische Verformungen über einen weiten Bereich, die eine entsprechend große Rotationsfähigkeit bewirken.

Analysis of Plates in Bending Using Large Finite Elements

Calcul des plaques fléchies à l'aide d'éléments finis de grandes dimensions

Berechnung der Biegung von Platten mittels großer endlicher Elemente

AMIN GHALI
Professor of Civil Engineering,
University of Calgary, Calgary, Alberta,
Canada

K. J. BATHE
Research Assistant, University of Calgary

Introduction

Solutions to plate bending problems can often only be obtained by taking recourse to numerical methods. A conventional finite element analysis can give a solution to practically any plate bending problem. In such analysis, the structure is idealized as an assemblage of a large number of small elements. It can be shown that a solution approaching the exact solution to the problem can be obtained as the number of elements used in the analysis increases [1].

In many practical plate bending problems, the continuum can be idealized to an assemblage of a small number of large rectangular and/or right angle triangular elements. For the analysis of such an assemblage, the flexibility or stiffness matrices of the large individual elements are needed. In this paper, the flexibility and the stiffness matrices of "large" rectangular and right-angle triangular elements in bending are derived by simple matrix operations with finite differences equations.

The two main difficulties arising in conventional finite differences (F.D.) analysis of complex plate bending problems may be outlined as follows:

1. To predict accurately the stress in the continuum it may be necessary to use a large number of F.D. equations. The solution of large systems of F.D. equations may become impossible due to the capacity of the computer used or due to round-off errors.

2. Boundary conditions and discontinuities of the plate can not be easily accounted for in the F.D. solution. It is mainly for this reason that in many

cases finite element analysis is preferred, although it usually involves the solution of a larger number of equations.

The object of this paper is to show how the general displacement method (as used in the finite element analysis) together with finite differences can overcome the difficulties mentioned above. The plate structures considered may be of any configuration but shall have linear boundaries. For the analysis, the structure is idealized as an assemblage of a small number of large triangular and/or rectangular elements (Fig. 1). The largest number of equations to be handled simultaneously are either the F. D. equation used in deriving the flexibility (or stiffness) of an individual element, or the force displacement relations of the assembled structure.

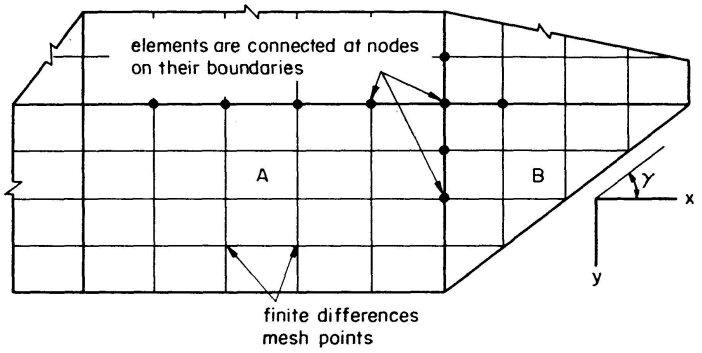


Fig. 1. Large Element Idealization of a Plate.

The method presented in this paper is developed to be used as a part of the analysis of box-girder skew bridges. An analysis of such structures by conventional finite differences appears difficult if not impossible for the reasons mentioned above. On the other hand a conventional solution by finite element may become expensive because of the large number of simultaneous equations involved.

If, for example, a single-cell box-girder skew bridge is considered as an assemblage of large plate elements subjected to in-plane and bending forces, a solution by displacement method can be obtained in which finite differences are used for the derivation of the element stiffness matrix. This paper deals only with the bending of plates while the stiffness matrix of the plate element corresponding to in-plane displacement is presented elsewhere [3].

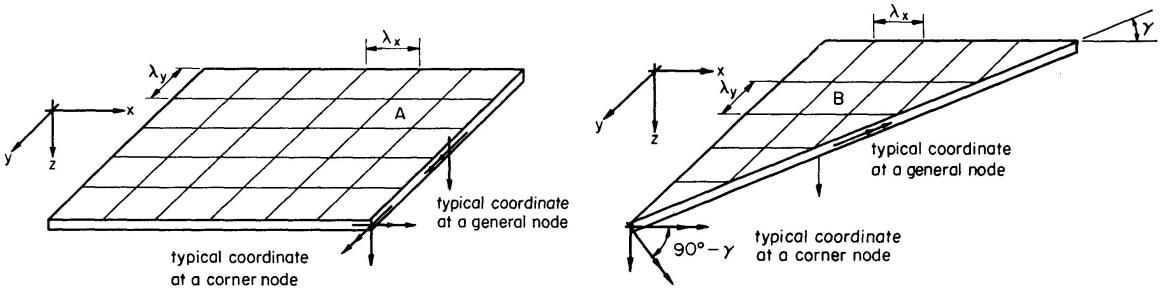
SZILARD [4] derived the stiffness matrix of a square plate element using finite differences. He used coordinates at the centre of each element side. The structure must be divided into a large number of small elements to obtain accurate results. In the method presented in this paper, the plates are divided into elements which are essentially large (as mentioned earlier). Accuracy is increased if the finite difference mesh size within the element is reduced and larger elements are chosen. ANG and NEWMARK [2] analyzed continuous slab panels by idealizing the plate as a system of rigid bars and springs, for which

the deflection and load are related by equations identical to the F.D. equations of the plate. First, the deflection of each slab panel is calculated assuming the edges to be fixed. Then the panel boundary displacements could be determined using a relaxation technique. In this manner, the solution of a large number of F.D. equations was avoided.

In the following section, the flexibility and stiffness matrices of rectangular and triangular elements are derived.

Derivation of Element Flexibility and Stiffness Matrices

The large elements idealizing the plate are assumed to be connected at a finite number of node points along their boundaries (Fig. 1). Fig. 2 shows a typical rectangular element A and a right-angle triangular element B. A F.D. mesh is chosen such that node points on the lines between the elements in the assembled plate coincide with F.D. mesh points. At node points on the element edges two degrees of freedom may be considered, a transverse deflection and



a) Rectangular Element A b) Right-Angle Triangular Element B

Fig. 2. Typical Coordinates at Nodes on Edges ant at Corners.

a rotation about an axis along the edge. At a corner node point, the degrees of freedom can be a transverse deflection and rotations about axes perpendicular to the two edges meeting at that corner. Compatibility of displacement of elements will be achieved at these nodes at the chosen coordinates (Fig. 1). If the boundary nodes are sufficiently close, the deformation of the assembled elements will represent that of the actual slab.

The differential equation to be satisfied at any mesh point on the element is [5]

$$\frac{\partial^4 w}{\partial x^4}+2\frac{\partial^4 w}{\partial x^2 \partial y^2}+\frac{\partial^4 w}{\partial y^4}=\frac{q}{N}, \tag{1}$$

where w is the deflection of the plate; q intensity of a distributed transverse applied load;

$$N=\frac{E h^3}{12(1-\nu^2)}. \tag{2}$$

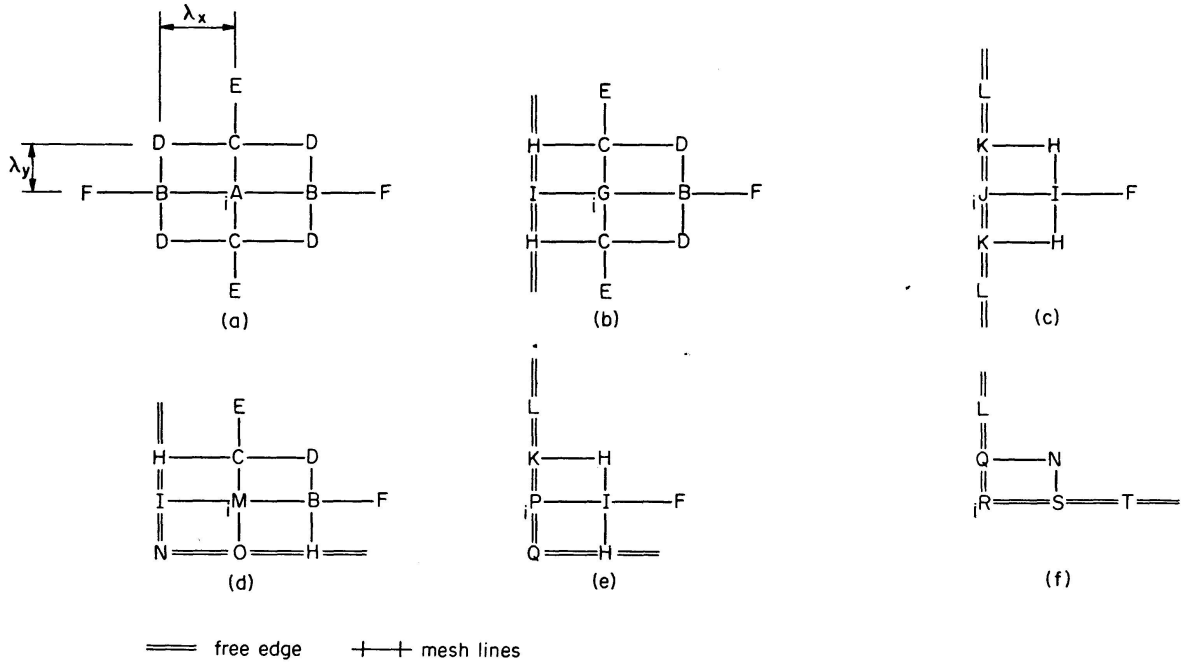
E is the modulus of elasticity; h the thickness (assumed constant for each element) and ν Poisson's ratio. Using central finite differences, Eq. (1) applied at a typical mesh point i, away from the boundary, can be written in the form [6]:

$$N\frac{\lambda_y}{\lambda_x^3}[A]\{w\} = Q_i, \tag{3}$$

where $[A]$ is a row matrix of dimensionless coefficients of the deflection at i and at 12 other points in its vicinity;

$$Q_i = q_i\lambda_x\lambda_y, \tag{4}$$

λ_x and λ_y being the mesh spacings in the x and y directions (Fig. 2).



$A = 6+6\alpha^2+8\alpha$ $\quad H = \alpha(2-\nu)$ $\quad O = -2\alpha(2-\nu+\alpha)$

$B = -4(1+\alpha)$ $\quad I = -2(2\alpha-\nu\alpha+1)$ $\quad P = 1+4\alpha(1-\nu)+\frac{5}{2}\alpha^2(1-\nu^2)$

$C = -4\alpha(1+\alpha)$ $\quad J = 1+4\alpha(1-\nu)+3\alpha^2(1-\nu^2)$ $\quad Q = -2\alpha\left[1-\nu+\frac{\alpha}{2}(1-\nu^2)\right]$

$D = 2\alpha$ $\quad K = -2\alpha[1-\nu+\alpha(1-\nu^2)]$ $\quad R = 2\alpha(1-\nu)+\frac{1}{2}(1+\alpha^2)(1-\nu^2)$

$E = \alpha^2$ $\quad L = \frac{1}{2}\alpha^2(1-\nu^2)$ $\quad S = -2\left[\alpha(1-\nu)+\frac{1}{2}(1-\nu^2)\right]$

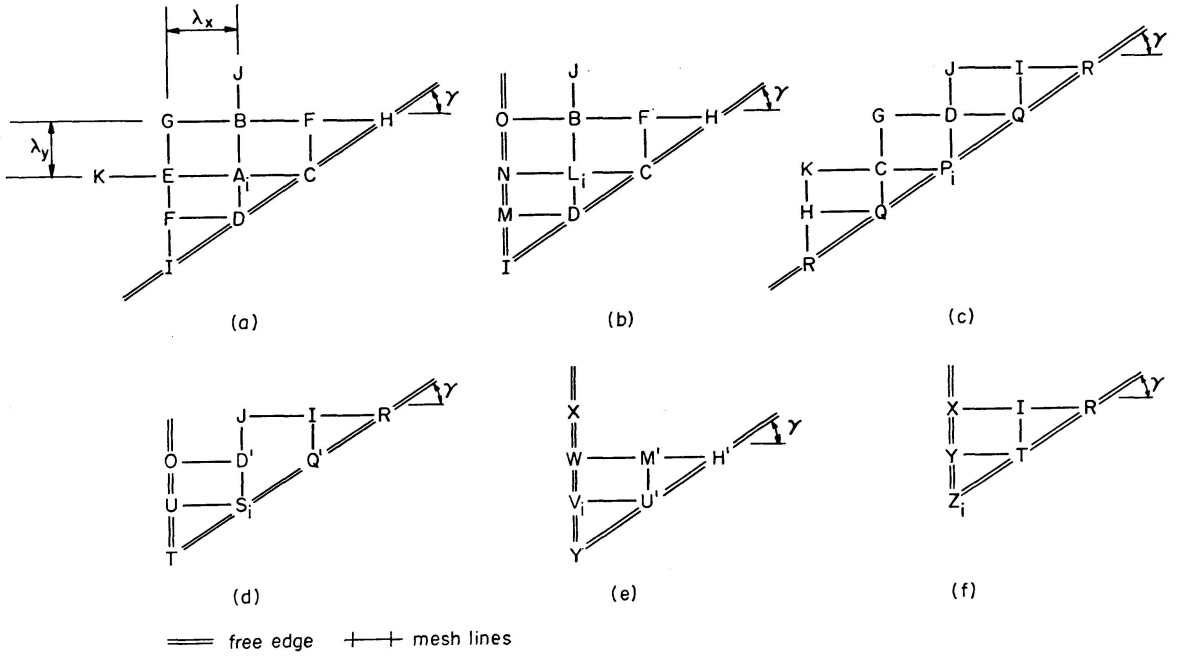
$F = 1$ $\quad M = 5+5\alpha^2+8\alpha$ $\quad T = \frac{1}{2}(1-\nu^2)$

$G = 5+6\alpha^2+8\alpha$ $\quad N = 2\alpha(1-\nu)$

Where $\alpha = \left(\frac{\lambda_x}{\lambda_y}\right)^2$

Fig. 3. Finite Difference Coefficients for a Rectangular Plate with Free Edges. Coefficients to be Used in the Equation:

$$\left(\frac{N\lambda_y}{\lambda_x^3}\right)[\text{coefficients}]\{w\} = Q_i.$$



$A = 5+5\alpha^2+8\alpha$

$B = -4\alpha(1+\alpha)$

$C = -2(1+\alpha)-\epsilon(2-\alpha)$

$D = -2\alpha(1+\alpha)-\epsilon(2\alpha-1)$

$D' = -2\alpha(1+\alpha)-\epsilon(2\alpha-1)+\epsilon c$

$E = -4(1+\alpha)$

$F = \alpha$

$G = 2\alpha$

$H = \epsilon$

$H' = \epsilon - c\nu(1-\nu)$

$I = \epsilon\alpha$

$J = \alpha^2$

$K = 1$

$L = 4+5\alpha^2+8\alpha$

$M = \alpha(1-\nu)$

$M' = \alpha(1-\nu)-c\alpha(1-\nu)$

$N = -2(2\alpha-\nu\alpha+1)$

$O = \alpha(2-\nu)$

$P = 1+\alpha^2+4\epsilon(1+\alpha)-3\epsilon^2$

$Q = 2\epsilon^2+\alpha-2\epsilon(1+\alpha)$

$Q' = 2\epsilon^2+\alpha-2\epsilon(1+\alpha)+\dfrac{\epsilon c\nu}{\alpha}$

$R = -\dfrac{1}{2}\epsilon^2$

$S = \alpha^2+4\epsilon(1+\alpha)-\dfrac{5}{2}\epsilon^2-2\epsilon n\left(1+\dfrac{\nu}{\alpha}\right)+\dfrac{\epsilon\nu}{\alpha}(1-c)$

$T = \alpha(1-\nu-2\epsilon)+\epsilon^2-2\epsilon(1-n)\left(1+\dfrac{\nu}{\alpha}\right)+\dfrac{\nu\epsilon}{\alpha}$

$U = -2\alpha(1-\nu)-2\epsilon+\epsilon\alpha+\epsilon(1-c)$

$U' = -2\alpha(1-\nu)-2\epsilon+\alpha(1-\nu)\left[2n\left(1+\dfrac{\nu}{\alpha}\right)-\dfrac{\nu}{\alpha}(1-c)\right]$

$V = \dfrac{5}{2}\alpha^2+4\alpha(1-\nu)-\dfrac{5}{2}\nu^2\alpha^2-\alpha(1-c)(1-\nu)$

$W = -2\alpha[1-\nu+\alpha(1-\nu^2)]$

$X = \dfrac{1}{2}\alpha^2(1-\nu^2)$

$Y = -2\alpha[1-\nu+\alpha(1-\nu^2)]+\epsilon+\alpha^2(1-\nu^2)$
$\quad +\alpha(1-\nu)\left[2(1-n)\left(1+\dfrac{\nu}{\alpha}\right)-\dfrac{\nu}{\alpha}\right]$

$Z = -(X+I+R+Y+T)$

Where $\alpha = \left(\dfrac{\lambda_x}{\lambda_y}\right)^2$, $n = \cos^2\gamma$, $\epsilon = n(1-\nu)$, $c = 1-2\sin^2\gamma$

Fig. 4. Deflection Coefficients of the F.D. Equation Applied at Point i on or Adjacent to a Free Edge of a Triangular Element. F.D. Equation Takes the Form:

$$\left(\frac{N\lambda_y}{\lambda_x^3}\right)[\text{coefficients}]\{w\} = Q_i.$$

The pattern of the deflection coefficients of Eq. (3) (elements of $[A]$) are shown in Fig. 3a. When the point i where the F.D. equation is applied is at or adjacent to the boundary, the coefficients must be modified to incorporate the boundary condition of a free edge [6]. The modified coefficients are given in Fig. 3b to f. The corresponding coefficients for the triangular element (Fig. 2b) are given in Fig. 4.

The F.D. equations applied at all mesh points of an element with free edges may be written in matrix form

$$[K]\{w\} = \{Q\}, \tag{5}$$

where $[K]$ is a square symmetric matrix formed by F.D. coefficients. It relates the deflection and the forces applied at the mesh points and can therefore be regarded as a stiffness matrix corresponding to the coordinates $\{w\}$. The matrix $[K]$ is singular. The element must be restrained at not less than three coordinates (not on a straight line) in order that its stiffness matrix can be inverted. If springs of arbitrary stiffness (say $N\lambda_y/\lambda_x^3$), are introduced at three (or more) boundary nodes, then the spring stiffness is added to the corresponding elements in $[K]$ to obtain $[K^*]$ which can be inverted. Thus,

$$\{w\} = [K^*]^{-1}\{Q\}. \tag{6}$$

Flexibility matrix $[K^*]^{-1}$ will now be transformed into another flexibility matrix $[f^*]$ corresponding to the degrees of freedom at the boundary (Fig. 2). The displacements $\{D\}$ at the coordinates in Fig. 2 are related by geometry to the deflections $\{w\}$ at the element mesh points as follows:

$$\{D\} = [C]\{w\}, \tag{7}$$

Therefore, the flexibility matrix of the element on spring supports corresponding to the $\{D\}$-coordinates is given by [7]

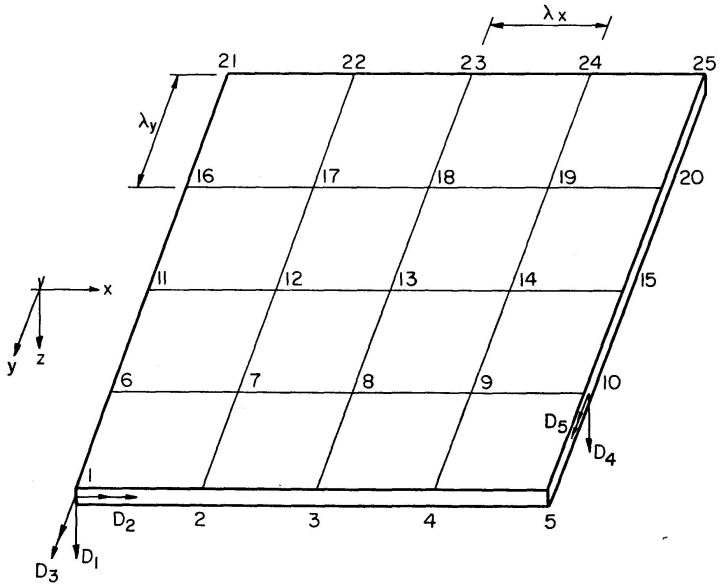


Fig. 5. Mesh Points and Coordinates Referred to in Equation 7a.

$$[f^*] = [C][K^*]^{-1}[C]^T, \tag{8}$$

where the superscript T means matrix transpose.

The elements of $[C]$ are either zero, 1, $1/\lambda_x$, or $1/\lambda_y$. Consider for example the plate in Fig. 5 which has 25 mesh points. The edge displacements $\{D\}$ at the five arbitrary coordinates shown in the figure are related to the deflections $\{w\}$ at the 25 mesh points by Eq. (7) as follows:

$$\begin{array}{l}\text{Column}\\ \text{Number}\end{array}\quad \begin{array}{ccccccccc} 1 & & 2 & \dots & 6 & \dots & 9 & 10 & \dots & 25 \end{array}$$

$$\underset{5\times 1}{\{D\}} = \begin{bmatrix} 1 & & & & & & & & \\ \dfrac{1}{\lambda_y} & & & & -\dfrac{1}{\lambda_y} & & & \text{Elements not} & \\ \dfrac{1}{\lambda_x} & -\dfrac{1}{\lambda_x} & & & & & & \text{shown are zero} & \\ & & & & & & & & \\ & & & & & & & 1 & \\ & & & & \cdot & & \dfrac{1}{\lambda_x} & -\dfrac{1}{\lambda_x} & \end{bmatrix} \underset{25\times 1}{\{w\}} \tag{9}$$

or

$$\{D\} = [C]\{w\}. \tag{9a}$$

In this equation any of the edge rotations, say D_5 (Fig. 5) is considered equal to the slope of the deflected surface midway between mesh points 10 and 9. This would be accurate if the mesh size λ_x is small or the curvature perpendicular to the free edge is small. Using $[C]$ in the above form in Eq. (9) would give a less accurate value for the elements f^*_{22}, f^*_{33} and f^*_{55} than the other elements of the matrix $[f^*]$. This is because these elements represent the rotation at a coordinate due to a unit couple applied at the same coordinate. A more accurate value of any of these elements, say f^*_{55}, is given by:

$$\begin{array}{l}\text{Colomn}\\ \text{Number}\end{array}\quad \begin{array}{ccccccccc} 1 & \dots & 7 & 8 & 9 & 10 & \dots & 25 \end{array}$$

$$f^*_{55} = \left(\frac{1}{6\lambda_x}\right)[0 \quad 0 \quad 2 \quad -9 \quad 18 \quad -11 \quad 0 \quad \dots \quad 0\,][K^*]^{-1} \begin{Bmatrix} 0 \\ \dots \\ \dots \\ 0 \\ \dfrac{1}{\lambda_x} \\ -\dfrac{1}{\lambda_x} \\ 0 \\ \dots \\ 0 \end{Bmatrix} \begin{array}{l}\text{Row}\\ \text{Number}\end{array} \begin{array}{l} 1 \\ \\ \\ \\ 9 \\ 10 \\ \\ \\ 25 \end{array} \tag{10}$$

In this equation the slope at the element edge is calculated from the deflections using the pattern of coefficients [8] $(1/6\lambda_x)$ [11, −18, 9, −2] and a unit couple at the edge is replaced by a pair of equal and opposite forces (of magnitude $1/\lambda_x$) at mesh points 9 and 10.

The flexibility matrix $[f^*]$ derived above (Eq. (8)) is for an element on spring supports.

From $[f^*]$ the flexibility matrix of the element supported in any manner can be derived [7]. The inversion of $[f^*]$ gives the stiffness matrix $[S^*]$ of the element on spring supports. When the arbitrarily chosen stiffness of the springs are deducted from the appropriate diagonal elements of the latter matrix, the stiffness matrix $[S]$ of the free (unsupported) element is obtained.

Fixed-end Forces

If the displacement method of analysis is used, the fixed-end forces $\{F_r\}$ at the $\{D\}$ coordinates will be needed for any transverse loading $\{Q\}$ on the element.

Combining Eq. (6) and (7), the node displacements of the element on spring supports due to forces at mesh points can be written as

$$\{D\} = [C][K^*]^{-1}\{Q\}. \tag{11}$$

These node displacements are reduced to zero by the restraining forces $\{F_r\}$. Hence,

$$[f^*]\{F_r\} + [C][K^*]^{-1}\{Q\} = \{0\},$$

from which

$$\{F_r\} = -[f^*]^{-1}[C][K^*]^{-1}\{Q\}. \tag{12}$$

Stress Resultants

The stress resultants at any mesh point can be calculated by F.D. Eqs. [7] from the final deflections $\{w\}$. In the displacement method, the final deflections are given by the superposition equation:

$$\{w\} = \{w_r\} + [w_u]\{D\}, \tag{13}$$

where $\{w_r\}$ are mesh point deflections of the element with restraint edges and $[w_u]$ are mesh point deflections corresponding to unit nodal displacement, and $\{D\}$ are the final nodal displacements. Eq. (13) can be put in the form:

$$\{w\} = [K^*]^{-1}(\{Q\} + [C]^T\{F_r + [f^*]^{-1}\{D\}\}). \tag{14}$$

General Remarks

1. A study of the finite difference coefficients in Fig. 4 shows that the stiffness matrix $[K]$ for a triangular element is not quite symmetric. The coefficients introducing unsymmetry in the matrix have been marked with a prime. For example, for symmetry, D' in Fig. 4d should be equal to D in Fig. 4b. The difficulty of obtaining finite differences coefficients which have reciprocal relationships at mesh points near skew edge corners is reported by JENSEN [6]. To overcome this difficulty, it is suggested that unsymmetric elements of $[K]$ are to be replaced by their average.

2. It should be noted that $[f^*]$ can only be inverted if a displacement at each of the D-coordinates can be imposed while the displacement at the other D-coordinates is prevented. For example, the rotation D_3 in Fig. 5, which is expressed in terms of the transverse deflection at points in edge 1–5, cannot be produced if at the same time the transverse deflection at points 1, 2, 3 and 4 are zero. This does not provide serious difficulty. It only has to be noted when choosing the system of the D-coordinates representing the element degrees of freedom.

3. The finite differences patterns of coefficients required for the derivation of the flexibility or stiffness matrices of rectangular and triangular elements are included in Fig. 3 and 4. However, in some cases, some saving in the computations may be achieved by using trapezoidal elements. The writers used trapezoidal elements for the analysis of skew bridges.

Application

To test the above method, a uniformly-loaded rectangular plate with two simply-supported edges, a built-in edge and a free edge was analyzed (Fig. 6). The plate was idealized as an assemblage of two elements A and B, with the F.D. mesh shown in Fig. 6. The finer mesh in the y-direction for element B

Table 1. Moments and Deflections of Plate in Fig. 6 ($\nu = 0.3$)

Mesh	Section CD		Section EF		
	Point	Moment M_y in terms of qL^2	Point	Moment M_x in terms of qL^2	Deflections in terms of $\frac{qL^4}{Eh^3}$
4×4	2	−0.097	6	0.091	0.114
	4	−0.134	8	0.121	0.159
6×6	4	−0.132	8	0.122	0.157
8×8	4	−0.130	8	0.123	0.156
Exact	4	−0.124	8	0.123	0.154

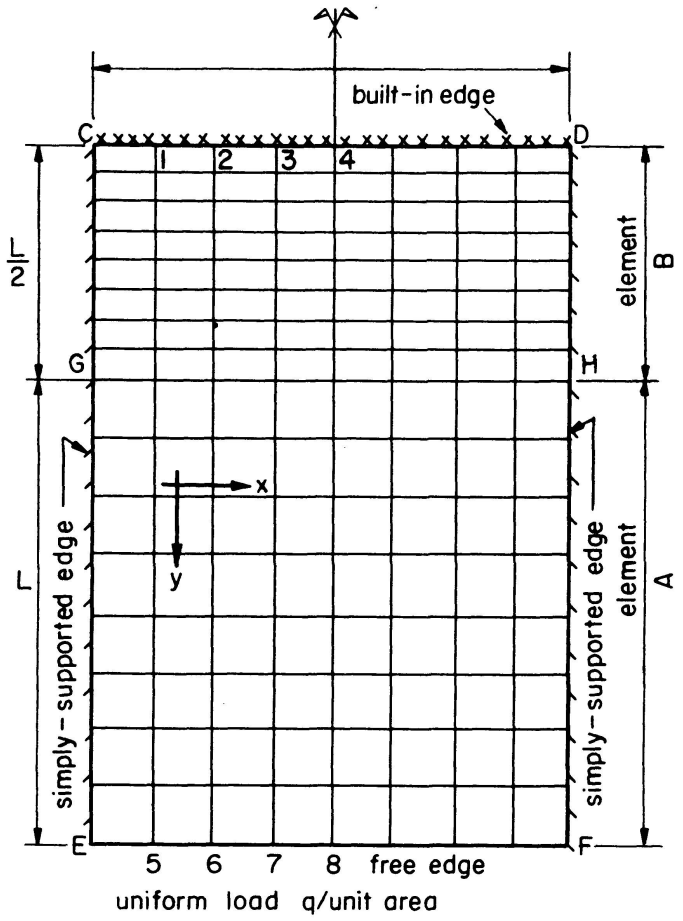


Fig. 6. Plate Used for Test Problem.

was chosen to get accurate values of M_y, which is known to change rapidly near the fixed edge. The two elements are connected at two coordinates at each of the internal mesh points on line GH.

Table 1 gives moments and deflections along CD and EF obtained by a solution in which a 4×4 mesh was taken for each of elements A and B. The table also includes the results of two other solutions in which the meshes were 6×6 and 8×8 instead of 4×4.

Conclusion

In conventional finite element analysis of a plate in bending, displacement functions are assumed to calculate the element stiffness matrices. For accurate results, it is necessary to idealize the plate as an assemblage of a (comparatively) large number of small elements. In this paper, the stiffness matrix is derived by finite differences, without assuming a displacement function. Therefore, the plate can be considered as an assemblage of a small number of large elements. In fact, the larger the elements used in the idealized structure, the smaller is the error caused by element division.

The results of the test problem show that the method gives accurate answers.

Acknowledgment

This research was supported by a grant from the National Research Council of Canada which is gratefully acknowledged.

Keywords

Computer matrix methods; finite differences; finite elements; numerical methods; plate bending; slabs.

Notation

$[C]$ transformation matrix defined in Eq. (7)
$\{D\}$ displacements at nodes on element edges
$[f]$ flexibility matrix corresponding to the $\{D\}$-coordinates
$\{F_r\}$ forces at the $\{D\}$-coordinates when $\{D\}=\{0\}$
$[K]$ "equivalent" stiffness matrix formed by F.D. coefficients (Eq. (5))
N flexural rigidity of plate (Eq. (2))
$\{Q\}$ concentrated mesh point transverse loads
q intensity of distributed load
$[S]$ stiffness matrix corresponding to the $\{D\}$-coordinates
$\{w\}$ mesh points transverse deflections
λ spacing between F.D. mesh lines
ν Poisson's ratio

Subscripts and Superscripts:

$*$ used as superscripts in $[K^*]$, $[f^*]$ and $[S^*]$ to refer to plate element on arbitrary chosen spring supports
r refers to restrained element, that is – displacements $\{D\}=\{0\}$
x, y rectangular coordinate axes

References

1. O. C. Zienkiewicz and Y. K. Cheung: The Finite Element Method in Structural and Continuum Mechanics. McGraw-Hill Book Co., New York, 1967.
2. A. H. S. Ang and N. M. Newmark: A Numerical Procedure for the Analysis of Continuous Plates. ASCE Second National Conference on Electronic Computation, Pittsburgh, Pennsylvania, September 1960, p. 379–413.
3. A. Ghali and K. J. Bathe: Analysis of Plates Subjected to In-Plane Forces Using Large Finite Elements. Publications I.A.B.S.E., Vol. 30/I, Zurich, 1970, p. 61–72.
4. R. Szilard: A Matrix and Computer Solution of Cylindrical Shells of Arbitrary Shape. Paper presented at the International Symposium on Shell Structures in Engineering Practice, Budapest, Hungary, 31 August to 3 September, 1965.

5. S. TIMOSHENKO: Theory of Plates and Shells. McGraw-Hill Book Co., New York, 1940.
6. V. P. JENSEN: Analysis of Skew Slabs. University of Illinois, Engineering Experiment Station, Bulletin Series No. 332.
7. J. S. PRZEMIENIECKI: Theory of Matrix Structural Analysis. McGraw-Hill Book Co., New York, 1968.
8. E. L. STIEFEL: An Introduction to Numerical Mathematics. Academic Press, New York, 1963.

Summary

Plates in bending are analyzed by idealizing the continuum as an assemblage of large rectangular and triangular elements. The flexibility and stiffness matrices of these elements corresponding to boundary displacements are derived using finite differences. The analysis involves simple matrix operations which can be easily computer programmed.

The stiffness matrices derived by this method are intended for use in the analysis of structures which can be idealized as an assemblage of large rectangular and triangular plate elements, e. g. box-girder skew bridges.

Résumé

On calcule les plaques fléchies au moyen d'une idéalisation du continu par un assemblage d'éléments rectangulaires et triangulaires de grandes dimensions. Les matrices de flexibilité et de rigidité de ces éléments pour les déplacements au contour sont obtenues à l'aide du calcul aux différences finies. Le calcul se fait à l'aide d'opérations matricielles simples et peut aisément être programmé.

Les matrices de rigidité assemblées par cette méthode sont destinées au calcul de structures qu'on peut idéaliser au moyen de grands éléments rectangulaires ou triangulaires, p. ex. des ponts biais à section fermée.

Zusammenfassung

Die Biegung der Platten wird durch eine Diskretisation des Kontinuums in eine Reihe von rechteckigen und dreieckigen Elementen großer Abmessungen berechnet. Die für die Randverschiebungen ausgedrückten Flexibilitäts- und Steifigkeitsmatrizen werden anhand endlicher Differenzen ermittelt. Die Analyse umfaßt einfache Matrix-Operationen, die für den Computer leicht programmierbar sind.

Die durch diese Methode abgeleiteten Streifigkeitsmatrizen sind für Tragwerke bestimmt, die zusammengesetzt aus großen rechteckigen und dreieckigen Plattenelementen idealisiert werden können, z. B. Kastenträger von schiefen Brücken.

Importance of Cell Symmetry in Flexural Finite Element Method

Importance de la symétrie des éléments finis pour le calcul des plaques

Bedeutung der Symmetrie der endlichen Elemente für die Plattenbiegung

A. HRENNIKOFF

Sc. D., Research Professor of Civil Engineering, Emeritus, The University of British Columbia, Vancouver, B.C., Canada

General

The use of Finite Element Method for solution of plate flexure problems is based on replacement of the plate by a cell model and development of the stiffness matrices of the individual cells composing it. Out of these the computer formulates the stiffness matrix of the whole model and solves the equations for the nodal displacements. The most common shapes of cells are triangular and quadrilateral, with the nodes located at the corners of the cells. In the usual presentation these cells possess three degrees of freedom for each node: a transverse displacement and the rotations about the two co-ordinate axes in the plane of the cell, making the size of the cell's stiffness matrix 9×9 in the triangular and 12×12 in the quadrilateral cells. Cells with more than three degrees of freedom per node and with additional nodes on the sides of the cells will not be considered in the present work.

The usual procedure is to assume the deflection function of the cell in the form of a polynomial in x and y satisfying the basic biharmonic equation of plate flexure

$$\frac{\partial^4 w}{\partial x^4} + 2\frac{\partial^4 w}{\partial x^2 \partial y^2} + \frac{\partial^4 w}{\partial y^4} = 0. \tag{1}$$

The right hand side of this equation is zero when the loads acting on the model are applied only at the nodes, which is usual.

The triangular cells are the most convenient for constructing models of non-rectangular plates or plates of irregular outline. However their non-symmetry leads to loss of precision and sometimes even to gross errors espe-

cially in flexural moments, not improved by the reduction of the mesh size. Demonstration of this proposition coupled with discussion of the necessary and desirable characteristics of the deflection polynomials is the subject of this paper.

The significance of displacement continuity on the edges of cells apart from the nodes will not be discussed here. The author's view is that the edge conformity of the adjacent cells is not a necessary condition in flexural (as well as the plane stress) elements and in this view he is supported by other investigators [1, 2].

General Deflection Polynomial

The generally used polynomials for the deflection w are composed of some or all of the following 12 terms

$$w = A_0 + A_1 x + A_2 x^2 + A_3 x^3 + B_1 y + B_2 y^2 + B_3 y^3 + C_1 x y + C_2 x^2 y + C_3 x^3 y + C_4 x y^2 + C_5 x y^3 \tag{2}$$

all of which satisfy the differential Eq. (1). The bending and torsional moments in the cell are expressed through the second derivatives of w. The three linear terms of the polynomial correspond to the three free body movements of the cell, resulting in no stresses, and the three second order terms – to the constant curvatures and torsion, the conditions which the cells must assume on infinite reduction of the mesh size, if they are to imitate faithfully the action of the plate prototype. This makes the six linear and quadratic terms compulsory irrespective of the shape of the cell. The remaining non-compulsory six terms in Eq. (2) are included or excluded depending on the type of the cell.

It may be observed that all the terms mentioned here are either symmetrical or antisymmetrical about the co-ordinate axes. The terms involving the odd powers of x and y are antisymmetrical about the y and x axes respectively, while the even power terms (including the zero power) are symmetrical.

Rectangular Cell

The rectangular cell of the dimensions a by ka is referred to the axes x and y coinciding with its symmetry axes. In deriving the stiffness matrix of this cell it is sufficient to consider only the three movements of the node 1, w_1, θ_1^x and θ_1^y. It is easy to see that each of these conditions may be replaced by four symmetrical and antisymmetrical cases presented in Figs. 1, 2 and 3, and designated by the symbols s_x, a_x, s_y and a_y. In each component case the corner movements are all equal to $^1/_4$ of the total corner movement, the node 1 being always moved in the positive direction, and the other nodes – in the directions determined by the nature of the intervening axes s or a.

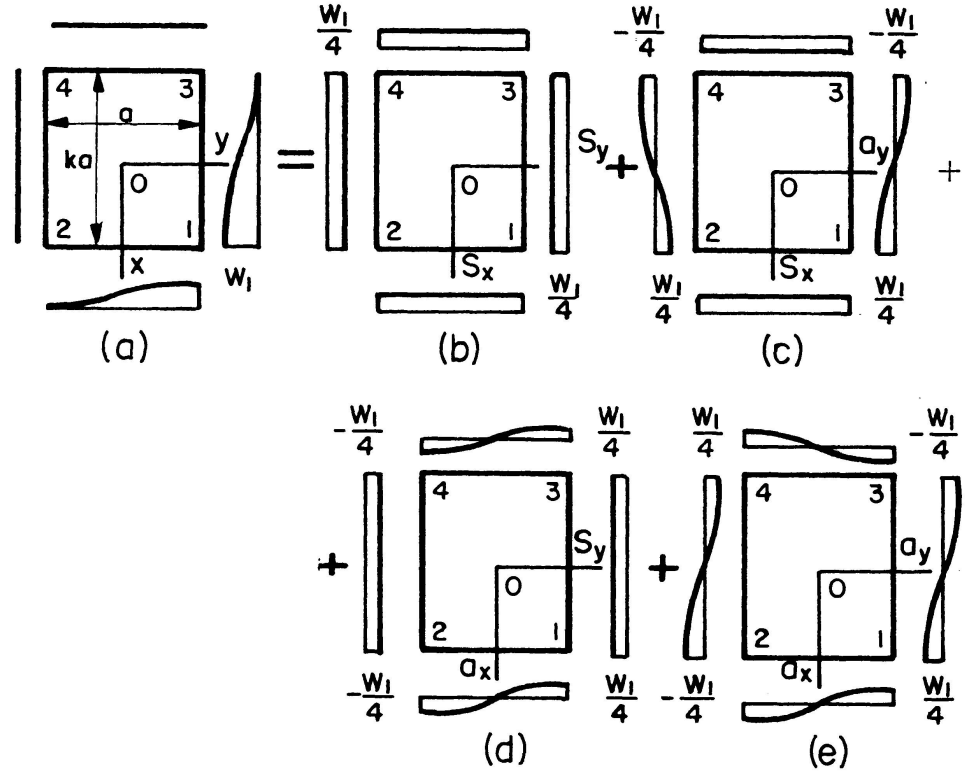


Fig. 1.

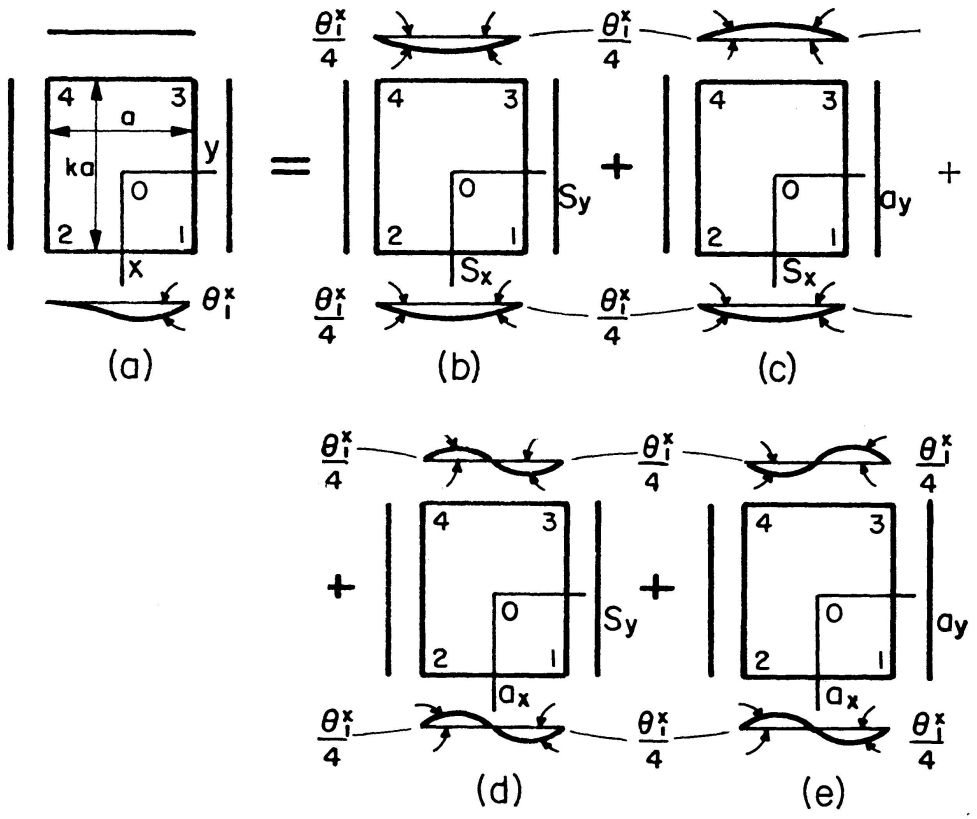


Fig. 2.

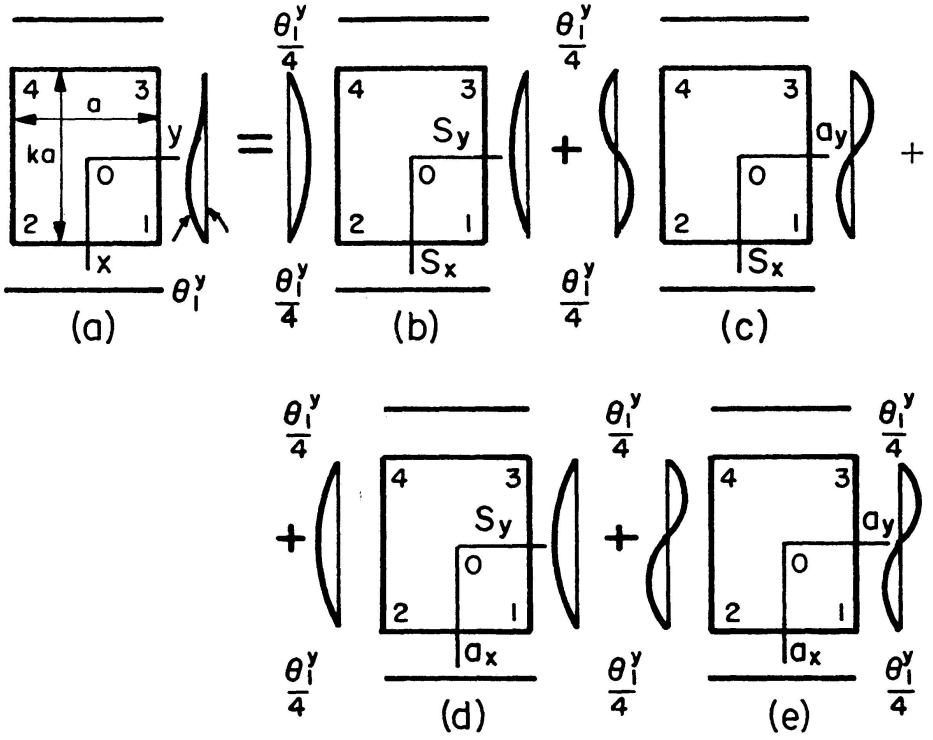


Fig. 3.

The displacement polynomials of each component case must accordingly consist of three terms, all of the same symmetry type as the case itself, i.e. $s_x s_y$, $s_x a_y$, $a_x s_y$ and $a_x a_y$. Here are the four symmetry components of the 12 term polynomial:

$$\left.\begin{aligned} s_x\, s_y \ldots w_{ss} &= A_0 + A_2 x^2 + B_2 y^2, \\ s_x\, a_y \ldots w_{sa} &= A_1 x + A_3 x^3 + C_4 x\, y^2, \\ a_x s_y \ldots w_{as} &= B_1 y + B_3 y^3 + C_2 x^2 y, \\ a_x a_y \ldots w_{aa} &= C_1 x\, y + C_3 x^3 y + C_5 x\, y^3. \end{aligned}\right\} \tag{3}$$

The partial derivatives of these polynomials are:

$$\left.\begin{aligned} \frac{\partial w_{ss}}{\partial x} &= 2 A_2 x, & \frac{\partial w_{sa}}{\partial x} &= A_1 + 3 A_3 x^2 + C_4 y^2, \\ \frac{\partial w_{as}}{\partial x} &= 2 C_2 x\, y, & \frac{\partial w_{aa}}{\partial x} &= C_1 y + 3 C_3 x^2 y + C_5 y^3, \end{aligned}\right\} \tag{4}$$

$$\left.\begin{aligned} \frac{\partial w_{ss}}{\partial y} &= 2 B_2 y, & \frac{\partial w_{sa}}{\partial y} &= 2 C_4 x\, y, \\ \frac{\partial w_{as}}{\partial y} &= B_1 + 3 B_3 y^2 + C_2 x^2, & \frac{\partial w_{aa}}{\partial y} &= C_1 x + C_3 x^3 + 3 C_5 x\, y^2. \end{aligned}\right\} \tag{5}$$

Each component polynomial is independent of the other three, and its coefficients are found by substituting into it and its derivatives the proper

corner movements of the node 1 (or any other node) and its co-ordinates, as shown in Figs. 1, 2 and 3. Here are the resultant expressions for the three displacement fields corresponding to the transverse displacement and the two rotations of the node 1:

$$\left.\begin{aligned} w &= \left(\frac{1}{4}+\frac{3}{4}\frac{x}{k\,a}-\frac{x^3}{k^3a^3}+\frac{3}{4}\frac{y}{a}-\frac{y^3}{a^3}+\frac{2\,x\,y}{k\,a^2}-\frac{2\,x\,y^3}{k\,a^4}-\frac{2\,x^3y}{k^3a^4}\right)w_1,\\ w &= \left(-\frac{a}{16}-\frac{x}{8\,k}-\frac{y}{8}+\frac{y^2}{4\,a}+\frac{y^3}{2\,a^2}-\frac{x\,y}{4\,k\,a}+\frac{x\,y^2}{2\,k\,a^2}+\frac{x\,y^3}{k\,a^3}\right)\theta_1^x,\\ w &= \left(\frac{k\,a}{16}+\frac{x}{8}-\frac{x^2}{4\,k\,a}-\frac{x^3}{2\,k^2a^2}+\frac{k\,y}{8}+\frac{x\,y}{4\,a}-\frac{x^2y}{2\,k\,a^2}-\frac{x^3y}{k^2a^3}\right)\theta_1^y. \end{aligned}\right\} \quad (6)$$

Examining the partial polynomials in Eq. (3), it may be seen that the three terms of the polynomial w_{ss} are of the compulsory types, while the three other partial polynomials possess each only one compulsory term, thus making permissible replacement of the other terms by appropriate substitutes. For example the term $C_4 x y^2$ in the polynomial $s_x a_y$ might be replaced by the combination $F_1(x^3y^2-xy^4)$ satisfying the differential equation and being of the same symmetry type. The stiffness matrix based on so modified polynomial is non-singular and would be fully suitable for solution of plate problems, but it would involve one undesirable feature; the properties of the displacements conforming to the modified polynomial would be different in the directions of the two co-ordinate axes with the result that the solution would change if the x and y axes were renamed y and x respectively. To avoid this unjustifiable non-similarity and the resultant decrease in precision, the terms of the type $x^m y^n$ must always be present in company with the terms $x^n y^m$. Thus in the example under consideration the terms $F_1(x^3y^2-xy^4)$ must be used together with the terms $F_2(x^2y^3-x^4y)$ in replacement of the part of the original polynomial $C_2 x^2 y + C_4 x y^2$. Although the suggested alternative is quite legitimate, the original polynomial appears preferable, since its lower power terms correspond to lower, i.e. less extreme, variations of displacements and stresses within the cell. Incidentally, combinations of several terms of the same symmetry type under single parameters such as $C_2(x^2y+x^2y^3-x^4y)$ and $C_4(xy^2+x^3y^2-xy^4)$ are possible, but their advantages seem questionable.

Combinations under the same parameter of the terms of two different symmetry types, such as $C_1(xy+x^2y^3)$ would lead to unsymmetrical displacement pattern in symmetrical modes, as will be demonstrated presently.

Isosceles Triangle Cell

The cell (Fig. 4) is referred to the co-ordinate axes with the origin at the vertex of the triangle and the x axis placed along the axis of symmetry. The shape of the triangle is described by the aspect ratio k. The required 9 term displacement polynomial consists of the six compulsory linear and quadratic

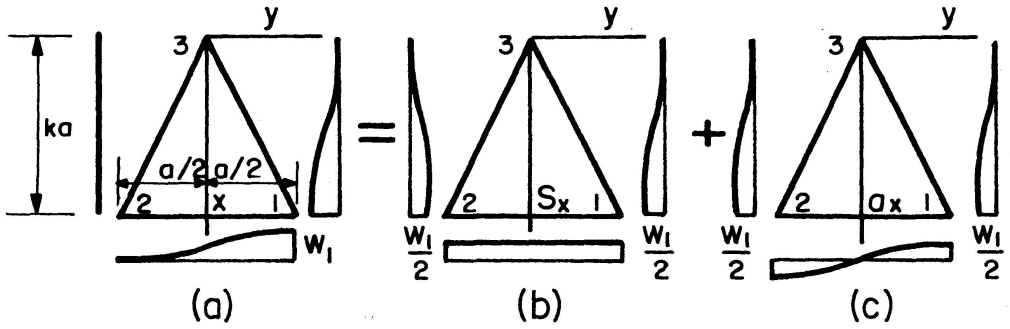


Fig. 4.

terms and the three additional terms to be chosen from the four available cubic members, A_3x^3, C_4xy^2, C_2x^2y and B_3y^3, the first two of which are s_x terms, and the other two $-a_x$. The question of symmetry of the terms about the y axis does not arise because the cell itself is unsymmetrical about it.

In order to form a correct polynomial it is desirable to separate the displacement modes w_1, θ_1^x and θ_1^y into their symmetrical and anti-symmetrical parts, as is done in Figs. 4, 5 and 6. The other three necessary unit movement modes w_3, θ_3^y and θ_3^x (Fig. 7) need no separation, because the first two are themselves symmetrical about the x axis and the last one – anti-symmetrical. Components of the displacement modes in Figs. 4, 5 and 6 add up to three s_x and three a_x conditions, while Fig. 7 depicts one a_x and two s_x conditions. Thus the displacement polynomial must be composed of five s_x and four a_x terms. Among the compulsory terms four are symmetrical and two – anti-

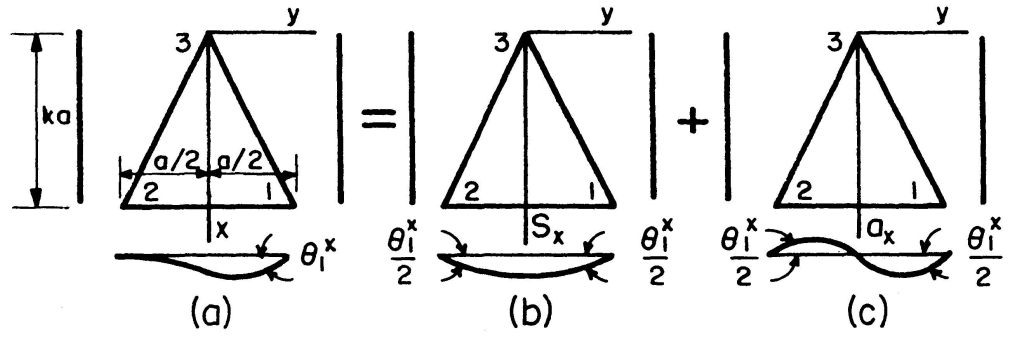


Fig. 5.

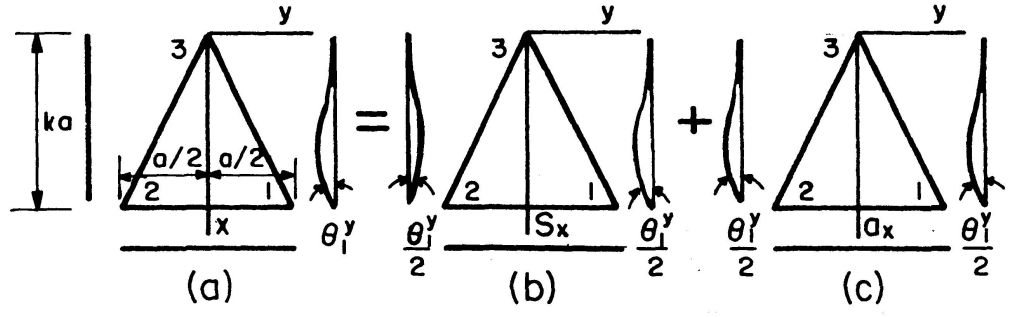


Fig. 6.

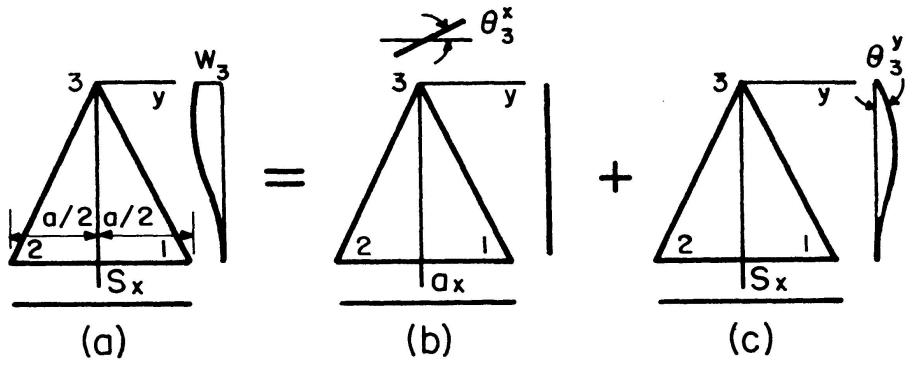


Fig. 7.

symmetrical. Therefore one more s_x term, i.e. either $A_3 x^3$ or $C_4 x y^2$, and both a_x terms $C_2 x^2 y$ and $B_3 y^3$ must be added on. Choosing arbitrarily $A_3 x^3$, the s and a parts of the displacement polynomial become

$$\left.\begin{aligned} w_s &= A_0 + A_1 x + A_2 x^2 + A_3 x^3 + B_2 y^2, \\ w_a &= B_1 y + B_3 y^3 + C_1 x y + C_2 x^2 y. \end{aligned}\right\} \tag{7}$$

Proceeding as with the rectangular cell, the six basic displacement fields are found to be

$$\left.\begin{aligned} w &= \left(\frac{3}{2k^2a^2}x^2 + \frac{3}{ka^2}xy - \frac{1}{k^3a^3}x^3 - \frac{3}{2k^2a^3}x^2y - \frac{2}{a^3}y^3\right) w_1, \\ w &= \left(-\frac{3}{8k^2a}x^2 + \frac{2}{2a}y^2 - \frac{1}{2ka}xy + \frac{1}{4k^3a^2}x^3 + \frac{1}{4k^2a^2}x^2y + \frac{1}{a^2}y^3\right)\theta_1^x, \\ w &= \left(\frac{1}{2ka}x^2 + \frac{1}{a}xy - \frac{1}{2k^2a^2}x^3 - \frac{1}{ka^2}x^2y\right)\theta_1^y, \end{aligned}\right\} \tag{8}$$

$$\left.\begin{aligned} w &= \left(1 - \frac{3}{k^2a^2}x^2 + \frac{2}{k^3a^3}x^3\right) w_3, \\ w &= \left(y - \frac{2}{ka}xy + \frac{1}{k^2a^2}x^2y\right)\theta_3^x, \\ w &= \left(-x + \frac{2}{ka}x^2 - \frac{1}{k^2a^2}x^3\right)\theta_3^y. \end{aligned}\right\} \tag{9}$$

It is desirable now to examine the outcome of using the combination of the s_x and a_x terms $C_2(x^2y + xy^2)$ under the cover of a single parameter. The polynomial for θ_3^x is taken for the demonstration of the ensuing result. By using the w_a polynomial in Eq. (7), the same expression is found for the anti-symmetric part of the field θ_3^x as the second of the Eqs. (9). However the presence of the term $\frac{1}{k^2a^2}x^2y$ on this expression brings in automatically the s_x term $\frac{1}{k^2a^2}xy^2$, augmenting the w_s part of the deflection polynomial in Eq. (7). With the procedure used earlier the complete deflection field is found to be

$$w = \left(y + \frac{1}{4k^3a}x^2 - \frac{1}{ka}y^2 - \frac{2}{ka}xy - \frac{1}{4k^4a}x^3 + \frac{1}{k^2a^2}x^2y + \frac{1}{k^2a^2}xy^2\right)\theta_3^x. \quad (10)$$

Although the nodal displacements imposed on the cell in this mode are purely anti-symmetrical, four of the terms in its displacement polynomial are symmetrical. The stiffness matrix terms corresponding to this deflection polynomial will not conform to the requirements of symmetry and the precision of the model solution based on this matrix will naturally suffer. Thus the use of a deflection polynomial with a superfluous term combined under the same parameter with a necessary term of a different symmetry type must be avoided.

It may be observed that if an isosceles triangle cell is referred to the axes x' and y' at an angle to the axes x and y, the single term x'^2y' in the new system will give rise to both x^2y and xy^2 terms in the old system, and for this reason will be inappropriate.

Triangle Cells of Irregular Shape

A plate model may include cells in the shape of irregular triangles, such as the triangle 1–2′–3 in Fig. 8 whose node 2′ is located not far from the node 2

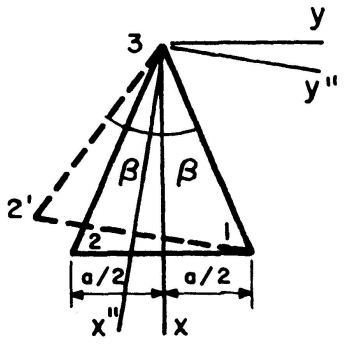


Fig. 8.

of the isosceles triangle 1–2–3, referred to the co-ordinate axes x and y, arranged as before.

Although the use of the term C_4xy^2 in the deflection polynomial of the isosceles triangle is not permissible, the 9 term polynomial of the irregular triangle may contain either C_2x^2y or C_4xy^2 terms. However in view of the closeness of the node 2′ to the node 2, it is felt intuitively that the anti-symmetrical term will be the more appropriate of the two. Even better results should ensue if the cell 1–2′–3 is referred to the axes x'', y'', of which the axis x'' bisects the angle at the node 3. It is felt that of the three vertices of an irregular triangle the bisector oriented axis should be placed at the vertex enclosed between the pair of sides whose ratio is closest to unity.

Transformation of Co-ordinates

The directions of co-ordinate axes at different nodes of a cell model may be different even with cells of regular shape, and so transformation of co-ordinates becomes necessary for equalization of displacements and rotations of different cells meeting at the common nodes. The most convenient resolution of this complication requires selection of the best set of co-ordinate axes in each cell in accordance with the considerations presented above, and determination of the terms of the stiffness matrix referred to these axes. Then at each node a convenient common set of co-ordinates is chosen to which the matrix terms of all adjoining cells belonging to this particular node are converted from their individual cell axes. This conversion of the cell stiffness matrix $[K]$ in the cell co-ordinates to the matrix $[K]_c$ in the common node co-ordinates [2] is effected through the transformation matrix $[T]$ and its transpose $[T]^*$ by the equation

$$[K]_c = [T][K][T]^*. \tag{11}$$

With the use of triangular cells direct employment of a nine term deflection polynomial referred to the common axes for all cells meeting at a node would be unsatisfactory, because a cubic term $x'^2 y'$ in common co-ordinates would give rise in cell co-ordinates to both $x^2 y$ and $x y^2$ terms, one of which would be unsatisfactory and might even lead to singularity of the matrix.

Cell Symmetry

Triangular (as well as trapezoidal) cells of isosceles shape, possess only one axis of symmetry as against two in the rectangular cells. Since the deformability of space in a uni-symmetrical cell is different in the directions of the x and y axes it may be expected that the precision of plate models composed of triangular or trapezoidal cells is lower than of the rectangular cell models. The truth of this deduction is demonstrated on the examples presented below.

Examples

Models composed of rectangular and triangular cells are compared on the examples of simply supported and fixed-ended uniformly loaded square plates of Poisson's ratio 0.3. The models (Figs. 9a to f) involve the actual (or "solid") squares and the ones made of pairs of rectangular isosceles triangles in contact along the diagonals. The model (f) is unsymmetrical about the plate axes x and y because its contact diagonals point in the same direction over the whole plate. The four other triangular cell models have symmetrical arrangement of triangles in the four quadrants of the plate, which in the models (b) and (c) is the same in all squares, and in the other two models different in the adjacent

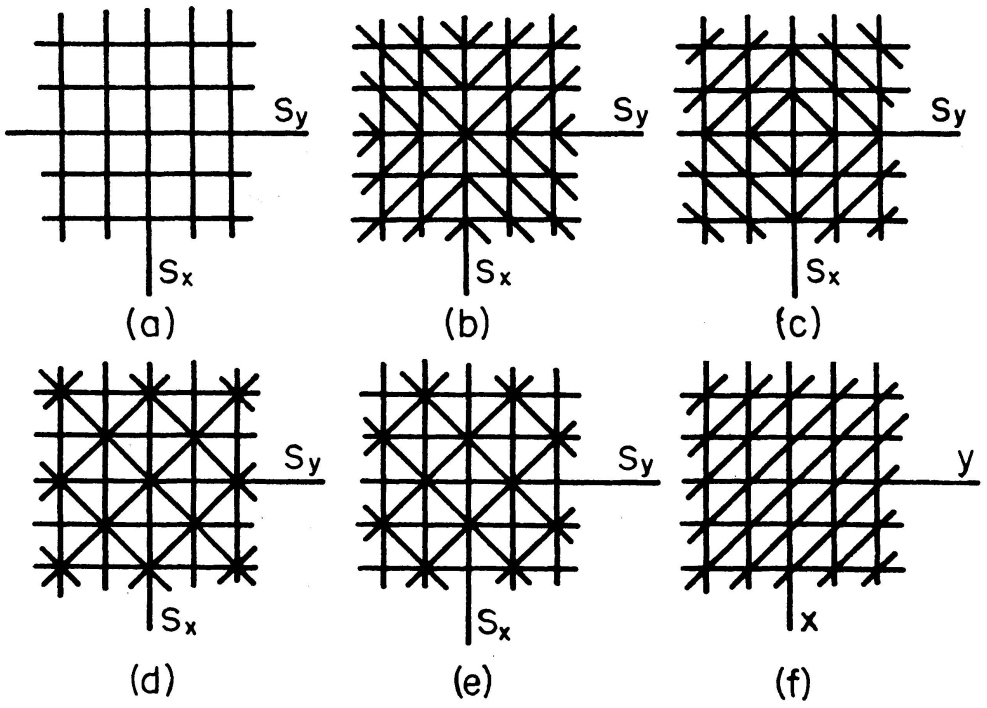


Fig. 9.

squares, with the contact diagonals pointing alternately in NE-SW and NW-SE directions.

The solutions are based on the stiffness matrix terms presented in the Appendix 1.

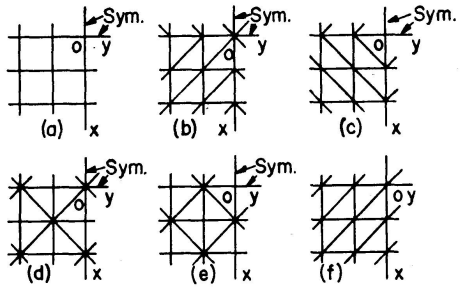
The distributed load is applied in the form of nodal concentrations coming from the areas tributary to the nodes, which means that the load of a rectangular element is divided equally between its four corners, and of a triangular one – between its three. The results of solutions are presented in Table 1.

This table contains the exact elasticity values of the central deflection and of the central bending moment M_x, as well as the bending moments M_x and M_y [2, 3] at the mid-edge of the fixed-ended plate. The precision of the finite element solutions is given by their % errors, with the plus signs corresponding to the condition when the exact value is greater than the approximate one. Models of 8×8 and 16×16 mesh were employed to indicate the convergence of the results. Plate moments were determined by dividing the nodal concentrations in the model by the tributary lengths. This method on the whole produced here better results than the deflection method.

The figures in the Table 1 show definite trends justifying, within the limits of the examples, the following deductions:

1. Of all models the ones involving the actual rectangular cells show the best precision and the best progress towards the exact values on reduction of the mesh size, in most of deflections and bending moments. The moment about the axis normal to the edge in the fixed ended plate, unlike the other moments, is inaccurate, but it improves fast as the mesh becomes finer.

Table 1. Uniformly Loaded Square Plate, Load q, Thickness t, Poisson's Ratio 0.3, % Errors of Finite Element Solutions



			Simply Supported Plate		Fixed Ended Plate			
			Deflection at 0, Exact $0.0443\frac{qL^4}{Et^3}$	Bending Moment M_x at 0, Exact $0.0479\,qL^2$	Deflection at 0, Exact $0.13868\frac{qL^4}{Et^3}$	Bending Moments		
						M_x at 0 Exact $0.0231\,qL^2$	M_x at Mid-edge, Exact $-0.0513\,qL^2$	M_x at Mid-edge, Exact $-0.01539\,qL^2$
	Cell Type	Mesh	% Errors		% Errors			
Finite Element Solutions	Squares (a)	8×8	+ 0.67%	+ 0.57%	− 2.65%	− 2.18%	+ 3.62%	+31.0 %
		16×16	+ 0.04%	+ 0.26%	− 0.41%	+ 0.06%	+ 0.83%	+16.6 %
	Squares of Triangles (b)	8×8	− 4.06%	− 3.55%	−10.9 %	− 9.4 %	+13.35%	>100 %
		16×16	− 3.63%	− 2.60%	− 4.30%	− 3.35%	+16.6 %	>100 %
	Squares of Triangles (c)	8×8	− 5.85%	+31.6 %	− 5.68%	+32.0 %	+ 0.22%	−45.3 %
		16×16	− 3.83%	+31.3 %	− 3.85%	+32.2 %	− 4.83%	>100 %
	Squares of Triangles (d)	8×8	−14.35%	+ 5.35%	−12.5 %	− 8.88%	−18.2 %	−15.15%
		16×16	−16.0 %	− 4.85%	−14.2 %	− 4.57%	−15.88%	>100 %
	Squares of Triangles (e)	8×8	−15.95%	+22.4 %	−15.3 %	+19.6 %	+19.2 %	>100%
		16×16	−16.40%	+22.5 %	−14.9 %	+22.9 %	+15.2 %	>100%
	Squares of Triangles (f)	8×8	+ 0.21%	+ 0.33%	− 6.26%	− 3.67%	+ 4.05%	+ 75%
		16×16	− 0.06%	+ 0.13%	− 3.25%	− 1.19%	+ 2.10%	+ 62%

2. The unsymmetrical model (*f*) of the similarly arranged triangles comes out the next best. In fact it is better than the rectangular cell model in very precise results of the simply supported plate, but is significantly behind the leader in the fixed-ended plate.

3. Of the symmetrical triangular models two, (*b*) and (*c*), have their deflections changing in the right directions on reduction of the mesh size, but the same does not always apply to the moments, some of which are very inaccurate.

4. The symmetrical models (*d*) and (*e*) with differently oriented triangles in the adjacent squares are inaccurate and erratic both with regard to the deflections and the bending moments.

Conclusions

The following conclusions based on theoretical considerations and supported in part by the numerical results seem to be justified:

1. The terms of the deflection polynomials of the cells must conform to certain requirements, some of which are general for all types of cells, while others depend on the shape of the cell and its symmetry. Some of these requirements are compulsory, while others are only desirable for better precision.

2. Cells of triangular shape are almost always inferior in precision to rectangular cells, because they cannot imitate homogeneous isotropic elastic material. Isosceles triangle cells, similarly oriented throughout the model, such as the ones in Fig. 9 (f), are the best of the triangular cells. As their size decreases to zero the space modelled by them approaches homogeneity, while remaining anisotropic. Such cells are capable of imitating uniform flexure or torsion condition in the plate.

3. Models composed of cells of irregular triangular shape or of differently oriented isosceles triangles, may under certain conditions lead to satisfactory results in deflections. This applies particularly to some recently proposed conforming triangular cells [4]. It is not believed however that any of these models are suitable for determination of moments because the irregularity of their cell arrangement effectively precludes true imitation of a uniform stress condition in the plate.

In this connection it may also be pointed out that the common practice of selection of the centre of gravity of the cell for the assignment of stresses determined from the displacement function has no rational basis when the stress condition in the cell is non-uniform.

4. Two situations appear appropriate for use of triangular cells:

a) When the triangles are used on the edges of the plate in order to approximate its irregular shape, provided that the plate region covered by the triangles is stressed lightly.

b) When analysing circular plates or plates in the form of circular sectors, using models formed of isosceles triangles near the centre of the circle and isosceles trapezoids over most of the model.

Appendix I

Tables 2 and 3 contain nodal forces in a rectangular cell and a cell in the form of an isosceles triangle, produced by unit displacements w_1 and unit rotations θ_1^x and θ_1^y of the node 1 (see Figs. 1 to 6). The latter table presents also the corner forces caused by the unit movements of the node 3. Forces produced by the movements of the other nodes are similar and easily follow from symmetry.

Table 2. Nodal Forces in a Rectangular Cell

(Figs. 1, 2, 3)

Action $w_1 = 1$	Action $\theta_1^x = 1$	Action $\theta_1^y = 1$
$Z_1 = \left(4k + \frac{4}{k^3} + \frac{2.8}{k} - \frac{0.8\mu}{k}\right)\frac{L}{a}$	$Z_1 = \left(-2k - \frac{0.2}{k} - \frac{0.8\mu}{k}\right)L$	$Z_1 = \left(\frac{2}{k^2} + 0.2 + 0.8\mu\right)L$
$Z_2 = \left(-4k + \frac{2}{k^3} - \frac{2.8}{k} + \frac{0.8\mu}{k}\right)\frac{L}{a}$	$Z_2 = \left(2k + \frac{0.2}{k} - \frac{0.2\mu}{k}\right)L$	$Z_2 = \left(\frac{1}{k^2} - 0.2 - 0.8\mu\right)L$
$Z_3 = \left(2k - \frac{4}{k^3} - \frac{2.8}{k} + \frac{0.8\mu}{k}\right)\frac{L}{a}$	$Z_3 = \left(-k + \frac{0.2}{k} + \frac{0.8\mu}{k}\right)L$	$Z_3 = \left(-\frac{2}{k^2} - 0.2 + 0.2\mu\right)L$
$Z_4 = \left(-2k - \frac{2}{k^3} + \frac{2.8}{k} - \frac{0.8\mu}{k}\right)\frac{L}{a}$	$Z_4 = \left(k - \frac{0.2}{k} + \frac{0.2\mu}{k}\right)L$	$Z_4 = \left(-\frac{1}{k^2} + 0.2 - 0.2\mu\right)L$
$m_1^x = \left(-2k - \frac{0.2}{k} - \frac{0.8\mu}{k}\right)L$	$m_1^x = \left(\frac{4}{15k} - \frac{4\mu}{15k} + \frac{4k}{3}\right)aL$	$m_1^x = \mu aL$
$m_2^x = \left(-2k - \frac{0.2}{k} + \frac{0.2\mu}{k}\right)L$	$m_{21}^x = \left(-\frac{1}{15k} + \frac{\mu}{15k} + \frac{2k}{3}\right)aL$	$m_2^x = 0$
$m_3^x = \left(-k + \frac{0.2}{k} + \frac{0.8\mu}{k}\right)L$	$m_{31}^x = \left(-\frac{4}{15k} + \frac{4\mu}{15k} + \frac{2k}{3}\right)aL$	$m_3^x = 0$
$m_4^x = \left(-k + \frac{0.2}{k} - \frac{0.2\mu}{k}\right)L$	$m_4^x = \left(\frac{1}{15k} - \frac{\mu}{15k} + \frac{k}{3}\right)aL$	$m_4^x = 0$
$m_1^y = \left(\frac{2}{k^2} + 0.2 + 0.8\mu\right)L$	$m_1^y = -\mu aL$	$m_1^y = \left(\frac{4}{3k} + \frac{4k}{15} - \frac{4\mu k}{15}\right)aL$
$m_2^y = \left(\frac{1}{k^2} - 0.2 - 0.8\mu\right)L$	$m_2^y = 0$	$m_2^y = \left(\frac{2}{3k} - \frac{4k}{15} + \frac{4\mu k}{15}\right)aL$
$m_3^y = \left(\frac{2}{k^2} + 0.2 - 0.2\mu\right)L$	$m_3^y = 0$	$m_3^y = \left(\frac{2}{3k} - \frac{k}{15} + \frac{\mu k}{15}\right)aL$
$m_4^y = \left(\frac{1}{k^2} - 0.2 + 0.2\mu\right)L$	$m_4^y = 0$	$m_4^y = \left(\frac{1}{3k} + \frac{k}{15} - \frac{\mu k}{15}\right)aL$

Note: $L = \frac{D}{a} = \frac{Et^3}{12(1-\mu^2)a}$.

Table 3. Nodal Forces in a Triangular Cell

(Figs. 4, 5, 6 and 7)

Action $w_1 = 1$	Action $\theta_1^y = 1$	Action $\theta_3^x = 1$
$Z_1 = \left(\frac{27}{16\,k^3} + \frac{3}{2\,k} + 3\,k\right)\frac{L}{a}$	$Z_1 = \left(\frac{9}{8\,k^2} + \frac{\mu}{2}\right)L$	$Z_1 = \left(-\frac{1}{8\,k^3} - \frac{1}{k} + \frac{\mu}{2\,k}\right)L$
$Z_2 = \left(\frac{21}{16\,k^3} - \frac{3}{2\,k} - 3\,k\right)\frac{L}{a}$	$Z_2 = \left(\frac{7}{8\,k^2} - \frac{\mu}{2}\right)L$	$Z_2 = \left(\frac{1}{8\,k^3} + \frac{1}{k} - \frac{\mu}{2\,k}\right)L$
$Z_3 = -\frac{3}{k^3}\,\frac{L}{a}$	$Z_3 = -\frac{2}{k^2}\,L$	$Z_3 = 0$
$m_1^x = \left(-\frac{13}{32\,k^3} - \frac{1}{4\,k} - \frac{3\,k}{2} - \frac{3\,\mu}{4\,k}\right)L$	$m_1^x = \left(-\frac{13}{48\,k^2} - \frac{3\,\mu}{4}\right)L\,a$	$m_1^x = \left(\frac{1}{48\,k^3} + \frac{1}{6\,k} + \frac{\mu}{12\,k}\right)L\,a$
$m_2^x = \left(\frac{11}{32\,k^3} - \frac{1}{4\,k} - \frac{3\,k}{2} + \frac{\mu}{4\,k}\right)L$	$m_2^x = \left(\frac{11}{48\,k^2} + \frac{\mu}{4}\right)L\,a$	$m_2^x = \left(\frac{1}{48\,k^3} + \frac{1}{6\,k} + \frac{\mu}{12\,k}\right)L\,a$
$m_3^x = \left(-\frac{1}{8\,k^3} - \frac{1}{k} + \frac{\mu}{2\,k}\right)L$	$m_3^x = -\frac{1}{12\,k^2}\,L\,a$	$m_3^x = \left(\frac{1}{12\,k^3} + \frac{2}{3\,k} - \frac{2\,\mu}{3\,k}\right)L\,a$
$m_1^y = \left(\frac{9}{8\,k^2} + \frac{\mu}{2}\right)L$	$m_1^y = \left(\frac{5}{6\,k} + \frac{k}{3} - \frac{\mu\,k}{3}\right)L\,a$	$m_1^y = -\frac{1}{12\,k^2}\,L\,a$
$m_2^y = \left(\frac{7}{8\,k^2} - \frac{\mu}{2}\right)L$	$m_2^y = \left(\frac{2}{3\,k} - \frac{k}{3} + \frac{\mu\,k}{3}\right)L\,a$	$m_2^y = \frac{1}{12\,k^2}\,L\,a$
$m_3^y = \frac{1}{k^2}\,L$	$m_3^y = \frac{1}{2\,k}\,L\,a$	$m_3^y = 0$

Action $\theta_1^x = 1$	Action $\theta_3^y = 1$	Action $w_3 = 1$
$Z_1 = \left(-\frac{13}{32\,k^3} - \frac{1}{4\,k} - \frac{3\,k}{2} - \frac{3\,\mu}{4\,k}\right)L$	$Z_1 = \frac{1}{k^2}\,L$	$Z_1 = -\frac{3}{k^3}\,\frac{L}{a}$
$Z_2 = \left(-\frac{11}{32\,k^3} + \frac{1}{4\,k} + \frac{3\,k}{2} - \frac{\mu}{4\,k}\right)L$	$Z_2 = \frac{1}{k^2}\,L$	$Z_2 = -\frac{3}{k^3}\,\frac{L}{a}$
$Z_3 = \left(\frac{3}{4\,k^3} + \frac{\mu}{k}\right)L$	$Z_3 = -\frac{2}{k^2}\,L$	$Z_3 = \frac{6}{k^3}\,\frac{L}{a}$
$m_1^x = \left(\frac{19}{192\,k^3} + \frac{1}{24\,k} + \frac{5\,k}{4} + \frac{\mu}{3\,k}\right)L\,a$	$m_1^x = -\frac{1}{4\,k^2}\,L\,a$	$m_1^x = \left(\frac{3}{4\,k^3} + \frac{\mu}{k}\right)L$
$m_2^x = \left(-\frac{17}{192\,k^3} + \frac{1}{24\,k} + \frac{k}{4} - \frac{\mu}{6\,k}\right)L\,a$	$m_2^x = \frac{1}{4\,k^2}\,L\,a$	$m_2^x = \left(-\frac{3}{4\,k^3} - \frac{\mu}{k}\right)L$
$m_3^x = \left(\frac{1}{48\,k^3} + \frac{1}{6\,k} + \frac{\mu}{12\,k}\right)L\,a$	$m_3^x = 0$	$m_3^x = 0$
$m_1^y = \left(-\frac{13}{48\,k^2} - \frac{3\,\mu}{4}\right)L\,a$	$m_1^y = \frac{1}{2\,k}\,L\,a$	$m_1^y = -\frac{2}{k^2}\,L$
$m_2^y = \left(-\frac{11}{48\,k^2} - \frac{\mu}{4}\right)L\,a$	$m_2^y = \frac{1}{2\,k}\,L\,a$	$m_2^y = -\frac{2}{k^2}\,L$
$m_3^y = -\frac{1}{4\,k^2}\,L\,a$	$m_3^y = \frac{1}{k}\,L\,a$	$m_3^y = -\frac{2}{k^2}\,L$

Note: $L = \frac{D}{a} = \frac{E\,t^3}{12\,(1-\mu^2)\,a}$.

Notation

a	Dimension of the cell.
k	Aspect ratio of the cell.
m	Nodal moments due to unit nodal movement.
t	Plate thickness.
w	Transverse deflection.
x, y	Co-ordinate axes, co-ordinates of a point.
s_x, s_y	Symmetry axes.
a_x, a_y	Anti-symmetry axes.
Z	Transverse nodal force.
A, B, C, F	Co-efficients in the displacement polynomial.
D	Elastic constant.
E	Modulus of elasticity.
K	Stiffness matrix.
L	Elastic constant.
M	Bending moment.
T'	Transformation matrix.
β	Angle.
μ	Poisson's ratio.
θ	Angle of rotation of a node.

Acknowledgement

This investigation was carried out with financial support of the National Research Council of Canada, whose contribution is gratefully acknowledged.

References

1. A. Hrennikoff: Precision of Finite Element Method in Plane Stress. Proceedings, International Association for Bridge and Structural Engineering, Zürich, Switzerland, Vol. 29-II, 1969.
2. O. C. Zienkiewicz and Y. K. Cheung: The Finite Element Method in Structural and Continuum Mechanics. McGraw-Hill Publishing Co., London.
3. S. Timoshenko: Theory of Elastic Stability. McGraw-Hill Publishing Co., New York and London.
4. K. Bell: A Refined Triangular Plate Bending Finite Element. International Journal for Numerical Methods in Engineering, Jan./March 1969.

Summary

In this study analysis is made of different terms used for deflection polynomials in the flexural finite elements of triangular and quadrilateral shapes, and the conclusion is reached that some terms are essential, while others are desirable and still others inadmissible. The triangular cells are found intrinsically inferior to the rectangular ones, especially for determination of bending moments. The theoretical expectations are confirmed by comparing the results of the finite element calculations with the values determined by the equations of elasticity.

Résumé

Dans cette étude, on examine l'influence des différents termes du polynôme de la déformée admise pour la flexion des éléments triangulaires et quadrilatères, et l'on aboutit à la conclusion que certains termes sont indispensables, tandis que d'autres sont utiles, et d'autres même inadmissibles. On a trouvé que les éléments triangulaires étaient de par leur nature inférieurs aux rectangulaires, particulièrement pour le calcul des moments de flexion. Les considérations théoriques sont confirmées par la comparaison des résultats numériques avec les valeurs obtenus par les équations d'élasticité.

Zusammenfassung

In dieser Untersuchung wurden verschiedene Terme für Durchbiegungspolynome endlicher Biegelemente von dreieckiger und viereckiger Form analysiert. Daraus folgte, daß einige Terme wesentlich, andere wünschenswert und wieder andere unzulässig sind. Die dreieckigen Elemente ergaben erheblich schlechtere Genauigkeit gegenüber den rechteckigen, insbesondere für die Bestimmung der Biegemomente. Die theoretischen Erwartungen wurden durch Vergleich mit den mittels Elastizitätsgleichungen bestimmten Werten bestätigt.

Dynamic Response of Highway Bridges to Moving Loads

Comportement dynamique des ponts-routes sous les surcharges mobiles

Dynamisches Verhalten von Straßenbrücken unter bewegter Last

K. T. SUNDARA RAJA IYENGAR
Professor of Civil Engineering
Indian Institute of Science,
Bangalore

K. S. JAGADISH
Lecturer in Civil Engineering
Indian Institute of Science,
Bangalore

1. Introduction

The Highway bridge is usually considered as a beam while analysing its response to moving loads. This approach neglects the effect of transverse flexibility on the bridge response. A good number of Highway bridges are known to have widths comparable to their spans. The use of beam theory is, therefore, not always satisfactory. The discrepancies of beam theory are especially clear while considering a bridge under eccentric loading. When the load moves along a line away from the centre line of the bridge, the cross-section of the bridge is subjected to torsion in addition to flexure. This behaviour cannot be taken into account by the beam theory. A more rigorous analysis, preferably appealing to plate theory, is then desirable.

Some experimental studies were conducted by PRINCE ALFARO and VELETSOS [1], and WALKER [2], on the influence of transverse flexibility of the bridge on the response to moving loads. They used an aluminium stiffened plate model to represent the beam and slab Highway bridge. A sprung-mass system was devised to simulate the dynamic action of the vehicle. The dynamic distribution effects of the moving load were studied.

The slab bridge and the beam and slab bridge are the two common types of Highway bridges. The slab bridge can be conveniently investigated by idealising it as an isotropic plate. The beam and slab bridge is a more complex structure and the dynamic analysis of such a bridge system has been carried out by ORAN and VELETSOS [3], by treating the bridge as an isotropic plate continuous over the supporting beams. The response under moving loads of

such a structure has been studied utilising the Lagrangian formulation. The equations of motion have been integrated using the Newmark-β procedure. The differences between the beam theory and the plate-over-beams theory have been discussed.

In this paper, the Highway bridge is represented as an orthotropic plate. The analysis can be applied either to slab bridges or to beam and slab bridges. This facility is provided by the fact that the isotropic plate happens to be a special case of the orthotropic plate. It is true that the orthotropic plate analysis is less rigorous in comparison with the plate-over-beams analysis of ORAN and VELETSOS, with reference to beam and slab bridges. Nevertheless, it is known from the literature [4, 5] that the orthotropic plate theory is a reasonable approximation for beam and slab Highway bridges. The orthotropic plate theory also offers certain advantages in the formulation of the bridge response problem. The normal modes of an orthotropic plate are easily analysed and this facilitates the application of the normal mode method in the response analysis.

A satisfactory treatment of the bridge response problem requires the selection of a suitable model to represent the dynamic behaviour of the moving vehicle. A complex three-degree freedom system, incorporating viscous and Coulomb damping mechanisms, has been suggested by HUANG and VELETSOS [6] for Highway bridges treated as beams. This model represents a tractor-trailer combination, the load being applied to the bridge through three axles. When the bridge is considered to be a two-dimensional structure, the representation of the vehicle becomes more complicated. In this case, a complete representation would require the consideration of the lateral rolling effect in addition to the longitudinal pitching effect in the vehicle. Such a representation would further increase the degrees of freedom of the vehicle model. In the following analysis, a simpler representation of the vehicle is preferred, and the vehicle is approximated by a sprung mass. It is believed that a more involved vehicle model may obscure the essential features of the two-dimensional behaviour of the bridge.

2. Analysis

An orthotropic plate, simply-supported at the edges $x=0$ and a and free at the edges $y = \pm b/2$ is now considered (Fig. 1). It is subjected to a moving sprung load of mass M and spring constant k. The plate and the load are assumed to have no damping. The load is considered to be distributed uniformly over a square area of side $2e$. The centre of this square area moves in the x-direction along the line $y=c$. The plate is assumed to be at rest initially.

The deflection of the bridge is denoted by W and the absolute deflection of the sprung mass by z. The deflection of the mass is measured positive down-

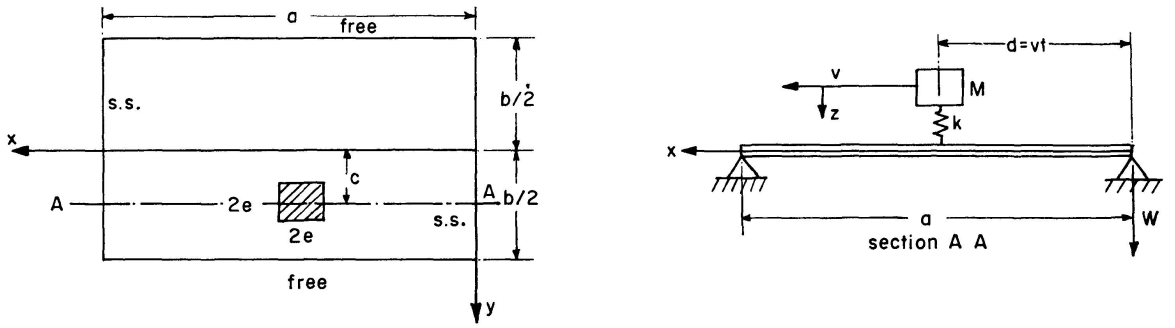


Fig. 1. Orthotropic Plate Under Moving Sprung Load.

wards from its position of equilibrium. The equations of motion of the orthotropic-plate-sprung mass system may be written as follows:

$$D_x \frac{\partial^4 W}{\partial x^4} + 2H \frac{\partial^4 W}{\partial x^2 \partial y^2} + D_y \frac{\partial^4 W}{\partial y^4} + \rho \frac{\partial^2 W}{\partial t^2} = M(g - \ddot{z}) f(x - vt, y) \tag{1}$$

and

$$M\ddot{z} + k[z - W(x, c, t)|_{x=vt}] = 0. \tag{2}$$

M represents the mass of the moving load, D_x, H and D_y are the orthotropic plate rigidities and ρ is the mass of the plate per unit area. f represents the time-dependent function distributing the load over the surface of the bridge. This function is constant over a small area over which the load is considered to be distributed and is zero elsewhere. g is the acceleration due to gravity.

The solution to the Eqs. (1) and (2) can now be obtained by using the characteristic functions of the orthotropic plate. These functions are briefly discussed in the Appendix.

Now the deflection of the orthotropic plate may be expressed as,

$$W = \sum_{m=1}^{\infty} \sum_{n=1}^{\infty} \Phi_{mn}(t) Y_{mn}(y) \operatorname{Sin} \frac{m\pi x}{a}, \tag{3}$$

where $Y_{mn}(y) \operatorname{Sin} \frac{m\pi x}{a}$ represents one of the characteristic functions of the plate and $\Phi_{mn}(t)$ is the corresponding normal co-ordinate. The function $f(x - vt, y)$ may be expressed algebraically as,

$$\begin{aligned} f(x - vt, y) &= \frac{1}{4e^2} \quad \text{if } vt - e < x < vt + e \text{ and } c - e < y < c + e, \\ &= 0 \quad \text{if } x < vt - e \text{ or } > vt + e \text{ and } y < c - e \text{ or } > c + e. \end{aligned} \tag{4}$$

This function can also be expanded by a series as follows:

$$f(x - vt, y) = \sum_{m=1}^{\infty} \sum_{n=1}^{\infty} b_{mn}(t) Y_{mn}(y) \operatorname{Sin} \frac{m\pi x}{a}. \tag{5}$$

Making use of the orthogonal property of the characteristic functions,

$$b_{mn}(t) = \frac{f_{mn}}{K_{mn} a b} \operatorname{Sin} \frac{m\pi vt}{a}, \tag{6}$$

where, $$K_{mn} = \frac{1}{a\,b}\int_0^a \int_{-b/2}^{+b/2} Y_{mn}^2 \operatorname{Sin}^2 \frac{m\pi x}{a}\,dx\,dy$$

and $$f_{mn} = \frac{\operatorname{Sin}\frac{m\pi e}{a}}{\frac{m\pi e}{a}} \frac{1}{2e}\int_{c-e}^{c+e} Y_{mn}\,dy.$$

Making use of (3) and (5) in (1),

$$\ddot{\Phi}_{mn} + p_{mn}^2 \Phi_{mn} = \frac{M(g-\ddot{z})}{a\,b}\frac{f_{mn}}{K_{mn}} \operatorname{Sin}\alpha_m t, \quad \begin{matrix} m = 1, 2 \ldots \\ n = 1, 2 \ldots \end{matrix} \tag{7}$$

where $\alpha_m = \frac{m\pi v}{a}$ and p_{mn} is the circular frequency of vibration of the plate when the shape function happens to be $Y_{mn} \operatorname{Sin}\frac{m\pi x}{a}$. Using (3) in (2),

$$\ddot{z} + \omega^2 z = \omega^2 \sum_{m=1}^{\infty}\sum_{n=1}^{\infty} \Phi_{mn}(t)\, Y_{mn}(c) \operatorname{Sin}\alpha_m t, \tag{8}$$

where $\omega^2 = k/M$.

Eqs. (7) and (8) constitute an infinite set of simultaneous differential equations for the normal co-ordinates $\Phi_{mn}(t)$ and the load displacement z. This set of equations may be solved by numerical means after truncating it suitably. The numerical integration has been carried out by the Runge-Kutta-Nyström method.

The Eq. (3) is found to be inconvenient for the computation of moments due to poor convergence. This difficulty can be surmounted by splitting the solution W into "quasi-static" and "inertia-force" solutions, as indicated below.

Let, $$W(x, y, t) = \overline{W}(x, y, t) + u(x, y, t). \tag{9}$$

$\overline{W}$, represents the quasi-static solution and u represents the inertia force solution. $\overline{W}$ is chosen so as to satisfy the equation,

$$D_x \frac{\partial^4 \overline{W}}{\partial x^4} + 2H \frac{\partial^4 \overline{W}}{\partial x^2 \partial y^2} + D_y \frac{\partial^4 \overline{W}}{\partial y^4} = M(g-\ddot{z}) f(x - v t, y). \tag{10}$$

It is presumed that z is already known by the numerical integration of the Eqs. (7) and (8). $\overline{W}$ then represents the instantaneous static response of the bridge to a moving variable force. This equation can be easily solved by a double series expansion. The quasi-static solution can now be conveniently expressed as,

$$\overline{W}(x, y, t) = \frac{M g}{D_x}\left(1 - \frac{\ddot{z}}{g}\right) a^2 \delta_D, \tag{11}$$

where δ_D is the influence coefficient for deflection at any point (x, y) of the bridge. This influence coefficient is obtained from the solution of Eq. (10) [7].

The coefficient δ_D is only a function of the position of the load and is independent of the speed of the moving load. The moment $\overline{M}_x$ at any point due to the quasi-static solution may be expressed in a similar way as follows:

$$\overline{M}_x(x, y. t) = M g\left(1-\frac{\ddot{z}}{g}\right)\delta_M. \tag{12}$$

δ_M is the influence coefficient for moment at any point.

With $\overline{W}$ defined as above, the function u must satisfy the following equation

$$D_x\frac{\partial^4 u}{\partial x^4}+2H\frac{\partial^4 u}{\partial x^2\partial y^2}+D_y\frac{\partial^4 u}{\partial y^4}=-\rho\frac{\partial^2 u}{\partial t^2}-\rho\frac{\partial^2 \overline{W}}{\partial t^2}=-\rho\frac{\partial^2 W}{\partial t^2}. \tag{13}$$

Making use of (3),

$$D_x\frac{\partial^4 u}{\partial x^4}+2H\frac{\partial^4 u}{\partial x^2\partial y^2}+D_y\frac{\partial^4 u}{\partial y^4}=-\rho\sum_{m=1}^{\infty}\sum_{n=1}^{\infty}\ddot{\Phi}_{mn}Y_{mn}\operatorname{Sin}\frac{m\pi x}{a}.$$

Solving this equation, one can write:

$$u(x, y, t)=-\frac{\rho a b}{D_x}a^2\frac{a}{b}\sum_{m=1}^{\infty}\sum_{n=1}^{\infty}\frac{\ddot{\Phi}_{mn}}{\lambda_{mn}}Y_{mn}\operatorname{Sin}\frac{m\pi x}{a}, \tag{14}$$

where

$$\lambda_{mn}=\frac{\rho p_{mn}^2 a^4}{D_x}.$$

Combining (11) and (14), the complete solution W becomes,

$$W=\frac{M g a^2}{D_x}\left[\left(1-\frac{\ddot{z}}{g}\right)\delta_D-\frac{\rho a b}{M}\frac{a}{b}\sum_{m=1}^{\infty}\sum_{n=1}^{\infty}\frac{\ddot{\Phi}_{mn}}{g\lambda_{mn}}Y_{mn}\operatorname{Sin}\frac{m\pi x}{a}\right]. \tag{15}$$

The bending moment M_x in the orthotropic plate is given by

$$M_x=-D_x\left(\frac{\partial^2 W}{\partial x^2}+\frac{\nu D_y}{D_x}\frac{\partial^2 W}{\partial y^2}\right), \tag{16}$$

where ν is the Poisson's ratio of the slab material. Here, it is assumed that $D_y=D$ where D is the flexural rigidity of the slab of the beam and slab bridge. D_1 is taken to be $\nu D=\nu D_y$ following the analysis of HUFFINGTON [8] for the selection of orthotropic plate rigidities. Applying the above equation to (15),

$$M_x=M g\left[\left(1-\frac{\ddot{z}}{g}\right)\delta_M-\frac{\rho a b}{M}\frac{a}{b}\sum_{m=1}^{\infty}\sum_{n=1}^{\infty}\frac{\ddot{\Phi}_{mn}}{g\lambda_{mn}}\operatorname{Sin}\frac{m\pi x}{a}\left(m^2\pi^2 Y_{mn}-\nu\frac{D_y}{D_x}\frac{a^2}{b^2}\overline{Y}_{mn}\right)\right], \tag{17}$$

where

$$\overline{Y}_{mn}=\frac{b^2 d^2 Y_{mn}}{dy^2}.$$

The values of δ_D and δ_M can be obtained by the static analysis using any routine method [7].

The amplification factors for deflection and moment at midspan can now be expressed as,

Amplification factor for deflection

$$= A F D = \frac{W(a/2, y, t)}{M g a^2 (\delta_D)_{max}} D_x. \tag{18}$$

Amplification factor for moment M_x

$$= A F M = \frac{M_x(a/2, y, t)}{M g (\delta_M)_{max}}. \tag{19}$$

Here $(\delta_D)_{max}$ and $(\delta_M)_{max}$ are the maximum values of the midspan influence coefficients.

3. Numerical Studies

Two typical Highway bridges are considered for detailed numerical study. One of them is a short-span slab bridge and the other is a medium span beam and slab bridge. The geometrical and structural characteristics of the two bridges are summarised in Table 1.

Table 1. Details of Bridges Considered

Bridge Type	Span Metres (Ft.)	a/b	D_x/D_y	$\frac{H}{\sqrt{D_x D_y}}$	$\sqrt{D_x}$ kg$^{1/2}$ m$^{1/2}$ (lb.$^{1/2}$ ft.$^{1/2}$)	ρ kg sec^2/m^3 (lb. sec^2/ft.^{3})	ν
Slab	5.00 (16.41)	1.0	1.0	1.0	2500.00 (6718.75)	60.00 (3.74)	0.0
Beam and Slab	20.00 (65.65)	2.0	100.0	0.4	25,000.00 (67 187.50)	90.00 (5.61)	0.0

In all the numerical results presented here, five modes of the bridge are considered while calculating the inertia-force solution. For these five modes, the value of m is equal to unity and n takes values from 1 to 5. In an earlier study [9], the authors have shown that the bridge response is influenced mostly by the first three modes. The use of five modes in the present case may therefore be considered to be more than adequate. As was mentioned earlier, the Runge-Kutta-Nyström method has been used to integrate the equations of motion. The time interval for the integration has been chosen to be one-tenth the period of the fifth mode in all the calculations.

The entire procedure for numerical integration and the evaluation of amplification factors for deflection and moment was programmed in Fortran to run on a CDC-3600 computer. The programme obtains the ordinates of the amplification history curves at midspan for deflection and moment. It also incorporates a scheme for picking out the peak values of deflection and moment amplifications.

A number of variables, mentioned below, were considered while making a detailed study of the problem.

a) The Speed Parameter

This parameter is given by $\alpha = \frac{v\,T}{2\,a}$ where v is the speed of the moving sprung load and T is the fundamental period of the bridge. The values considered for this parameter lie between 0.06 and 0.20. This range covers most of the practical bridge dimensions and vehicle speeds.

b) The Frequency and Mass Ratios

The frequency ratio is denoted by $\delta_1 = \omega/p_{11}$ and the mass ratio by $\delta_2 = M/\rho a b$. These two ratios are important as they control the oscillation in the sprung load. The practical vehicle frequencies are mostly less than the fundamental frequency of bridges. Accordingly the values of δ_1 between 0.2 and 1.0 are considered. The weight of the vehicle would normally be less than the weight of the bridge even if vehicles in excess of 30 tons are considered. The values of δ_2 between 0.25 and 1.0 are considered in the numerical studies.

c) The Transverse Vehicle Position

This variable is denoted by c. It has a significant influence on the participation of the various modes of the bridge as the load moves over the bridge. In this paper, two values of c i.e. $c = 0.0$ and $0.45\,b$ are considered.

d) Initial Oscillation of the Sprung Load

The initial oscillation of the sprung load can be described by its initial velocity and displacement. A detailed study would require that these two variables should be varied independently. Such an elaborate study was not envisaged in this paper and the initial oscillation is prescribed only by the initial displacement. The initial velocity is taken to be zero for all the calculations. The magnitude of the initial displacement may be conveniently expressed with reference to the static displacement of the spring under load. If z_0 is the initial displacement, then it may be expressed as,

$$z_0 = \delta_3 \frac{M\,g}{k}.$$

Values of $\delta_3 = 0.2$ and 0.75 are considered.

4. Amplification Spectra

The values of AFD_{max} and AFM_{max} at the midspans of the beam and slab bridge are presented in Figs. 2 to 5 for typical loadings against α. Figs. 2 and 3 refer to the beam and slab bridge and the other two figures refer to the slab bridge. The details of these two bridges are given in Table 1.

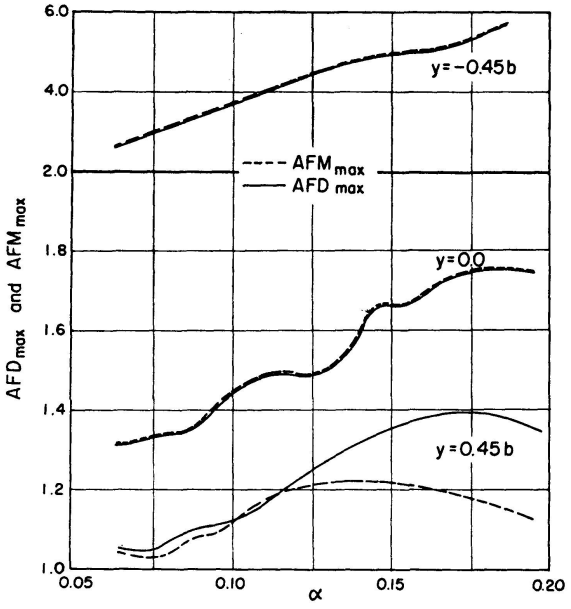


Fig. 2. Amplification Spectra for the Beam and Slab Bridge. Sprung Load Moves Along $y = 0.45b$; $\delta_1 = 0.6$; $\delta_2 = 0.5$; $\delta_3 = 0.0$.

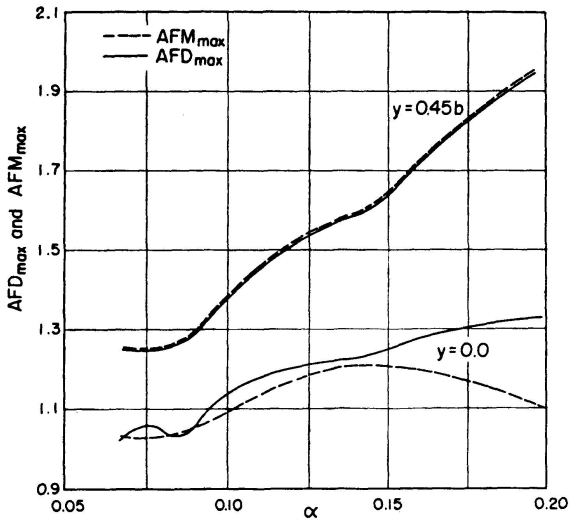


Fig. 3. Amplification Spectra for the Beam and Slab Bridge. Sprung Load Moves Along $y = 0.0$; $\delta_1 = 0.6$; $\delta_2 = 1.0$; $\delta_3 = 0.0$.

Figs. 2 and 3 show the amplification spectra for typical eccentric and concentric loadings respectively, of the beam and slab bridge. The spectra are presented for points at midspan given by $y = \pm 0.45b$ and $y = 0.0$. In general, the amplifications are large for points away from the line of loading. For the midspan point under the loading, the AFM_{max} values are generally smaller than AFD_{max} values. This effect is pronounced for the higher values of the speed parameter. For points away from the line of loading, the AFD_{max} and AFM_{max} values are practically equal. The unloaded edge ($y = -0.45b$) experiences larger amplifications in the eccentrically loaded case than in the concentrically loaded case. However, these large amplifications are not serious, since the static values at the unloaded edge would be quite small due to the nature of the load distribution.

Typical cases of eccentric and concentric loading of the slab bridge are studied in Figs. 4 and 5. All the characteristics noticed in the beam and slab bridge are to be found in this bridge as well. The magnitudes of AFD_{max} and AFM_{max} values at the unloaded edges are much smaller for this bridge.

The amplification spectra obtained by beam theory are presented along with the results of the orthotropic plate theory in Figs. 6 and 7. The beam and slab bridge under eccentric and concentric loadings is considered. For purposes of comparison, the midspan points of the beam and slab bridge lying on the lines of loading are considered. The spectra for such points, by the orthotropic plate theory, are plotted along with the spectra obtained by beam theory. The points indicated in the above happen to be the critically stressed points in the bridge. The amplifications at these points would therefore be of interest to the bridge designer.

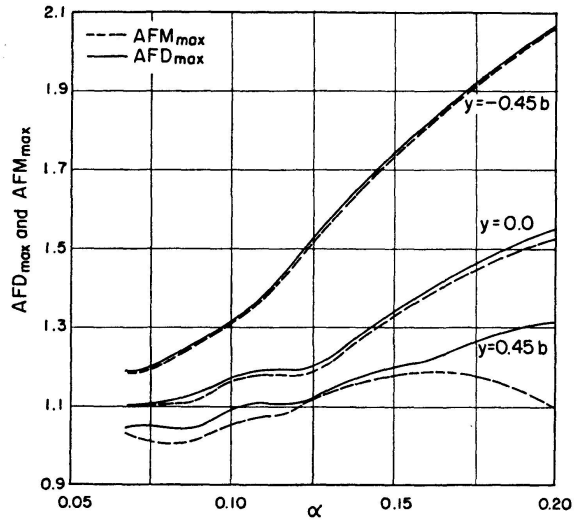


Fig. 4. Amplification Spectra for the Slab Bridge. Sprung Load Moves Along $y = 0.45b$; $\delta_1 = 0.6$; $\delta_2 = 0.5$; $\delta_3 = 0.0$.

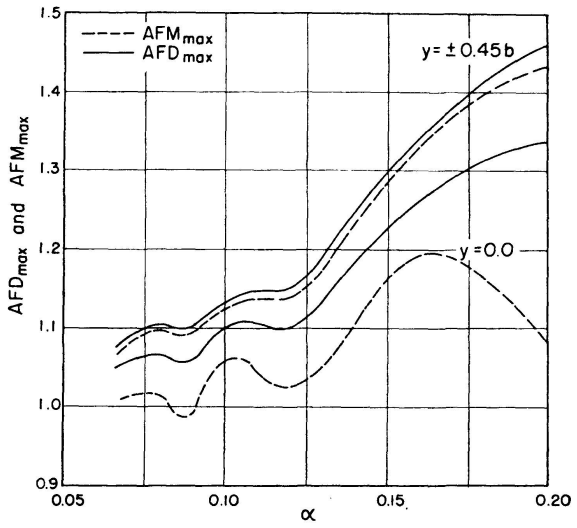


Fig. 5. Amplification Spectra for the Slab Bridge. Sprung Load Moves Along $y = 0.0$; $\delta_1 = 0.6$; $\delta_2 = 0.5$; $\delta_3 = 0.0$.

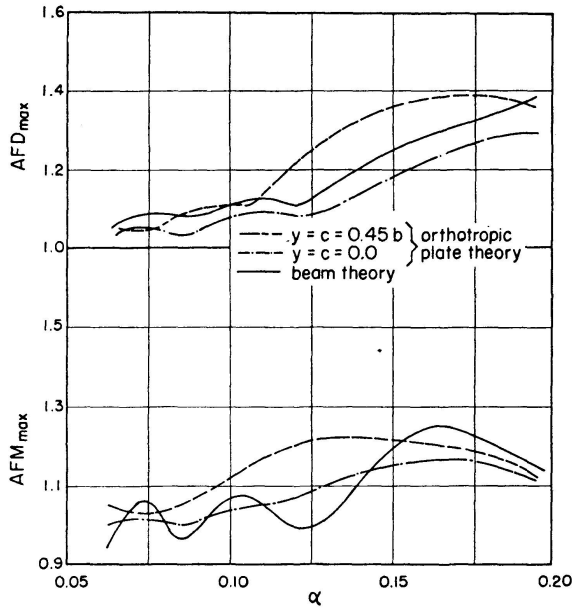


Fig. 6. Comparison of the Spectra by Beam Theory and Orthotropic Plate Theory for the Beam and Slab Bridge. $\delta_1 = 0.6$; $\delta_2 = 0.5$; $\delta_3 = 0.0$.

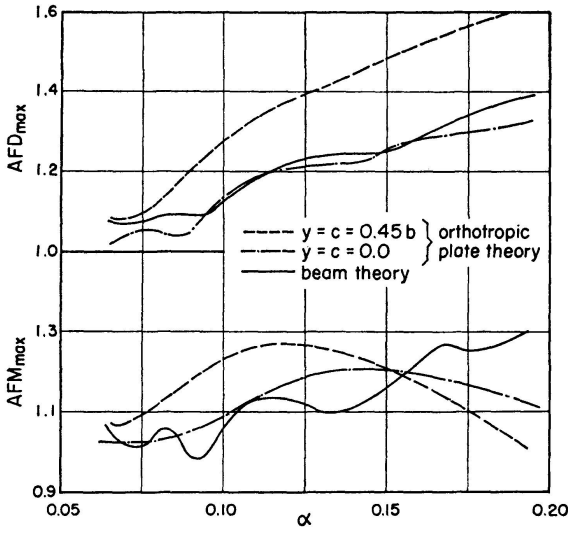


Fig. 7. Comparison of the Spectra by Beam Theory and Orthotropic Plate Theory for the Beam and Slab Bridge. $\delta_1 = 0.6$; $\delta_2 = 1.0$; $\delta_3 = 0.0$.

The shapes of the spectra for AFD_{max} given by the orthotropic plate theory and the beam theory are quite similar. The values of AFD_{max} in the eccentrically loaded case are generally larger than the values given by beam theory. The deflection amplifications for concentric loading are nearly of the same order of magnitude as the amplifications given by beam theory.

There are considerable differences between the shapes of the AFM_{max} spectra given by the orthotropic plate theory and the beam theory. The AFM_{max} values in eccentric loading are larger than the values of the beam theory for the smaller speeds. For the higher speeds, the values by beam

theory are found to be larger than the values in eccentric loading. The magnitudes of AFM_{max} in concentric loading do not differ significantly from the magnitudes found by the beam thory.

A study of a good number of spectral curves [7], besides those presented here, showed that the AFM_{max} for the critically stressed point (i. e. the midspan point in the line of loading) rarely exceeds a value of 1.3, for speed parameter values below 0.2. The study of WALKER and VELETSOS [11] showed that the midspan moment amplification by beam theory does not exceed a value of 1.4 for the same range of speeds. This indicates that the absolute maximum value of the moment amplification given by the beam theory is slightly on the conservative side with reference to the critically stressed point of the Highway bridge. The same conclusion was also obtained by the detailed studies conducted at the University of Illinois [12] on multigirder bridges.

5. The Effect of Mass and Frequency Ratios

The maximum amplification factors for the midspan moment in the slab bridge for eccentric and concentric loadings, are presented in Figs. 8 and 9, as functions of the frequency ratio. The values of α equal to 0.174 and 0.126 are considered. The larger values of AFM_{max} at points on the line of loading, are experienced for δ_1 between 0.6 and 1.0. The same trend is found in beams

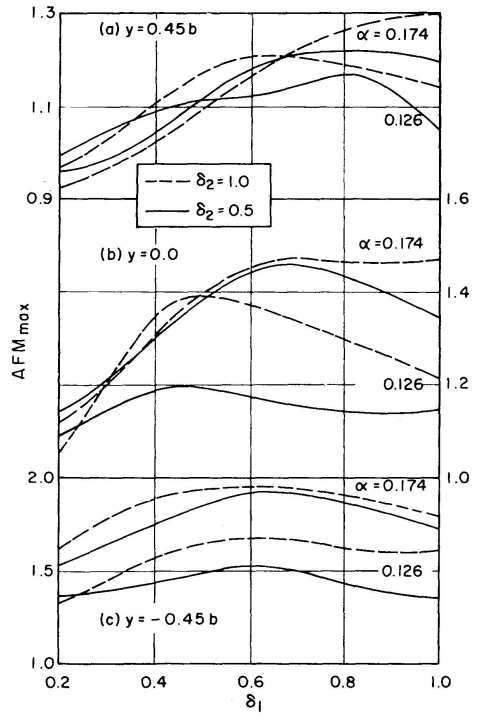


Fig. 8. Influence of Frequency and Mass Ratios on the Maximum Moment Amplification at Midspan. Slab Bridge Under Eccentric Loading. Load Along $y = 0.45b$.

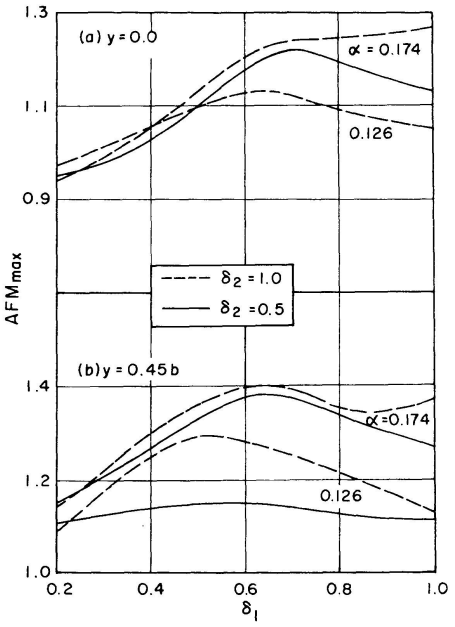


Fig. 9. Influence of Frequency and Mass Ratios on the Maximum Moment Amplification at Midspan. Slab Bridge Under Concentric Loading. Load Along $y = 0.0$.

as observed by WALKER and VELETSOS [11]. When the slab bridge is loaded eccentrically, the unloaded edge is not influenced noticeably, by a change in δ_1. The point $y = 0.0$ at midspan, for eccentric loading, shows increased dynamic effects for δ_1 between 0.6 and 1.0 (Fig. 8), when the speed parameter is 0.174. When the speed parameter is 0.126, the AFM_{max} values at the same point are larger for δ_1 between 0.4 and 0.6. Thus, the figure shows that there can be no simple relationship between the frequency ratio and the maximum amplification factor. The speed parameter affects the instant of bottoming of the sprung load, and this is responsible for the complexity in the dependence of AFM_{max} on δ_1. The same trends are observed even in the concentric loading of the slab bridge (Fig. 9). The effect of mass ratio δ_2 is less pronounced when compared to the frequency ratio. The AFM_{max} values are generally larger for the higher mass ratio, except when δ_1 is small. For the smaller values of δ_1, the mass ratio does not have any noticeable influence.

The detailed studies conducted by JAGADISH [7] showed that similar effects are present in the beam and slab bridge as well.

6. History Curves

The history curves presented here show the variation of AFM and AFD, at certain points, as the sprung load moves over the bridge. Figs. 10 to 13 show some of the typical history curves. The AFM variations for the midspan points $y = \pm 0.45b$ and $y = 0.0$ are plotted in these curves and the AFD variation is shown only for the midspan point in the line of loading. The AFD values were found to be practically equal to the AFM values for points away from the loading. The force of interaction between the sprung load and the bridge is also presented with each graph. This interaction force is represented by $R = Mg(1 - \frac{\ddot{z}}{g})$. All the curves are presented for a speed parameter value of 0.174.

Figs. 10 and 11 show the history curves for the eccentric loading of the beam and slab bridge. In Fig. 10, $\delta_1 = 0.2$ and the unloaded edge shows a beating type of motion. The earlier studies of the authors [7, 9] had shown that the unloaded edge of this beam and slab bridge shows a beating motion as a constant force moves along one of the edges. In Fig. 10, the interaction force R does not vary within wide limits since δ_1 is well below unity. As such, the moving constant force effect may be expected to dominate the response. As the frequency of the sprung load is increased to make $\delta_1 = 0.6$ (Fig. 11), the oscillation of the load becomes more pronounced. The interaction force reaches a value as large as 2.3 Mg when the load is near the third quarter point. The oscillation of the load now interferes with the beating phenomenon at the unloaded edge. When the load is near the third quarter point, the mass bottoms and the negative peaks of the motion of the unloaded edge are reduced in

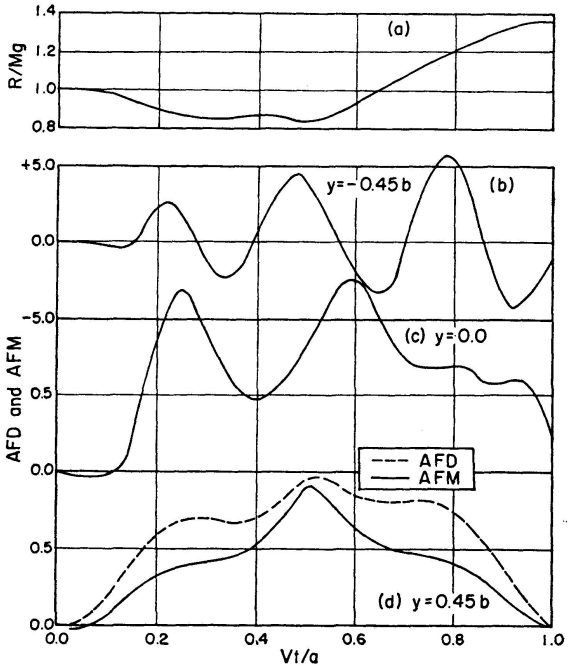


Fig. 10. History Curves for Interaction Force and Midspan Amplifications. Beam and Slab Bridge Under Eccentric Load. Load Along $y = 0.45b; \alpha = 0.174; \delta_1 = 0.2; \delta_2 = 1.0; \delta_3 = 0.0$.

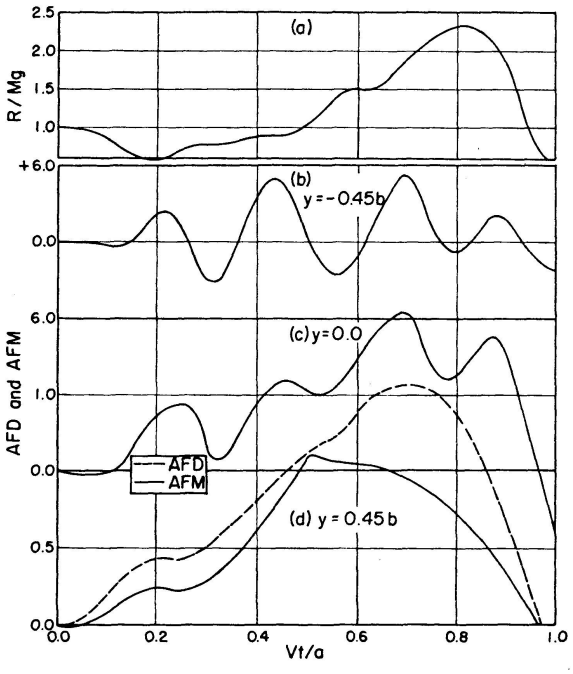


Fig. 11. History Curves for Interaction Force and Midspan Amplifications. Beam and Slab Bridge Under Eccentric Load. Load Along $y = 0.45b; \alpha = 0.174; \delta_1 = 0.6; \delta_2 = 1.0; \delta_3 = 0.0$.

magnitude. In spite of the sharp bottoming near the third quarter, the maximum moment at midspan of the loaded edge occurs when the load is at midspan. However, the moment at midspan remains quite large as the load moves from midspan to the third quarter point. The maximum deflection at midspan of the loaded edge occurs when the load has moved away from midspan. The same feature was observed [9] in the moving constant force problem. It is thus seen that the maximum moment and the maximum deflection at midspan of the loaded edge do not occur at the same instant. This may be explained by the fact that the static influence line for the midspan moment is highly peaked near midspan (for the midspan point on the line of loading) and this causes the maximum dynamic moment to occur when the load is at midspan. The influence line for midspan deflection, on the other hand, is relatively flat near midspan, and the inertia effects may cause the maximum dynamic deflection to occur when the load is away from midspan. This also explains the considerable differences between the AFD_{max} and the AFM_{max} spectra for the loaded edge shown in Figs. 2 and 4. Large values of dynamic deflection can be expected even when the load bottoms well away from midspan. For a large dynamic moment to occur at midspan of the loaded edge, the load must bottom when it is at midspan.

Fig. 12 shows the history curve for the slab bridge under eccentric loading, with $\delta_1 = 0.6$ and $\delta_2 = 1.0$. The unloaded edge of this bridge does not show as large AFM values as were found in the beam and slab bridge. This difference in the behaviour of the two bridges may be attributed to the nature of their

Table 2. Frequencies of Bridges Considered

Type	Frequencies in cycles/sec.			
	Fundamental	I Asymmetric	II Symmetric	II Asymmetric
Slab	20.27	36.73	80.57	159.3
Beam and Slab	10.34	12.09	18.98	33.88

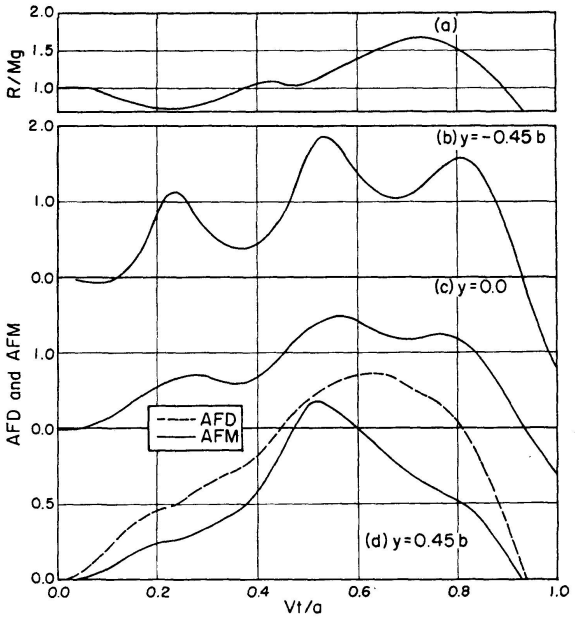


Fig. 12. History Curves for Interaction Force and Midspan Amplifications. Slab Bridge Under Eccentic Load. Load Along $y = 0.45b$; $\alpha = 0.174$; $\delta_1 = 0.6$; $\delta_2 = 1.0$; $\delta_3 = 0.0$.

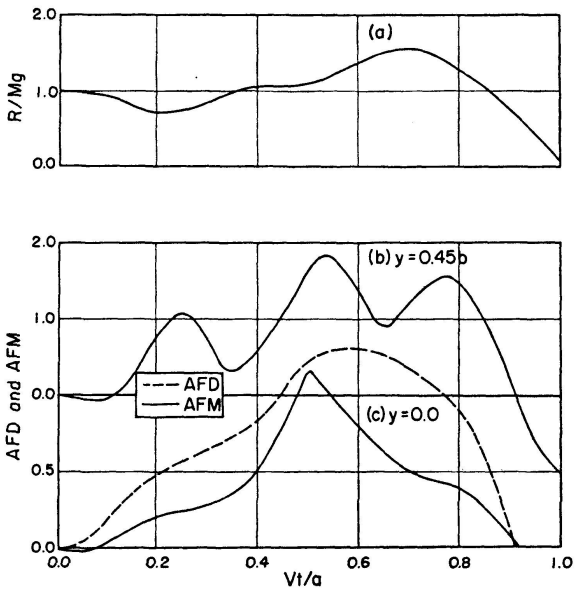


Fig. 13. History Curves for Interaction Force and Midspan Amplifications. Beam and Slab Bridge Under Concentric Load. Load Along $y = 0.0$; $\alpha = 0.174$; $\delta_1 = 0.6$; $\delta_2 = 1.0$; $\delta_3 = 0.0$.

frequency spectra. Table 2 shows the values of the frequencies of the first four modes of the bridges. It is clear that there is a relatively dense distribution of frequencies in the beam and slab bridge. This is especially true of the first two frequencies. Consequently, there is a significant participation by the second mode in the response of the beam and slab bridge.

The history curves for the beam and slab bridge with concentric loading are shown in Fig. 13. The variation in the interaction force is not generally as drastic as it would be for eccentric loading. The differences between the AFD_{max} and AFM_{max} under the load are not so pronounced in this case. The amplification at the points $y = \pm 0.45\,b$ is larger than what is to be found at $y = 0.0$. The maximum moment at the midspan point on the line of loading, is seen to occur when the load is close to midspan.

7. Initially Oscillating Sprung Load

A few history curves for the midspan moment in the beam and slab bridge, with initially oscillating moving load, are presented in Fig. 14 to 16. The

initial oscillation is specified by a positive displacement of the sprung load which is expressed as a fraction δ_3 of the static displacement of the spring under the load. The values of δ_1 and δ_2 are held constant at 0.6 and 1.0 respectively. The parameter δ_3 is given values of 0.2 and 0.75 in these numerical studies.

Figs. 14 and 15 consider the eccentric loading of the beam and slab bridge for speed parameter values of $\alpha = 0.174$ and $\alpha = 0.126$ respectively. The history curves for the case with no initial oscillation are also presented. It is clearly observed that the initially oscillating sprung load undergoes much the same type of oscillation it shows when there is no initial oscillation. The locations

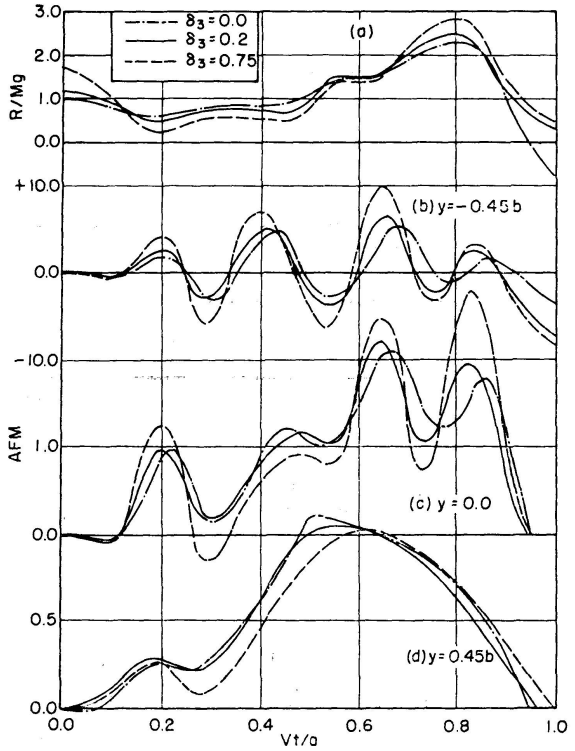


Fig. 14. History Curves for Beam and Slab Bridge Under Eccentric and Initially Oscillating Load. Load Along $y = 0.45b$; $\alpha = 0.174$; $\delta_1 = 0.6$; $\delta_2 = 1.0$.

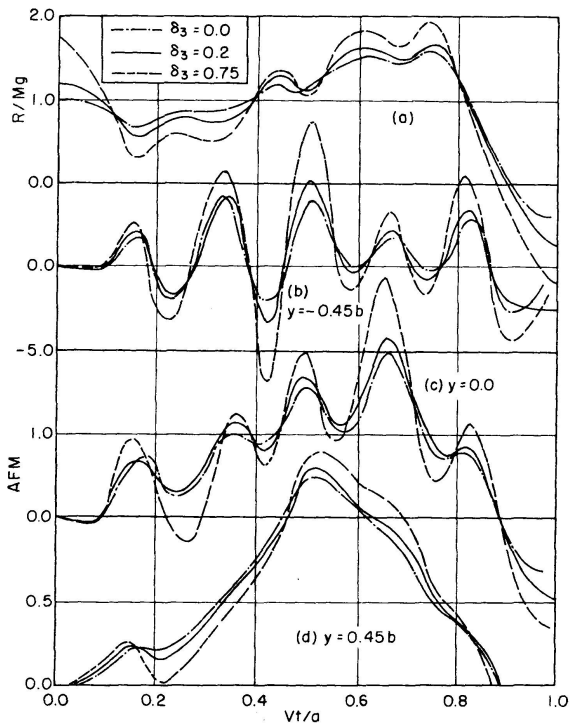


Fig. 15. History Curves for Beam and Slab Bridge Under Eccentric and Initially Oscillating Load. Load Along $y = 0.45b$; $\alpha = 0.126$; $\delta_1 = 0.6$; $\delta_2 = 1.0$.

of the peaks and depressions in the interaction force curve are not shifted as the initial displacement is increased. The amplitudes of the sprung load motion are greater when there is a larger initial displacement. The moment history curves for the different values of initial displacement also follow each other, the oscillations being more violent with the higher value of initial displacement. For $\alpha = 0.174$, a large bottoming of the load occurs, when it is near the third quarter point. As the bottoming occurs well away from midspan, the moment amplification under the line of loading at midspan is not seriously affected by initial oscillation. For midspan points away from the line of loading, the amplitudes of oscillation are affected to a marked degree and the maximum moment

amplifications occur when the load is well away from midspan. With $\alpha = 0.126$, the significant bottoming occurs when the load is nearer midspan. The maximum moment under the line of loading at midspan is therefore considerably influenced by the amplitude of initial oscillation.

Fig. 16 shows the moment response at midspan of the beam and slab bridge under concentric loading, with $\alpha = 0.126$. Features observed for the eccentrically loaded case are repeated here. There is a sharp bottoming of the load when it is at midspan and the increase in initial displacement loads to larger moment at the midspan point on the line of loading.

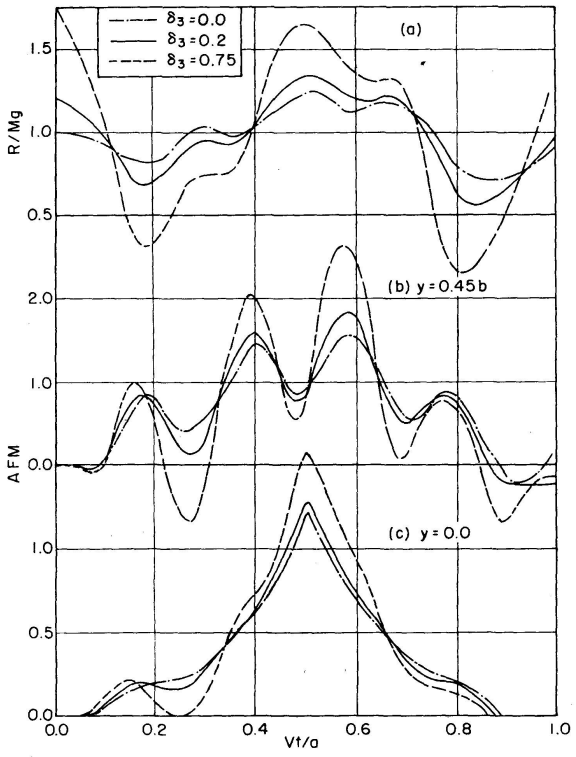


Fig. 16. History Curves for Beam and Slab Bridge Under Concentric and Initially Oscillating Load. Load Along $y = 0.0$; $\alpha = 0.126$; $\delta_1 = 0.6$; $\delta_2 = 1.0$.

8. Transverse Distribution of Dynamic Effects

The transverse distributions of dynamic deflection and moment at midspan, for various positions of the moving load, are shown in Figs. 17 and 18. The beam and slab bridge is considered with $\alpha = 0.174$, $\delta_1 = 0.6$ and $\delta_2 = 0.5$. Initial oscillation is not considered. The distribution of maximum static deflection and moment are shown in dashed lines.

In general, it may be observed that the dynamic profiles do not vary as sharply across the width as the maximum static profiles. This is due to the fact that the maximum dynamic increments of deflection and moment are of the same order of magnitude across the width. This feature of the distribution of dynamic increments was also observed by REILLY and LOONEY [13], in their

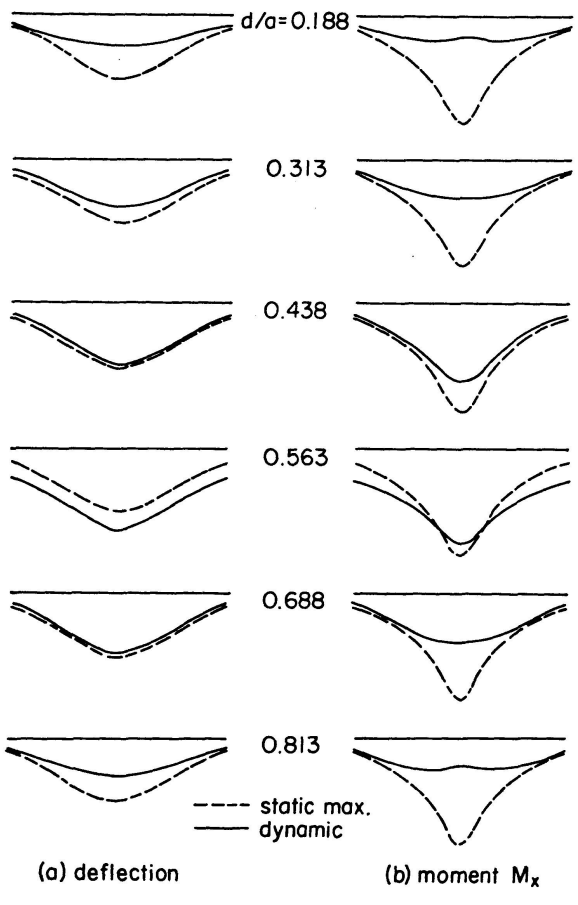


Fig. 17. Transverse Distribution of Dynamic Deflection and Moment at Midspan of the Beam and Slab Bridge. Sprung Load Along $y = 0.0$; $\alpha = 0.174$; $\delta_1 = 0.6$; $\delta_2 = 0.5$; $\delta_3 = 0.0$.

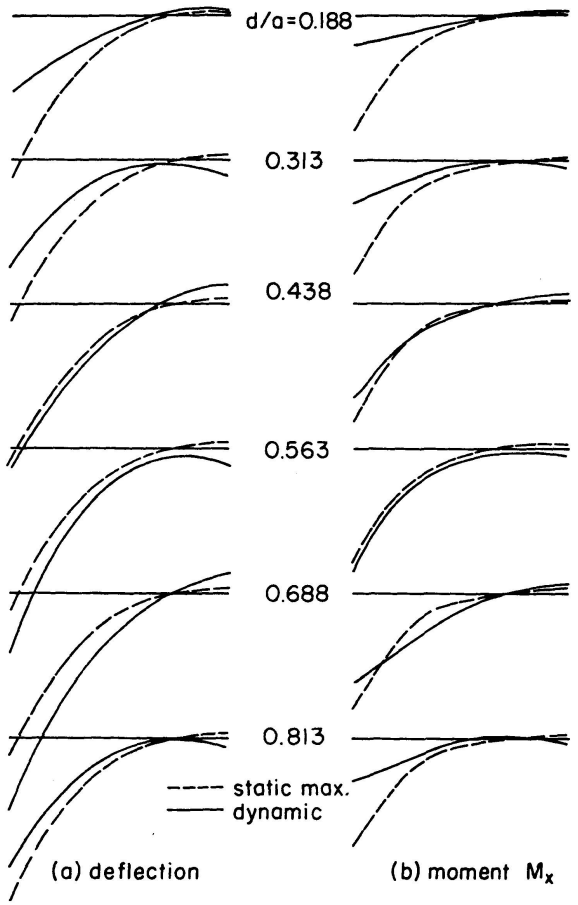


Fig. 18. Transverse Distribution of Dynamic Deflection and Moment at Midspan of the Beam and Slab Bridge. Sprung Load Along $y = 0.45b$; $\alpha = 0.174$; $\delta_1 = 0.6$; $\delta_2 = 0.5$; $\delta_3 = 0.0$.

test results. It may be attributed to the distributing effect of the inertia forces developed in the bridge. In the eccentrically loaded case, the unloaded edge experiences small negative deflections and moments.

9. Conclusions

A study of a large number of results [7], besides those presented here, lead to some general observations about the two dimensional behaviour of Highway bridges. The numerical study was restricted to two typical bridges and this places a limitation on the generality of the conclusions obtained here. However, it is believed that the major trends observed here will be present in most of the other types of beam and slab Highway bridges.

The maximum amplification factors are found to be larger for points in the bridge away from the line of loading. This effect is more pronounced for an eccentrically loaded bridge. In this type of loading, the unloaded edge experiences quite large amplifications irrespective of the frequency and mass ratios.

The amplifications in the beam and slab bridge are much larger than the amplifications in the slab bridge. The amplifications given by the beam theory are slightly on the conservative side when compared to the amplifications of the critically stressed point in the orthotropic plate theory.

For points away from the line of loading, the moment and deflection amplifications are practically equal. For points on the line of loading, the maximum moment amplification factors are generally smaller than the deflection amplification factors. This effect is more pronounced for larger values of the speed parameter. The maximum moment, at the midspan point on the line of loading, always occurs when the load is at or very close to the midspan even if the interaction force is not large at this instant. For the larger values of the speed parameter, the load bottoms near the third quarter point and the maximum deflection amplification occurs when the load has travelled away from the midspan. Thus, the interaction force variation has a stronger influence on the maximum deflection rather than the maximum moment, for points on the line of loading. This accounts for the considerable differences between AFD_{max} and AFM_{max} for such points.

The frequency and mass ratios have definite, although secondary, influences on the response characteristics. When the frequency ratio is between 0.6 and 1.0, large dynamic effects are observed. The effect of mass ratio is less pronounced, although the amplifications generally increase with the mass ratio.

The initial oscillation generally leads to higher amplitude oscillations all over the bridge. The maximum moment, at the midspan point on the line of loading, would be increased significantly by initial oscillation only if the load bottoms at or near the midspan. In a flexible bridge, eccentric loading with initial oscillation may produce pronounced oscillations at the unloaded edge.

Appendix

The expressions for $Y_{mn}(y)$ are presented in this appendix. The functions $Y_{mn}\,\mathrm{Sin}\frac{m\pi x}{a}$ happen to be the shape functions of an orthotropic plate with two opposite edges simply-supported and the other two free. The expressions for the functions may be easily obtained by a free-vibration analysis of the plate.

Modes Symmetric in $y-n$ is Odd

1. $D_1 \neq 0$

$$Y_{mn}(y) = \frac{\mathrm{Cosh}\,\alpha_{mn}\frac{y}{b}}{\mathrm{Cosh}\frac{\alpha_{mn}}{2}} + \frac{\alpha_{mn}^2 - \frac{D_1}{D_y}\frac{m^2\pi^2 b^2}{a^2}}{\beta_{mn}^2 + \frac{D_1}{D_y}\frac{m^2\pi^2 b^2}{a^2}} \frac{\mathrm{Cos}\frac{\beta_{mn} y}{b}}{\mathrm{Cos}\frac{\beta_{mn}}{2}},$$

where α_{mn} and β_{mn} satisfy the equations

$$\tan\frac{\beta_{mn}}{2} = -\frac{\alpha_{mn}}{\beta_{mn}}\left[\frac{\beta_{mn}^2+\frac{D_1}{D_y}\frac{m^2\pi^2b^2}{a^2}}{\alpha_{mn}^2-\frac{D_1}{D_y}\frac{m^2\pi^2b^2}{a^2}}\right]^2\tanh\frac{\alpha_{mn}}{2}$$

and

$$\alpha_{mn}^2 = 2\frac{H}{D_y}\frac{m^2\pi^2b^2}{a^2}+\beta_{mn}^2.$$

2. $D_1=0$

$$Y_{m1}(y) = 1$$

and

$$\beta_{m1} = 0.$$

For values of n greater than unity, expressions of (1) may be used.

Modes Antisymmetric in $y-n$ is Even

$$Y_{mn}(y) = \frac{\operatorname{Sinh}\frac{\alpha_{mn}y}{b}}{\operatorname{Sinh}\frac{\alpha_{mn}}{2}}+\frac{\alpha_{mn}^2-\frac{D_1}{D_y}\frac{m^2\pi^2b^2}{a^2}}{\beta_{mn}^2+\frac{D_1}{D_y}\frac{m^2\pi^2b^2}{a^2}}\frac{\operatorname{Sin}\frac{\beta_{mn}y}{b}}{\operatorname{Sin}\frac{\beta_{mn}}{2}},$$

where α_{mn} and β_{mn} satisfy the equations

$$\tan\frac{\beta_{mn}}{2} = \frac{\beta_{mn}}{\alpha_{mn}}\left[\frac{\alpha_{mn}^2-\frac{D_1}{D_y}\frac{m^2\pi^2b^2}{a^2}}{\beta_{mn}^2+\frac{D_1}{D_y}\frac{m^2\pi^2b^2}{a^2}}\right]^2\tanh\frac{\alpha_{mn}}{2}$$

and

$$\alpha_{mn}^2 = \frac{2H}{D_y}\frac{m^2\pi^2b^2}{a^2}+\beta_{mn}^2.$$

Notation

a, b	Sides of the orthotropic plate.
c	Transverse position of the moving load.
D_1, D_x, H, D_y	Orthotropic plate rigidities.
g	Acceleration due to gravity.
k	Spring constant of the moving load.
M	Mass of the moving load.
p_{mn}	Natural frequency of the orthotropic plate.
R	Force of interaction between the load and the bridge.
v	Speed of the moving load.
W	Deflection of the orthotropic plate.
z	Absolute deflection of the sprung load.
$\alpha=\frac{vT}{2a}$	Speed parameter.

$\alpha_m = \frac{m\pi v}{a}$	Crossing frequency.
$\alpha_{mn}, \beta_{mn}, \lambda_{mn}$	Frequency parameters of orthotropic plate.
$\delta_1 = \omega/p_{11}$	Frequency ratio.
$\delta_2 = M/\rho a b$	Mass ratio.
δ_3	Initial oscillation parameter.
ω	Frequency of the sprung load.
ν	Poisson's ratio of the bridge material.
ρ	Mass per unit area of the orthotropic plate.

References

1. J. Prince Alfaro and A. S. Veletsos: Dynamic Behaviour of an I-Beam Bridge Model under a Smoothly Rolling Load. Eighth Progress Report of the Highway Bridge Impact Investigation, University of Illinois, Urbana, Illinois, October 1958.
2. W. H. Walker: Studies on the Dynamic Response of an I-Beam Bridge Model. Part B, Ninth Progress Report, Highway Bridge Impact Investigation, University of Illinois, Urbana, Illinois, October 1959.
3. C. Oran and A. S. Veletsos: Analysis of Static and Dynamic Response of Simple-span Multi-girder Highway Bridges. Eleventh Progress Report, Highway Bridge Impact Investigation, University of Illinois, Urbana, Illinois, July 1961.
4. C. L. Huang and W. H. Walker: On Free Vibration of Simple-Span I-Beam Bridges. Part D, Ninth Progress Report, Highway Bridge Impact Investigation, University of Illinois, Urbana, Illinois, October 1959.
5. K. T. Sundara Raja Iyengar, K. S. Jagadish and R. Narayana Iyengar: Free Vibration of Beam and Slab Bridges. Journal of the Institution of Engineers (India), Vol. XLVIII, No. 1, Pt. CI 1, September 1967 (Special).
6. T. Huang and A. S. Veletsos: Dynamic Response of Three-Span Continuous Highway Bridges. Structural Research Series No. 190, University of Illinois, Urbana, Illinois, 1960.
7. K. S. Jagadish: The Dynamic Response of Simple-Span Beam and Slab Bridges to Moving Loads. Thesis submitted for the Ph. D. degree, Indian Institute of Science, Bangalore, 1968.
8. N. J. Huffington Jr.: Theoretical Determination of Rigidity Properties of Orthogonally Stiffened Plates. Journal of Applied Mechanics, Vol. 23, p. 15, March 1956.
9. K. T. Sundara Raja Iyengar and K. S. Jagadish: The Dynamic Response of Beam and Slab Bridges to Moving Forces. Publication of the International Association of Bridge and Structural Eng., Vol. 28, No. 2, 1968.
10. C. L. Huang and W. H. Walker: Analysis of Data Obtained from Tests on a Highway Bridge Model. Part D, Tenth Progress Report, Highway Bridge Impact Investigation, University of Illinois, 1960.
11. W. H. Walker and A. S. Veletsos: Response of Simple-Span Highway Bridges to Moving Vehicles. Engineering Expt. Station Bulletin No. 486, University of Illinois, Urbana, Illinois, 1966.
12. A. S. Veletsos: Private Communication.
13. R. J. Reilly and C. T. G. Looney: Dynamic Behaviour of Highway Bridges. Final Report for Maryland State Roads Commission and U.S. Bureau of Public Roads, Civil Engineering Department, University of Maryland at College Park, Maryland, April 1966.

Summary

The response of beam and slab Highway bridges, under the action of moving loads, is studied by the orthotropic plate theory. The moving load is idealised as a mass-spring system. The equations of motion for the problem are solved numerically by the Runge-Kutta-Nyström method. The results are presented in the form of amplification spectra and history curves.

Résumé

On étudie, à l'aide de la théorie des plaques orthotropes, le comportement dynamique des ponts d'autoroutes, formés de dalles ou de poutres. La charge mobile est remplacée par un système de masses sur ressorts. On donne une résolution numérique des équations du problème à l'aide de la méthode de Runge-Kutta-Nyström. Les résultats sont présentés sous forme de spectres d'amplification et de courbes de réponse.

Zusammenfassung

Das dynamische Verhalten von Platten- und Balken-Straßenbrücken unter der Einwirkung bewegter Lasten wird mittels der orthotropen Plattentheorie untersucht. Die bewegte Last wird als ein System federnder Massen idealisiert. Die für das Problem erforderlichen Gleichungen werden numerisch anhand der Runge-Kutta-Nyström-Methode gelöst. Die Resultate werden in Form von Vergrößerungs-Spektren und Hysteresis-Kurven dargestellt.

On the Problem of Edge Disturbances in Lattice Domes

Problèmes des perturbations aux bords dans les coupoles à treillis

Zum Randstörungsproblem in den Gitterkuppeln

JAYME MASON

Graduate Professor of Applied Mechanics – Consulting Engineer – Pontificia Universidade Católica do Rio de Janeiro, Brazil; Presently Visiting Professor Ruhr-Universität Bochum, Germany

1. Introduction

The analysis of lattice shells has attained a considerable importance in recent years, particularly in connection with the design of large-span geodesic domes.

The purpose of the present paper is to present an approximate method of determining the magnitude of edge disturbances in such shells. Both rotationally symmetrical and non-symmetrical perturbations are dealt with, by assuming an analogue model for the structural behaviour of the shell lattice. By an appropriate reasoning, the constitutive equations of isotropic shell theory can be replaced by relationships associated with the properties of the lattice members and dimensions.

The treatment of rotationally symmetric perturbations is performed under the usual assumption that it is possible to neglect lower order, as compared to higher order derivatives of shell quantities. In the case of rotationally non-symmetrical perturbations, the shallow shell theory is used, which is also mathematically equivalent to the above assumption.

The results obtained in the present paper were part of the studies for the design of Manaus Dome, a geodesic dome with 300 m in diameter, to be built in the Amazon jungle in Brazil, by Companhia Tropical de Hoteis. The architect was Mr. Sérgio Bernardes and the structural engineer Mr. Paulo

Fragoso. The development of the methods of analysis of the dome structure was entrusted to the present author.

The examination of the theoretical assumptions and results was entrusted to Prof. W. ZERNA, at the Ruhr-Universität Bochum, Germany.

Following the requirements in the design, only triangular meshes in the lattice were considered.

2. The Analogue Model

In order to account for the lattice properties in the calculations, we must supply an analogue model for the bending and the extensional rigidities of the shell, in terms of the characteristics of the lattice members. We refer to Fig. 1 for notations. The moment of inertia and the cross section of a bar are J and F respectively and a is the height of an equilateral triangle.

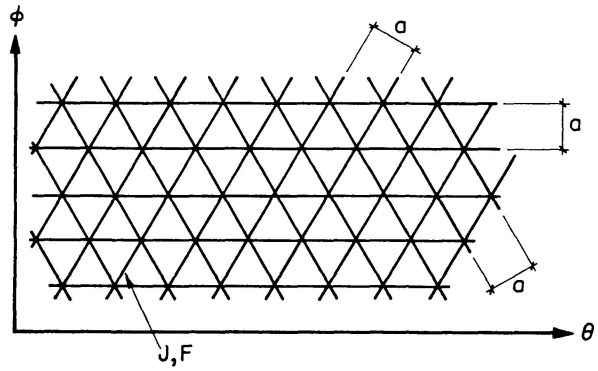


Fig. 1.

A meridional (ϕ) and parallel (θ) coordinate system is used. The stiffness properties of the lattice model are derived in a simple way, by subjecting the lattice to unit generalized deformations, as unit changes of curvature and twist and unit extensions and shears. The contributions of each group of bars to the shell stress resultants are collected together and the results referred to the unit length of the lattice plane. We refer to [2] and [3] for detailed demonstrations. If coupling of in-plane and bending effects is neglected, this analysis will lead to the following constitutive equations (see Fig. 2b):

$$M_\phi = D^\phi_\phi k_\phi + D^\theta_\phi k_\theta\,; \qquad M_\theta = D^\theta_\theta k_\theta + D^\phi_\theta k_\phi\,; \qquad M_{\phi\theta} = D^{\phi\theta}_{\phi\theta} k_{\phi\theta}\,. \tag{1}$$

$$\epsilon_\phi = \Delta^\phi_\phi N_\phi + \Delta^\theta_\phi N_\theta\,; \qquad \epsilon_\theta = \Delta^\theta_\theta N_\theta + \Delta^\phi_\theta N_\phi\,; \qquad \epsilon_{\phi\theta} = \Delta^{\phi\theta}_{\phi\theta} N_{\phi\theta}\,. \tag{2}$$

In these relationships k_ϕ, k_θ and $k_{\phi\theta}$ are changes of curvature and twist respectively and ϵ_ϕ, ϵ_θ, $\epsilon_{\phi\theta}$ the strains of the shell middle surface. The appropriate sign for the changes of curvature and twist must be inserted in (1) according to the circumstances.

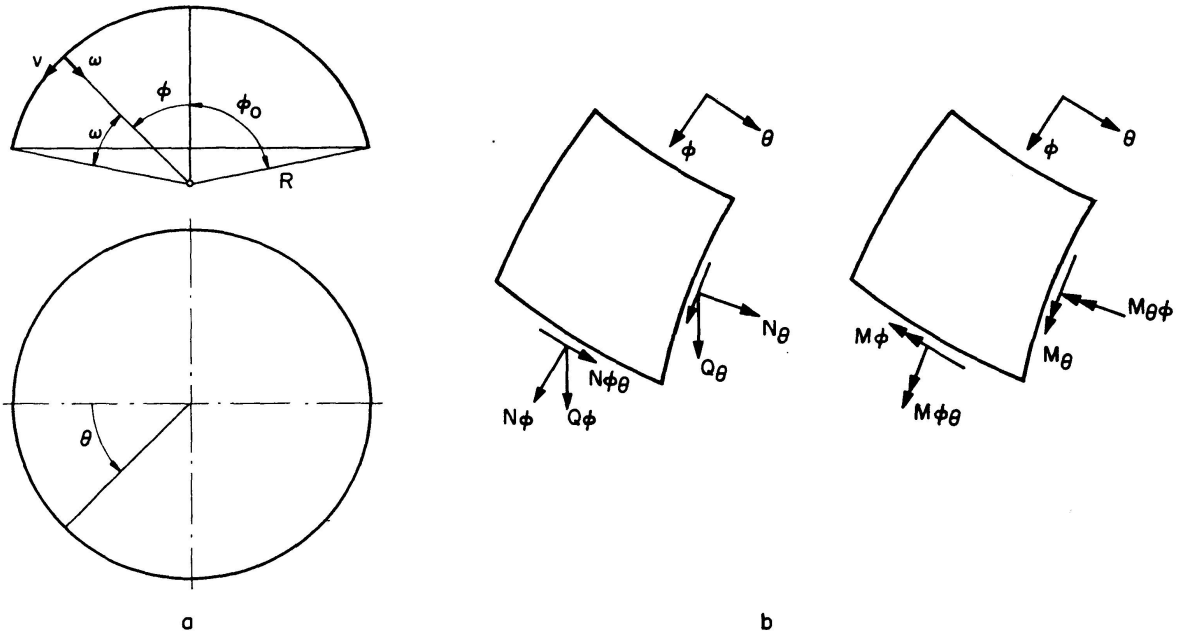


Fig. 2.

For the coefficients D_{ϕ}^{ϕ}, $D_{\phi}^{\theta} \ldots \Delta_{\phi}^{\phi} \ldots \Delta_{\phi\theta}^{\phi\theta}$, following results are found (Fig. 1):

$$D_{\phi}^{\phi} = D_{\theta}^{\theta} = \frac{3EJ}{8a}(3+\mu); \qquad D_{\phi}^{\theta} = D_{\theta}^{\phi} = \frac{3EJ}{8a}(1-\mu);$$
$$D_{\phi\theta}^{\phi\theta} = \frac{3EJ}{4a}(1+\mu) \tag{3}$$

where

$$\mu = \frac{GJ_d}{EJ} \tag{4}$$

(GJd = Saint Venant's torsional stiffness of a lattice member; EJ = Bending stiffness of a lattice member.)

$$\Delta_{\phi}^{\phi} = \Delta_{\theta}^{\theta} = \frac{a}{EF}; \qquad \Delta_{\phi}^{\theta} = \Delta_{\theta}^{\phi} = \frac{a}{3EF}; \qquad \Delta_{\phi\theta}^{\phi\theta} = \frac{8a}{EF}. \tag{5}$$

It can be checked that the coefficients (3) on the one hand and the coefficients (5) on the other hand, have the same structure as in the theory of isotropic uniform shells.

Nevertheless, the coefficients (3) are not related in a simple way to the coefficients (5), as in the constitutive equations of the isotropic shell theory, because in this case we have only two basic elastic constants.

The analogue shell thickness as evaluated by means of (3) is different from the membrane thickness as determined from (5). In particular, for the case of double-layer shells, the difference between bending and membrane thickness is very large and we may be led to considerable errors if we make estimates

by means of the results from the isotropic shell theory, by using offhand analogies.

3. Axissymmetric Edge Disturbances

In the sequel, we shall summarize the basic relations for rotationally symmetrical edge perturbations [1]. The notation $(\ldots)'$ holds for $\frac{d}{d\phi}(\ldots)$.

a) *Equilibrium:*

$$\begin{aligned} -N_\theta \cos\phi + (N_\phi \sin\phi)' - Q_\phi \sin\phi &= 0, \\ N_\theta \sin\phi + N_\phi \sin\phi + (Q_\phi \sin\phi)' &= 0, \\ M_\theta \cos\phi + (M_\phi \sin\phi)' - Q_\phi R \sin\phi &= 0. \end{aligned} \tag{6}$$

b) *Strain displacement relations* (Fig. 2a)

$$\epsilon_\phi = \frac{1}{R}(v' - w)\ ; \qquad \epsilon_\theta = \frac{1}{R}(v\cot\phi - w)\ ; \qquad \chi = \frac{1}{R}(v + w'); \tag{7}$$

$$k_\phi = -\frac{1}{R}\chi'\ ; \qquad k_\theta = -\frac{\chi}{R}\cot\phi. \tag{8}$$

(χ = rotation of tangent to the meridian, positive if the center of curvature is raised.)

By eliminating the displacement components v and w in (7), the equations of compatibility

$$\chi = (\epsilon_\phi - \epsilon_\theta)\cot\phi - \frac{d\,\epsilon_\theta}{d\phi} \tag{9}$$

is found. Furthermore, the first two equations of (6) can be combined to yield

$$N_\phi = -Q_\phi \cot\phi; \quad N_\theta = Q'_\phi. \tag{10}$$

The equilibrium and the compatibility equations for symmetric edge disturbances are now readily derived.

The relevant equilibrium equation is the third of (6) and we eliminate the bending moments by means of the constitutive relations (1), combined with (3) and (8). The result is

$$\chi'' + [(1+\nu^*)\cot\phi - \nu^*\cot\phi]\chi' + [-\nu^* - \cot^2\phi]\chi + \frac{R^2 Q_\phi}{D_\phi^\phi} = 0 \tag{11}$$

where

$$\nu^* = \frac{D_\phi^\theta}{D_\phi^\phi} = \frac{1-\mu}{3+\mu}. \tag{12}$$

In the compatibility Eq. (9), we eliminate ϵ_ϕ and ϵ_θ by means of (2) and consider thereby (10), so that

$$\chi = -(\Delta_\phi^\phi - \Delta_\theta^\phi)\cot^2\phi\, Q_\phi + (\Delta_\theta^\theta - \Delta_\phi^\theta)\cot\phi\, Q'_\phi + \Delta_\theta^\theta Q''_\phi - (1+\cot^2\phi)\Delta_\theta^\phi Q_\phi + \Delta_\theta^\phi \cot\phi\, Q'_\phi . \tag{13}$$

In the relationships (11) and (13) we have a system of differential equations in the variables χ and Q_ϕ. As soon as these are determined, all other quantities are easily derived.

In the case of isotropic shells, obviously $\nu^* = \nu$, the Poisson ratio, and $\Delta_\phi^\phi = \frac{1}{Eh}$, $\Delta_\theta^\phi = -\frac{\nu}{Eh}$, where h is the shell thickness.

Then, (11) and (13) simplify to

$$\chi'' + \cot\phi\,\chi' - (\nu + \cot^2\phi)\chi + \frac{R^2 Q_\phi}{D_\phi^\phi} = 0$$

with $$D_\phi^\phi = \frac{E h^3}{12(1-\nu^2)}$$

and $$E h \chi = Q''_\phi + \cot\phi\, Q'_\phi + (\nu - \cot^2\phi)\, Q_\phi$$

which are well known.

By neglecting first order derivatives and functional values as compared to second order derivatives in (11) and (13), these reduce to

$$\chi'' + \frac{R^2 Q_\phi}{D_\phi^\phi} = 0; \quad Q''_\phi = \frac{\chi}{\Delta_\phi^\phi}. \tag{14}$$

With the notation $$4k^4 = \frac{R^2}{\Delta_\theta^\theta D_\phi^\phi}$$

or, from (3) and (5), $$k^4 = \frac{R^2}{\frac{3(3+\mu)}{2}\frac{J}{F}}. \tag{15}$$

Eqs. (14) are combined to yield

$$\chi^{IV} + 4k^4\chi = 0; \quad Q_\phi^{IV} + 4k^4 Q_\phi = 0. \tag{16}$$

With the usual coordinate transformation in order to measure the azimuthal angle from the edge (see Fig. 2a), the solutions of (16) which decrease from the edge are

$$Q_\phi = C e^{-k\omega}\cos(k\omega + \psi),$$

$$\chi = \frac{2ak^2}{EF} C e^{-k\omega}\sin(k\omega + \psi) \tag{17}$$

where C and ψ are amplitude and phase constants respectively. The expressions for the bending moments are now found right-away by means of the second of (17), (8) and (1). As a result,

$$M_\phi = \frac{3}{4}\frac{J k^2}{R F}(3+\mu) C e^{-k\omega}\left[\sqrt{2}\, k \cos\left(k\omega+\psi+\frac{\pi}{4}\right) - \frac{1-\mu}{3+\mu}\cot\phi \sin(k\omega+\psi)\right], \tag{18}$$

$$M_\theta = \frac{3}{4}\frac{J k^2}{R F}(3+\mu) C e^{-k\omega}\left[-\cot\phi \sin(k\omega+\psi) + \frac{1-\mu}{3+\mu}\sqrt{2}\, k \cos\left(k\omega+\psi+\frac{\pi}{4}\right)\right].$$

The membrane stresses are readily obtained from the first of (17), with (10):

$$N_\phi = -C\cot\phi\, e^{-k\omega}\cos(k\omega+\psi),$$
$$N_\theta = -C k\sqrt{2}\, e^{-k\omega}\sin\left(k\omega+\psi+\frac{\pi}{4}\right). \tag{19}$$

We shall now derive some formulas for edge thrusts and edge moments in the dome (Fig. 3), which are useful in accounting for boundary conditions along the foundation.

For the case of an edge thrust H (Fig. 3a), the boundary conditions are $M_\phi = 0$ and $Q_\phi = -H\sin\phi_0$ for $\omega = 0$ and therefore $\psi = \pi/4$ and $C = -\sqrt{2}\, H\sin\phi_0$. The stress resultants become now

$$Q_\phi = -H\sqrt{2}\sin\phi_0\, e^{-k\omega}\cos\left(k\omega+\frac{\pi}{4}\right)$$

$$M_\phi = \frac{3\sqrt{2}}{4}\frac{k^2 J}{R F}(3+\mu) H\sin\phi_0\, e^{-k\omega}\left[\sqrt{2}\, k\sin k\omega - \frac{1-\mu}{3+\mu}\cot\phi\sin\left(k\omega+\frac{\pi}{4}\right)\right],$$

$$M_\theta = \frac{3\sqrt{2}}{4}\frac{k^2 J}{R F}(3+\mu) H\sin\phi_0\, e^{-k\omega}\left[\cot\phi\sin\left(k\omega+\frac{\pi}{4}\right) + \frac{1-\mu}{3+\mu}\sqrt{2}\, k\sin k\omega\right], \tag{20}$$

$$N_\phi = \sqrt{2}\, H\sin\phi_0\cot\phi\, e^{-k\omega}\cos\left(k\omega+\frac{\pi}{4}\right),$$

$$N_\theta = 2 H\sin\phi_0\, k\, e^{-k\omega}\cos k\omega.$$

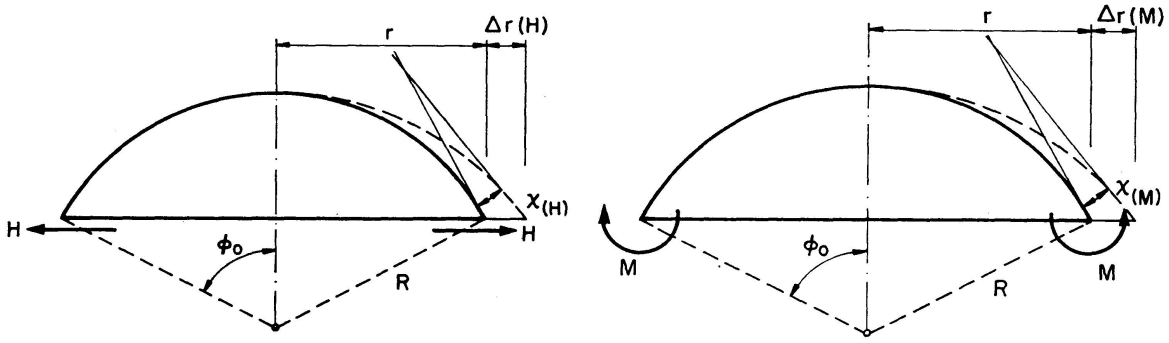


Fig. 3.

For the edge displacement, $\Delta_r(H) = R\sin\phi_0\,\epsilon_{\theta(\omega=0)}$ and, on account of (17) we find

$$\chi_{(H)} = -\frac{2 H\sin\phi_0\, a\, k^2}{E F}; \qquad \Delta_{r(H)} = \frac{2 a\sin^2\phi_0\, R\, k\, H}{E F}. \tag{21}$$

In the case of an edge moment (Fig. 3b), $M_\phi = M$ and $Q_\phi = 0$, for $= 0$ so that

$$
\begin{aligned}
Q_\phi &= \frac{4}{3}\frac{M R F}{k^3 J (3+\mu)} e^{-k\omega} \sin k\omega, \\
M_\phi &\cong M e^{-k\omega} (\sin k\omega + \cos k\omega), \\
M_\theta &= M e^{-k\omega}\left[\frac{1}{k}\cot\phi \cos k\omega + \frac{1-\mu}{3+\mu}(\cos k\omega + \sin k\omega)\right], \\
N_\phi &= -\frac{4}{3}\frac{M R F}{k^3 J (3+\mu)} \cot\phi\, e^{-k\omega} \sin k\omega, \\
N_\theta &= \frac{4}{3}\frac{M R F}{k^2 J (3+\mu)} e^{-k\omega}(\cos k\omega - \sin k\omega)
\end{aligned}
\tag{22}
$$

and

$$
\chi_{(M)} = -\frac{8}{3}\frac{M a R}{k J (3+\mu) E}; \qquad \Delta_{r(M)} = \frac{4}{3}\frac{M a R^2 \sin\phi_0}{k^2 J (3+\mu) E}. \tag{23}
$$

A simple control may be obtained for the above results, by using the reciprocity principle. According to this principle, $|\chi_{(H)}| = |\Delta_{r(M)}|$ for $H = M = 1$, so that we must have

$$
\frac{2 a k^2}{F} = \frac{4}{3}\frac{a R^2}{k^2 J (3+\mu)}.
$$

If we substitute here k from (15), we conclude in fact that this is an identity and both sides will reduce to

$$
\frac{2\sqrt{2}}{3}\frac{a R}{\sqrt{(3+\mu) J F}}.
$$

4. Non-symmetrical Edge Disturbances

The treatment of non-symmetrical edge disturbances by accounting for the analogue model of the lattice structure is associated with considerable difficulties. Therefore an approximate analysis must be attempted.

It has been shown elsewhere [5] that the usual mathematical simplification of neglecting lower order derivatives in edge perturbation problems in shells of revolution is equivalent to the assumptions of the theory of shallow shells. The mathematical equivalence is particularly apparent in a tensor presentation of the theory.

Therefore, the shallow shell theory with an obvious modification for the analogue lattice model will be used here. WLASSOW [4] has shown that the equations of the shallow shell theory, in the case of unloaded isotropic uniform shells are

$$
\frac{1}{E h}\nabla^2\nabla^2\Phi - \nabla_k^2 w = 0; \qquad \nabla_k^2\Phi + \frac{E h^3}{12(1-\nu^2)}\nabla^2\nabla^2 w = 0, \tag{24}
$$

where Φ and w are well known stress and normal displacement functions. $\nabla^2(\ldots)$ and $\nabla_k{}^2(\ldots)$ are certain operators in surface coordinates. The first equation is the compatibility equation and the second, the equation of equilibrium.

If we follow the derivation of (24) and observe the new expressions for the bending and the membrane coefficients (3) and (5) of the lattice model, we come to the conclusion that (24) must be modified to

$$\frac{a}{EF}\nabla^2\nabla^2\Phi-\nabla_k^2 w=0\ ;\quad \nabla_k^2\Phi+\frac{3EJ}{8a}(3+\mu)\nabla^2\nabla^2 w=0. \tag{25}$$

for lattice domes.

In spherical coordinates, with the notations $(\ldots)'=\frac{d}{d\phi}(\ldots)$ and $(\ldots)^{\cdot}=\frac{d}{d\theta}(\ldots)$, the operator ∇^2 is written as

$$\nabla^2(\ldots)=\frac{1}{R^2}[(\ldots)''+\cot\phi\,(\ldots)'+\operatorname{cosec}^2\phi\,(\ldots)^{\cdot\cdot}]\text{ and }\nabla_k^2(\ldots)=\frac{1}{R}\nabla^2(\ldots).$$

The membrane stresses are derived from the stress function through

$$\begin{gathered}N_\phi=\frac{1}{R^2}(\operatorname{cosec}^2\Phi^{\cdot\cdot}+\cot\phi\,\Phi')\ ;\qquad N_\theta=\frac{1}{R^2}\Phi''\ ;\\ N_{\phi\theta}=-\frac{1}{R^2}(\operatorname{cosec}\phi\,\Phi'^{\cdot}-\cos\phi\operatorname{cosec}^2\phi\,\Phi').\end{gathered} \tag{26}$$

For the bending moments, we use again (1), along with (3), with the formulas

$$\begin{gathered}k\phi=-\frac{1}{R^2}w''\ ;\quad k_\theta=-\frac{1}{R^2}(\operatorname{cosec}^2\phi\,w^{\cdot\cdot}+\cot\phi\,w')\ ;\\ k_{\phi\theta}=\frac{2}{R^2}\operatorname{cosec}\phi\,(w'^{\cdot}-\cot\phi\,w^{\cdot})\end{gathered} \tag{27}$$

for the changes of curvature and twist.

We shall next obtain an approximate solution of Eqs. (25)

By expressing w and Φ as $w=\nabla^2\nabla^2 F$; $\Phi=\frac{EF}{a}\nabla_k{}^2 F$ in terms of an auxiliary function F, the first of (25) is satisfied identically. By observing that $\nabla_k{}^2(\ldots)=\frac{1}{R}\nabla^2(\ldots)$, the second equation reduces to

$$\nabla^2\nabla^2 w+\frac{8F}{3(3+\mu)R^2J}w=0 \tag{28}$$

where now $$\nabla^2(\ldots)=(\ldots)''+\cot\phi\,(\ldots)'+\operatorname{cosec}^2\phi\,(\ldots)^{\cdot\cdot}. \tag{29}$$

After integrating (28), we determine Φ from the first of (25) which now may be written as

$$\nabla^2\left(\nabla^2\Phi-\frac{EF}{a}Rw\right)=0. \tag{30}$$

By putting
$$\nabla^2\Phi - \frac{EF}{a} R w = \psi \tag{31}$$

we see that
$$\nabla^2\psi = 0. \tag{32}$$

Thus, we first integrate (32) and substitute the result in (31), so that

$$\nabla^2\Phi = \frac{EF}{a} R w + \psi. \tag{33}$$

The integration of (33) yields finally the stress function Φ. The differential Eq. (28) can be replaced by two second order differential equations

$$\nabla^2\nabla^2 w + \mu w = 0 \tag{34}$$

with
$$\mu = \pm i R \sqrt{\frac{8F}{3(3+\mu)J}}. \tag{35}$$

For real particular solutions, we need only to account for one sign in (35).

We assume the Fourier expansions

$$w = \sum_{n=1}^{\infty} w_n \cos n\theta; \qquad \Phi = \sum_{n=1}^{\infty} \Phi_n \cos n\theta; \qquad \psi = \sum_{n=1}^{\infty} \psi_n \cos n\theta \tag{36}$$

and then, from (34), we conclude that

$$w_n'' + \cot\phi\, w_n' + (\mu - n^2 \operatorname{cossec}^2\phi)\, w_n = 0. \tag{37}$$

We now make a simplifying assumption, in order to avoid complicate functions of mathematical physics in the integration of (37). The assumption is very appropriate for hemispherical large span domes, as in the case of Manaus Dome, in which the edge disturbances are highly localized. In (37) we shall neglect the variability of the coefficients in the differential equation and set them equal to their functional values at $\phi = \pi/2$. In other cases, the approximation should be tolerable with the numerical values of the coefficients at $\phi = \phi_0$.

Eq. (37) then simplifies to

$$w_n'' + (\mu - n^2)\, w_n = 0 \tag{38}$$

with μ defined by (35). The real form of the solution of (38) is shown to be

$$w_n = A_n e^{a_n\phi}\cos b_n\phi + B_n e^{a_n\phi}\sin b_n\phi + C_n e^{-a_n\phi}\cos b_n\phi + D_n e^{-a_n\phi}\sin b_n\phi$$

with
$$a_n = p_n \cos\omega_n; \quad b_n = p_n \sin\omega_n \tag{39}$$

where
$$p_n = \sqrt[4]{n^4 + \mu_{Re}^2}; \quad \omega_n = \frac{1}{2}\arctan\frac{\mu_{Re}}{n^2}; \quad \mu_{Re} = R\sqrt{\frac{8F}{3(3+\mu)J}}. \tag{40}$$

For edge disturbances at $\phi = \pi/2$, we must retain only the solutions

$$w_n = A_n e^{a_n\phi}\cos b_n\phi + B_n e^{a_n\phi}\sin b_n\phi \tag{41}$$

and by testing this solution in the exact Eq. (37), we can make sure that the approximation is very appropriate.

Table I. Fourier Coefficients for Bending Stress Resultants

	Stiffness	A_n	B_n
M_{ϕ_n}	$-\frac{3(3+\mu)EJ}{8aR^2}$	$e^{a_n\phi}\left[\left(a_n^2-b_n^2-\frac{1-\mu}{3+\mu}\right)\cos b_n\phi - 2a_nb_n\sin b_n\phi\right]$	$e^{a_n\phi}\left[\left(a_n^2-b_n^2-\frac{1-\mu}{3+\mu}n^2\right)\sin b_n\phi + 2a_nb_n\cos b_n\phi\right]$
M_{θ_n}	$\frac{3(3+\mu)EJ}{8aR^2}$	$e^{a_n\phi}\left[\left(n^2-\frac{1-\mu}{3+\mu}(a_n^2-b_n^2)\right)\cos b_n\phi + 2\frac{(1-\mu)}{(3+\mu)}a_nb_n\sin b_n\phi\right]$	$e^{a_n\phi}\left[\left(n^2-\frac{(1-\mu)}{(3+\mu)}(a_n^2-b_n^2)\right)\sin b\phi - 2\frac{(1-\mu)}{(3+\mu)}a_nb_n\cos b_n\phi\right]$
$M_{\phi\theta_n}$	$-\frac{3(1-\mu)EJ}{2aR^2}$	$e^{a_n\phi}(na_n\cos b_n\phi - nb_n\sin b_n\phi)$	$e^{a_n\phi}(na_n\sin b_n\phi + nb_n\cos b_n\phi)$
Q_{ϕ_n}	$-\frac{3(3+\mu)EJ}{8aR^3}$	$e^{a_n\phi}[((a_n^2-b_n^2)a_n - 2a_nb_n^2 - n^2a_n)\cos b_n\phi + (-(a_n^2-b_n^2)b_n - 2a_n^2b_n + n^2b_n)\sin b_n\phi]$	$e^{a_n\phi}[((a_n^2-b_n^2)a_n - 2a_nb_n^2 - n^2a_n)\sin b_n\phi + ((a_n^2-b_n^2)b_n + 2a_n^2b_n - n^2b_n)\cos b_n\phi]$
Q_{θ_n}	$\frac{3(3+\mu)EJ}{8aR^3}$	$e^{a_n\phi}[((a_n^2-b_n^2)n+n^3)\cos b_n\phi - 2a_nb_nn\sin b_n\phi]$	$e^{a_n\phi}[((a_n^2-b_n^2)n+n^3)\sin b_n\phi + 2a_nb_n\cos b_n\phi]$
$Q^*_{\phi_n}$	$-\frac{3(3+\mu)EJ}{8aR^3}$	$e^{a_n\phi}\left[\left((a_n^2-b_n^2)a_n - 2a_nb_n^2 - n^2a_n + 4\frac{(1+\mu)}{(3+\mu)}n^2a_n\right)\cos b_n\phi + \left(-(a_n^2-b_n^2)b_n - 2a_n^2 + n^2b_n - 4\frac{(1+\mu)}{(3+\mu)}n^2b_n\right)\sin b_n\phi\right]$	$e^{a_n\phi}\left[\left((a_n^2-b_n^2)a_n - 2a_nb_n^2 - n^2a_n + 4\frac{(1+\mu)}{(3+\mu)}n^2a_n\right)\sin b_n\phi + \left((a_n^2-b_n^2)b_n + 2a_n^2b_n - n^2b_n + 4\frac{(1+\mu)}{(3+\mu)}n^2b_n\right)\cos b_n\phi\right]$

Table II. Fourier Coefficients for Membrane Stresses

	C_n	D_n	A_n	B_n
N_{ϕ_n}	$-\frac{n^2}{R}e^{n\phi}$	$-\frac{n}{2R^2}\phi e^{n\phi}$	$-\frac{EF}{aR}\frac{e^{a_n\phi}}{[\ldots][\ldots]}[n^2(a_n^2-b_n^2-n^2)\cos b_n\phi + 2a_n b_n n^2 \sin b_n\phi]$	$-\frac{EF}{aR}\frac{e^{a_n\phi}}{[\ldots][\ldots]}[n^2(a_n^2-b_n^2-n^2)\sin b_n\phi - 2a_n b_n \cos b_n\phi]$
N_{θ_n}	$\frac{n^2}{R^2}e^{n\phi}$	$\frac{1}{R^2}(e^{n\phi} + \frac{1}{2}n\phi e^{n\phi})$	$\frac{EF}{aR}\frac{e^{a_n\phi}}{[\ldots][\ldots]}[((a_n^2+b_n^2)^2 - n^2(a_n^2-b_n^2))\cos b_n\phi + 2a_n b_n \sin b_n\phi]$	$\frac{EF}{aR}\frac{e^{a_n\phi}}{[\ldots][\ldots]}[((a_n^2+b_n^2)^2 - n^2(a_n^2-b_n^2))\sin b_n\phi - 2a_n b_n n^2 \cos b_n\phi]$
$N_{\phi\theta_n}$	$n^2 e^{n\phi}$	$\frac{1}{2}(e^{n\phi} + n\phi e^{n\phi})$	$\frac{EF}{a}\frac{e^{a_n\phi}}{[\ldots][\ldots]}[(-b_n(a_n^2-b_n^2-n^2) + 2a_n^2 b_n)\sin b_n\phi + (2a_n b_n^2 + a_n(a_n^2-b_n^2-n^2))\cos b_n\phi]$	$\frac{EF}{aR}\frac{e^{a_n\phi}}{[\ldots][\ldots]}[(b_n(a_n^2-b_n^2-n^2) - 2a_n^2 b_n^2)\cos b_n\phi + (2a_n b_n^2 + a_n(a_n^2-b_n^2-n^2))\sin b_n\phi]$

$$[\ldots][\ldots] = [(a_n-n)^2+b_n^2][(a_n-n)^2-b_n^2]$$

We next integrate (32). By considering (36),

$$\psi_n'' + \cot\phi\,\psi_n' - n^2\psi_n = 0$$

and, under the same assumptions it reduces to $\psi_n'' - n^2\psi_n = 0$, with the solutions $e^{n\phi}$ and $e^{-n\phi}$. We must discard $e^{-n\phi}$ and retain only $e^{n\phi}$.

We introduce this result in (31) and consider again the expansion (36).

Then, by taking account of the same simplifying assumptions,

$$\Phi_n'' - n^2\Phi_n = \frac{EF}{a}\left(A_n e^{a_n\phi}\cos b_n\phi + B_n e^{a_n\phi}\sin b_n\phi\right) + D_n e^{n\phi}.$$

The general solution of this differential equation is

$$\begin{aligned}\Phi_n = {} & C_n e^{a_n\phi} + D_n\frac{1}{2n}\phi\, e^{n\phi} + \frac{EFR}{a}\frac{e^{a_n\phi}}{[(a_n-n)^2+b_n^2][(a_n+n^2+b_n^2]} \\ & [A_n\{(a_n^2-b_n^2-n^2)\cos b_n\phi + 2a_n b_n\sin b_n\phi\} \\ & + B_n\{(a_n^2-b_n^2-n^2)\sin b_n\phi - 2a_n b_n\phi\}].\end{aligned} \tag{42}$$

On account of the Fourier expansion (36), the stress resultants will have also the expansions below:

$$M_\phi = \sum_{n=1}^{\infty} M_{\phi_n}\cos n\theta; \quad M_\theta = \sum_{n=1}^{\infty} M_{\theta_n}\cos n\theta; \quad M_{\phi\theta} = \sum_{n=1}^{\infty} M_{\phi\theta_n}\sin n\theta. \tag{43}$$

$$N_\phi = \sum_{n=1}^{\infty} N_{\phi_n}\cos n\theta; \quad N_\theta = \sum_{n=1}^{\infty} N_{\theta_n}\cos n\theta; \quad N_{\phi\theta} = \sum_{n=1}^{\infty} N_{\phi\theta_n}\sin n\theta. \tag{44}$$

The amplitudes of the stress resultants are now determined by simple differentiations by means of (1) and (26), by accounting for (27). On account of the simplifying assumption, we are allowed to write instead

$$\begin{aligned} & N_\phi \cong \frac{1}{R^2}\Phi^{\cdot\cdot}; \quad N_\theta \cong \frac{1}{R^2}\Phi''; \quad N_{\phi\theta} = -\frac{1}{R^2}\Phi'^{\cdot}; \\ & k_\phi \cong -\frac{1}{R^2}w''; \quad k_\theta = -\frac{1}{R^2}w^{\cdot\cdot}; \quad k_{\phi\theta} = \frac{2}{R^2}w'^{\cdot}. \end{aligned} \tag{45}$$

The results are summarized in Tables I and II. The tables should be self-explaining, all Fourier coefficients being given as

$$\textit{Fourier coefficient} = \textit{stiffness} \times [f_n(\phi)A_n + g_n(\phi)B_n + \ldots].$$

For example,

$$\begin{aligned} M_{\phi_n} = {} & -\frac{3(3+\mu)}{8aR^2}\left\{e^{a_n\phi}\left[\left(a_n^2-b_n^2-\frac{1-\mu}{3+\mu}n^2\right)\cos b_n\phi - 2a_n b_n\sin b_n\phi\right]A_n\right. \\ & \left. + e^{a_n\phi}\left[\left(a_n^2-b_n^2-\frac{1-\mu}{3+\mu}n^2\right)\sin b_n\phi + 2a_n b_n\cos b_n\phi\right]\right\}. \end{aligned}$$

The generalized shear forces Q_ϕ^* and the shear forces Q_ϕ and Q_θ are also given.

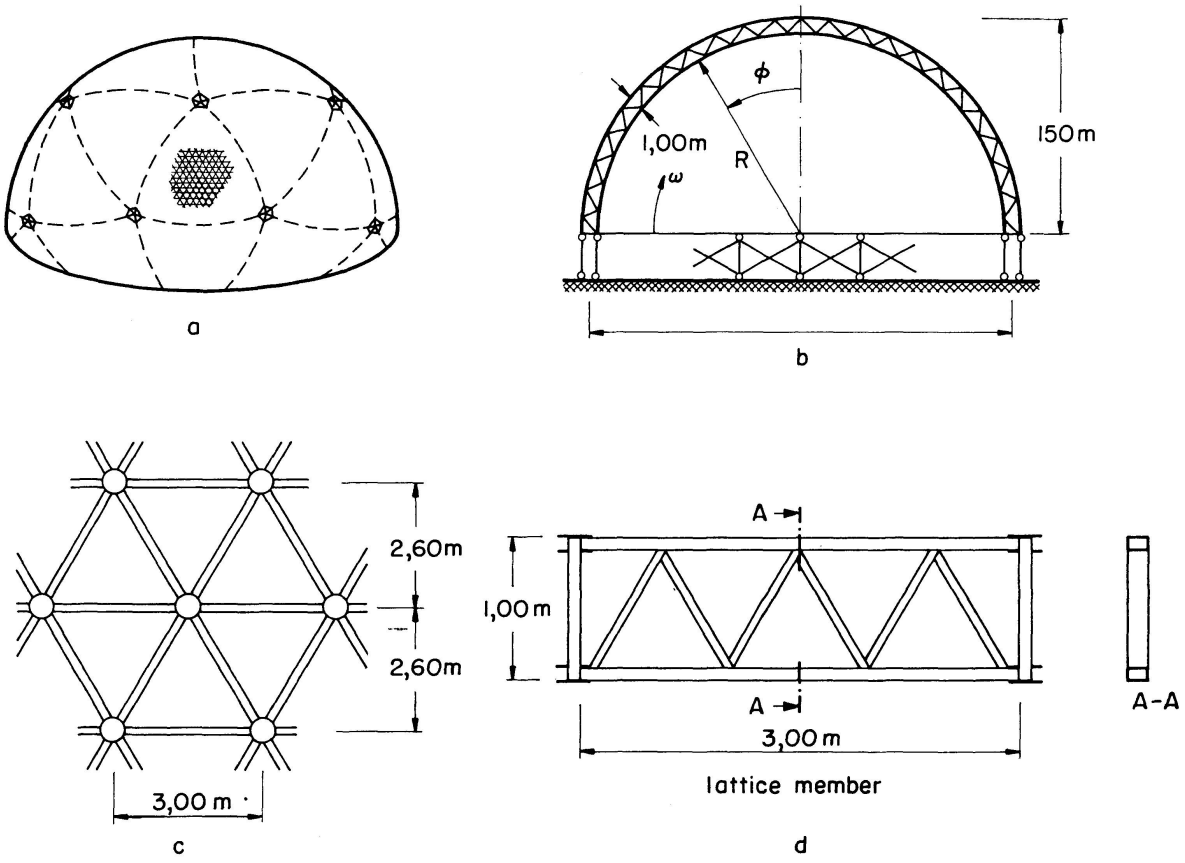


Fig. 4.

5. Numerical Applications

For a numerical illustration of the above theory, we shall report some concrete results obtained in the design of Manaus Dome, a geodesic dome with 300 m in diameter, in high tensile steel.

The main characteristics of Manaus Dome are sketched in Fig. 4, and it is a double-layer shell, each lattice member being a truss with a 1 m depth and 3 m length (see Fig. 4c, d). The dome is supported along the fundation in such a way, that the tangential displacements (normally denoted by u and v) and the meridian rotation vanish. The support is also not able to resist a horizontal thrust, so that $Q_\phi^* = 0$ at $\phi = \pi/2$. The characteristics of the lattice in the edge zone are

$$a = 260\,\text{cm};\ F = 89\,\text{cm}^2;\ J = 1.80 \times 10^5\,\text{cm}^4 \text{ and } R = 150\,\text{m}.$$

5.1. Axissymmetric Edge Disturbances

With the above values (15) gives

$$k = 12.5.$$

The moment of restraint at the foundation will be determined for dead weight, which was variable from 124 kg/m² to 182 kg/m². A calculation of edge displacements was performed by means of the membrane theory with an equivalent membrane thickness determined from

$$\frac{1}{E\,h} = \frac{a}{E\,F} \quad \text{[See (5)]}, \quad \text{i.e.,} \quad h = \frac{F}{a} = 0.34 \text{ cm},$$

The results were

$$\Delta_r^{(g)} = \frac{1.61 \times 10^6}{E}; \quad \chi^{(g)} = -\frac{1.87 \times 10^4}{E}.$$

The elasticity modulus must be inserted in t/m².

With these results and $k = 12{,}5$ above, $\phi_0 = \pi/2$, $\mu = 0$, $H = M = 1$, formulas (21) and (23) yield

$$\chi_{(H=1)} = -\frac{2a\,k^2}{E\,F} = -\frac{9.1 \times 10^4}{E}; \quad \Delta_{r(H=1)} = \frac{2a\,R\,k}{E\,F} = \frac{110 \times 10^4}{E};$$

$$\chi_{(M=1)} = -\frac{8}{3}\frac{a\,R}{k\,J\,(3+\mu)\,E} = -\frac{1.54 \times 10^4}{E}; \quad \Delta_{r(M=1)} = \frac{4}{3}\frac{a\,R^2}{k^2\,J\,(3+\mu)\,E} = \frac{9.1 \times 10^4}{E}.$$

With these results, any boundary conditions may be accounted for.

The condition for a vanishing meridian rotation, with no thrust is obviously

$$\chi_{(M=1)}\,M + \chi^{(g)} = 0 \quad \text{so that} \quad -\frac{1.54 \times 10^4}{E}\,M - \frac{1.87 \times 10^4}{E} = 0$$

and therefore

$$M = -1.21 \text{ tm/m}.$$

The corresponding hoop stress at the edge is found from the last formula of (22) and it is

$$N_{\theta(\omega=0)} = \frac{4}{3}\frac{M\,R\,F}{k^2\,J\,(3+\mu)} = -2.55 \text{ t/m}.$$

5.2. Non-symmetrical Edge Disturbances

We report the results of the calculation for the first and second harmonics of the wind loading.

The wind pressure was determined from a wind tunel test and the result of the calculations for the first and the second harmonics of the meridian rotation were

$$\chi_1^{(w)} = -\frac{5530}{E} \quad \text{and} \quad \chi_2^{(w)} = -\frac{1880}{E},$$

where E must be inserted in t/m². With the present numerical values (40) yields

$$\mu_{R_e} = 315; \quad p_n = 17.8; \quad \omega_n = \frac{\pi}{4}$$

so that

$$a_n \cong b_n = 17.8 \times 0.707 = 12.6$$

from (39). As a_n and b_n are responsible for the damping of the perturbations, we see that this result is very close to the corresponding parameter $k = 12.5$ for the axissymmetric edge disturbances. This conclusion is a further concrete demonstration of the equivalence of Geckler's and the shallow shell theory.

The meridian rotation for bending effects is obtained from (41), as the derivative w_n' for $\phi = \pi/2$. By taking instead $a_n = b_n = 12$ in order to simplify computations, we find

$$w_1' = A_1 a_1 e^{a_1(\pi/2)} + B_1 b_1 e^{a_1(\pi/2)}; \quad w_2' = A_2 a_2 e^{a_2(\pi/2)} + B_2 b_2 e^{a_2(\pi/2)}.$$

The conditions of vanishing meridian rotation are then

$$w_1' + \chi_1^{(w)} = 0; \quad w_2' + \chi_2^{(w)} = 0$$

from which

$$A_1 + B_1 = \frac{1}{12 e^{6\pi}} \frac{5530}{E}, \qquad A_2 + B_2 = \frac{1}{12 e^{6\pi}} \frac{1880}{E}. \tag{a}$$

The other boundary condition of vanishing generalized normal shear Q_ϕ^* at $\phi = \pi/2$ is obtained from the last line of Table I ($a_n = b_n$), which now reduces to

$$\left(-2 a_n b_n^2 - n^2 a_n + \frac{4}{3} n^2 a_n\right) A_n + \left(2 a_n^2 b_n - n^2 b_n + \frac{4}{3} n^2 b_n\right) B_n = 0.$$

By inserting the numerical values we see that $A_n \cong B_n$, so that (a) reduces to

$$A_1 \cong B_1 = \frac{1}{2 \times 12 e^{6\pi}} \frac{5530}{E}; \quad A_2 = B_2 = \frac{1}{2 \times 12 e^{6\pi}} \frac{1880}{E}.$$

The corresponding bending moments are determined from the first line of Table I, with $\phi = \pi/2$.

We would find

$$M_{\phi_1} = -\frac{3(3+\mu) E J}{8 a R^2} e^{6\pi} \left(-\frac{1}{3} A_1 + 2 a_1 b_1 B_1\right)$$

and

$$M_{\phi_2} = -\frac{3(3+\mu) E J}{8 a R^2} e^{6\pi} \left(-\frac{1}{3} A_2 + 2 a_2 b_2 B_2\right).$$

By inserting the numerical values

$$M\phi_1 = -2.26 \times 10^{-3} \text{ tm/m}; \quad M\phi_2 = -0.76 \times 10^{-3} \text{ tm/m}$$

which are negligible.

6. Concluding Remark

An important difference between lattice shells and isotropic shells is the essential deviation between membrane and bending stiffness. Particularly, in the case of double-layer lattice shells, the equivalent bending thickness of the shell is a multiple of the corresponding membrane thickness.

If we estimate the edge effects in a lattice shell by means of the equivalent isotropic shell, by using a meridian stiffness obtained from the bending stiffness, the forces will be highly overestimated.

The edge displacements are more directly connected with the hoop stresses, which depend directly on the membrane stiffness.

The appropriate combination of both effects yields the correct results.

7. References

[1] K. Girkmann: Flächentragwerke. Springer-Verlag, Wien. 5. Auflage.
[2] K. Klöppel, R. Schardt: Systematische Ableitung von Differentialgleichungen für ebene, anisotrope Flächentragwerke. Stahlbau 2, 1960.
[3] J. Mason: Contribuicao à Teoria das Estruturas em Superficie Anisótropa (in portuguese). Rio de Janeiro, 1963.
[4] W. S. Wlassow: Allgemeine Schalentheorie und ihre Anwendung in der Technik. Akademie Verlag, Berlin, 1958.
[5] H. Duddeck: Das Randstörungsproblem der technischen Biegetheorie dünner Schalen in drei korrespondierenden Darstellungen. Österreichisches Ingenieurarchiv, 1962.
[6] T. Langendonck: Spherical domes under unsymmetrical loading. Abh. der IVBH, 1960.
[7] K. Klöppel, R. Schardt: Zur Berechnung von Netzkuppeln. Der Stahlbau 5, 1962.
[8] W. Schönbach: Netzkuppeln als Radome. Der Stahlbau 2, 1969.

Summary

The problem of edge disturbances for lattice shells with triangular meshes is investigated approximately considering both the rotationally symmetric and the asymmetric edge stresses.

The behaviour of the lattice is accounted for by means of a continuous analogue model. Numerical results are reported from the design of the Manaus Dome, with 300 m in diameter.

Résumé

Le problème des perturbations aux coupoles en treillis à subdivision triangulaire est étudié par voie approximative, en tenant compte des sollicitations rotationnelles symétriques et des sollicitations asymétriques.

Le comportement du treillis est simulé par un modèle continu. On donne des résultats numériques basés sur le projet de construction pour la coupole de Manaus mesurant 300 m en diamètre.

Zusammenfassung

Das Randstörungsproblem für Gitterkuppeln mit dreieckiger Unterteilung wird in angenäherter Weise untersucht, wobei sowohl drehsymmetrische als auch unsymmetrische Randbeanspruchungen berücksichtigt werden.

Das Verhalten des Gitters wird mit einem kontinuierlichen Modell nachgebildet. Es werden numerische Resultate aus dem Entwurf der Manaus-Kuppel mit 300 m Durchmesser mitgeteilt.

Leere Seite
Blank page
Page vide

Substructures Analysis of Plate Systems

Calcul des systèmes de plaques par la méthode des substructures

Berechnung von Plattensystemen mittels Substrukturen

ROBERT P. McBEAN
Assistant Professor of Civil Engineering
University of Missouri, Columbia, Missouri

WILLIAM WEAVER, Jr.
Associate Professor of Structural Engineering, Stanford University, Stanford, California

Introduction

Frequently a structure to be analyzed by matrix methods possesses so many degrees of freedom that it cannot be treated within the core memory of the computer. In such cases the analyst must resort to the use of auxiliary storage facilities and accept an inevitable increase in computer time due to relatively slow access to information. For the substructures method, the structure is physically partitioned into several units, each of which can be treated in the available computer core. The books by Przemieniecki [7] and Weaver [10] include extensive descriptions of substructures techniques. Of interest in this report is a special procedure which has proved to be very versatile when applied to plate systems with rectangular boundaries. To illustrate, an assemblage of complex finite elements subjected to bending and plane stress is used herein. This situation is typical of stiffened plate problems [6].

Substructures Analysis

For multistory framed buildings Clough et al. [1, 2, 3] and Weaver et al. [11, 12] partitioned the stiffness matrix into submatrices defining the action-displacement relations for joints at a given floor level, those at the level below, and those coupling the two levels. For planar frames all but the horizontal displacements at each level are progressively eliminated by matrix condensation as the analysis proceeds downward from the top story. The horizontal response due to static or dynamic forcing functions thus involves only one

degree of freedom per floor level (assuming the floor systems perform as rigid diaphragms). All nonhorizontal displacements and member stress resultants are determined by backward substitution.

The similarity between a rectangular plane frame and a discretized rectangular plate in bending is apparent. The geometric configuration is essentially the same. Each row of finite elements in a plate is considered to be a substructure, as are the floor beams and columns of a story in a building frame. There are, however, important inherent differences. While a multistory building is restrained only at the base, the plate may be restrained arbitrarily. Furthermore, there is only one degree of freedom per story in the two-dimensional building model, whereas many lateral (normal to the plate) degrees of freedom are retained for each row of elements in the plate. Although all displacements could be eliminated for each substructure in a static analysis, a dynamic analysis is facilitated by retaining the lateral degrees of freedom.

Elimination Procedure for Rectangular Plates

Fig. 1 illustrates a substructure for a plate subjected to both bending and plane stress. Conforming bending and linear-strain membrane elements,

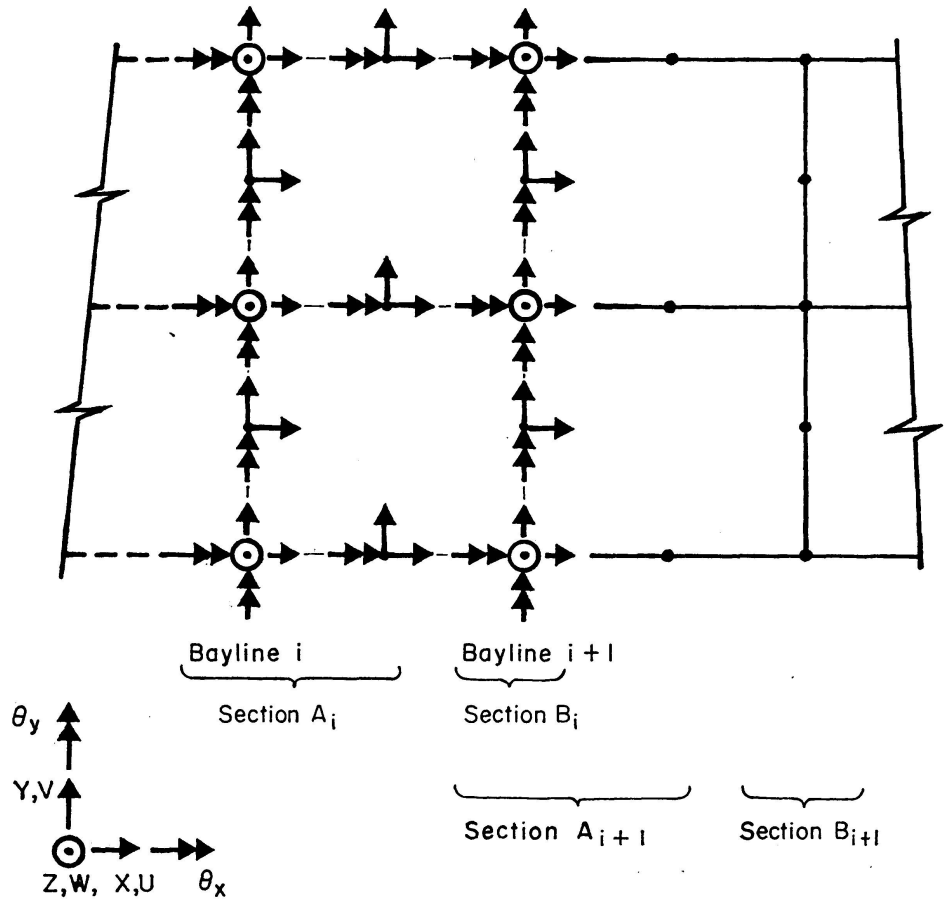


Fig. 1. A typical substructure.

suggested by FRAEIJS de VEUBEKE [4,5], have been used by the first co-author [6] for the analysis of stiffened plates. That study required a finite element with 32 nodal displacements, as indicated in Fig. 1.

The elimination proceeds in the X-direction. Each network line in the Y-direction will be called a bayline. Those nodes lying on bayline i, and those mid-edge nodes in the panel immediately following are considered to be in section A of bayline i, as indicated in Fig. 1. The nodes lying on the next bayline are considered to be in section B of bayline i. This identification is typical for any bayline. The row of plate elements delimited by baylines i and $i+1$ constitutes a substructure. Additional subscript notation is required to identify several types of displacements, as follows:

W = lateral displacement, referring to all sections in the structure;
A = nonlateral $(U, V, \theta_x, \theta_y)$ displacement associated with section A of bayline i;
B = nonlateral $(U, V, \theta_x, \theta_y)$ displacement associated with section B of bayline i.

Lower-case subscripts a and b refer to the corresponding restrained displacements associated with bayline i. The lower-case subscript w refers to the restrained lateral displacements of both sections of bayline i. It must be emphasized that upper-case W refers to all free lateral displacements in the structure, not merely to a section. All displacements of the A, B, a, b, and w types are to be eliminated in the analysis. The w-type (restrained) displacements could be included in the a and b type displacements, but they are considered separately here for convenience.

At a typical bayline in the forward-elimination process the action-displacement relation, in partitioned form, can be written as follows:

$$\begin{bmatrix} K_{AA} & K_{AB} & K_{AW} & K_{Aa} & K_{Ab} & K_{Aw} \\ & K_{BB} & K_{BW} & K_{Ba} & K_{Bb} & K_{Bw} \\ & & K_{WW} & K_{Wa} & K_{Wb} & K_{Ww} \\ & & & K_{aa} & K_{ab} & K_{aw} \\ & \text{Symmetric} & & & K_{bb} & K_{bw} \\ & & & & & K_{ww} \end{bmatrix} \begin{bmatrix} D_A \\ D_B \\ D_W \\ D_a \\ D_b \\ D_w \end{bmatrix} = \begin{bmatrix} F_A \\ F_B \\ F_W \\ F_a \\ F_b \\ F_w \end{bmatrix}. \tag{1}$$

The subscripts of the stiffness submatrices identify their association with the six displacement types. In an effort to give an uncluttered appearance, matrix symbols are not used in Eq. (1), but each item represents a submatrix. Expanding Eq. (1) produces:

$$K_{AA} D_A + K_{AB} D_B + K_{AW} D_W + F_{AS} = F_A, \tag{2}$$

$$K^t_{AB} D_A + K_{BB} D_B + K_{BW} D_W + F_{BS} = F_B, \tag{3}$$

$$K^t_{AW} D_A + K^t_{BW} D_B + K_{WW} D_W + F_{WS} = F_W, \tag{4}$$

$$K^t_{Aa} D_A + K^t_{Ba} D_B + K^t_{Wa} D_W + F_{as} = F_a, \tag{5}$$
$$K^t_{Ab} D_A + K^t_{Bb} D_B + K^t_{Wb} D_W + F_{bs} = F_b, \tag{6}$$
$$K^t_{Aw} D_A + K^t_{Bw} D_B + K^t_{Ww} D_W + F_{ws} = F_w, \tag{7}$$

in which the superscript t denotes transposition.

Equivalent generalized forces, associated with the specified displacements, appear in Eqs. (2), (3), and (4). They carry the following definitions:

$$F_{AS} = K_{Aa} D_a + K_{Ab} D_b + K_{Aw} D_w, \tag{8}$$
$$F_{BS} = K_{Ba} D_a + K_{Bb} D_b + K_{Bw} D_w, \tag{9}$$
$$F_{WS} = K_{Wa} D_a + K_{Wb} D_b + K_{Ww} D_w. \tag{10}$$

F_{as}, F_{bs}, and F_{ws} in Eqs. (5), (6), and (7) are similarly defined. It is convenient to abbreviate the subsequent development by the substitutions:

$$\bar{F}_A = F_A - F_{AS}, \tag{11}$$
$$\bar{F}_B = F_B - F_{BS}, \tag{12}$$
$$\bar{F}_W = F_W - F_{WS}. \tag{13}$$

The six vectors to be determined in Eqs. (2) through (7) are the unrestrained displacements D_A, D_B, and D_W, and the generalized nodal restraint forces F_a, F_b, and F_w.

Solve for D_A in Eq. (2):

$$D_A = K^{-1}_{AA} (\bar{F}_A - K_{AB} D_B - K_{AW} D_W). \tag{14}$$

By substitution of Eq. (14) into Eqs. (3) and (4), D_A is eliminated. The resulting equations are:

$$K^*_{BB} D_B + K^*_{BW} D_W = \bar{F}^*_B, \tag{15}$$
$$K^{*t}_{BW} D_B + K^*_{WW} D_W = \bar{F}^*_W, \tag{16}$$

in which,

$$K^*_{BB} = K_{BB} - K^t_{AB} K^{-1}_{AA} K_{AB}, \tag{17}$$
$$K^*_{BW} = K_{BW} - K^t_{AB} K^{-1}_{AA} K_{AW}, \tag{18}$$
$$K^*_{WW} = K_{WW} - K^t_{AW} K^{-1}_{AA} K_{AW}, \tag{19}$$
$$\bar{F}^*_B = \bar{F}_B - K^t_{AB} K^{-1}_{AA} \bar{F}_A, \tag{20}$$
$$\bar{F}^*_W = \bar{F}_W - K^t_{AW} K^{-1}_{AA} \bar{F}_A \tag{21}$$

are the condensed stiffness and load matrices.

The displacements of type B for the current bayline become displacements of type A for the following bayline. In the process, matrix K^*_{BB} assumes the role of initializing matrix K_{AA} for the following bayline, where it is augmented by the contributions from that bayline. The initialization is accomplished simply by shifting the contents of K^*_{BB} into matrix K_{AA} at the end of an elimination step. A similar treatment applies to the load vectors.

The elimination (or condensation) procedure is performed for every bayline in the plate. At the last bayline section B is undefined, and section A contains only those nodes along this last bayline. Therefore, the vector of lateral displacements can be directly determined from

$$K^*_{WW} D_W = \bar{F}^*_W. \tag{22}$$

The nonlateral displacements can be calculated by backward substitution, beginning at the last bayline and working toward the first. Displacements D_A for the last bayline are found from Eq. (14) with $D_B = 0$. These displacements D_A become the D_B for the next bayline. This simple procedure is repeated for each bayline until all displacements have been determined.

During the backward-substitution phase, the generalized restraint forces F_a, F_b, and F_w are found directly from Eqs. (5), (6), and (7) as the displacement vectors D_A and D_B become available. If any loads are directly applied to the restraints, then their contribution must be included in the final reactions. Such direct contributions occur when the consistent load vector for a distributed or concentrated load on a finite element is calculated and assigned to the restrained nodes. The generalized forces so calculated are useful for checking overall equilibrium, although they are not of interest themselves because they represent fictitious forces. If desired, the stress resultants can be described in terms of these nodal forces.

The stresses, or stress resultants, are also calculated during the back-substitution phase. A detailed computer algorithm is available from the first co-author on request.

Vibrational Analysis

When a lumped-mass approach is considered adequate for a free-vibration study, d'Alembert's principle gives

$$M_W \ddot{D}_W + K^*_{WW} D_W = 0, \tag{23}$$

where M_W is a diagonal mass matrix. For harmonic motion with circular frequency p, Eq. (23) becomes the eigenvalue problem:

$$K^*_{WW} D_{W_n} = p^2 M_W D_{W_n}, \tag{24}$$

where D_{W_n} denotes the vector of peak amplitudes (mode shape).

The condensed stiffness matrix K^*_{WW} can be obtained by the forward-elimination process described above for static analysis. This array, together with the diagonal mass matrix, may then be used to determine the natural frequencies and the associated mode shapes for the plate.

Numerical Example

A computer program based on the substructures approach has been applied to the analysis of both stiffened and unstiffened plates. For purposes of illustration, the static and free-vibration analysis of a square, simply-supported plate subjected only to bending is presented here (see Fig. 2).

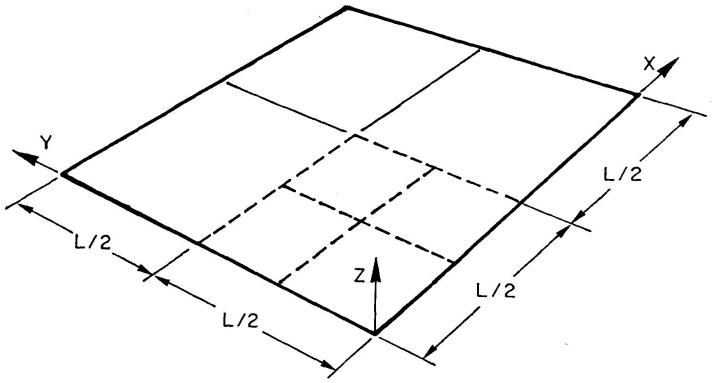


Fig. 2. Square, simply-supported plate ($N = 2$).

The conforming quadrilateral element with mid-edge nodes [5] is used to idealize the plate. Associated with each corner node are a translation and two rotations; associated with each mid-edge node is a normal slope. The letter N denotes the number of square elements along half the side of the plate. For example, $N = 2$ means that four elements are used to represent one-quarter of the plate, as shown in Fig. 2.

For a uniform load q, the maximum deflection is given in Table 1, in terms of a coefficient α, where

$$W_{max} = \frac{\alpha q L^4}{D}. \tag{25}$$

The symbol D in Eq. (25) represents the flexural rigidity, and L is the side length of the plate.

Table 1. Maximum Deflection of a Square, Simply-Supported Plate under Uniform Load

N	Maximum Deflection Coefficient α	
	Consistent Load	Lumped Load
1	0.0040824	0.0027189
2	0.0040624	0.0036870
4	0.0040617	0.0039663
6	0.0040615	0.0040189
Exact [8]	0.004062	0.004062

Usually the bending moments are of greater interest to the structural engineer than are the deflections. The convergence characteristics for the

bending moment M_{xx} along the centreline are given in Table 2, in terms of a coefficient β, where:

$$M_{xx} = \beta q L^2. \tag{26}$$

Table 2. Moment M_{xx} on Centreline of a Square, Simply-Supported Plate under Uniform Load

x/L	Moment Coefficient β			
	$N=1$	$N=2$	$N=4$	Exact [8]
0.0	0.01036	0.00400	0.00117	0.0
0.125			0.02591 0.02560	0.02488
0.250		0.04201 0.04019	0.03968 0.03940	0.03891
0.375			0.04637 0.04622	0.04582
0.500	0.05616	0.04933	0.04830	0.04789

Two values of β are given for the intermediate values of x/L to show the moment discontinuity to be expected at the node. The moment variation is linear between the nodes, and follows the exact curve [8] very closely.

From the static load analysis the condensed stiffness matrix K^*_{WW} is available. For $N=1$ and $N=2$ respectively:

$$K^*_{WW} = [2.1049], \tag{27}$$

$$M_W = [0.0625] \tag{28}$$

and

$$K^*_{WW} = \begin{bmatrix} 52.1821 & & \text{Symmetric} & \\ -19.1298 & 26.0910 & & \\ -19.1298 & 2.0763 & 26.0910 & \\ 2.0763 & -9.5649 & -9.5649 & 13.0455 \end{bmatrix}, \tag{29}$$

$$M_W = \begin{bmatrix} 0.0625 & 0 & 0 & 0 \\ 0 & 0.03125 & 0 & 0 \\ 0 & 0 & 0.03125 & 0 \\ 0 & 0 & 0 & 0.015625 \end{bmatrix}. \tag{30}$$

Assumed for this example are a plate length of 1.0, a flexural rigidity D of 0.091575, and a mass per unit area of 1.0. With the lumped-mass approach the lowest natural frequency is found to be 0.9236 cps for $N=1$, and 0.9501 cps for $N=2$. The exact solution, given by TIMOSHENKO and YOUNG [9] is 0.9506 cps.

If the complete stiffness matrix were used to find the natural frequencies, then the order of the eigenvalue problem to be solved would be 5 by 5, 20 by 20, and 80 by 80 for $N=1$, 2, and 4 respectively instead of the reduced orders of 1 by 1, 4 by 4, and 16 by 16. The reduction of order is even more dramatic

for the case of eccentrically-stiffened plates where in-plane displacements in the x and y directions must be considered at every node. The original orders of the eigenvalue problem would then be 5 by 5, 52 by 52, and 200 by 200 for $N = 1$, 2, and 4 respectively. Thus, the eigenvalue problem to be solved is of much lower order when all but the lateral degrees of freedom have been eliminated. Because the elimination is done in a row-by-row manner, large numbers of nodal displacements do not create a great problem.

It should be noted that only the symmetric modes of vibration can be obtained when one-quarter of the plate is used, and a number of elements sufficient to represent all desired mode shapes must be specified.

Conclusions

A substructures approach to the static and dynamic analysis of plate systems has been described. The order of the set of equations to be solved at any stage is relatively low; so a large core capacity in a digital computer is not required. Specified support displacements are easily considered in the general treatment presented. A great advantage of this substructures technique is that a lumped-mass, free-vibration analysis, involving only the lateral degrees of freedom in the plate, may be performed with little extra effort once a static analysis has generated the reduced stiffness matrix. This advantage would be sacrificed if all of the degrees of freedom in each substructure were eliminated. It should be noted that no information need be transferred to auxiliary storage if the analyst is concerned only with natural frequencies and mode shapes. The appropriate segments of the computer program can simply be by-passed. Results for an example of a simply-supported square plate compare closely with known exact solutions [8].

References

1. R. W. Clough, and I. P. King: Analysis of Three-Dimensional Building Frames. Pub. International Association for Bridge and Structural Engineering, Vol. 24, 1964.
2. R. W. Clough, I. P. King, and E. L. Wilson: Structural Analysis of Multistory Buildings. Journal of the Structural Division, ASCE, Vol. 90, No. ST 3, June, 1964.
3. R. W. Clough, E. L. Wilson, and I. P. King: Large Capacity Multistory Frame Analysis Programs. Journal of the Structural Division, ASCE, Vol. 89, No. ST 4, Aug., 1963.
4. B. M. Fraeijs de Veubeke: Displacement and Equilibrium Models in the Finite Element Method. Chapter 9 of Stress Analysis, edited by Zienkiewicz, O. C., and Holister, G. S., Wiley, 1965.
5. B. M. Fraeijs de Veubeke: A Conforming Finite Element for Plate Bending. International Journal of Solids and Structures, Vol. 4, No. 1, Jan., 1968.

6. R. P. McBean: Analysis of Stiffened Plates by the Finite Element Method. Ph. D. Dissertation, Department of Civil Engineering, Stanford University, Stanford, California, June, 1968.
7. J. S. Przemieniecki: Theory of Matrix Structural Analysis. McGraw-Hill Book Co., New York, N. Y., 1968.
8. S. P. Timoshenko, and S. Woinowsky-Krieger: Theory of Plates and Shells. McGraw-Hill Book Co., New York, N. Y., 1959.
9. S. P. Timoshenko, and D. H. Young: Vibration Problems in Engineering. D. Van Nostrand Co., Princeton, N. J., 1955.
10. W. Weaver, Jr.: Computer Programs for Structural Analysis. D. Van Nostrand Co., Princeton, N. J., 1967.
11. W. Weaver, Jr., and M. F. Nelson: Three-Dimensional Analysis of Tier Buildings. Journal of the Structural Division, ASCE, Vol. 92, No. ST 6, Dec., 1966.
12. W. Weaver, Jr., M. F. Nelson, and T. A. Manning: Dynamics of Tier Buildings. Journal of the Engineering Mechanics Division, ASCE, Vol. 94, No. EM 6, Dec., 1968.

Summary

A substructures approach to the static and dynamic matrix analysis of rectangular plate systems is described. For each substructure the nodal displacement vector is partitioned to consider both unconstrained and constrained displacements in the plane of the plate and perpendicular to it. The order of the set of simultaneous equations to be solved for any substructure is relatively low; so a large capacity computer core is not required. Furthermore, by retention of only the lateral degrees of freedom, a lumped-mass, free-vibration analysis may be performed with little effort once a static analysis has generated the reduced stiffness matrix. The static and free-vibration behaviour of a square, simply-supported plate is presented to illustrate the technique.

Résumé

Les auteurs décrivent une méthode des substructures pour le calcul matriciel, statique et dynamique, des systèmes de plaques rectangulaires. Pour chaque substructure, on sépare le vecteur des déplacements en déplacements forcés et déplacements libres, dans le plan de la plaque et dans la direction perpendiculaire. Le nombre des équations simultanées à résoudre pour chaque substructure étant relativement limité, on peut donc renoncer à l'usage d'un ordinateur de grande capacité. De plus, en ne retenant que les déplacements perpendiculaires à la plaque, on peut effectuer aisément une analyse des vibrations libres, une fois que l'on dispose de la matrice de rigidité réduite. Pour illustrer cette technique, on décrit le comportement statique et les vibrations libres d'une plaque carrée simplement supportée.

Zusammenfassung

Die Berechnung der statischen und dynamischen Matrizen für rechteckige Plattensysteme mittels Substrukturen wird beschrieben. In jeder Substruktur ist der Vektor, der die Knotenverschiebungen darstellt, in zwei Komponenten unterteilt, die sowohl die erzwungenen als auch die freien Verschiebungen in der Plattenebene sowie die senkrecht dazu darstellen. Die Anzahl der für jede Substruktur zu lösenden simultanen Gleichungen ist verhältnismäßig gering, so daß ein relativ kleiner Digitalrechner benutzt werden kann. Da nur die Freiheitsgrade normal zur Plattenebene verwendet werden, ist eine einfache Analyse der freien Schwingungen mittels konzentrierter Punktmassen möglich, die eine durch statische Analyse berechnete reduzierte Steifheitsmatrix benützt. Als Beispiel sind das statische Verhalten und die freien Schwingungen einer quadratischen, frei unterstützten Platte dargestellt.

Calculation of Stress in Knee Joints of Rigid Steel Frames of Thin Walled Section and Its Application

Le calcul des contraintes dans l'assemblage d'angle de portiques en acier à nœuds rigides et parois minces et son application

Spannungsberechnung der dünnwandigen, steifknotigen Rahmenecke und deren Anwendung

TOSHIE OKUMURA
Professor of University of Tokyo, Tokyo, Japan

NARUO ISHIZAWA
Technical Division, Miyaji Iron Works Co., Ltd., Tokyo, Japan

Introduction

Rigid frame construction is employed in many of crossroads in cities, and its dynamic properties are now required to be reexamined. From our past experiences, it is known that the knee joints are in most cases weak points in rigid frame construction. Efforts have been made to pursue the properties of knee joints in designing based on the theory of elastic design, and recently the rigid frame construction has been taken up as an example in which the theory of plastic design can effectively be applied. All these have brought knee joints under examination from new angles. Essential property required of knee joints of rigid frame construction is, in general, the property to correctly transfer bending moment from beam to column, which causes a large shearing stress in the knee joints. Particularly, the web of straight knee joints with thin walled box section is subjected to shearing collapse due to this large shearing stress. Therefore, it will be required to have thorough understanding of such shearing stress and to devise a means to reduce it. Concerning this matter, there have been published some reports on utilization of wide flange steel for columns and beams having I-section. The present authors have confirmed from their actual survey of shearing stress distribution in knee joints of rigid frame construction having box section that it is almost a parabolic distribution, and suggested that the calculation made on the assumption that it is a uniform distribution should be corrected.

In straight knee joints, the stress from the inside flange of a column acts on the inside flange of beam as concentrated load, which causes shear lag, and this shear lag produces stress concentration on flange near the beam web. Due consideration must be paid to the stress distribution determined by the dimensions of the section. Reports so far published are, in many cases, on the study of wide flange steel for columns and beams having I-section. The trouble is that the stress is concentrated on the part of flange or web near the line of intersection of inside corners of column and beam, and that when the section formed by welding is used, the point of stress concentration coincides the point of intersection of welded joint. This may affect the ultimate strength of welded composite section under some conditions. From the viewpoint of welding, box section must be considered to be somewhat different so far as the ultimate strength is concerned.

In this report, the authors explain about the calculation of stress due to shear lag in straight knee joint flanges with box section and the diagrams used in estimating the stress, and mention the application of this theory to other types which differ somewhat from the type described.

Cylindrical columns have come to be more used in recent days in view of the advantages of cylindrical construction. Such problems as shearing stress in cylinders at knee joints and shear lag in beam flanges are no exception to this type. With reference to shearing stress in cylinder at knee joints, a system, in which beam web is inserted into cylinder, has been developed and its advantages have been examined in comparison with the simple system to butt beam web to cylinder. Simplified way of thinking has been presented so that the theory on straight knee joint flanges with box section might be applied to the stress in beam flange at knee joint of cylindrical construction.

A circular arc haunch type has been adopted in knee joints of rigid frame construction for railway bridge piers which are subjected to repeated load. Shearing stress in knee joints is generally lessened in this type as compared with other types. The flange force from column to beam is distributed within the range that the arc projection covers the beam axis, on account of which the effect of shear lag on the straight flange is relatively small. In this type, however, the warping of web and arc flange at knee joint is large, which causes fairly high stress concentration in the proximity of the web of arc flange. This report treats of the calculation of stress in arc flange at arc knee joint with box section and provides the results of the experiments.

1. Straight Knee Joint

This type is in the most popular use. In most cases, square steel is fixedly arranged on the line of intersection of the inside flanges of a column and beam. This arrangement is made to cope with problems related to a possible lowering

of yield strength incident to a steel plate subjected to stress in the direction of its thickness and the rigidity of the flanges on the line of intersection and to look for the effect of stress in column flanges distributed in and acting on beam webs.

The Tokyo Expressway Corporation adopts the design method proposed by the present author for the calculation of knee joints. This method is a revised version of L. S. Beedle's theory with respect to shearing stress in webs at knee joints. As regards stress in flanges, due regard is paid to the stress due to shear lag. It is expressly indicated that the stress due to shear lag in flanges can be obtained by model calculation and diagrams used for estimating the stress due to shear lag are presented with the aim of simplifying the calculation.

1.1. Shearing Stress in Webs

Prof. Beedle has published the valuable results of his study on the design of knee joints of rigid frames. He sets forth the advantages of designing knee joints in straight form on the following assumptions:

a) Shearing stress is distributed uniformly in webs.

b) The theory of the maximum shearing stress is observed with respect to yield condition for safety's sake. Therefore, $\tau_y = \sigma_y/2$.

c) Only shearing stress acts on webs, while only normal stress on flanges.

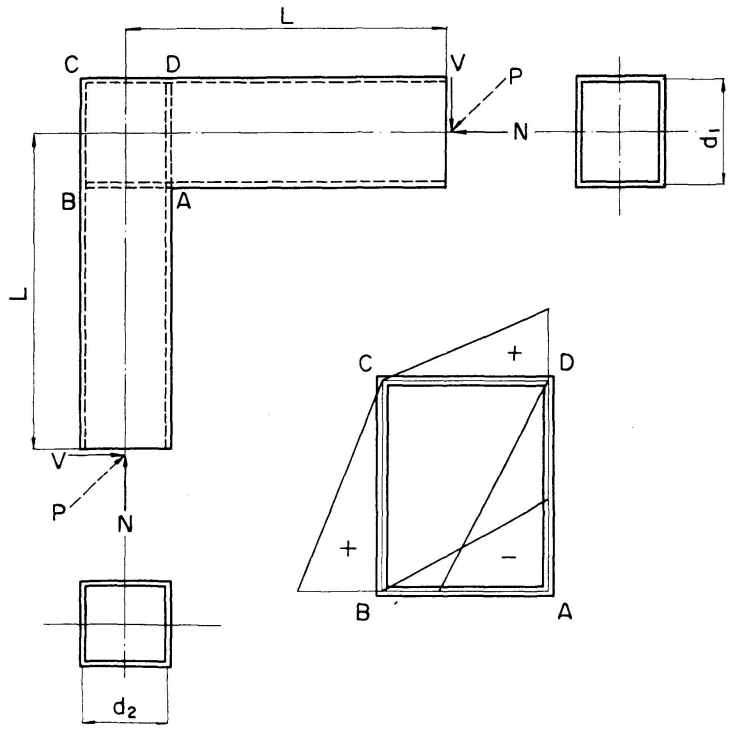


Fig. 1.

According to these assumptions, when members are subjected to loads as shown in Fig. 1, normal stresses in the flanges DC and AB of the beam and the flanges BC and AD of the column attenuate linearly and differences in normal stress are transmitted to their respective webs as shearing stress.

This way facilitates calculation of stress. It is also applicable to straight knee joints of box section.

Let M and N be bending moment and axial force. By referring to Fig. 2, the flange force F can be written in the form

$$F_{01} = \frac{M_1}{d_1} - \frac{N_1}{2}, \quad F_{i1} = \frac{M_1}{d_1} + \frac{N_1}{2}, \quad F_{02} = \frac{M_2}{d_2} - \frac{N_2}{2}, \quad F_{i2} = \frac{M_2}{d_2} + \frac{N_2}{2}. \tag{1}$$

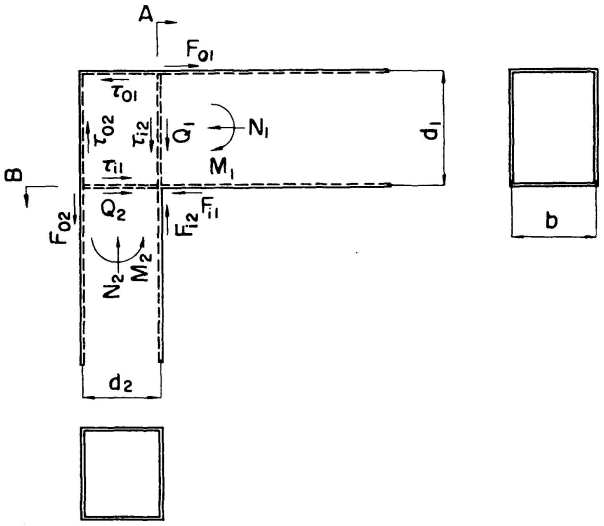


Fig. 2.

Let Q be shearing force, and the shearing stress τ can be written in the form

$$\tau_{01} = \frac{F_{01}}{2d_2t_2}, \quad \tau_{i1} = \frac{F_{i1} - Q_2}{2d_2t_2} = \tau_{01}, \quad \tau_{02} = \frac{F_{02}}{2d_1t_2}, \quad \tau_{i2} = \frac{F_{i2} - Q_1}{2d_1t_2} = \tau_{02}, \tag{2}$$

By referring to Fig. 1, the bending moment at which the webs are caused to yield by shearing stress may be obtained in the form

$$M_{h(\tau)} = \frac{t_2 d_1 d_2 \sigma_y}{2}\left[\frac{1}{1 - \frac{d_1 + d_2}{2L}}\right]. \tag{3a}$$

The bending moment at which the flanges are caused to yield by normal stress is defined as

$$M_{h(\sigma)} = \frac{\sigma_y}{\frac{1 - \frac{d}{2L}}{S} + \frac{1}{AL}}, \tag{3b}$$

where S and A denote the modulus of section and sectional area of the member which is smaller in web height, respectively, and d is the web height of the other member.

Let τ_a be allowable shearing unit stress in Eq. (2) for τ.

$$\tau_{01} = \tau_{i1} \leqq \tau_a,$$

$$\tau_{02} = \tau_{i2} \leqq \tau_a.$$

And τ_a is assumed to be related to allowable tensile unit stress σ_a in the form

$$\tau_a = 0.45\,\sigma_a. \tag{4}$$

The ratio of allowable shearing unit stress to allowable tensile unit stress is estimated at a lower value than that in other parts of bridges in due consideration of the difference between the shearing stress distributed in knee joints assumed in Eq. (2) and that actually observed. It is assumed in Eq. (2) that shearing stress is distributed uniformly in the webs at a knee joint, while, according to the results of actual observations, shearing stress has a somewhat larger value at the middle of the knee joint and near the point of intersection of the inner flanges. In other words, it is disributed approximately in parabolic form rather than uniformly. When the relation between a load and a change in the interval between load points is viewed from the results of experiments, the condition of initial yield is more definitely expressed by the theory in support of the parabolic distribution of shearing stress. By applying $\tau_{av}/\tau_{max} \fallingdotseq 0.9$ (where τ_{max} is the maximum value of the shearing stress assumed to be distributed in parabolic form and τ_{av} is the value of the shearing stress assumed to be distributed uniformly in an ordinary section) to the yield condition $\tau = 0.5\,\sigma_y$ based on the theory of the maximum shearing stress, $\tau_a = 0.45\,\sigma_a$ was proposed for the calculation in which shearing stress is assumed to be distributed uniformly.

Webs tend to become thicker according to this method of calculation than according to conventional methods of calculation. This means a less tendency to stress concentration in flanges due to shear lag. That is to say, welded flanges and webs intersect at one point in three directions in a straight knee joint of box section and the maximum stress is exerted on this point of intersection. In this type, about 1.5 to 3 stress concentration brought about at this point leaves a defect coupled with the quality of welded joints. This knee joint is subject to repeated alternate stress under vehicle and earthquake loads. As the mean stress in this type of knee joint has been allowed to come down to the proximity of the yield point of steel under designed earthquake load, it is subject to high stress low cycle fatigue according to the degree of stress concentration coupled with residual stress due to welding. This is why stress concentration at this part is desired to be reduced to a minimum in some way or other.

1.2. Calculation of Shear Lag Arising in Flanges at Knee Joints and Diagrams Used for Estimating Stress Due to Shear Lag

The problem taken up in designing thin walled section is the phenomenon of shear lag arising in flanges and webs near concentrated load. The phenomenon of shear lag is caused by inner constraint when there is a difference in shearing strain between adjoining sections in the longitudinal direction of flanges. As the stress due to shear lag generally has the same sign as the stress due to bending moment, it comes into question at that part of a member which is subjected to the maximum bending moment. It should be corrected to bending stress to which the law pertaining to the retention of plane can be applied.

Shear lag is analyzed on the following assumptions:

1. Beams have uniform sectional form and are made of a uniform and isotropical elastic body.
2. The flanges are joined to the web at right angle to each other.
3. Bernoulli-Euler's assumption holds good in the web plate and the flanges are the plates on which shearing force and normal stress act along the boundary.
4. Strain remains unchanged at that part where the flanges and the web are welded together on the ground of continuity.

This is shown in terms of boundary condition in Fig. 3. This condition is used for solving the Airy's stress function ϕ.

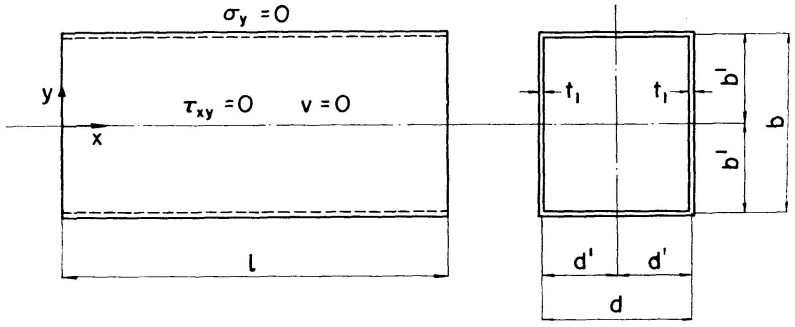


Fig. 3.

From the fact that the strain in the web plate is equal to that in the flanges at $y=b'$ in Fig. 3,

$$\sigma_w = (\sigma_x - \nu\,\sigma_y)_{y=b'} = \left(\frac{\partial^2 \phi}{\partial y^2} - \nu \frac{\partial^2 \phi}{\partial x^2}\right)_{y=b'}. \tag{5}$$

The effective width of the flanges is defined as

$$\bar{b}' = \frac{\int_0^{b'} \sigma_x \, dy}{\sigma_w} = \frac{\left[\frac{\partial \phi}{\partial y}\right]_0^{b'}}{\sigma_w}. \tag{6}$$

The modulus of section S can be written in the form

$$S = \frac{12A_1A_2 + 4A_w(A_1+A_2) + A_w^2}{2A_2 + A_w}\frac{d'}{3} \tag{7}$$

or

$$S = \frac{12A_1A_2 + 4A_w(A_1+A_2) + A_w^2}{2A_1 + A_w}\frac{d'}{3}, \tag{8}$$

where A_w: sectional area of web plate,
$2d'$: height of web plate,
A_1: effective sectional area of upper flange,
A_2: effective sectional area of lower flange.

Hence

$$M = \sigma_w S = \left(\frac{\partial^2\phi}{\partial y^2} - \nu\frac{\partial^2\phi}{\partial x^2}\right)_{y=b'} S. \tag{9}$$

This represents the fourth boundary condition.

By putting

$$M = a\cos(\zeta x + \eta) \tag{10}$$

we obtain

$$\phi = (A\cosh\zeta y + B\sinh\zeta y + C\zeta y\cosh\zeta y + D\zeta y\sinh\zeta y)\cos(\zeta x+\eta). \tag{11}$$

By inserting this in the boundary condition, the effective width $\bar{b}'$ is defined as

$$\bar{b}' = \frac{\cosh\zeta b'\sinh\zeta b' + \zeta b'}{2\zeta\cosh^2\zeta b'} \tag{12}$$

in box section.

Developing the moment acting on the beam into the Fourier series

$$M = \sum_{n=1}^{\infty} a_n \sin\frac{n\pi}{l}x. \tag{13}$$

The stress caused by bending is defined as

$$\sigma = \frac{M}{S} = \sum_{n=1}^{\infty}\frac{a_n}{S}\sin\frac{n\pi}{l}x. \tag{14}$$

When shear lag is taken into account

$$\sigma = \frac{M}{S_n} = \sum_{n=1}^{\infty}\frac{a_n}{S_n}\sin\frac{n\pi}{l}x. \tag{15}$$

Therefore, the stress σ_S due to shear lag can be written in the form

$$\sigma_s = \sum_{n=1}^{\infty}\left(\frac{1}{S_n} - \frac{1}{S}\right)a_n\sin\frac{n\pi}{l}x. \tag{16}$$

The part at which shear lag comes into question in the rigid frame construction is a knee joint. Great shearing force is exerted on the knee joint through which the moment in the column is transmitted to the beam, resulting in shearing deformation and high stress due to shear lag in the section of the knee joint. Moreover, the maximum moment acts on the knee joint, making it necessary to give consideration to the stress due to shear lag.

Let us calculate moment distribution by regarding the variation of shearing force as the concentrated load W applied to the middle of a simple beam.

Developing the moment exerted on the middle of the simple beam into Fourier series

$$M = \sum_{n=1}^{\infty} a_n \sin \frac{n\pi}{l} x.$$

Putting $x = l/2$ in the above equation

$$M = \frac{2Wl}{\pi^2} \sum_{n=1}^{\infty} \frac{1}{n^2}, \qquad (n = 1, 3, 5, 7, \ldots). \tag{17}$$

Hence, the stress due to shear lag in this case is written in the form

$$\sigma_s = \frac{2Wl}{\pi^2} \sum_{n=1}^{\infty} \left(\frac{1}{S_n} - \frac{1}{S}\right) \frac{1}{n^2}, \quad (n = 1, 3, 5, 7, \ldots). \tag{18}$$

Assume that the upper and lower flanges have the same section and let t_1 be the thickness of the flanges, and we can derive from Eq. (7) and (8)

$$S = 4b' t_1 d' + \frac{d'}{3} A_w. \tag{19}$$

Hence

$$\begin{aligned} \left(\frac{1}{S_n} - \frac{1}{S}\right) &= \frac{1}{4b_n' t_1 d' + \frac{d'}{3} A_w} - \frac{1}{4b' t_1 d' + \frac{d'}{3} A_w} \\ &= \frac{3}{A_w d'} \frac{R_S}{1 + R_S} \frac{1 - \frac{b_n'}{b'}}{1 + \frac{b_n'}{b'} R_S}, \end{aligned} \tag{20}$$

where

$$R_S = \frac{6A_f}{A_w} \tag{21}$$

and A_f is the sectional area of each of the upper and lower flanges. Hence

$$\begin{aligned} \sigma_s &= \frac{2Wl}{\pi^2} \sum_{n=1}^{\infty} \frac{3}{A_w d'} \frac{R_S}{1 + R_S} \frac{1 - \frac{b_n'}{b'}}{1 + R_S \frac{b_n'}{b'}} \frac{1}{n^2} \\ &= \frac{Wb'}{A_w d'} \sum_{n=1}^{\infty} \frac{6}{\pi^2} \frac{l}{b'} \frac{R_S}{1 + R_S} \frac{1 - \frac{b_n'}{b'}}{1 + R_S \frac{b_n'}{b'}} \frac{1}{n^2} \\ &= \frac{b'}{d'} \frac{W}{A_w} \boldsymbol{S}_S = \frac{b}{d} \frac{W}{A_w} \boldsymbol{S}_S, \end{aligned} \tag{22}$$

where $$S_S = \sum_{n=1}^{\infty} \frac{6}{\pi^2} \frac{l}{b'} \frac{R_S}{1+R_S} \frac{1-\frac{b'_n}{b'}}{1+R_S\frac{b'_n}{b'}} \frac{1}{n^2}, \quad (n = 1, 3, 5, 7, \ldots). \tag{23}$$

In box section

$$\frac{\bar{b}'_n}{b'} = \frac{\cosh \zeta b' \sinh \zeta b' + \zeta b'}{2 \zeta b' \cosh^2 \zeta b'}, \tag{24}$$

where $$\zeta b' = n\pi \frac{b'}{l}. \tag{25}$$

Therefore, if the value of n is taken far enough, the value of S_S can be calculated accurately. S_S is the function of R_S, $\frac{l}{b'}$ and $\frac{b'_n}{b'}$. Assuming $\frac{l}{b'}=10$, the value of S_S is calculated with respect to all possible values of $R_S=\frac{6A_f}{A_w}$ as shown in Fig. 4. It has been confirmed that, if $\frac{l}{b'}>4$, S_S is little related to $\frac{l}{b'}$.

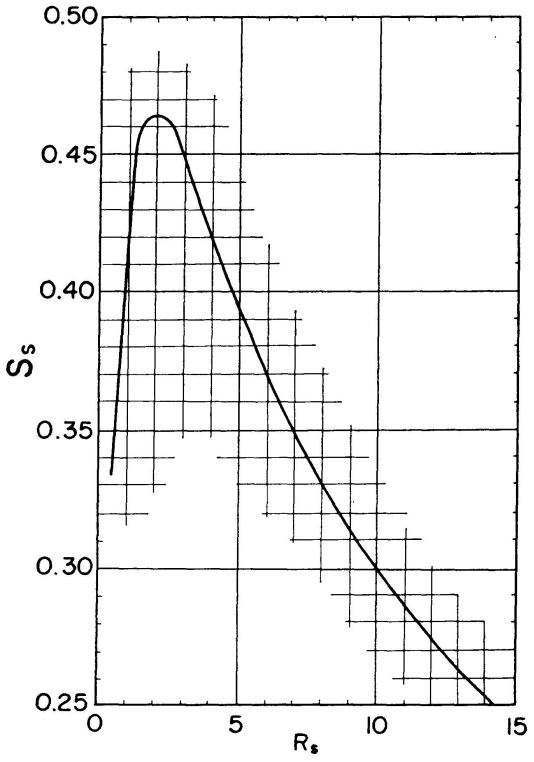


Fig. 4.

Assuming that the web plate of the column transmits no moment and the axial force is only born by the flanges, the inside flange force F_{i2} of the column can be defined as

$$F_{i2} = \frac{M_2}{d_2} + \frac{N_2}{2}.$$

The variation of shearing force in the section AD is defined as

$$W = F_{i2}.$$

If an arbitrary box section is given, we can calculate

$$R_S = \frac{6A_f}{A_w}$$

and find out the value of S_S to R_S by referring to Fig. 4. Therefore, σ_S can be calculated easily from

$$\sigma_S = \frac{b}{d}\frac{F_{i2}}{A_w} S_S. \tag{26}$$

The maximum stress in the flanges can be calculated from the bending stress σ_B and the stress due to axial force σ_N on the assumption that the beam is subjected to pure bending moment.

$$\sigma_{max} = \sigma_B + \sigma_N + \sigma_S. \tag{27}$$

1.3. Results of Experiments

The results of experiments with this type are illustrated as follows.

Fig. 6 shows shearing stress in the webs at the knee joint and Fig. 7 and 8 show axial stress in the flanges.

The results of these experiments indicate that the values obtained by the above-mentioned calculations are very close to the measured values.

An $M - \Delta i$ curve is shown in Fig. 9. Δi is the amount of a change in load

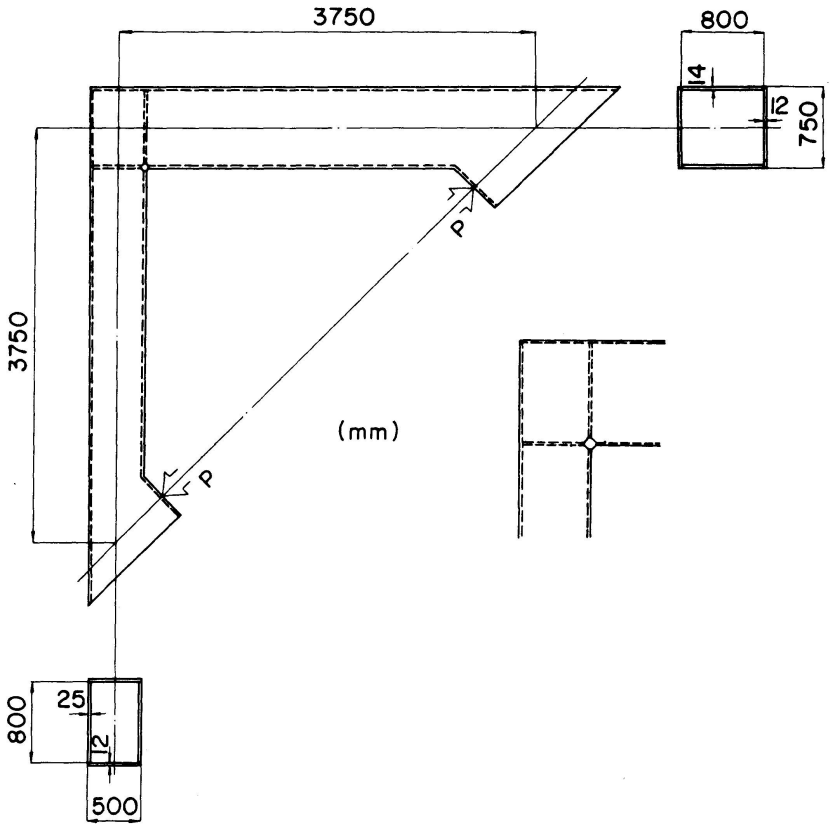


Fig. 5.

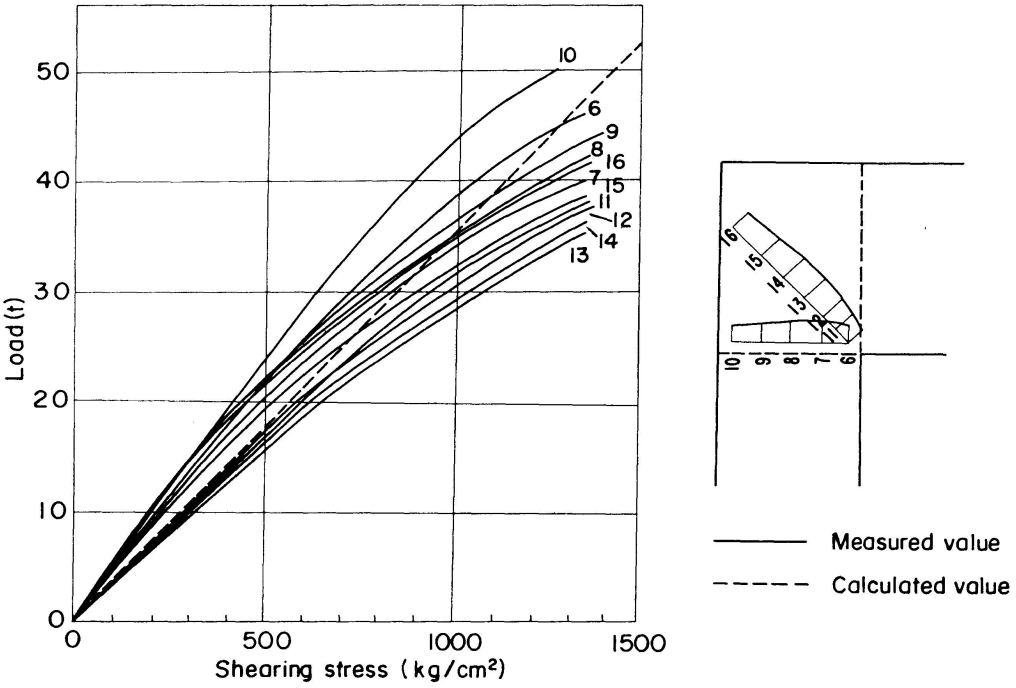


Fig. 6.

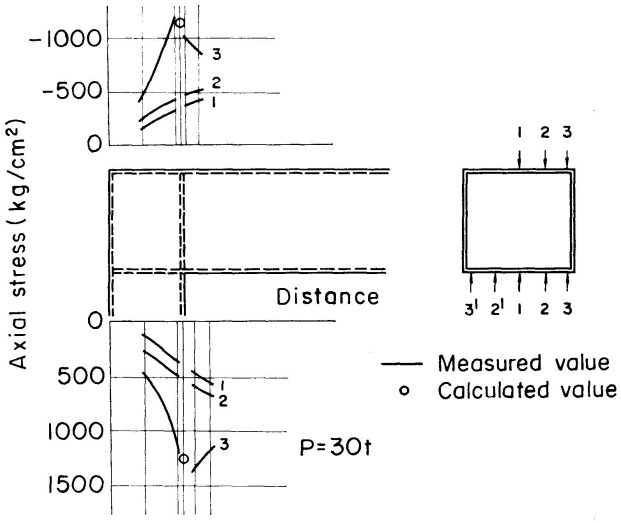


Fig. 7.

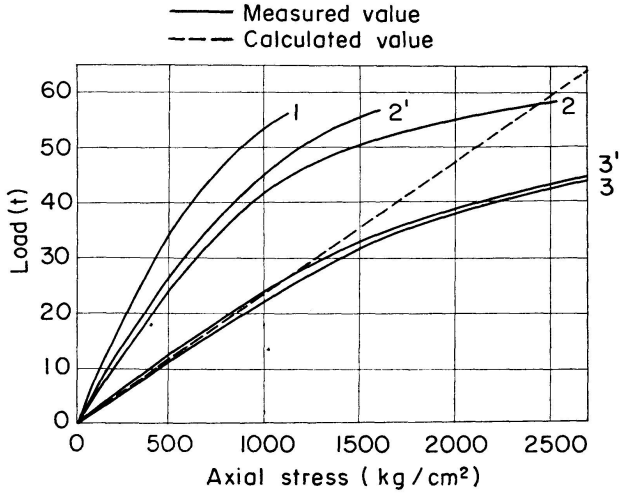


Fig. 8.

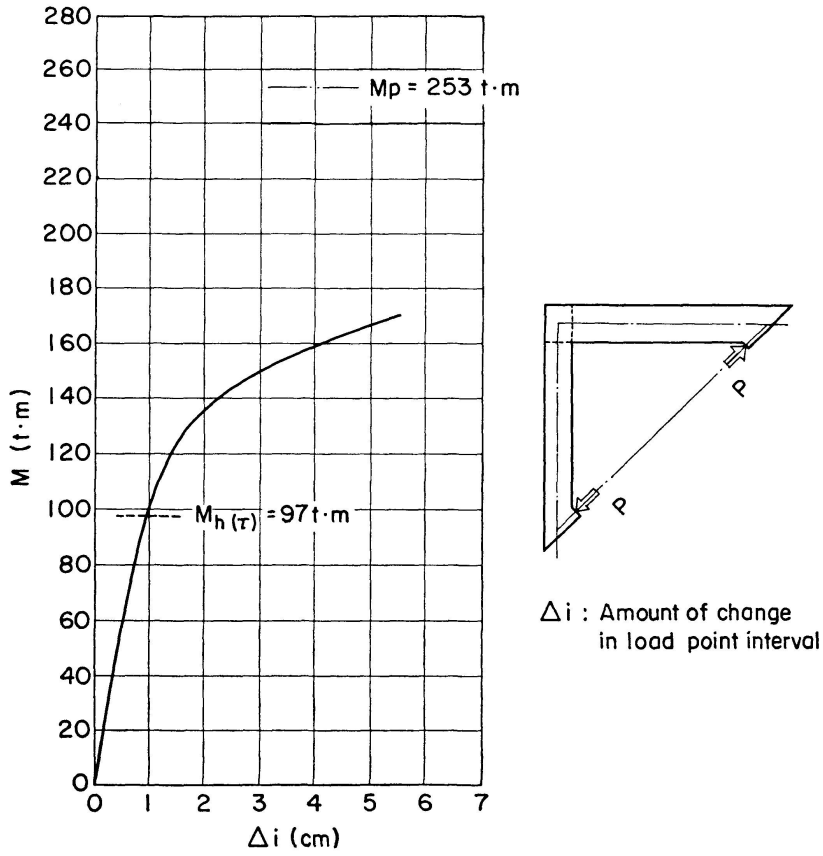


Fig. 9.

point interval. According to this diagram, the yield condition is satisfied by the bending moment $M_{h(\tau)}$ derived from $\tau_y = 0.45\,\sigma_y$ in the knee joint, giving no play to the total plastic moment M_p.

That is to say, the yield condition is satisfied by the shearing force in this type of knee joint, resulting in a possible lowering of the total plastic moment in the column or beam. Therefore, it is necessary to pay careful attention to the thickness of the web at the knee joint.

Great stress concentration is brought about in the proximity of the inner point in the knee joint. This makes it necessary to keep the welded joining part transmissible of the total strength of the plate.

As the stress concentration due to shear lag is reduced by increasing the web at the knee joint in thickness, any consideration given to shearing force in the knee joint will also have an effect on the stress concentration in the proximity of the inner point.

1.4. Application to Other Types

A straight haunch type knee joint is seen when an increase in the height of a web is limited to the proximity of the knee joint to cope with great bending moment exerted on it. It is also applied to the middle column in a multi-span rigid frame to which beams are joined at somewhat different heights from each other (Fig. 10).

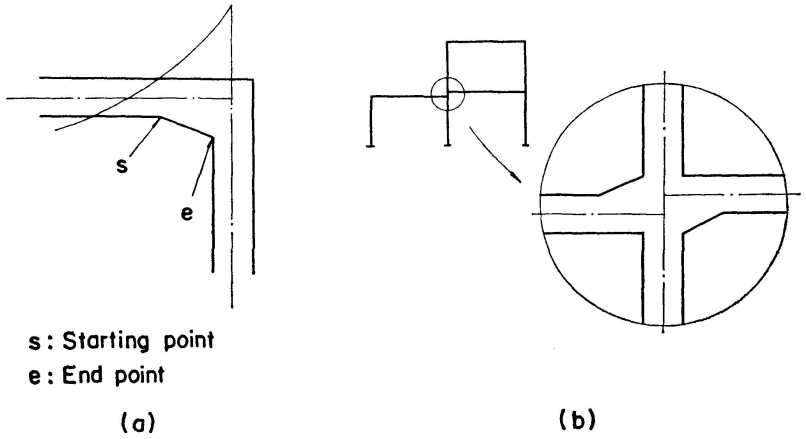


Fig. 10.

In this type, stress concentration at the starting or end point of the straight haunch comes into question. The stress at this point is presumed to be affected considerably by the haunch angle, the radius of curvature R of a flange and the use of a diaphragm at the starting point or end point of the haunch.

It is of great importance for designers to give a detailed experimental examination to these factors. So far as the present author knows, the results of experiments on the straight haunch type knee joint in members of box section have not been published.

Shearing stress in webs of this type is treated in the same way as that in straight rectangular type knee joints.

F_{01}, F_{i1}, F_{02} and F_{i2} are the same as given in Eq. (1). From Fig. 11

$$Q_2 = N_1, \qquad Q_1 = N_2 - F_{i1}\tan\theta. \tag{28}$$

From Eq. (28)

$$\tau_{01} = \frac{F_{01}}{2d_2t_2}, \qquad \tau_{i1} = \frac{F_{i1}-Q_2}{2d_2t_2} = \tau_{01},$$
$$\tau_{02} = \frac{F_{02}}{2d_1't_2}, \qquad \tau_{i2} = \frac{F_{i2}-F_{i1}\tan\theta-Q_1}{2d_1't_2} = \tau_{02}. \tag{29}$$

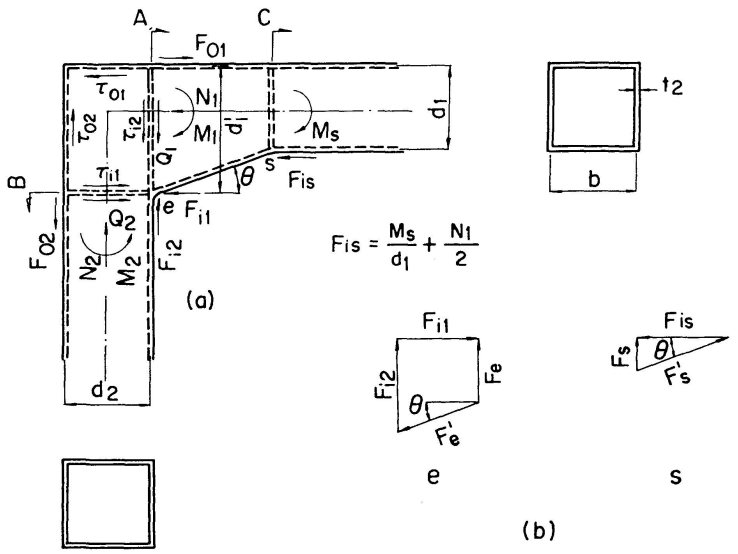


Fig. 11.

The axial stress in flanges of this type can be calculated in the same way as that in the above-mentioned straight rectangular type.

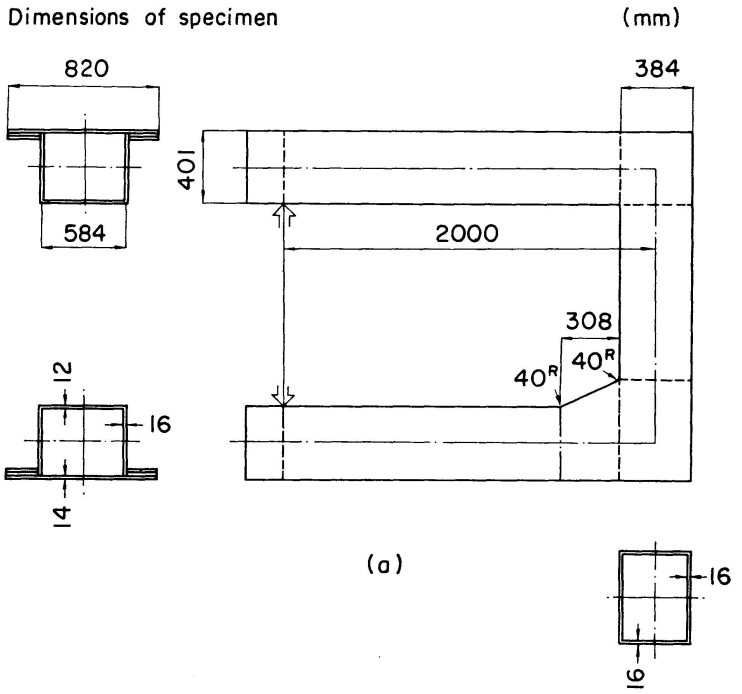
Suppose that the forces acting on the points e and s in Fig. 11 (a) are arranged as shown in Fig. 11 (b) and the resultant forces are concentrated in the sections A and C. According to this figure,

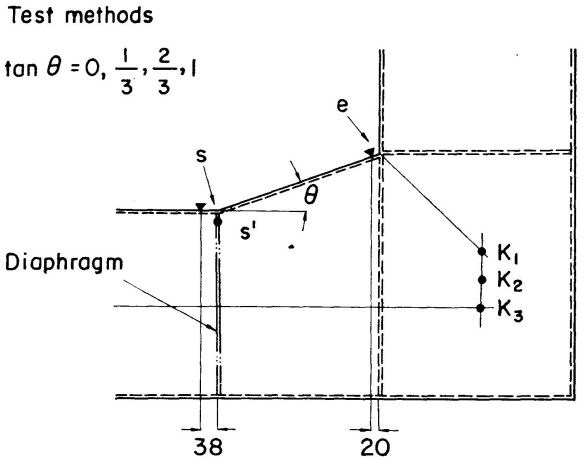
$$F_e = F_{i2} - F_{i1} \tan\theta, \qquad F_S = F_{iS} \tan\theta. \tag{30}$$

Stress due to shear lag in the sections A, B and C are defined respectively as

$$\sigma_{S1} = \frac{b}{d_1'} \frac{F_e}{A_{w1}} S_1, \qquad \sigma_{S2} = \frac{b}{d_2} \frac{F_{i1}}{A_{w2}} S_2, \qquad \sigma_{SC} = \frac{b}{d_1} \frac{F_S}{A_{wC}} S_C, \tag{31}$$

where S_1, S_2 and S_C can be found from the above-mentioned estimated dia-





▼ : Axial stress in the flange
● : Shearing stress in the web

Fig. 12.

grams used for estimating the stress due to shear lag with respect to R_S of the respective sections.

In this case, the section C in which the starting point of the haunch lies is provided with a diaphragm.

The results of experiments in this type are illustrated in Fig. 12, 13 and 14.

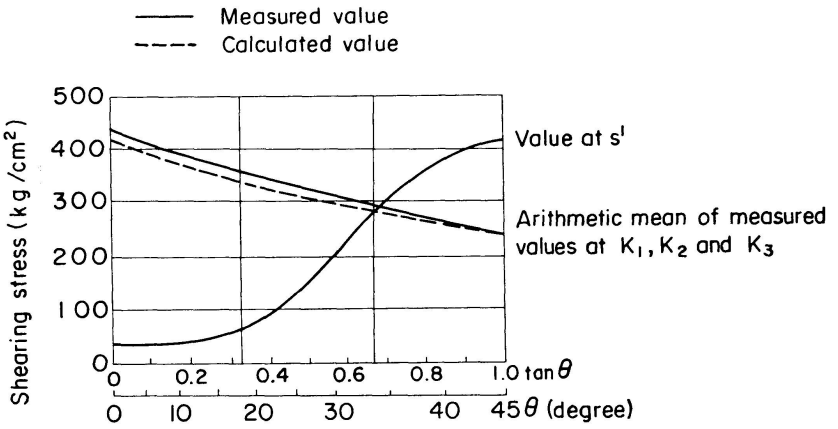


Fig. 13.

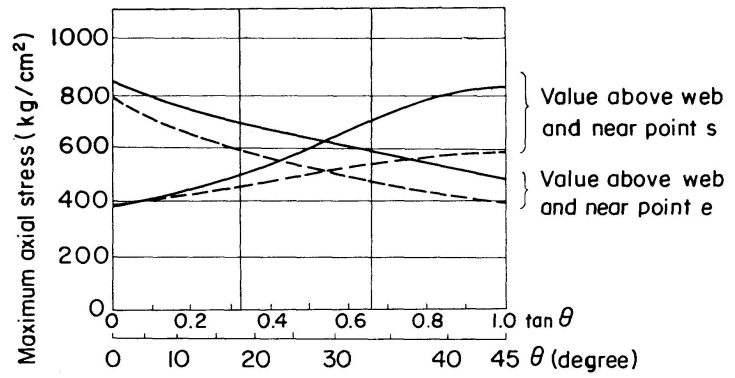


Fig. 14.

According to these figures, shearing stress in the knee joint decreases and shearing stress in the part in which the starting point of the haunch lies increases with an increase in haunch angle. The calculated values of shearing stress in the knee joint come nearly in coincidence with the measured values. With an increase in haunch angle, the maximum axial stress in the flanges increases in the section in which the starting point of the haunch lies but decreases in the section in which the end point of the haunch lies. The calculated values of the maximum axial stress in the flanges are a little smaller than the measured values, while they show practically the same tendency with regard to variation with a change in haunch angle. As the specimens used in this experiment are devised to show a difference caused by the presence of a diaphragm in the section C, the diaphragm is designed to be removably attached to the section C with bolts. Judging from the fact that sizable deformation was found in the section C even when a diaphragm was attached to the section in this experiment, the large measured values in the section where the starting point

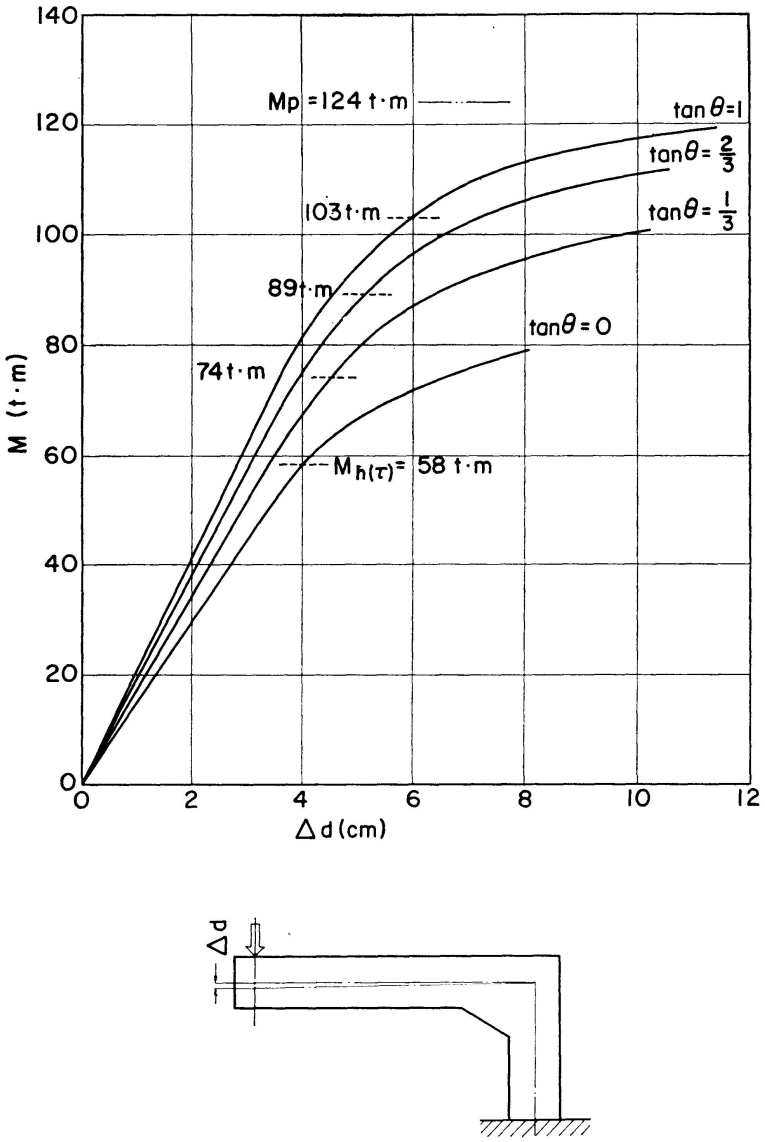


Fig. 15.

of the haunch with large haunch angel lies may be attributed mainly to how fightly the diaphragm is bolted.

An $M-\Delta d$ curve is shown in Fig. 15. According to this figure, these initial yields arise, for the most part, at $M_{h(\tau)}$, indicating that careful attention must be paid to the thickness of webs at this point in a knee joint as in the case of the straight rectangular type. A fairly large value of $M_{h(\tau)}$ can be expected by enlarging the haunch angle. The local shearing stress at the starting point of the haunch has a less effect on $M_{h(\tau)}$ and Δd than the shearing stress in the whole knee joint.

The application of this theory to straight flanges at an arc knee joint will be described hereinafter. (The calculation of stress in circular arc flanges at circular arc knee joints will be described in Chapter 3.)

Assuming that flange force is uniformly distributed in the arc part, the

distributed load F_i/R_i acts in the normal direction of the flange as shown in Fig. 16 (b). Let the rigid frame be substituted by a beam, and the force down $F_i \Delta\theta \sin\theta$ will act on Δx as shown in Fig. 16 (a), placing the beam under the distributed load $\frac{F_i \Delta\theta \sin\theta}{\Delta x} = \frac{F_i}{R_i}$ within $d \leqq x \leqq d + R_i$.

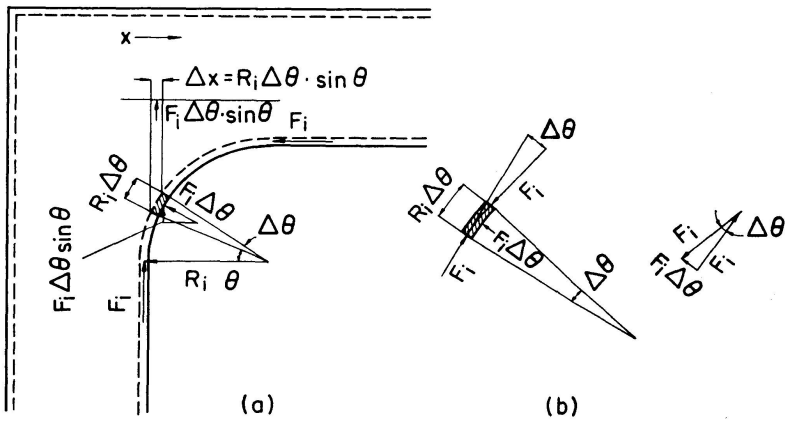


Fig. 16.

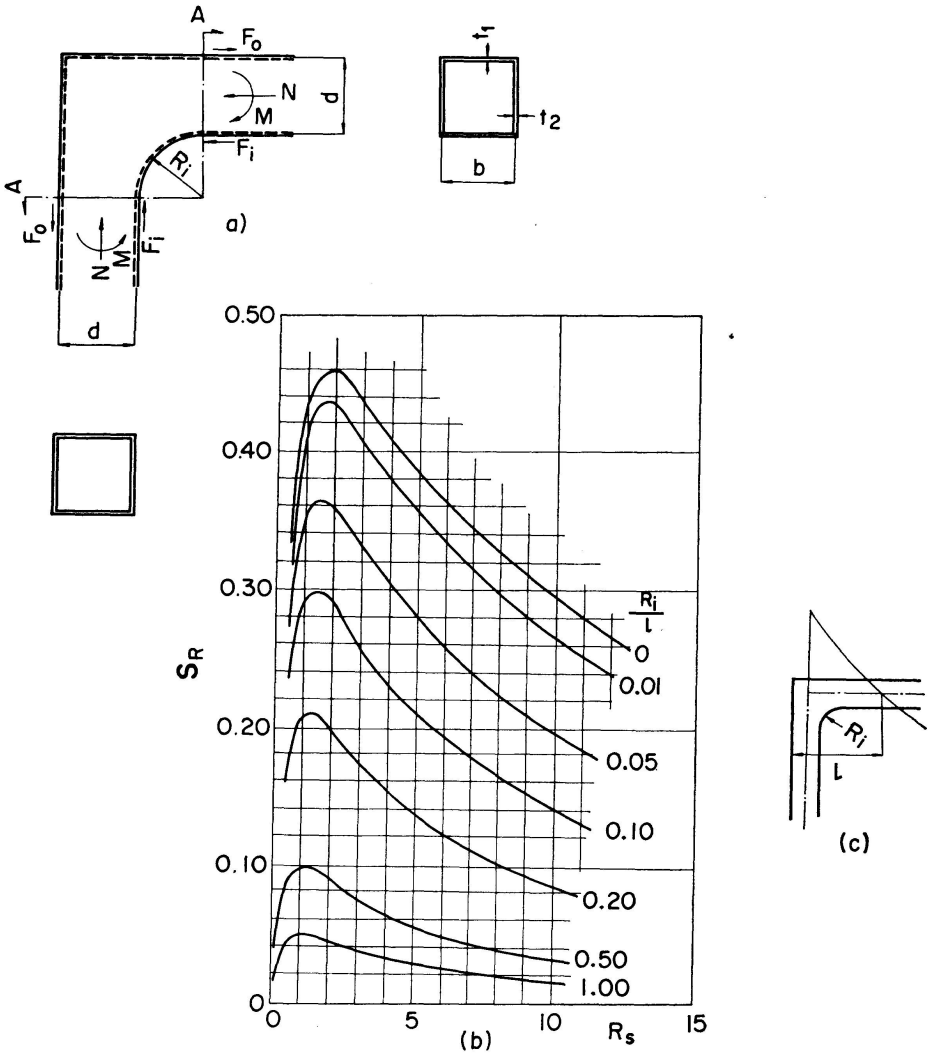


Fig. 17.

Expanding the moment acting on the beam into Fourier series

$$M = \frac{4l^2}{\pi^3}\frac{F_i}{R_i}\sum_{n=1}^{\infty}\frac{1}{n^3}\sin\left\{\zeta_n\left(d+\frac{R_i}{2}\right)\right\}\sin\frac{\zeta_n R_i}{2}\sin(\zeta_n x), \tag{32}$$

where

$$\zeta_n = \frac{n\pi}{l}. \tag{33}$$

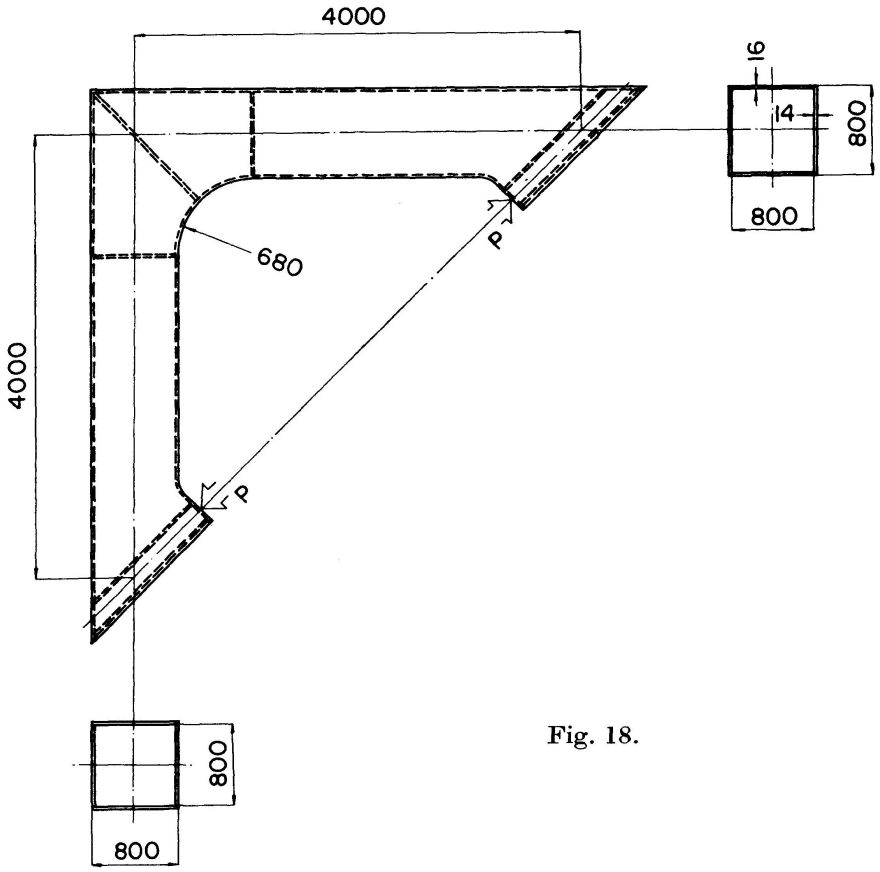


Fig. 18.

Let us find out the stress due to shear lag according to the method described in Section 1—2. When the distributed load F_i/R_i is applied in the middle of the span of a simple beam over the length of R_i, the bending moment in the middle of the span can be written in the form

$$M = \frac{2F_i l}{\pi^2}\sum_{n=1}^{\infty}\frac{1}{n^2}\frac{\sin\frac{n\pi R_i}{2l}}{\frac{n\pi R_i}{2l}}, \quad (n = 1, 3, 5, \ldots), \tag{34}$$

$$\left(\frac{1}{S_n}-\frac{1}{S}\right) = \frac{3}{A_w d'}\frac{R_S}{1+R_S}\frac{1-\frac{b'_n}{b'}}{1+\frac{b'_n}{b'}R_S},$$

$$\sigma_S = M\left(\frac{1}{S_n}-\frac{1}{S}\right) = \frac{F_i b'}{A_w d'}\sum_{n=1}^{\infty}\frac{6}{\pi^2}\frac{l}{b'}\frac{R_S}{1+R_S}\frac{1-\frac{b'_n}{b'}}{1+\frac{b'_n}{b'}R_S}\frac{1}{n^2}\frac{\sin\frac{n\pi R_i}{2l}}{\frac{n\pi R_i}{2l}} = \frac{b}{d}\frac{F_i}{A_w}S_R, \tag{35}$$

where $$S_R = \sum_{n=1}^{\infty} \frac{6}{\pi^2} \frac{l}{b'} \frac{R_S}{1+R_S} \frac{1-\frac{b'_n}{b'}}{1+\frac{b'_n}{b'}R_S} \frac{1}{n^2} \frac{\sin\frac{n\pi R_i}{2l}}{\frac{n\pi R_i}{2l}}, \quad (n = 1, 3, 5, \ldots). \quad (36)$$

Therefore, the estimated diagram shown in Fig. 17 (b) can be obtained for shear lag in the straight flange at the arc knee joint. In this diagram, the curve for $R_i/l = 0$ is identical with the one shown in Fig. 4. The result of measurement of the straight flange of this type used in the experiment is shown in Fig. 19. The calculated values are fairly close to the measured values.

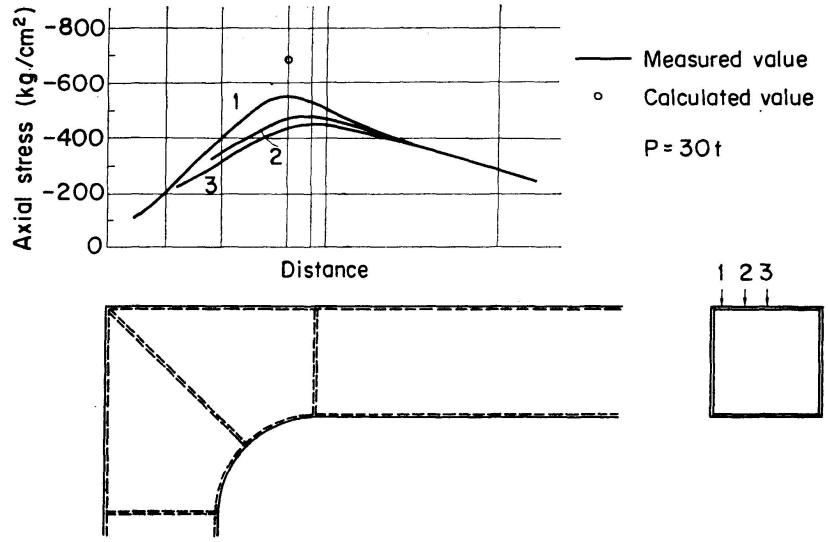


Fig. 19.

2. Knee Joint in Which a Cylinder is Used as a Column

The type in which a cylinder is used as a column has been adopted in various places. The use of a cylinder as a column is attributed to its fine appearance, its excellence in local buckling and torsional resistance featuring the cylindrical construction and its section characteristics free from directionality.

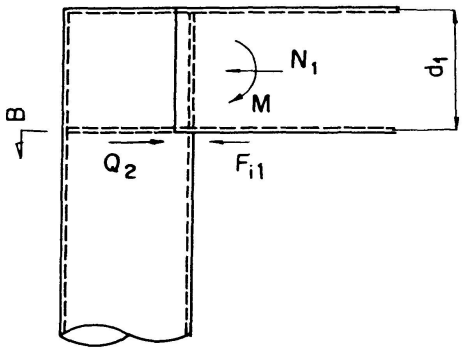


Fig. 20.

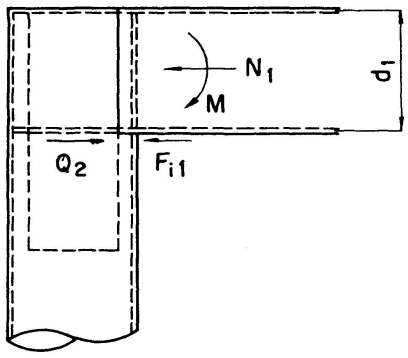


Fig. 21.

This type of knee joint has two varieties, one having the beam web butted to the cylinder and the other having the beam web interlocked with the cylinder (Fig. 20 and 21). Although the one having the beam web interlocked with the cylinder is complicated and hard to manufacture, the cylinder at the knee joint can be reduced in thickness to some extent because the thickness of the interlocked web can be taken into consideration in calculating shearing stress at the knee joint.

Shear lag must be taken into consideration in calculating the bending stress of the beam as in the case of the straight type, while the circumferential stress at the point on which beam flange force acts and the stress of a diaphragm must be taken into account in calculating the stress of the column.

Shearing Stress of Cylinder

The case in which the web of a beam is simply butted to the side of a cylindrical column:

Shearing stress at the knee joint can be written by referring to Fig. 22 in the form

$$\tau_1 = \frac{F_{i1}-Q_2}{\pi R t_p}\sqrt{1-\left(\frac{y}{R}\right)^2}, \qquad \tau_{1max} = \frac{F_{i1}-Q_2}{A_C} \leqq \tau_a, \tag{37}$$

$$\tau_a = 0.5\,\sigma_a, \tag{38}$$

where

$$F_{i1} = \frac{M}{d_1} + \frac{N_1}{2},$$

τ_1 = shearing stress,
τ_a = allowable shearing unit stress,
A_C = sectional area of cylinder.

A diaphragm is provided on the section of the column to which the beam flange is butted.

The case in which the web of a beam is interlocked with a cylinder:

When an opening is provided in the position shown in Fig. 23, the statically determinate shear flow function κ_0 is defined as

$$\begin{aligned} \kappa_0 &= R^2 t_p \sin\varphi, && (\varphi = 0 \sim \alpha), \\ \kappa_0 &= R^2 t_p \sin\varphi + \tfrac{1}{8} d_2^2 t_2, && (\varphi = \alpha \sim (\pi-\alpha)), \\ \kappa_0 &= R^2 t_p \sin\varphi, && (\varphi = (\pi-\alpha) \sim \pi) \end{aligned} \tag{39}$$

in the cylinder, and

$$\kappa_0 = \frac{1}{2} y^2 t_2, \qquad \left(y = 0 \sim \frac{d_2}{2}\right) \tag{40}$$

in the interlocked web.

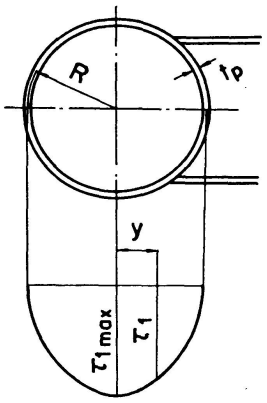


Fig. 22.

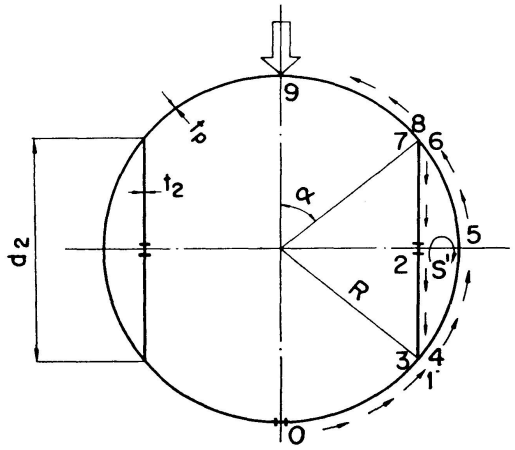


Fig. 23.

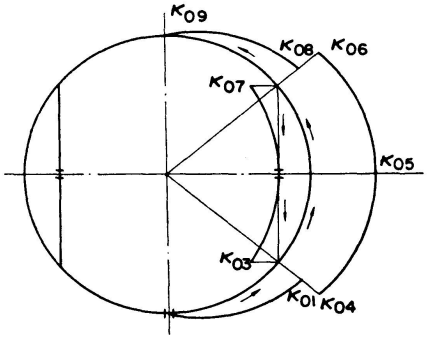


Fig. 24.

The statically indeterminate shear flow function S' attributable to closed section is defined as

$$S' \oint \frac{du}{t} + \oint \frac{\kappa_0 \, du}{t} = 0, \tag{41}$$

$$\begin{aligned} \oint \frac{\kappa_0 \, du}{t} &= \frac{1}{t_p} \int_{\alpha}^{\pi-\alpha} \left(R^2 t_p \sin\varphi + \frac{1}{8} d_2^2 t_2 \right) R \, d\varphi + \frac{2}{t_2} \int_0^{\frac{d_2}{2}} \frac{y^2}{2} t_2 \, dy \\ &= 2 R^3 \cos\alpha + \frac{t_2}{8 t_p} d_2^2 R (\pi - 2\alpha) + \frac{d_2^3}{24}, \end{aligned} \tag{42}$$

$$\oint \frac{du}{t} = \frac{R}{t_p} (\pi - 2\alpha) + \frac{d_2}{t_2}. \tag{43}$$

From Eqs. (41), (42) and (43)

$$S' = - R^2 t_2 \cos\alpha \, \frac{(2 + \frac{1}{3}\cos^2\alpha) t_p + \frac{1}{2}(\pi - 2\alpha) t_2 \cos\alpha}{(\pi - 2\alpha) t_2 + 2 t_p \cos\alpha} \tag{44}$$

at $\varphi = \alpha \sim (\pi - \alpha)$.

The shear flow function is given in the form

$$\kappa = \kappa_0 + S'. \tag{45}$$

The shearing stress in the knee joint can be written by referring to Fig. 25 in the form

$$\tau_1 = \frac{F_{i1}-Q_2}{I_x t_p}\kappa, \qquad \tau_2 = \frac{F_{i1}-Q_2}{I_x t_2}\kappa, \tag{46}$$

where I_x: geometrical moment of inertia with respect to the x-axis of the cylinder having the interlocked web,

τ_1: shearing stress of the cylinder,

τ_2: shearing stress of the interlocked web.

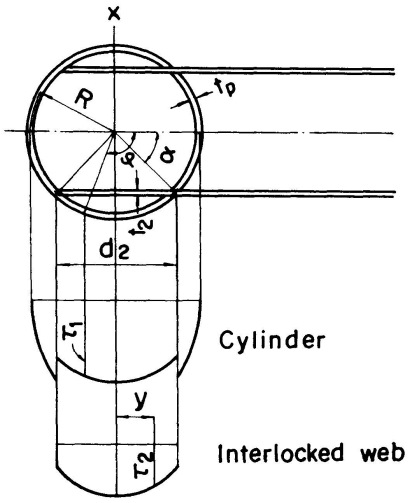


Fig. 25.

The shearing stress of the cylinder reaches its maximum value at $\varphi=\alpha$ or $\varphi=\pi/2$ as written in the form

$$\begin{aligned} \tau_{max} &= \frac{F_{i1}-Q_2}{I_x} R^2 \sin\alpha, && (\varphi=\alpha), \\ \tau_{max} &= \frac{F_{i1}-Q_2}{I_x t_p}\left(R^2 t_p + \frac{1}{8} d_2^2 t_2 + S'\right), && \left(\varphi=\frac{\pi}{2}\right). \end{aligned} \tag{47}$$

The shearing stress of the interlocking web reaches its maximum value at $\varphi=\pi/2$ as written in the form

$$\tau_{max} = \frac{F_{i1}-Q_2}{I_x t_2} S'. \tag{48}$$

Allowable shearing unit stress has been determined in accordance with the theory of the maximum shearing stress. As the maximum value obtained by measurement is practically the same as that obtained by calculation according to the result of an experiment made with this type as described later, this type differs from the straight rectangular type knee joints in that there is no necessity for estimating the allowable shearing unit stress still lower.

Flange Stress of Beam

The stress of beam flanges is calculated in the same way as described above by supposing a knee joint consisting of a column of box section in which

interlocking depth is regarded as the height of the web and the sum of the thickness of an interlocked web and that of a cylinder is regarded as the thickness of the web. The stress of beam flanges in the type in which the beam is not interlocked with the column can be calculated in the same way as mentioned above.

$$\sigma_{01} = \frac{M_1}{S_b} - \frac{N_1}{A_b}, \qquad \sigma_{i1} = \frac{M_1}{S_b} + \frac{N_1}{A_b}, \qquad \sigma_{S1} = \frac{b}{d_1}\frac{F_{i2}}{A_{w1}} S_{S1},$$

$$\sigma_{m01} = \sigma_{01} + \sigma_{S1}, \qquad \sigma_{mi1} = \sigma_{i1} + \sigma_{S1}.$$

Since the value of F_{i2} increases rapidly with an increase in the value of α by this method of calculation, it may be suggested to substitute the distance between centroids in the circular arc for the interlocking depth as d_2 as shown in Fig. 26 (b).

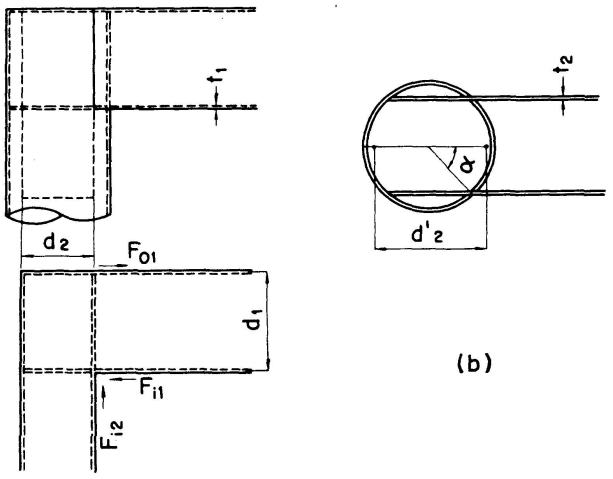


Fig. 26.

However, in the case of $\alpha = 50°$, the value of the maximum stress of the flanges calculated by d_2 is closer to the measured value than that calculated by d_2', the value calculated by d_2' being smaller than the measured value. The practical value of α is found to range from 45° to 55° according to the sectional dimensions of beams and the detailed design of joints. Within this range, the value of F_{i2} will not increase rapidly.

Circumferential Stress of the Cylinder and the Stress of the Diaphragm

The cylindrical column of this type must be examined carefully.

When diaphragms are provided on the section of a cylinder to which beam flanges are butted, it has been confirmed that the measured value of the axial stress of the cylindrical column is close to the calculated value based on the conventional beam theory. It is proposed to prove circumferential stress in the following way in providing the section of a cylinder with diaphragms.

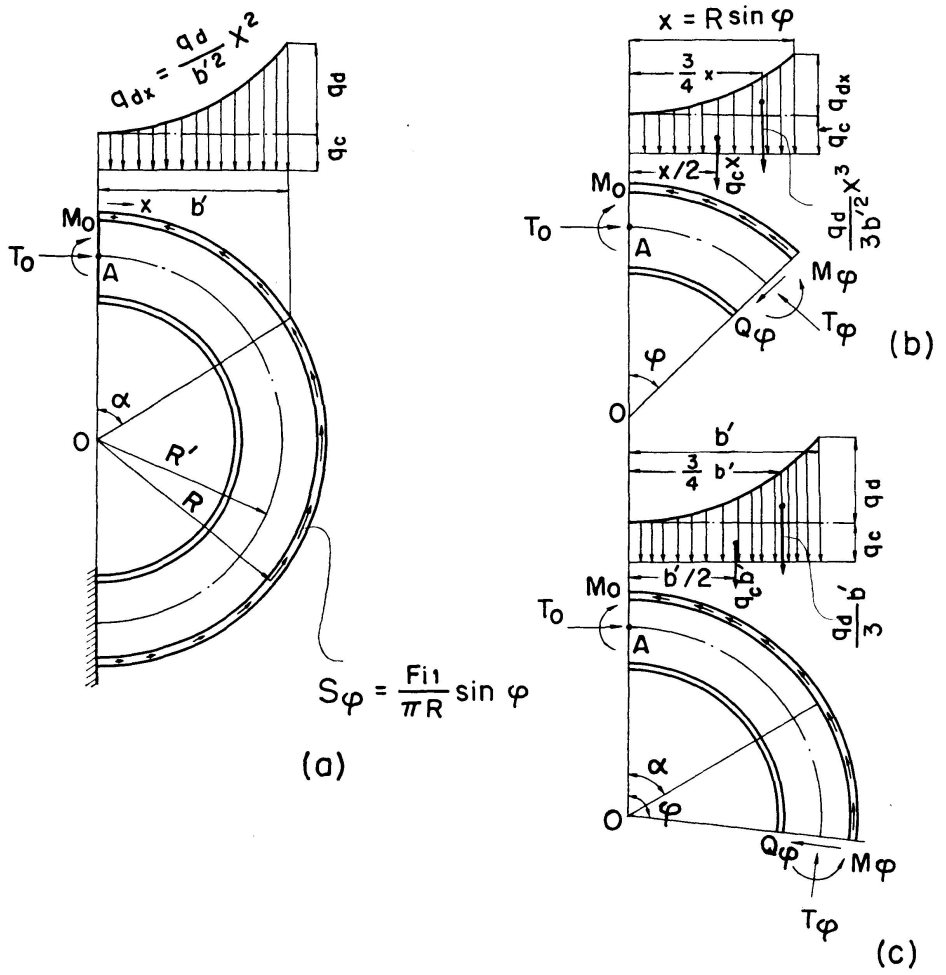


Fig. 27.

The load which is put on a cylindrical column is assumed to be distributed in the form of quadratic parabola over the width of beam flanges as shown in Fig. 27.

$$q = q_C + \frac{q_d}{b'^2} x^2. \tag{49}$$

The resultant force F_{i1} of the load can be written in the form

$$F_{i1} = 2 \int_0^{b'} q \, dx = 2b' \left(q_C + \frac{q_d}{3} \right). \tag{50}$$

It is assumed that F_{i1} is balanced by the shear flow S_φ in the section of the cylinder.

$$S_\varphi = \frac{F_{i1}}{\pi R} \sin\varphi, \tag{51}$$

where R is the radius of the cylinder extending to the center line of the thickness of its wall.

Let T_0 and M_0 be statically indeterminate axial force and bending moment as shown in Fig. 27. We obtain,

when $0 \leqq \varphi \leqq \alpha$

$$T_\varphi = T_0 \cos\varphi - \frac{F_{i1}}{2\pi}\varphi \sin\varphi + q_C R \sin^2\varphi + \frac{q_d}{3b'^2} R^3 \sin\varphi, \tag{52}$$

$$\begin{aligned} M_\varphi = {} & M_0 + T_0 R'(1-\cos\varphi) - \frac{F_{i1} R}{\pi}\left(1-\cos\varphi - \frac{R'}{2R}\varphi\sin\varphi\right) \\ & - R\left(R' - \frac{R}{2}\right) q_C \sin^2\varphi - \frac{q_d}{3b'^2} R^3 \left(R' - \frac{3}{4}R\right)\sin^4\varphi, \end{aligned} \tag{53}$$

$$Q_\varphi = T_0 \sin\varphi - \frac{F_{i1}}{2\pi}(\sin\varphi - \varphi\cos\varphi) - q_C R \sin\varphi\cos\varphi - \frac{q_d}{3b'^2} R^3 \sin^3\varphi\cos\varphi, \tag{54}$$

when $\alpha \leqq \varphi \leqq \pi$

$$T_\varphi = T_0 \cos\varphi - \frac{F_{i1}}{2\pi}\varphi\sin\varphi + \frac{F_{i1}}{2}\sin\varphi, \tag{55}$$

$$\begin{aligned} M_\varphi = {} & M_0 + T_0 R'(1-\cos\varphi) - \frac{F_{i1} R}{\pi}\left(1-\cos\varphi - \frac{R'}{2R}\varphi\sin\varphi\right) \\ & - q_C b'\left(R'\sin\varphi - \frac{b'}{2}\right) - \frac{q_d}{3} b'\left(R'\sin\varphi - \frac{3}{4}b'\right) \\ = {} & M_0 + T_0 R'(1-\cos\varphi) - \frac{F_{i1} R}{\pi}\left(1-\cos\varphi - \frac{R'}{2R}\sin\varphi\right) \\ & - \frac{F_{i1} R'}{2}\sin\varphi + \frac{b'^2}{4}(2q_C + q_d), \end{aligned} \tag{56}$$

$$Q_\varphi = T_0 \sin\varphi - \frac{F_{i1}}{2\pi}(\sin\varphi - \varphi\cos\varphi) - \frac{F_{i1}}{2}\cos\varphi. \tag{57}$$

Rewriting T_φ, M_φ and Q_φ in terms of $k = F_C{}^*)/F_{i1}$ and $\lambda = R/R'$,

when $0 \leqq \varphi \leqq \alpha$

$$T_\varphi = T_0 \cos\varphi - \frac{F_{i1}}{2}\left(\frac{\varphi}{\pi}\sin\varphi - \frac{k}{\sin\alpha}\sin^2\varphi - \frac{1-k}{\sin^3\alpha}\sin^4\varphi\right), \tag{58}$$

$$\begin{aligned} M_\varphi = {} & M_0 + R'\left[T_0(1-\cos\varphi) - \frac{F_{i1}}{2}\left\{\frac{2\lambda}{\pi}(1-\cos\varphi) - \frac{\varphi}{\pi}\sin\varphi\right.\right. \\ & \left.\left. + \frac{k\left(1-\frac{\lambda}{2}\right)}{\sin\alpha}\sin^2\varphi + \frac{(1-k)\left(1-\frac{3}{4}\lambda\right)}{\sin^3\alpha}\sin^4\varphi\right\}\right], \end{aligned} \tag{59}$$

$$Q_\varphi = T_0 \sin\varphi - \frac{F_{i1}}{2}\left\{\frac{1}{\pi}(\sin\varphi - \varphi\cos\varphi) + \frac{k}{\sin\alpha}\sin\varphi\cos\varphi + \frac{1-k}{\sin^3\alpha}\sin^3\varphi\cos\varphi\right\}, \tag{60}$$

---

*) $F_C = 2 q_C b'$ and $k = \dfrac{q_C}{q_C + \frac{q_d}{3}} = \dfrac{\sigma_{i1} - \frac{1}{2}\sigma_{S1}}{\sigma_{i1}} = \dfrac{2\sigma_{i1} - \sigma_{S1}}{2\sigma_{i1}}$ in Fig. 27 (a) and 28 (a).

when $\alpha \leqq \varphi \leqq \pi$

$$T_\varphi = T_0 \cos\varphi - \frac{F_{i1}}{2}\left(\frac{\varphi}{\pi} - 1\right)\sin\varphi, \tag{61}$$

$$M_\varphi = M_0 + R'\left[T_0(1-\cos\varphi) - \frac{F_{i1}}{2}\left\{\frac{2\lambda}{\pi}(1-\cos\varphi) - \frac{\varphi}{\pi}\sin\varphi + \sin\varphi - \frac{\lambda(3-k)}{4}\sin\alpha\right\}\right], \tag{62}$$

$$Q_\varphi = T_0 \sin\varphi - \frac{F_{i1}}{2}\left\{\frac{1}{\pi}(\sin\varphi - \varphi\cos\varphi) + \cos\varphi\right\}. \tag{63}$$

Assuming that M_φ, T_φ and Q_φ have plus signs in the direction shown in Fig. 27 (b) and (c), the total energy V of the curved beam can be written in the form

$$V = \int_0^\pi \left(\frac{M_\varphi^2}{2EeR'} + \frac{T_\varphi^2}{2A_rE} + \frac{M_\varphi T_\varphi}{A_rER'} + \frac{Q_\varphi^2}{2A_dG}\right) R'\,d\varphi. \tag{64}$$

From Castigliano's theorem in which it is conditioned that the point A will neither rotate nor be displaced in the x-direction

$$\frac{\partial V}{\partial M_0} = 0, \tag{65}$$

$$\frac{\partial V}{\partial T_0} = 0. \tag{66}$$

From Eq. (65)

$$\frac{\partial V}{\partial M_0} = \int_0^\pi \left\{\frac{M_\varphi}{A_rEeR'}\frac{\partial M_\varphi}{\partial M_0} + \frac{T_\varphi}{A_rE}\frac{\partial T_\varphi}{\partial M_0} + \frac{M_\varphi}{A_rER'}\frac{\partial T_\varphi}{\partial M_0} + \frac{T_\varphi}{A_rER'}\frac{\partial M_\varphi}{\partial M_0} + \frac{Q_\varphi}{A_dG}\frac{\partial Q_\varphi}{\partial M_0}\right\} R'\,d\varphi = 0. \tag{67}$$

By inserting $\frac{\partial M_\varphi}{\partial M_0} = 1$, $\frac{\partial T_\varphi}{\partial M_0} = 0$ and $\frac{\partial Q_\varphi}{\partial M_0} = 0$ into Eq. (67), we obtain

$$\frac{\partial V}{\partial M_0} = \int_0^\pi \left\{\frac{M_\varphi}{A_rEeR'} + \frac{T_\varphi}{A_rER'}\right\} R'\,d\varphi = \frac{1}{A_rEe}\left\{\int_0^\pi M_\varphi\,d\varphi + e\int_0^\pi T_\varphi\,d\varphi\right\} = 0. \tag{68}$$

Hence

$$\int_0^\pi M_\varphi\,d\varphi + e\int_0^\pi T_\varphi\,d\varphi = 0. \tag{69}$$

From Eq. (69)

$$\pi M_0 = -\pi R' T_0 + F_{i1}R'\left[\lambda + \left\{\frac{1}{8}\left(1 - \frac{e}{R'}\right)(3-k) + \frac{\lambda}{24}(4-k)\right\}\cos\alpha + \frac{k}{4}\left(1 - \frac{e}{R'} - \frac{\lambda}{2}\right)\frac{\alpha}{\sin\alpha} + \frac{3(1-k)}{16}\left(1 - \frac{e}{R'} - \frac{3}{4}\lambda\right)\frac{\alpha}{\sin^3\alpha} - \frac{3(1-k)}{16}\left(1 - \frac{e}{R'} - \frac{3}{4}\lambda\right)\frac{\cos\alpha}{\sin^2\alpha} - \frac{3-k}{8}\lambda(\pi-\alpha)\sin\alpha\right]. \tag{70}$$

From Eq. (66)

$$\frac{\partial V}{\partial T_0} = \int_0^{\pi} \left\{ \frac{M_\varphi}{A_r E e R'} \frac{\partial M_\varphi}{\partial T_0} + \frac{T_\varphi}{A_r E} \frac{\partial T_\varphi}{\partial T_0} + \frac{M_\varphi}{A_r E R'} \frac{\partial T_\varphi}{\partial T_0} + \frac{T_\varphi}{A_r E R'} \frac{\partial M_\varphi}{\partial T_0} + \frac{Q_\varphi}{A_d G} \frac{\partial Q_\varphi}{\partial T_0} \right\} R' d\varphi = 0. \tag{71}$$

By inserting $\frac{\partial M_\varphi}{\partial T_0} = R'(1-\cos\varphi)$, $\frac{\partial T_\varphi}{\partial T_0} = \cos\varphi$ and $\frac{\partial Q_\varphi}{\partial T_0} = \sin\varphi$ in Eq. (71)

$$\frac{1-\frac{e}{R'}}{A_r E e} \int_0^{\pi} M_\varphi \cos\varphi \, d\varphi - \frac{1}{A_d G} \int_0^{\pi} Q_\varphi \sin\varphi \, d\varphi = 0, \tag{72}$$

When $e \ll R'$, $\frac{R'\left(1-\frac{e}{R'}\right)}{A_r E e} \gg \frac{1}{A_d G}$.

It follows that

$$\int_0^{\pi} M_\varphi \cos\varphi \, d\varphi = 0. \tag{73}$$

From the above-mentioned equations

$$T_0 = \frac{F_{i1}}{\pi}\left\{\lambda - \frac{1}{4} + \frac{1}{30}(9 - 4k - 18\lambda + 8\lambda k)\sin^2\alpha\right\}, \tag{74}$$

$$\begin{aligned} M_0 = \frac{F_{i1} R'}{\pi}\Bigg[& \frac{1}{4} - \frac{1}{30}(9 - 4k - 18\lambda + 8\lambda k)\sin^2\alpha \\ & + \left\{\frac{1}{8}\left(1-\frac{e}{R'}\right)(3-k) + \frac{\lambda}{24}(4-k)\right\}\cos\alpha + \frac{k}{4}\left(1 - \frac{e}{R'} - \frac{\lambda}{2}\right)\frac{\alpha}{\sin\alpha} \\ & + \frac{3(1-k)}{16}\left(1 - \frac{e}{R'} - \frac{3}{4}\lambda\right)\left(\frac{\alpha}{\sin^3\alpha} - \frac{\cos\alpha}{\sin^2\alpha}\right) - \frac{3-k}{8}\lambda(\pi-\alpha)\sin\alpha\Bigg]. \end{aligned} \tag{75}$$

Therefore, the circumferential stress in the section B of the cylinder (Fig. 20) and the stress of the diaphragm can be derived from

$$\sigma_0 = -\frac{T_\varphi}{A_r} - \frac{M_\varphi h_1}{A_r e j}, \tag{76}$$

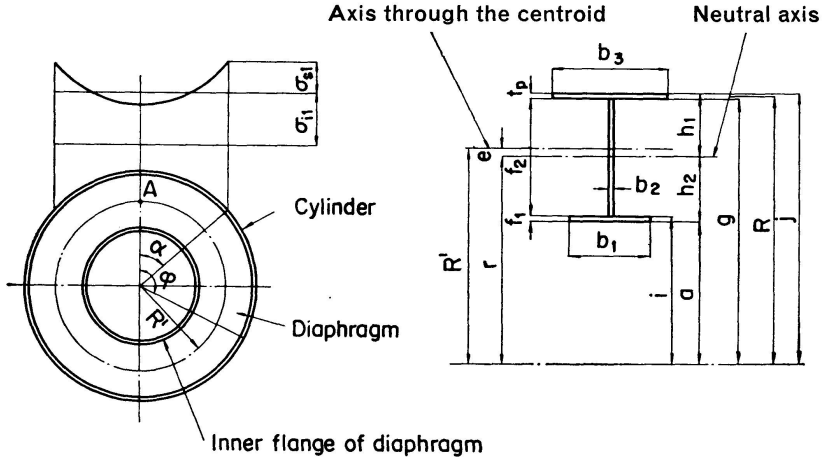
$$\sigma_i = -\frac{T_\varphi}{A_r} + \frac{M_\varphi h_2}{A_r e a}, \tag{77}$$

$$\tau = \frac{Q_\varphi}{A_d}, \tag{78}$$

where σ_0 is the circumferential stress of the cylinder, σ_i is the circumferential stress of the inner flange and τ is the shearing stress of the diaphragm. Generally, σ_i reaches its maximum value in the proximity of $\varphi = \pi/2$ (compression) and $\varphi = \pi$ (tension). When the value of σ_i at $\varphi = \pi/2$ is regarded as its maximum value approximately, T_φ and M_φ can be written in the form

$$T_\varphi = \frac{F_{i1}}{4},$$
$$M_\varphi = M_0 + T_0 R' - F_{i1} R' \left\{ \frac{\lambda}{\pi} + \frac{1}{4} - \frac{\lambda}{8}(3-k)\sin\alpha \right\}. \tag{79}$$

And at $\varphi = \pi$
$$T_\varphi = -T_0,$$
$$M_\varphi = M_0 + 2T_0 R' - F_{i1} R' \left\{ \frac{2\lambda}{\pi} - \frac{\lambda}{8}(3-k)\sin\alpha \right\}. \tag{80}$$



$$A_r = b_1 f_1 + b_2 f_2 + b_3 t_p, \qquad A_d = b_2 f_2, \qquad r = \frac{A_r}{b_1 \log_e \frac{i}{a} + b_2 \log_e \frac{g}{i} + b_3 \log_e \frac{j}{g}}.$$

Fig. 28.

The effective width of the cylinder shown in Fig. 28 (b) is derived from the results of experiments and the reference material [7] in the form

$$b_3 = b_2 + 1.56\sqrt{R t_p}. \tag{81}$$

The following results have been obtained according to the above-mentioned calculations:

1. Relation between α and σ_{mi1}. When the width of a beam or α is changed with the thickness of the web and the flanges of the beam and the height of the web left unchanged in the case of a cylinder with a diameter of 2 meters, σ_{mi1} of the beam flanges is calculated to reach its minimum value in the proximity of $\alpha = 45°$ and shows a large value at $\alpha \leqq 35°$ or $\alpha \geqq 60°$ (Fig. 29 (a)). Similar results are obtained in the case of a cylinder with a diameter of one meter (Fig. 29 (b)).

2. Relations between α and σ_0, σ_i and τ. When the width of a beam or α is changed with k, b_1 and b_2 left unchanged in the case of a cylinder with a diameter of 2 meters, the maximum values of σ_0, σ_i and τ are calculated to decrease with an increase in the value of α. All of them are affected greatly

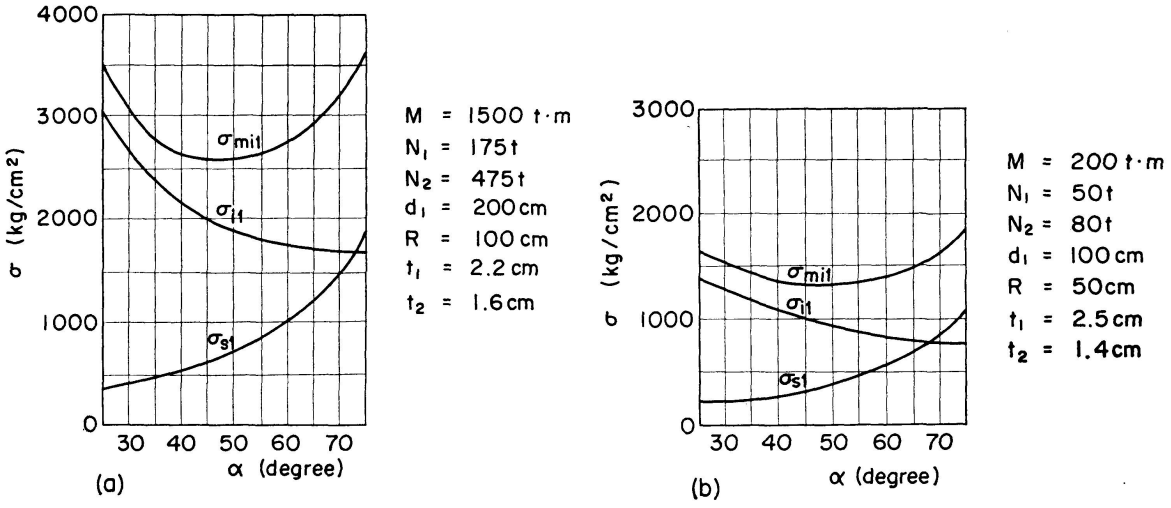


Fig. 29.

by a and decrease with a decrease in the value of a (Fig. 30 (a), (b) and (c)). The maximum value of σ_0 is more liable to be affected by t_p than the others and that of σ_i is affected by f_1 (Fig. 30 (b) and 31).

The position at which σ_i reaches its maximum value varies with α. It reaches its maximum value in the proximity of $\varphi = 76°$ for $\alpha = 45°$ and in the proximity of $\varphi = 84°$ for $\alpha = 75°$ (Fig. 30 (d)). The maximum value is affected by a for $\alpha = 45°$, but it is little affected by a for $\alpha = 75°$. Denoting σ_i at $\varphi = 90°$ by σ_{i90}, $\frac{\sigma_{imax}}{\sigma_{i90}}$ can be expressed against α as shown in Fig. 30 (e).

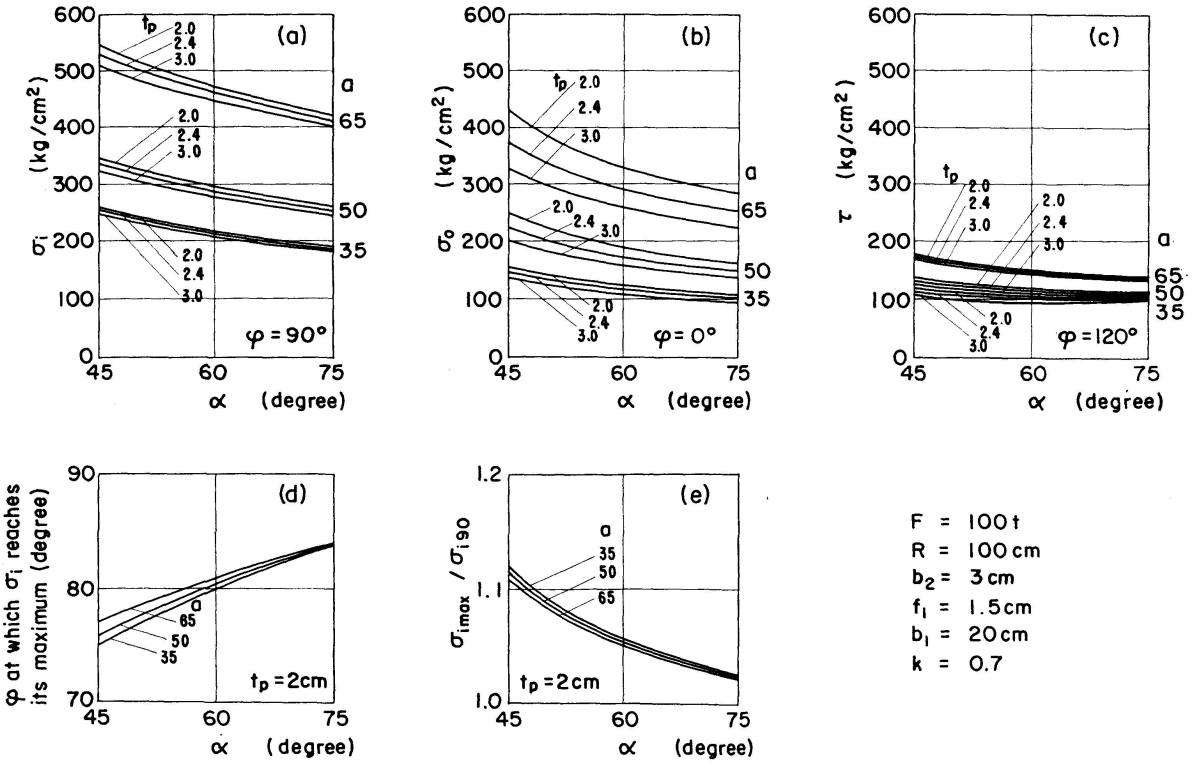


Fig. 30.

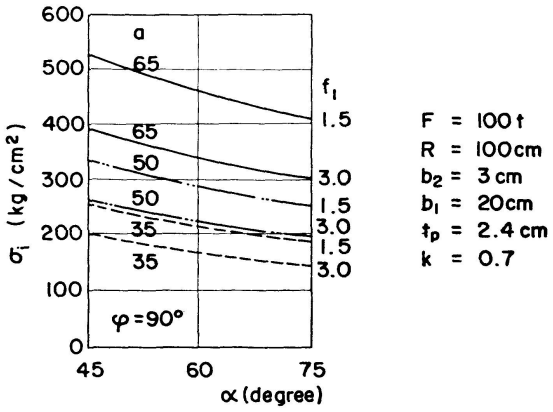


Fig. 31.

3. Relations between k and b_1 and σ_i, σ_0 and τ. σ_i increases with an increase in the value of k. However, the former is not affected greatly by the latter. Both σ_i and σ_0 decrease with an increase in the value of b_1. The effect of b_1 on σ_i is considerably great (Fig. 32).

4. Relations between $b_1 f_1$ and σ_i, σ_0 and τ. According to this method of calculation, the relations between σ_i, σ_0 and τ and $b_1 f_1$ or the area of the manhole

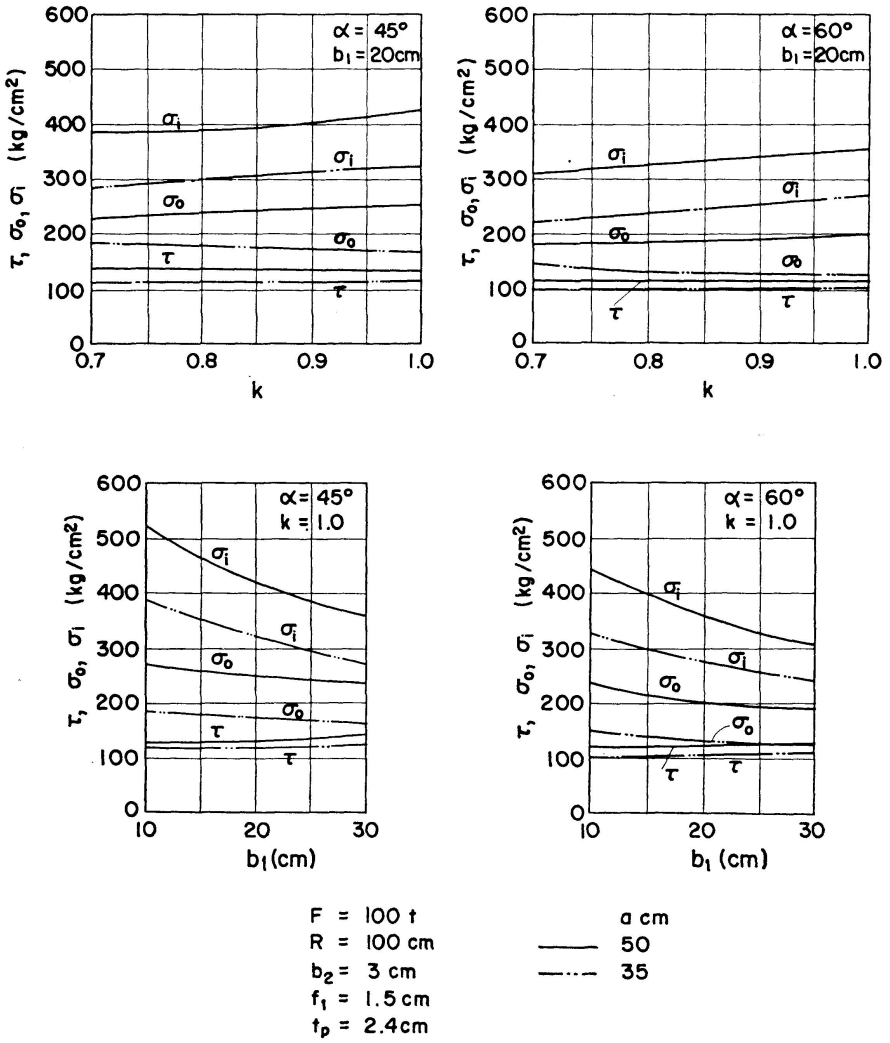


Fig. 32.

flange can be diagrammatically shown with a taken as a parameter when α, R, t_p, k and b_2 are given. An example of the relations is shown in Fig. 33. Practical values of b_1 and f_1 can be determined from such a diagram.

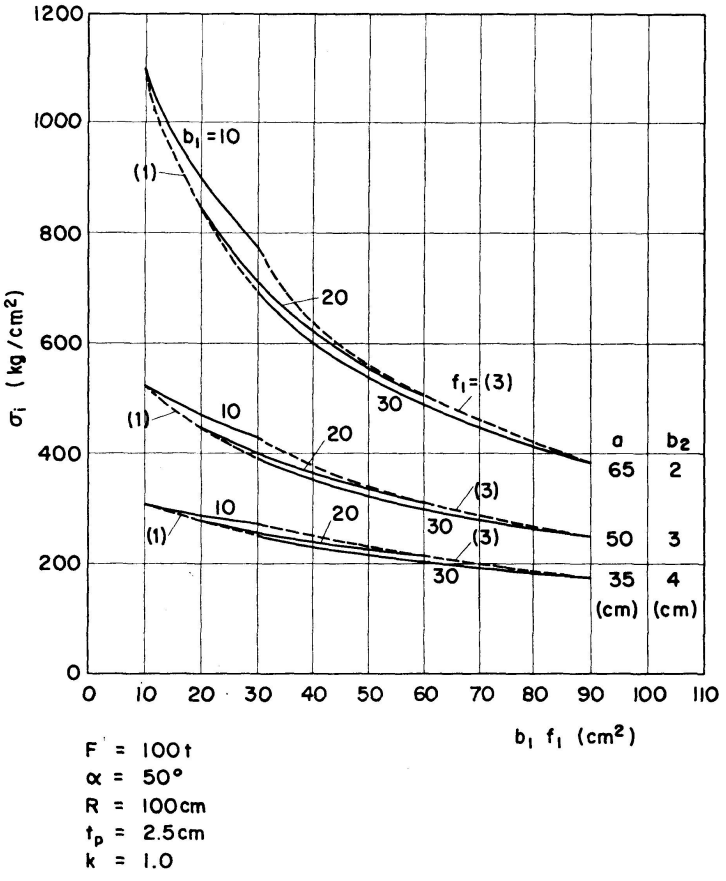


Fig. 33.

Results of Experiments

The results of experiments with this type are shown in Fig. 35 through 41. According to these results, the distribution of shearing stress is found to be disturbed in the proximity of the part at which the cylinder is joined to the beam web. The position of its maximum value lies toward the web side. The maximum value obtained by calculation is fairly close to the maximum value obtained by measurement.

The axial stress of the beam flanges is concentrated in the proximity of the web and the maximum value lies at the points where the cylinder is joined to the flanges in the axial distribution of the stress. The maximum value obtained by calculation is appropriate.

The maximum value of circumferential stress lies at the point C and that in the case of B with no interlocked webs is a little larger than that in the case of A with interlocked webs. The maximum value obtained by calculation is appropriate in the case of B.

The maximum value of the axial stress of the cylinder lies at the point D where the lower flange of the beam is joined to the cylinder. The value cal-

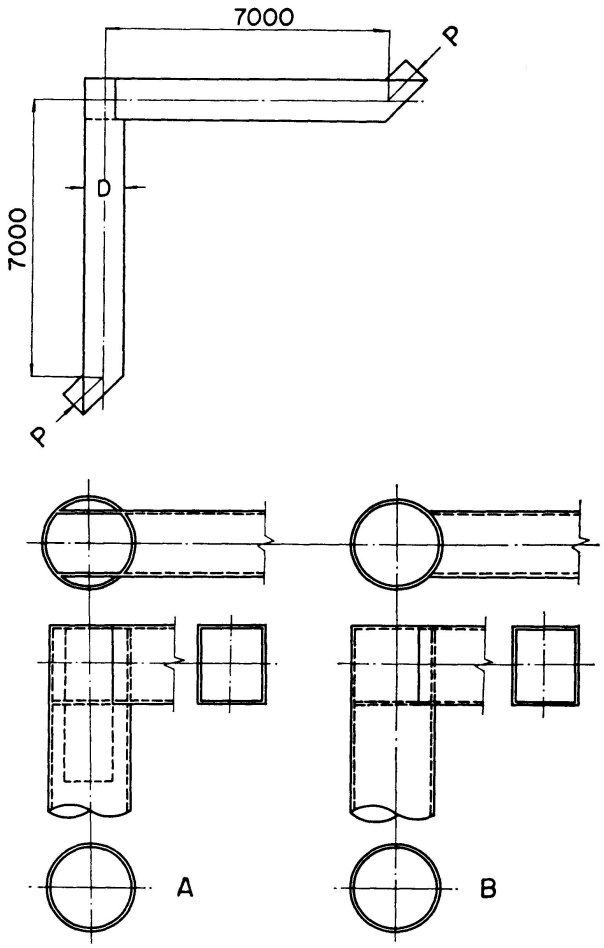
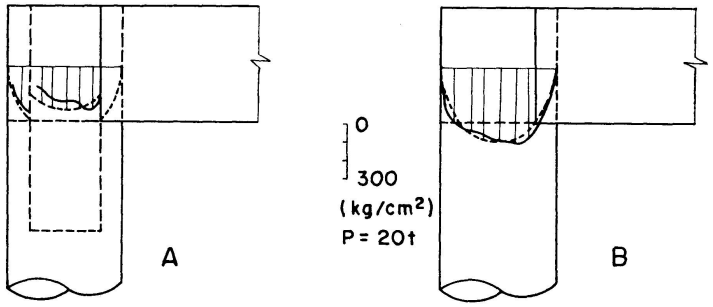


Fig. 34. With interlocked webs A
With no interlocked webs B



Shearing stress
—— Measured value
----- Calculated value

Fig. 35.

culated by the conventional beam theory comes in coincidence with the value measured in the proximity of the point *D*. Local bending occurs in this proximity, causing values measured on the inside and outside of the cylinder wall to differ from each other. The mean of two different values is shown in Fig. 40.

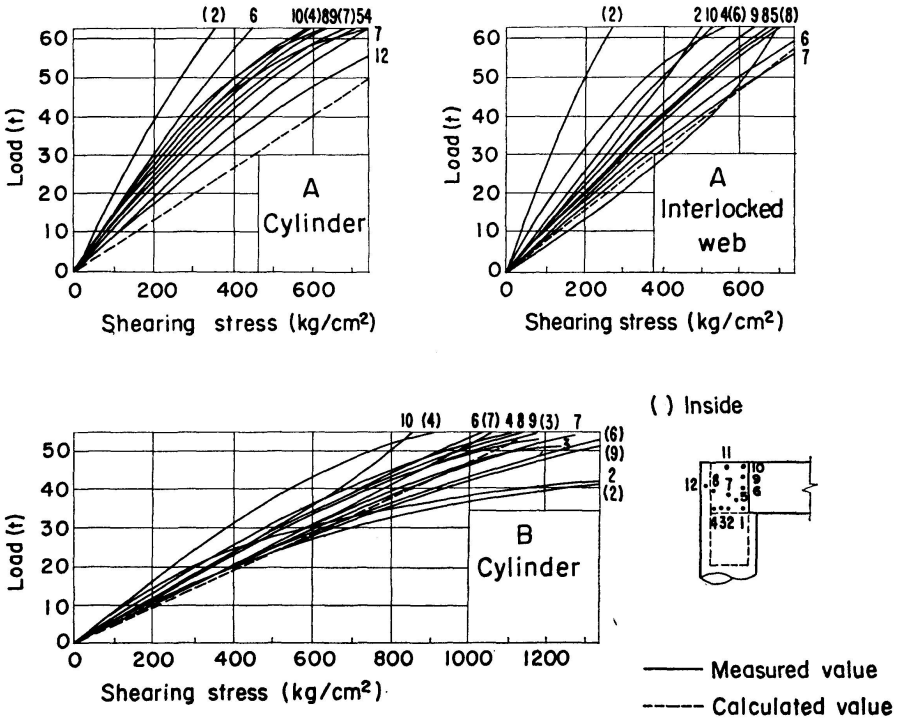


Fig. 36.

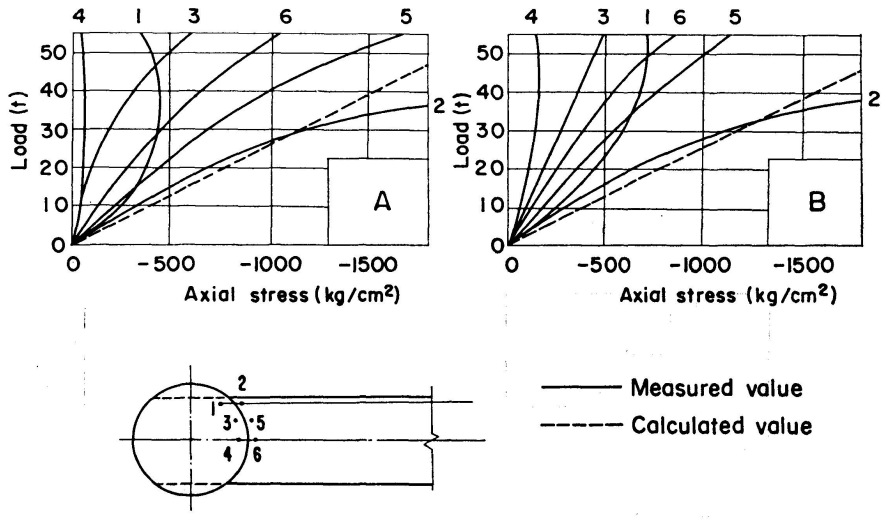


Fig. 37.

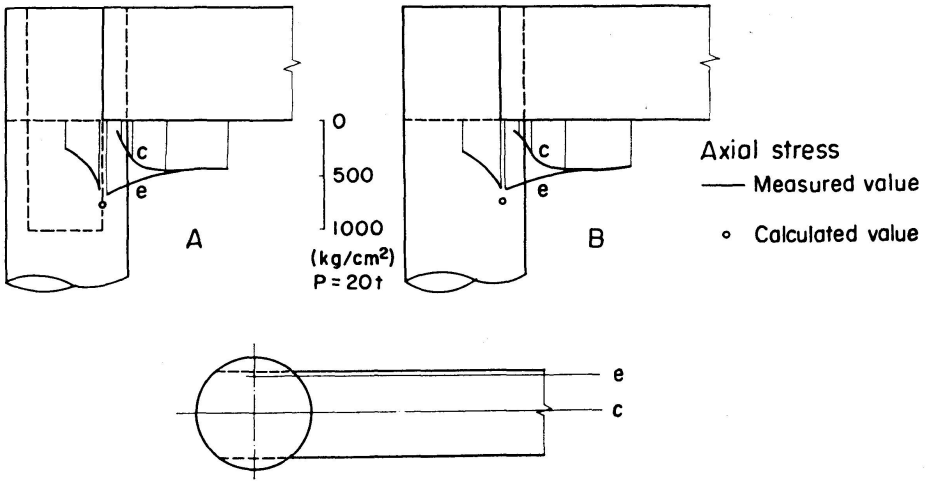
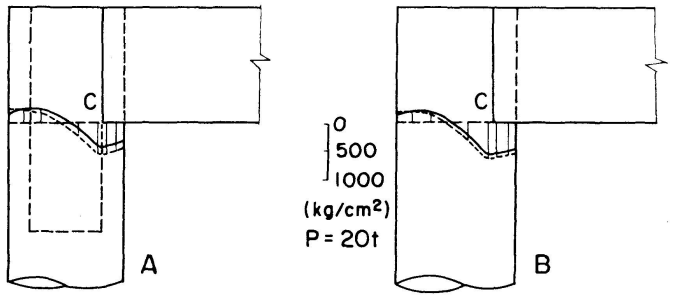


Fig. 38.

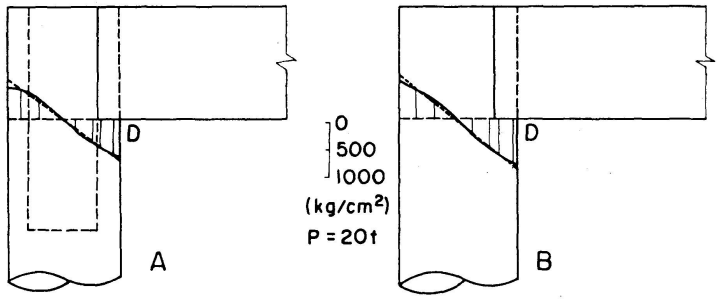


Circumferential stress

—— Measured value

----- Calculated value

Fig. 39.

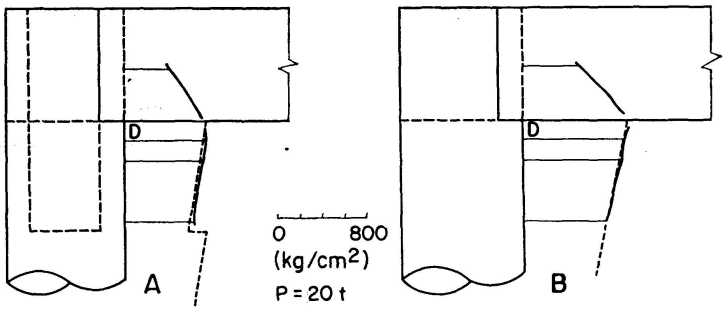


Axial stress

—— Measured value

----- Calculated value

Fig. 40.



Axial stress

—— Measured value

------ Calculated value

Fig. 41.

The dimensions of the diaphragms used with the specimens are shown in Table 1.

An $M-\Delta i$ curve is given in Fig. 42. According to this curve, butting type showed initial yield in the proximity of $M_{h(\tau)}$. The interlocked web has the effect of lowering the shearing stress of the knee joint and raising the value of $M_{h(\tau)}$.

Table 1. Dimensions of the Specimen

Symbol of specimen		A	B
Outside diameter of cylinder	D (cm)	100 (radius to the center of the thickness of the cylinder wall: 49.3)	
Thickness of cylinder	t_p (cm)	1.4	
t_p/R		1/35.7	
Distance between beam flanges	d_1 (cm)	98.1	
Thickness of interlocked web	t_2 (cm)	1.4	—
Distance between beam webs	b (cm)	78.6 (total width: 85.0)	
$b/2R$		0.797	
Thickness of beam flanges	t_1 (cm)	1.9	
t_1/b		1/41.4	
Thickness of diaphragms	b_2 (cm)	1.4	
Radius of manhole a (dimensions of flange f_1, b_1) (cm)		50 (1.2,10)	
Sectional area of beam	A_b (cm²)	592.4	
Sectional area of column	A_c (cm²)	601.5	433.5
A_b/A_c		1/1.015	1/0.732
Modulus of section of beam	S_b (cm³)	19697	
Modulus of section of column	S_c (cm³)	12217	10537
S_b/S_c		1/0.620	1/0.535

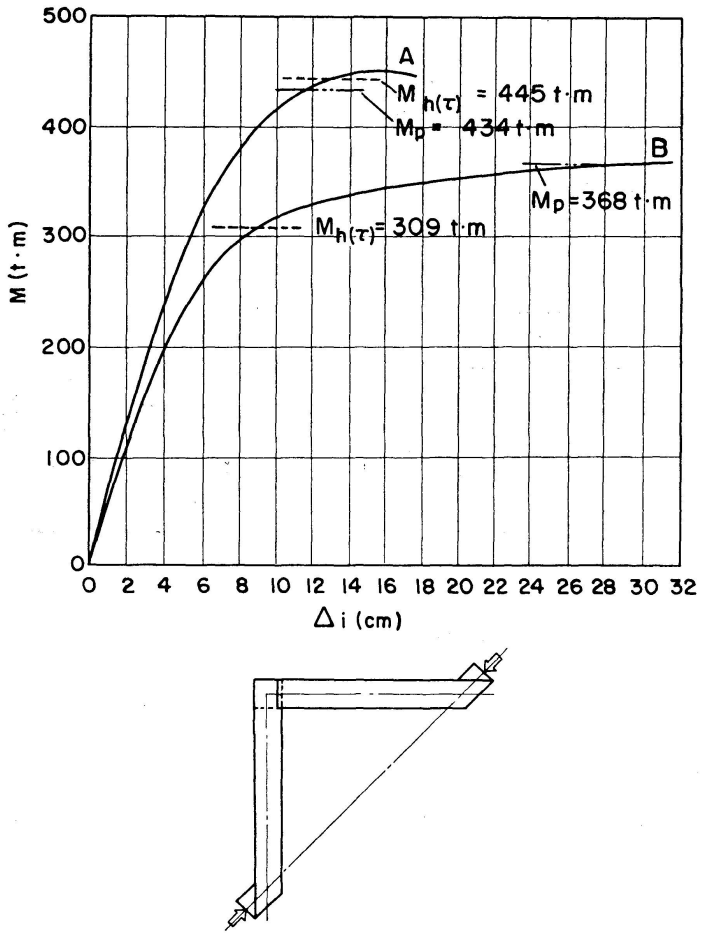


Fig. 42.

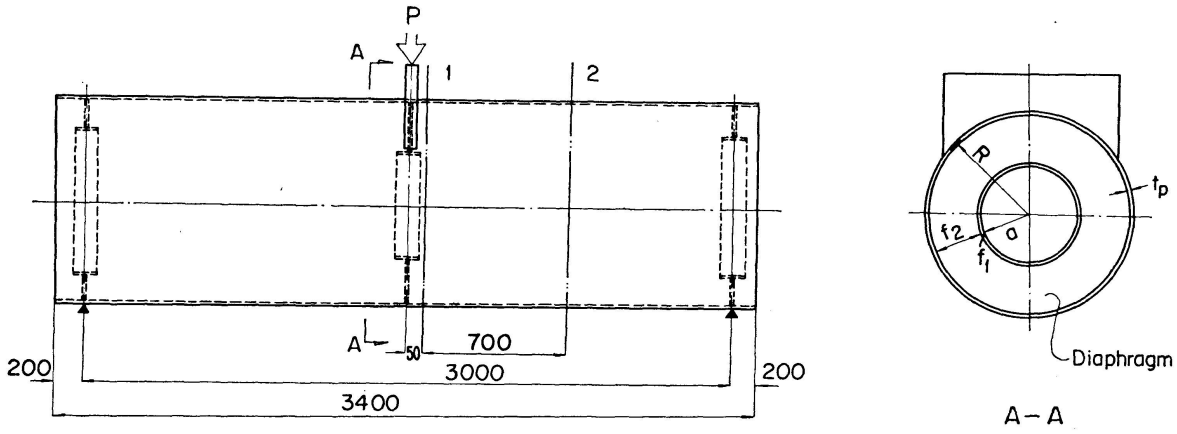


Fig. 43.

Table 2. Dimensions of the Bending Specimen

Symbol of specimen			10–350	14–350	14–500	17–350
	Outside diameter of cylinder	D (cm)	100			
	Thickness of cylinder	t_p (cm)	1.0	1.4		1.7
	t_p/R		1/49.5	1/35.2		1/28.9
	Length of span	l (cm)	300			
	Sectional area	A (cm²)	308.8	433.5		525.0
	Modulus of section	S (cm³)	7513	10537		12686
Diaphragm	Thickness of Web	b_2 (cm)	1.4			
	Radius of Manhole	a (cm)	17.5	17.5	25.0	17.5
	Dimensions of flange	f_1, b_1 (cm)	1.2,10			
	a/R		1/2.83	1/2.82	1/1.97	1/2.81
	b_2/f_2		1/21.6	1/21.3	1/16.0	1/21.1

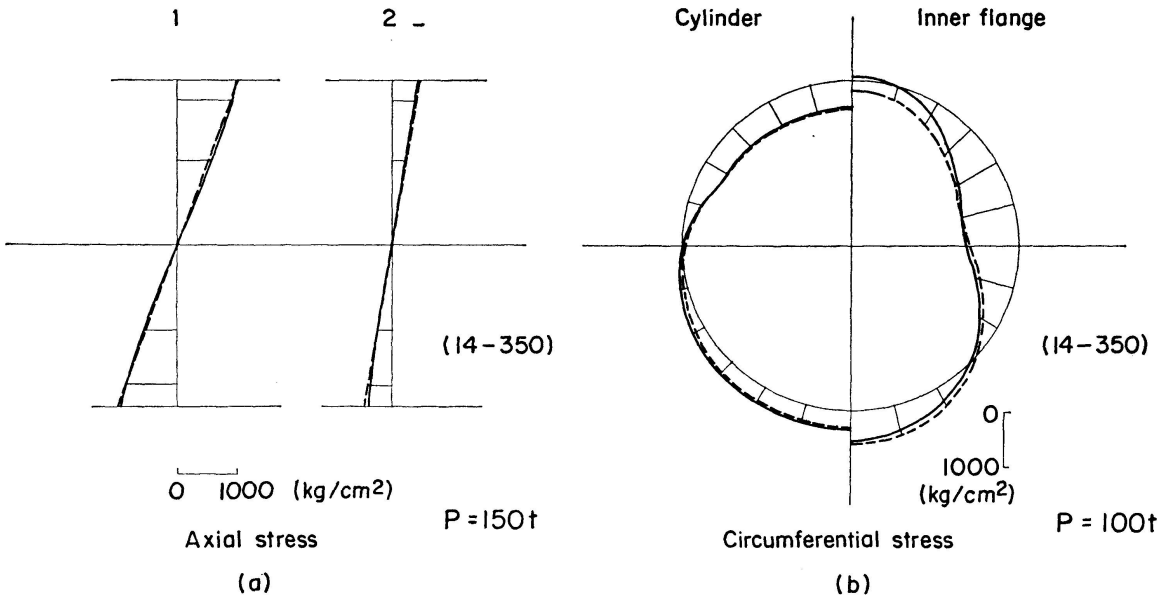


Fig. 44.

The interlocking type is nearly strong enough to satisfy M_p, while the butting type is a little short in strength but has relatively large rotating capacity.

A simplified form of bending test as shown in Fig. 43 was carried out for checking the stress of a cylinder and that of diaphragms.

According to the results of the test, the axial stress of the cylinder is close to the value calculated by the conventional beam theory as shown in Fig. 44 (a), and the circumferential stress of the cylinder and the stress of the diaphragms are nearly in coincidence with the above-mentioned calculated value as shown in Fig. 44 (b). How the diaphragms and the cylinder cooperate with each other was calculated from the axial distribution of the circumferential stress of the cylinder, the result of which is shown against R/t_p in Fig. 45. The value of b_3 calculated from Eq. (81) is fairly close to the measured value in thick-walled cylinders.

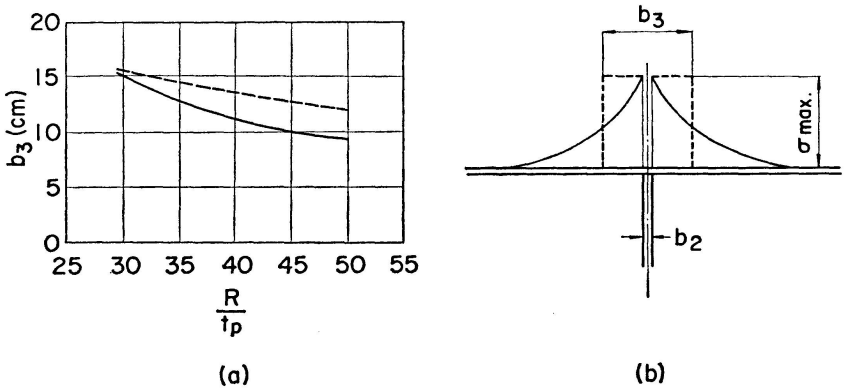


Fig. 45.

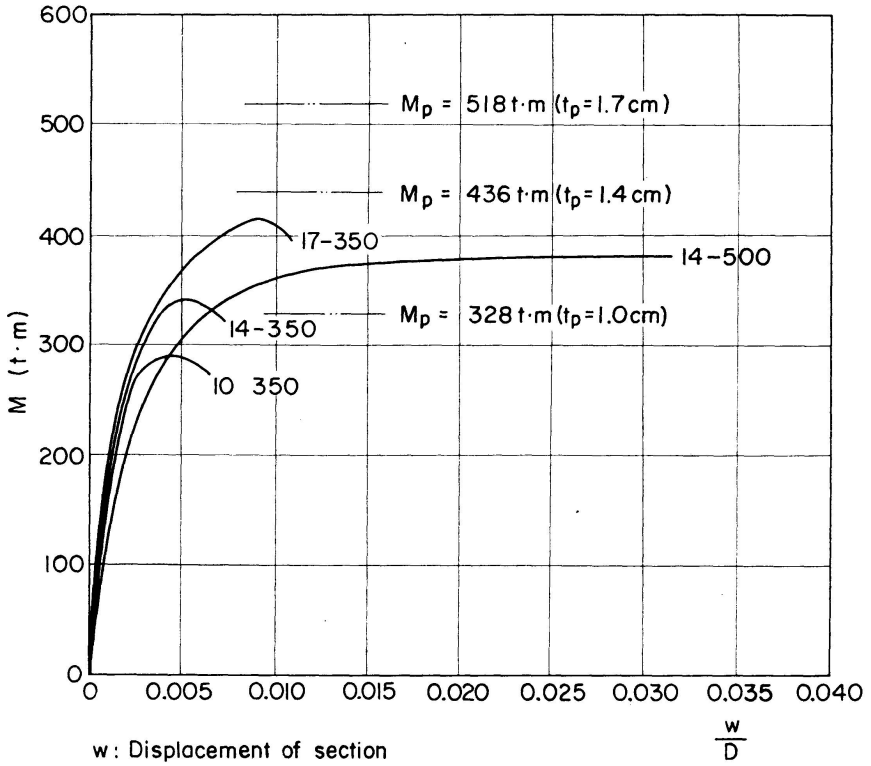
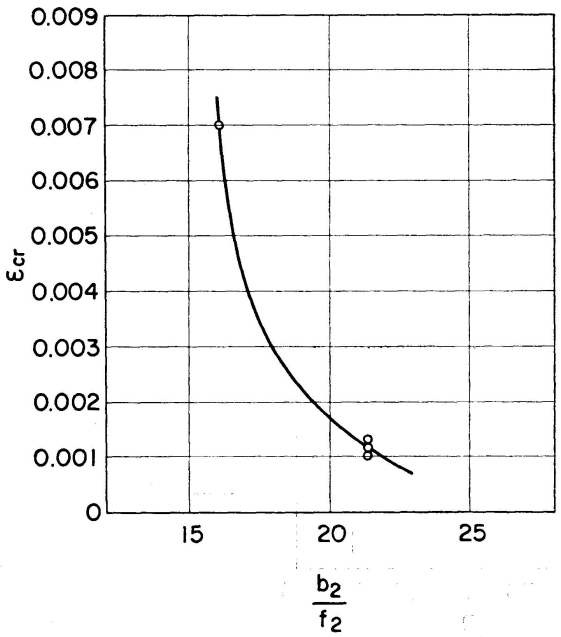


Fig. 46.

Diaphragms with a small value of a buckled in a rupture test, resulting in a premature lowering of yield strength (Fig. 46). It is necessary to pay due regard to the thickness of diaphragms with a small manhole radius. Even if diaphragms are provided with inner flanges, it is recommended that the thick-



ε_{cr} : Limits of buckling strain

o Measured value

Fig. 47 (a).

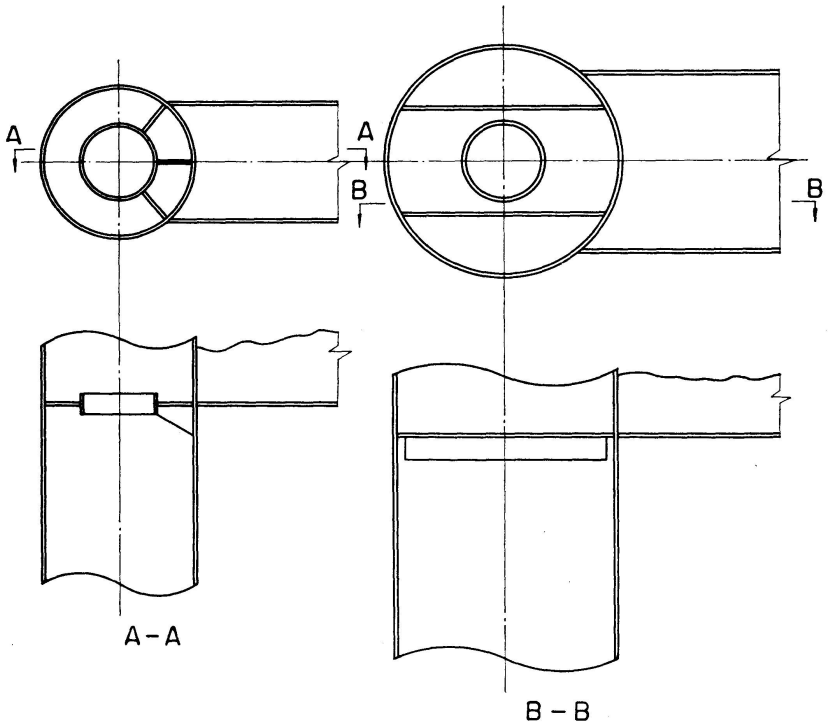


Fig. 47 (b).

ness of diaphragms be determined according to the conventional rule $b_2 \geqq \frac{f_2}{17}$ on the thickness of an intermediate stiffener or a free outstanding leg of a secondary member (Fig. 47 (a)). The stiffener shown in Fig. 47 (b) can be effectively used.

When the width of a beam is larger than the diameter of a cylindrical column, they are joined as shown in Fig. 48. They do not differ basically from the above-mentioned types. Fig. 49 shows a case applicable not only to force acting within the surface of rigid frame construction but to force acting outside its surface. It has been confirmed that, if diaphragms are arranged as shown in this figure and the oblique diaphragms extending from the cylinder to the beam flanges are made as thick as the cylinder wall and those extending in the axial direction of the beam are made as thick as the beam web in this case, it results in an appropriate value of the shearing stress in the knee joint and a fairly small value of the stress due to shear lag in the beam flanges.

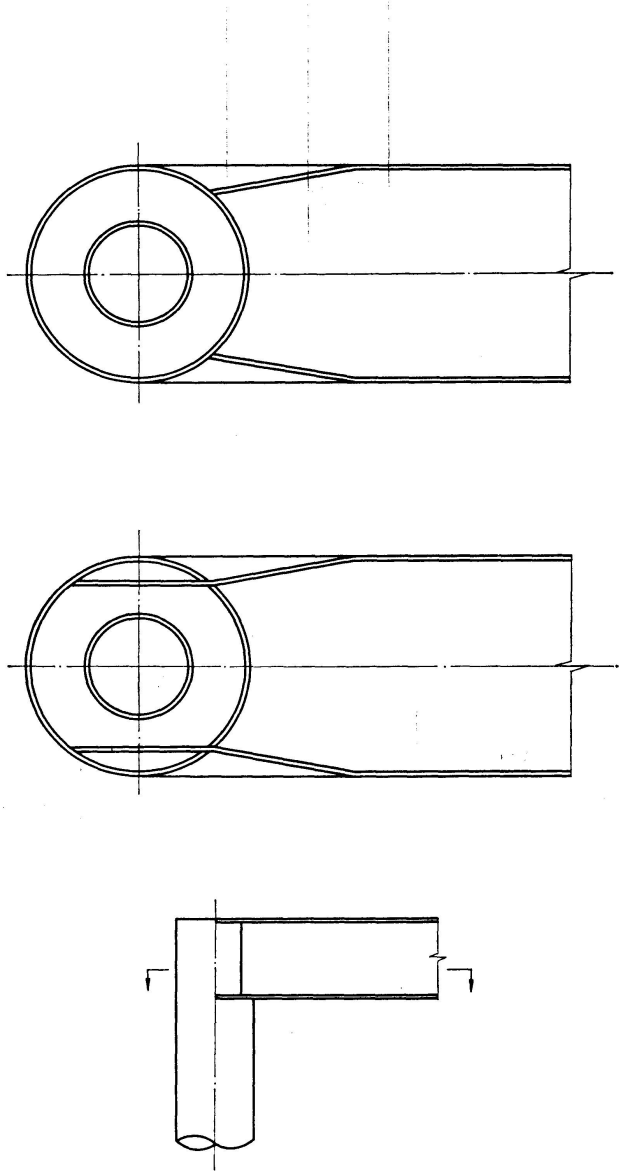


Fig. 48.

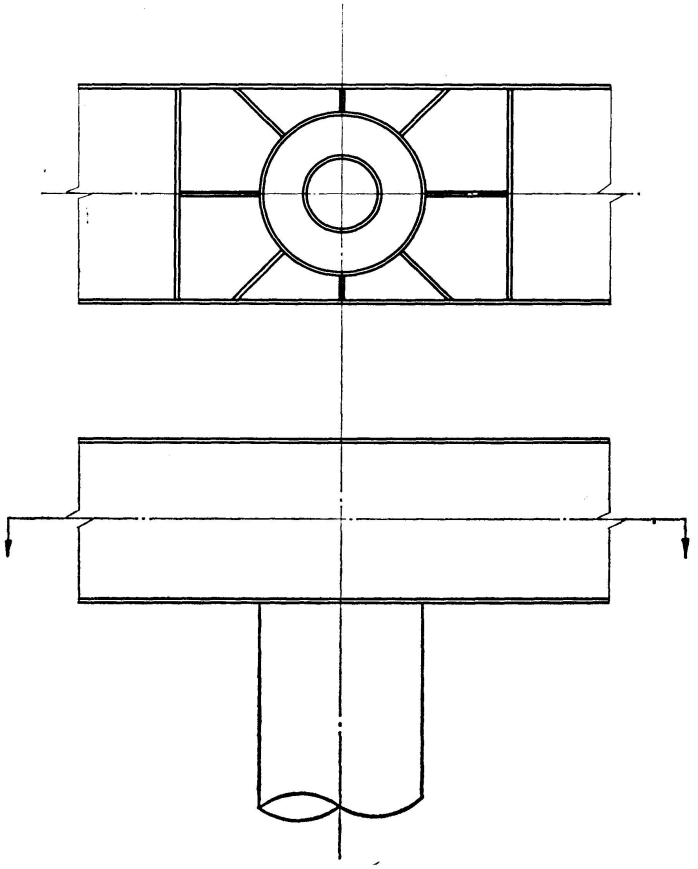


Fig. 49.

3. Circular Arc Knee Joint

When bending moment is applied to the rigid frame knee joint of box section shown in Fig. 50, stress exerted in the acute outer corner is very low. Therefore, the rigid frame knee joint is regarded as a bent tube of box section by assuming that the hatched part does not exist.

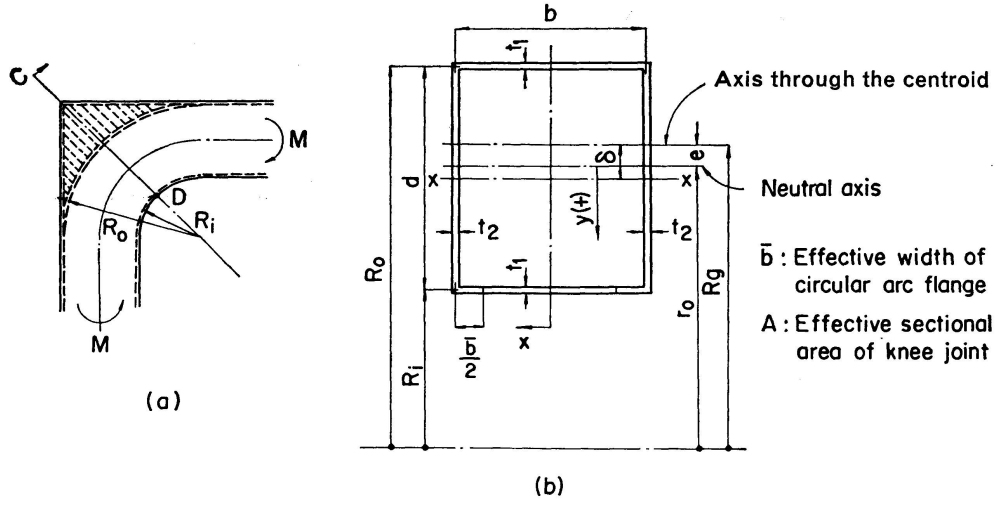


Fig. 50.

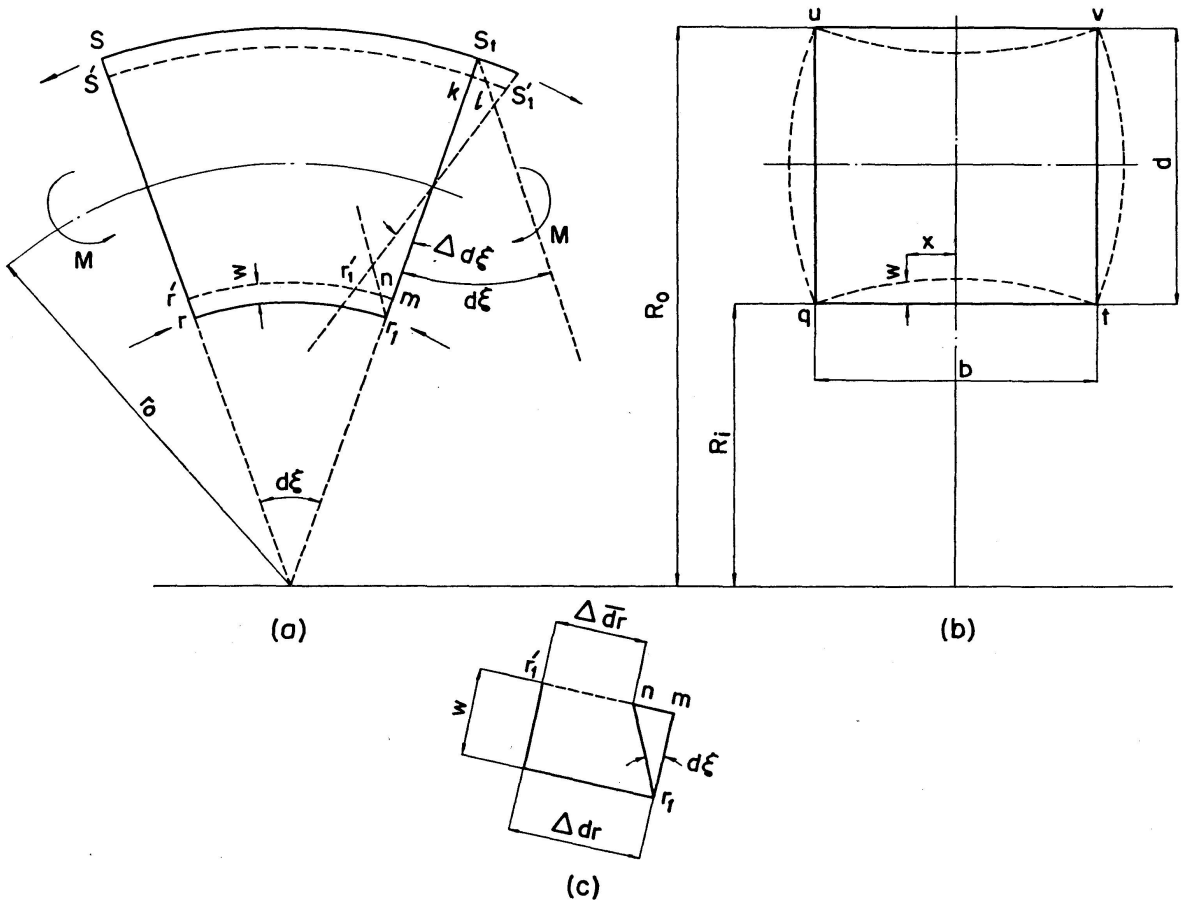


Fig. 51.

In the bent tube shown in Fig. 51, tensile force and compressive force are created in the outer and inner flanges, respectively, by bending moment. They give rise to resultant forces, each directed toward the neutral axis. These resultant forces cause the section to be deformed as shown in Fig. 51 (b). If it is assumed that the section of the bent tube continues to be a plane even after it is bent, the elongation (contraction) of the flange elements $S S_1$ ($r r_1$) at a distance of x from the symmetrical axis y is related not only to the increment $\Delta d\xi$ of the angle $d\xi$, but also to the displacement w in the radial direction of the section.

The strain in the lengthwise direction of the flange element $r r_1$ can be expressed in the form

$$\frac{\Delta \bar{dr}}{dr} = \frac{\Delta dr - w d\xi}{dr}. \tag{82}$$

And

$$\sigma_x = \frac{E}{1-\nu^2}\epsilon = \frac{E}{1-\nu^2}\left(\frac{\Delta dr}{dr} - w\frac{d\xi}{dr}\right) = \sigma_{max} - \frac{E}{1-\nu^2}\frac{w}{R_i}, \tag{83}$$

where σ_{max} is the flange stress right above the web, the value of which is taken at the center of the thickness of the flange.

The differential equation with respect to the displacement w of the flange plate can be written in the form

$$\frac{E t_1^3}{12(1-\nu^2)} \frac{d^4 w}{d x^4} = \sigma_x \frac{t_1}{R_i}. \tag{84}$$

By inserting Eq. (83) in Eq. (84) and putting $\sigma_{max} \frac{t_1}{R_i} = q'$ and $\frac{E}{1-\nu^2} \frac{t_1}{R_i^2} = k'$

$$\frac{E t_1^3}{12(1-\nu^2)} \frac{d^4 w}{d x^4} = q' - k' w. \tag{85}$$

Taking into account the symmetry to the y-axis and putting

$$\beta = \frac{b}{2} \sqrt[4]{\frac{3}{R_i^2 t_1^2}} \tag{86}$$

we obtain the solution in the form

$$w = \frac{q'}{k'} \left(1 - \boldsymbol{C}_1 \sin\frac{2\beta x}{b} \sinh\frac{2\beta x}{b} - \boldsymbol{C}_2 \cos\frac{2\beta x}{b} \cosh\frac{2\beta x}{b}\right). \tag{87}$$

Supposing that the webs uq and vt in a rigid frame having rigid joints u, v, t and q as shown in Fig. 51 (b) are deformed in circular arc form, the radius of curvature ρ of the web plates is expressed in the form

$$\left(\frac{d w}{d x}\right)_{x=\frac{b}{2}} = \frac{\frac{d}{2}}{\rho}. \tag{88}$$

On the other hand, the bending moment at the points q and t of the flange qt is defined as

$$\frac{E t_1^3}{12(1-\nu^2)} \left(\frac{d^2 w}{d x^2}\right)_{x=\frac{b}{2}} = \frac{E t_2^3}{12(1-\nu^2)} \frac{1}{\rho}.$$

From the above equation

$$\left(\frac{d w}{d x}\right)_{x=\frac{b}{2}} = \frac{d}{2} \left(\frac{t_1}{t_2}\right)^3 \left(\frac{d^2 w}{d x^2}\right)_{x=\frac{b}{2}}. \tag{89}$$

From Eq. (88) and $w_{x=b/2} = 0$, $\boldsymbol{C}_1$ and $\boldsymbol{C}_2$ can be derived in the form

$$\boldsymbol{C}_1 = \frac{\boldsymbol{s}\boldsymbol{C} - \boldsymbol{c}\boldsymbol{S} - \gamma \boldsymbol{s}\boldsymbol{S}}{\boldsymbol{c}\boldsymbol{s} + \boldsymbol{C}\boldsymbol{S} - \gamma(\boldsymbol{S}^2 + \boldsymbol{c}^2)}, \qquad \boldsymbol{C}_2 = \frac{\boldsymbol{s}\boldsymbol{C} + \boldsymbol{c}\boldsymbol{S} - \gamma \boldsymbol{c}\boldsymbol{C}}{\boldsymbol{c}\boldsymbol{s} + \boldsymbol{C}\boldsymbol{S} - \gamma(\boldsymbol{S}^2 + \boldsymbol{c}^2)}, \tag{90}$$

where

$$\gamma = 2\beta \frac{d}{b} \left(\frac{t_1}{t_2}\right)^3 \tag{91}$$

and

$$\sin\beta = \boldsymbol{s}, \quad \sinh\beta = \boldsymbol{S}, \quad \cos\beta = \boldsymbol{c} \quad \text{and} \quad \cosh\beta = \boldsymbol{C}. \tag{92}$$

Hence

$$\sigma_x = \sigma_{max} \left(\boldsymbol{C}_1 \sin\frac{2\beta x}{b} \sinh\frac{2\beta x}{b} + \boldsymbol{C}_2 \cos\frac{2\beta x}{b} \cosh\frac{2\beta x}{b}\right). \tag{93}$$

The flange force is defined as

$$2t_1\int_0^{\frac{b}{2}}\sigma_x\,dx = t_1\,\bar{b}\,\sigma_{max}. \tag{94}$$

From the above equation

$$\frac{\bar{b}}{b} = \frac{1}{2\beta}\frac{\gamma(\sin 2\beta+\sinh 2\beta)-2(-\cos 2\beta+\cosh 2\beta)}{\gamma(\cos 2\beta+\cosh 2\beta)-(\sin 2\beta+\sinh 2\beta)}. \tag{95}$$

If the value of β grows, for instance, $\beta \geqq 3$, Eq. (95) may be substituted by

$$\frac{\bar{b}}{b} = \frac{1}{2\beta}\frac{\gamma-2}{\gamma-1}. \tag{96}$$

$\frac{\bar{b}}{b}$ is morely related to the dimensions of the section and R_i.

If the value of $\bar{b}$ is made known, the maximum value of the flange stress can be calculated.

$$\sigma_{max} = \frac{M\left(r_0-R_i+\frac{t_1}{2}\right)}{A\,e\left(R_i-\frac{t_1}{2}\right)}. \tag{97}$$

The distance r_0 between the neutral axis and the center of curvature can be written in the form

$$r_0 = \frac{A}{(b+t_2)\log_e\frac{R_0+\frac{t_1}{2}}{R_0-\frac{t_1}{2}}+2t_2\log_e\frac{R_0-\frac{t_1}{2}}{R_i+\frac{t_1}{2}}+(\bar{b}+t_2)\log_e\frac{R_i+\frac{t_1}{2}}{R_i-\frac{t_1}{2}}}. \tag{98}$$

Results of Experiment

An experiment was carried out to prove that the above-mentioned presumptive calculations were correct from a practical point of view.

The shape and dimensions of the specimen used in the experiment is shown in Fig. 52. The axial distribution of the axial stress of the circular arc flange is shown in Fig. 53 and 54.

According to the result of the experiment, the stress distribution of the axial stress of the circular arc flange at the point D is concentrated in the proximity of the web. The stress distribution along the circular arc is found not to change greatly in the circular arc. It will be seen that the above-mentioned calculations provide values close to the measured values. These calculations were made on the assumption that the effective width of the outer flange is equal to b or it is effective over its total width.

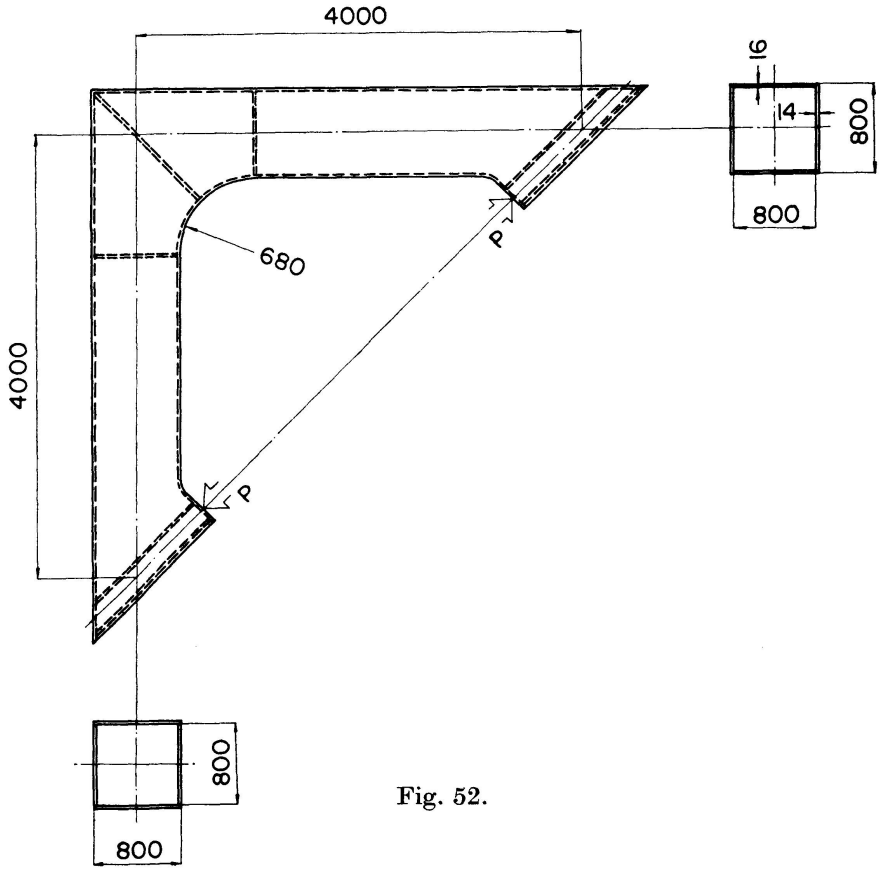


Fig. 52.

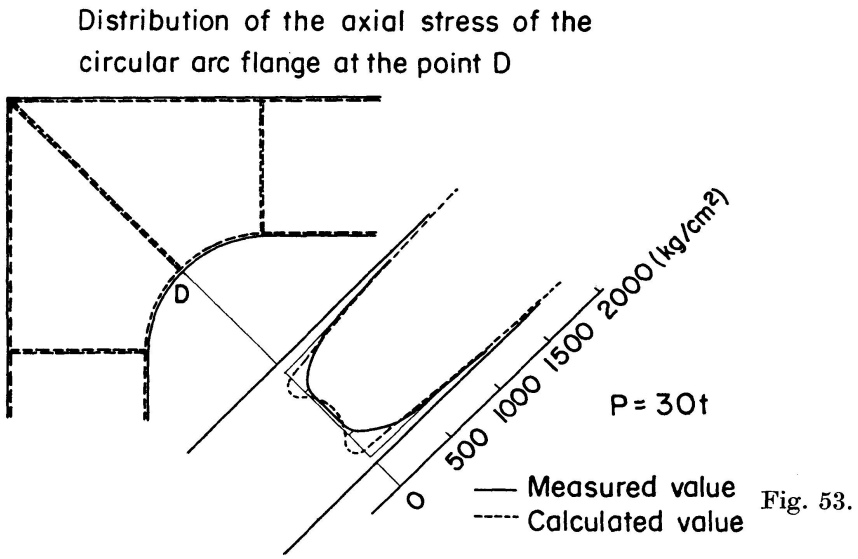


Fig. 53.

An $M-\Delta i$ curve is shown in Fig. 55. The load is of open type. According to this, it will be seen that M_p can be reached easily. In this case, however, careful attention must be paid to great stress concentration arising in the proximity of the flange web because the section is warped in the proximity of the circular arc flange of the knee joint. For this reason, the oblique reinforcements shown in Fig. 56 may serve effectively.

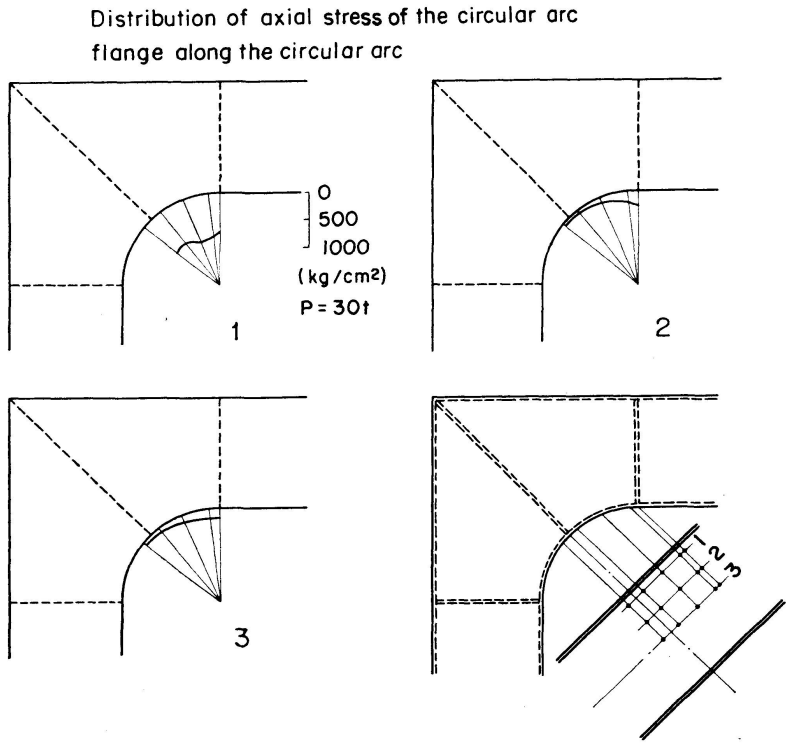


Fig. 54.

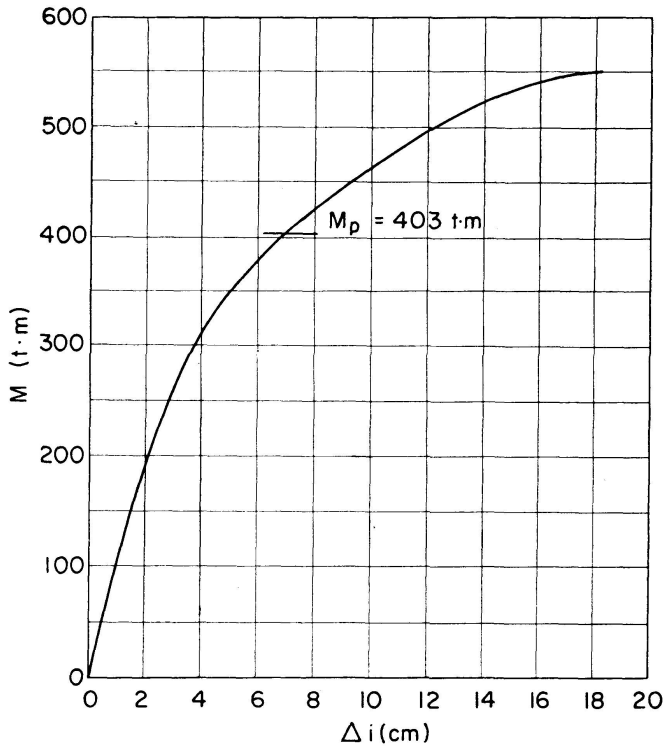


Fig. 55.

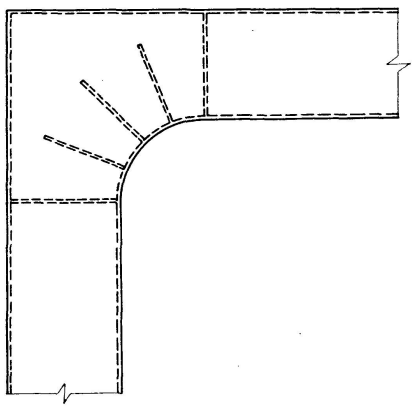


Fig. 56.

Conclusion

In this report are presented some proposals for the calculation of stress at rigid frame knee joints in which beams with box section are used, and the

results of examination of the proposals through experiments have been described.

It is suggested that conventional methods of calculation made on the assumption that shearing stress is uniformly distributed in the web of straight rectangular knee joints should be corrected. It is also suggested that the stress due to shear lag obtained by model calculation must be considered with respect to flange stress. Diagrams used for estimating the stress due to shear lag are made available for this purpose. At the same time, it is pointed out that these ideas are applicable to such types as straight haunch type and circular arc type straight flanges. When the application of plastic design is considered, it is necessary to pay due regard to the thickness of knee joints, because, generally in such knee joints, the total plastic moment of column or beam is apt to be lowered by shearing stress. As large stress concentration will occur near the inside of knee joints, it is necessary to render the total strength of flange to the joints to be welded. The effect of inserted web on shearing stress in knee joints, when a cylindrical column is used, has been detailed in this paper. The necessity of paying due regard to shear lag is also discussed in considering the stress to beam flange as in the case of straight rectangular type. As fairly large stress is generated in the inner flange of diaphragm, or as the diaphragm possibly buckles at too early a stage, depending on its dimension, the method of calculation of the diaphragm stress and the limitation of the thickness of diaphragm were called to particular attention.

As for the circular arc knee joint, this report shows the method of calculation of the circular arc flanges, in which the warping of web and flange of knee joint is taken into consideration. In this case, section arrangement and the thickness of the plate must be determined carefully because fairly large stress concentration is observed in the proximity of the web of the circular arc flange. According to the results of experiments with the above-mentioned types, the calculated values generally come in coincidence with the values obtained by the experiments.

These are the points which must be considered in designing knee joints of welded construction. While some more problems are yet to be examined as to stress concentration at the inner point in the knee joints or stress disturbance in the proximity of the inner point in the web, the methods of calculation proposed herein are believed to provide some references for solving these problems.

Reference Materials

1. T. Okumura: Problems Involved in Design and Working of Thin-Walled Section. Publication of Recent Problems in Structural Engineering, Japan Society of Civil Engineers, August 1965.
2. L. S. Beedle, A. A. Topractsoglou, and B. G. Johnston: Connections for Welded Continuous Portal Frames, Welding Journal, 30 (7), 30 (8) and 31 (11), 1951 and 1952.

3. D. T. WRIGHT: The Design of Knee Joints for Rigid Steel Frames. British Welding Journal, B.W.R.A., April 1954.
4. I. LYSE, and W. E. BLACK: An Investigation of Steel Rigid Frames. Trans. A.S.C.E., 107–186, 1942.
5. I. M. YUILLE: Shear Lag in Stiffened Plating. Originally published for Written Discussion, Transactions of the Institute of Naval Architects, Vol. 97.
6. T. OKUMURA, K. MAEDA, and N. ISHIZAWA: Knee Joints of Rigid Frames in These Days. Journal of the Japan Society of Civil Engineers, November 1964.
7. Valves Gates and Steel Conduits, Chapter 2, Department of Interiors Bureau of Reclamation, U.S.A.
8. S. TIMOSHENKO: Bending Stress in Curved Tubes of Rectangular Cross-Section. A.S.M.E., Vol. 45, p. 135, 1923.
9. F. BLEICH: Stahlhochbauten, Bd. 2.
10. KAYSER und HERZOG: Versuche zur Klärung des Spannungsverlaufes in Rahmenecken. Der Stahlbau, Jahrgang 12, Heft 2, 20. Jan. 1939.
11. C. G. ANDERSON: Flexural Stresses in Curved Beam of I – and Box-Sections. Proceedings Applied Mechanics, The Institution of Mechanical Engineers, London, Vol. 163, 1950.
12. I. OHNO: Formulas for Design of Corner of Steel Rigid Frame. Journal of The Japan Society of Civil Engineers, Sept. 1952.
13. T. OKUMURA, M. ITO, Y. NISHINO, K. MAEDA, N. ISHIZAWA: Connections on Rigid Frame Steel Structures Recently Adopted in Japan. Proceedings of the Conference on Experimental Methods of Investigating Stress and Strain in Structures, Praha, October 1965.
14. T. OKUMURA, N. ISHIZAWA: The Design of Knee Joints for Rigid Steel Frames with Thin Walled Section. Proceedings of The Japan Society of Civil Engineers, No. 153, May 1968.

Summary

The authors present some proposals in this paper regarding calculation of stress at knee joints of rigid frame construction, and confirm the applicability through several experiments. A few types of knee joints, such as straight rectangular, straight haunch and circular arc haunch, have been investigated.

One of the features of this report is that the stress due to shear lag is taken into consideration with respect to flange stress in knee joints formed by welded beam and column of box section. The stress due to shear lag can be calculated by means of model, and diagrams are used for estimation of the stress. Not only columns with box section but cylindrical columns are discussed in this paper.

Résumé

Le présent article contient quelques propositions pour le calcul des nœuds de cadres rigides et confirme son application par divers essais. On a examiné plusieurs types de nœuds: forme rectangulaire, polygonale et en arc de cercle.

Ce qui caractérise cet article est le fait que nous avons considéré l'influence

de la déformation du cisaillement sur les contraintes des semelles. Cette influence peut être obtenue à partir de modèles mathématiques et de graphiques. En outre, on examine le cas des colonnes cylindriques.

Zusammenfassung

Die Verfasser unterbreiten in diesem Beitrag einige Vorschläge zur Spannungsberechnung an Rahmenecken und bestätigen die Anwendbarkeit durch verschiedene Versuche. Etliche Typen von Rahmenecken, wie rechtwinklige, polygonale und kreisförmige werden untersucht.

Eines der Merkmale im vorliegenden Aufsatz äußert sich darin, daß die Spannungsänderungen in den Flanschen infolge der Schubverformung in Betracht gezogen werden. Der Einfluß der Schubverformung kann anhand von Modellen ermittelt und zur Schätzung der Spannung können Diagramme benutzt werden. In dieser Arbeit werden nicht allein Stützen mit kastenförmigem Querschnitt, sondern auch zylindrische Stützen behandelt.

Eine strenge Lösung des Biegebruchsicherheitsnachweises für den rechteckigen Spannbetonbalken ohne Verbund

A Rigorous Analysis for the Moment Carrying Capacity of an Unbonded Prestressed Concrete Beam

Solution rigoureuse pour l'analyse de la résistance à la rupture en flexion d'une poutre isolée en béton précontraint et de section rectangulaire

JÜRGEN PLÄHN
Madras/Indien

1. Einführung

Die Vorausberechnung des Bruchmoments bereitet für den Spannbetonbalken ohne Verbund zwischen Spannglied und Beton wesentlich größere Schwierigkeiten als für den mit Verbund hergestellten. Bei fehlendem Verbund ist der unmittelbare Zusammenhang zwischen den Verformungen des Stahls und des Betons an den einzelnen Querschnitten nicht mehr gegeben, aus dem das widerstehende innere Kräftepaar in einfacher Weise bestimmt werden könnte. Der genaue Nachweis erfordert vielmehr die vollständige Bestimmung des Spannungszustandes des bei statisch bestimmter Lagerung in der Regel 1fach innerlich statisch unbestimmten Balkens. Dabei sind die im Bruchzustand vorliegenden Verhältnisse, insbesondere das nichtlineare Spannungsdehnungsverhalten der Werkstoffe und die Veränderlichkeit der Querschnittswerte zu berücksichtigen, die infolge des Aufreißens der Zugzone von dem angreifenden Biegemoment abhängen.

Die Aufgabe ist früher bereits von H. RÜSCH, K. KORDINA und C. ZELGER [1] unter Verwendung der in Heft 120 des DAfStB [2] mitgeteilten Verformungsbeziehungen für Beton behandelt worden. Die dort nicht in Form mathematischer Beziehungen, sondern nur als Zahlenpaare vorliegenden Spannungsdehnungsbeziehungen scheinen die Lösung erheblich zu erschweren. Um das Verfahren anwendbar zu machen, waren außer einer Reihe von Hilfstafeln gewisse Korrekturen erforderlich, die nur durch Vergleich mit Versuchsergebnissen bestimmt werden konnten.

Für den Rechteckbalken ohne zusätzliche schlaffe Bewehrung ist kürzlich in [3] eine Lösung angegeben worden, die von leichter zu handhabenden Annahmen für das Verformungsverhalten des Betons ausgeht. Es zeigte sich, daß damit eine exakte und vergleichsweise einfache mathematische Behandlung möglich war.

Im folgenden wird die vollständige Lösung unter Berücksichtigung schlaffer Bewehrungseinlagen mitgeteilt.

2. Übersicht, Annahmen

Den folgenden Untersuchungen wird der statisch bestimmt gelagerte, mit einem Spannglied versehene Spannbetonbalken mit unveränderlichem, rechteckigem Querschnitt zugrunde gelegt. Es wird Reibungsfreiheit zwischen Spannglied und Beton vorausgesetzt. Das Tragwerk ist somit 1fach innerlich statisch unbestimmt.

Die zur Ermittlung der statisch Überzähligen zu erfüllende Verformungsbedingung ist die Verträglichkeit der Gesamtverformungen des Spanngliedes nach dem Verankern gegen den Beton und der des Betons entlang des Balkens in Höhe der Spanngliedachse:

$$\int_0^l (\epsilon_s - \epsilon_{s0})\, dx - \int_0^l \epsilon_{bs}\, dx = 0. \tag{1}$$

Darin bedeuten ϵ_s die Stahldehnung, ϵ_{s0} die zum Vorspannen erforderliche Vordehnung des Spannstahls bei unbeansprucht gedachtem Beton, die daher auch als fiktive Spannbettdehnung aufgefaßt werden kann, ϵ_{bs} die Betondehnung in Höhe der Spanngliedachse. Als Überzählige wird die Spanngliedkraft benutzt. Die Dehnungen in Gl. (1) werden in Abhängigkeit von ihr ausgedrückt. Bei der hier eingeführten Verformungsbeziehung für den Beton folgt daraus die Bestimmungsgleichung für die Spanngliedkraft in algebraischer Form. Sie kann durch Probieren, d. h. Einsetzen geschätzter Werte gelöst werden.

Im Hinblick auf das unterschiedliche Verhalten des Balkens im Bereich der gerissenen und der ungerissenen Zugzone ist es zweckmäßig, die bei der Aufstellung der Bestimmungsgleichung erforderliche Integration der Betonverformungen in entsprechenden Teilabschnitten vorzunehmen. Bei Symmetrieverhältnissen folgt dann anstelle der Gl. (1):

$$\int_0^l (\epsilon_s - \epsilon_{s0})\, dx - 2\int_0^{x_1} \epsilon_{bs}\, dx - 2\int_{x_1}^{l/2} \epsilon_{bs}\, dx = 0. \tag{1a}$$

Der auflagernahe Bereich $0 \leqq x \leqq x_1$ ist durch die Mitwirkung des vollen Betonquerschnitts gekennzeichnet, während in dem Mittelabschnitt $x_1 \leqq x \leqq 1/2$ die Zugzone des Betonquerschnitts im Bruchzustand gerissen ist. Die Grenze

x_1 ist durch das Erreichen der Biegzugfestigkeit des Betons am unteren Querschnittsrand bestimmt.

Für den auflagernahen Bereich wird mit Rücksicht auf die hier in allen praktischen Fällen durchweg vorliegenden niedrigen Beanspruchungen angenommen, daß der Beton dem Hookeschen Gesetz folgt,

$$\sigma = E_b \epsilon_b . \tag{2}$$

Diese Annahme ermöglicht eine einfache Bestimmung der Integrationsgrenze x_1. Lediglich für den mittleren, hochbeanspruchten Bereich wird das Verformungsverhalten des Betons nichtlinear eingeführt. Es wird eine quadratische Parabel

$$\sigma = E_b \left(\epsilon_b + \frac{E_b}{4K} \epsilon_b^2 \right); \quad \epsilon_b \leqq 0 \tag{3}$$

benutzt; sie ist in normierter Form in Fig. 1 dargestellt. Ihre Anwendung ist

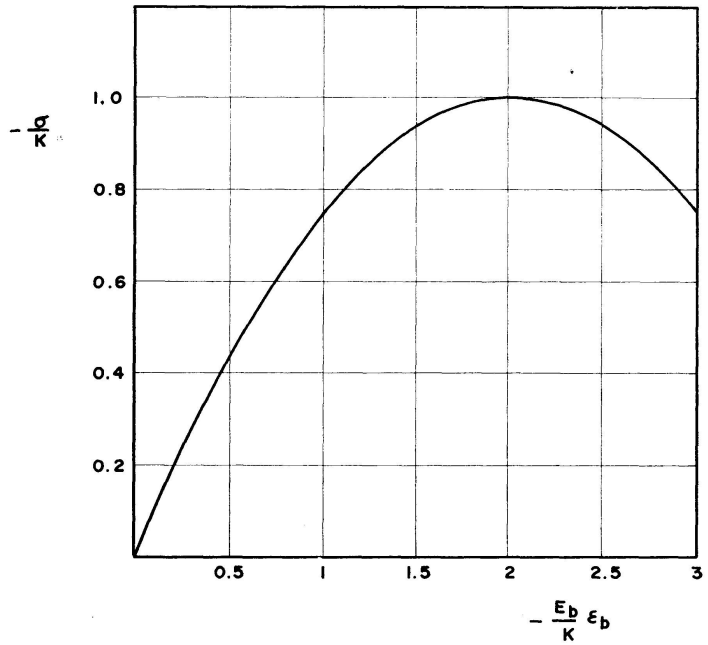


Fig. 1. Spannungsdehnungslinie des Betons.

nur im Sinne monoton nicht zunehmender Dehnungen zulässig.

Das Spannungsdehnungsdiagramm des Spannstahls wird als gegeben vorausgesetzt. Der Einfluß in der Zugzone des Balkens angeordneter schlaffer Bewehrungseinlagen wird berücksichtigt. Es wird eine idealisierte Spannungsdehnungslinie nach Fig. 2 zugrunde gelegt.

Die Untersuchungen werden auf den im Spannbetonbau üblichen schlanken Träger beschränkt, für den der Cosinus des Neigungswinkels des Spanngliedes gegenüber der Stabachse überall zu eins angenommen werden darf.

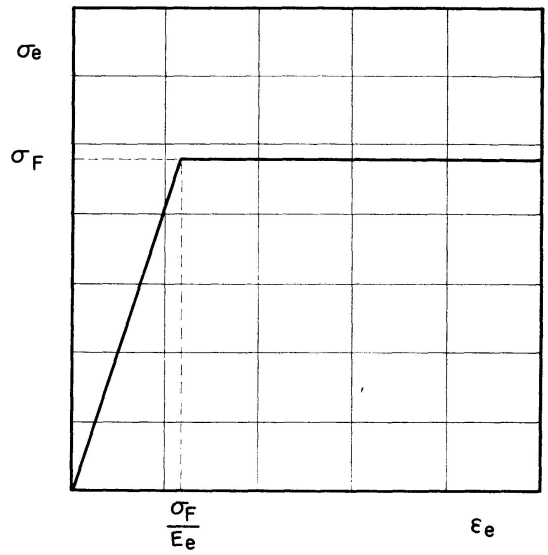


Fig. 2. Spannungsdehnungslinie des Betonstahls.

3. Die Verformungen des Spanngliedes

Es wird davon ausgegangen, daß die Lösung der aus Gl. (1a) folgenden Bestimmungsgleichung für die Spanngliedkraft Z_s im Bruchzustand durch wiederholtes Einsetzen eines geschätzten Wertes zu suchen ist. Damit sind für jeden angenommenen Wert die Gesamtverformungen ϵ_s, denen das Spannglied nach dem Einbau im spannungslosen Zustand unterworfen ist, aus der vorliegenden Spannungsdehnungslinie des Spannstahls bekannt. Hier interessieren indes nur die von den Betonverformungen abhängigen Anteile, ohne die zum Vorspannen erforderlichen Vordehnungen. Die Verformungen aus der Stahldehnung ϵ_{s0} im sogenannten Spannbettzustand müssen somit von den Gesamtverformungen abgezogen werden. Diese Spannbettdehnungen ϵ_{s0} wird man dabei zweckmäßig gleich aus der durch die Vorspannverluste (Kriechen und Schwinden des Betons usw.) reduzierten Vorspannkraft bestimmen.

Die Vorspannkraft V_0 im sogenannten Spannbettzustand wird aus der wirklichen Vorspannkraft V nach

$$V_0 = \frac{V}{1-\zeta}$$

errechnet. Die Größe ζ folgt bekanntlich mit den für das 1fach statisch unbestimmte, elastische System ermittelten Verschiebungsgrößen, vgl. z. B. [4],

$$\delta_{b\,11} = \int_0^l \frac{M_1^2}{E_b\, I_b} dx + \int_0^l \frac{N_1^2}{E_b\, F_b} dx$$

und $$\delta_{s11} = \int_0^l \frac{N_1^2}{E_s F_s} dx$$

zu $$\zeta = \frac{\delta_{b11}}{\delta_{b11} + \delta_{s11}}.$$

M_1 und N_1 sind dabei das Biegemoment bzw. die Normalkraft am statisch bestimmten Hauptsystem infolge der als Überzählige eingeführten Spanngliedkraft $X_1 = 1$.

Die Vordehnung des Stahls im Spannbettzustand ist dann

$$\epsilon_{s0} = \frac{V_0}{E_s F_s}.$$

Den Anteil der Stahlverformungen in Gl. (1a) erhält man damit zu

$$\delta_s = \int_0^l (\epsilon_s - \epsilon_{s0})\, dx = l\left(\epsilon_s - \frac{V_0}{E_s F_s}\right). \tag{4}$$

4. Verformungen des Betons im ungerissenen Bereich

Als Stabachse wird vereinfachend die geometrische Achse benutzt. Der Abstand der Spanngliedachse vom Schwerpunkt des Rechteckquerschnittes mit der Gesamthöhe d nach Fig. 3 sei $\lambda(x)\, d$. Für parabolisch geführtes Spannglied gilt somit z. B.

$$\lambda(x) = \lambda_0 + \frac{4(\lambda_m - \lambda_0)}{l^2}(l\,x - x^2), \tag{5}$$

wobei $\lambda_m d$ den Abstand in Balkenmitte und $\lambda_0 d$ den am Balkenende bedeuten. Für $\lambda_0 = \lambda_m$ geht das gekrümmte Spannglied in ein gerades mit konstantem Abstand $\lambda_m d$ über.

Bei voller Mitwirkung des Betonquerschnitts und unter der Annahme der Gültigkeit des Hookeschen Gesetzes für den Beton ergeben sich die Betonspannungen am unteren Querschnittsrand genau genug zu

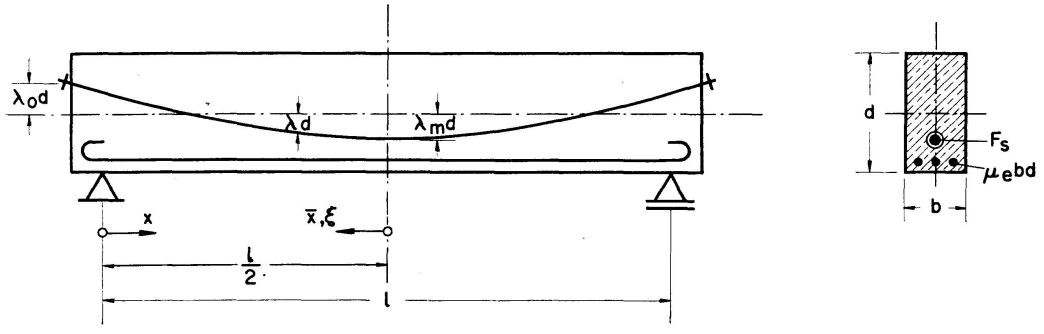


Fig. 3. Prinzipskizze des Balkens mit Bezeichnungen.

$$\sigma_{bu} = -\frac{Z_s}{b\,d} - \frac{6}{b\,d} Z_s \lambda(x) + \frac{6}{b\,d^2} M(x). \tag{6}$$

Für gegebenes äußeres Biegemoment $M(x)$ erhält man daraus den Abstand $x = \beta \frac{l}{2}$, an dem die untere Randspannung die Biegezugfestigkeit σ_R des Betons erreicht. Ist insbesondere die äußere Belastung durch eine gleichmäßig verteilte Last gegeben

$$M(x) = \frac{4}{l^2} M_m (l\,x - x^2), \tag{7}$$

so folgt für Spanngliedprofile nach Gl. (5)

$$\beta = 1 - \sqrt{1 + \frac{\rho(6\lambda_0 + 1) - \frac{\sigma_R}{\sigma_v}}{6\rho(\lambda_m - \lambda_0) + \frac{\sigma_{bg}}{\sigma_v}}}. \tag{8}$$

Hierin bedeuten

$\rho = \frac{Z_s}{V}$ das Verhältnis der Spanngliedkraft im Bruchzustand zu der für den Lastfall Vorspannung nach Kriechen und Schwinden,

$\sigma_v = -\frac{V}{b\,d}$ die mittlere Vorspannung des Querschnitts aus dem Lastfall Vorspannung nach Kriechen und Schwinden und

$\sigma_{bg} = \frac{6\,M_m}{b\,d^2}$ die aus dem Maximalmoment der äußeren Lasten und dem vollen Betonquerschnitt errechnete Biegerandzugspannung.

Als Integrationsgrenze zwischen der ungerissenen und der gerissenen Zugzone kann nun nicht $\beta \frac{l}{2}$ selbst gewählt werden. Wenn z. B. σ_R nur an einer Stelle, der Balkenmitte, erreicht wird, also $\beta = 1$ ist, so würde dann trotz des hier aufgetretenen Risses die Integration der Betonverformungen über die gesamte Balkenlänge für ungerissene Zugzone durchzuführen sein. Um dies sicherlich unzulässige Vorgehen auszuschließen, wird angenommen, daß der Übergang von der Spannungsverteilung mit gerissener Zugzone zur Spannungsverteilung mit ungerissener Zugzone nach dem St. Venantschen Prinzip ungefähr eine Länge entsprechend der Querschnittshöhe d benötigt (Fig. 4). Damit wird man die Grenze zwischen den beiden Bereichen mit gerissener und ungerissener Zugzone hinreichend genau zu

$$x_1 = \beta \frac{l}{2} - \frac{d}{2} = \frac{l}{2}\left(\beta - \frac{d}{l}\right) = \frac{l}{2}\bar{\beta}$$

annehmen können.

Aus den Betonspannungen in Höhe der Spanngliedachse

$$\sigma_{bs} = -\frac{Z_s}{b\,d} - \frac{12\,Z_s}{b\,d}[\lambda(x)]^2 + \frac{12\,M(x)}{b\,d^2}\lambda(x)$$

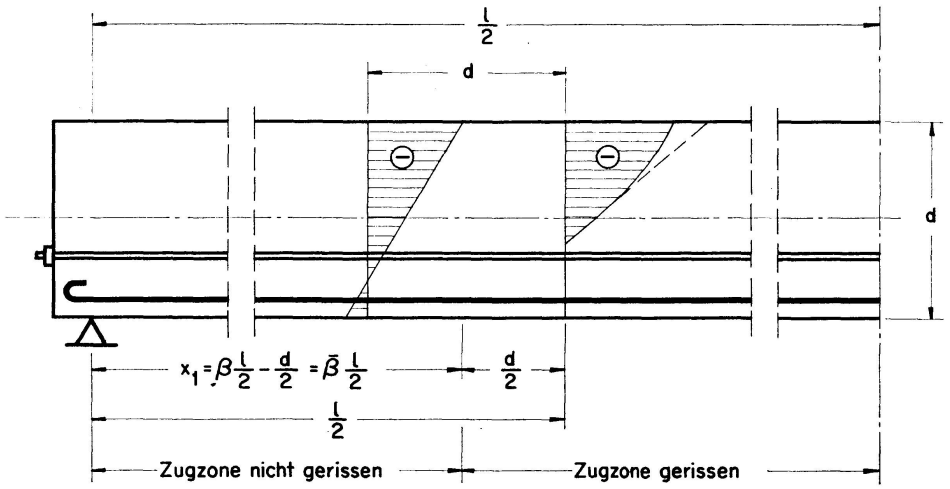


Fig. 4. Erläuterungsskizze zur Festlegung der Integrationsgrenze zwischen dem gerissenen und dem ungerissenen Teil des Balkens. (Die eingezeichneten Spannungsverteilungen geben die Verhältnisse für Balken «München I» im Bruchzustand maßstäblich richtig wieder.)

folgt die gesamte Verlängerung

$$2\int_0^{x_1} \epsilon_{bs}\,dx = \delta_{b1} = \frac{2}{E_b}\int_0^{(l/2)\bar{\beta}} \epsilon_{bs}\,dx$$

der Betonfaser neben dem Spannglied im ungerissenen Bereich für einen Spanngliedverlauf nach Gl. (5) und gleichmäßig verteilte Belastung zu

$$\begin{aligned}\delta_{b1} = \frac{2\,l}{E_b}\{&\tfrac{1}{2}\rho\,\sigma_v\,(1+12\,\lambda_0^2)\,\bar{\beta} - [4\,\rho\,\sigma_v\,(\lambda_m-\lambda_0)+\tfrac{1}{3}\,\sigma_{bg}]\,\lambda_0\,(3\,\bar{\beta}^2-\bar{\beta}^3)\\ &+[\rho\,\sigma_v\,(\lambda_m-\lambda_0)+\tfrac{1}{6}\,\sigma_{bg}]\,(\lambda_m-\lambda_0)\,(8\,\bar{\beta}^3-6\,\bar{\beta}^4+1{,}2\,\bar{\beta}^5)\}.\end{aligned} \tag{9}$$

5. Verformungen des Betons im Bereich der gerissenen Zugzone

5.1. Ausgangsgleichungen

Mit den Bezeichnungen nach Fig. 5 erhält man die Betondehnung in der Spanngliedfaser aus der Randdehnung ϵ_R am gedrückten Rand, der Höhe der Biegedruckzone $\alpha\,d$ und der Lage $\lambda\,d$ des Spanngliedes im Querschnitt zu

$$\epsilon_{bs} = -\frac{\frac{1}{2}+\lambda-\alpha}{\alpha}\,\epsilon_R. \tag{10}$$

Die Größen α und ϵ_R müssen darin in geeigneter Weise durch die Überzählige Z_s bzw. das Verhältnis ρ ausgedrückt werden. Aus

$$M = Z_s\,d\,(\tfrac{1}{2}+\lambda-\gamma)+Z_e\,d\,(\vartheta-\gamma) \tag{11}$$

folgt zunächst die Lage γ der Druckresultierenden im Querschnitt mit $Z_e=\sigma_e\,\mu_e\,b\,d$ zu

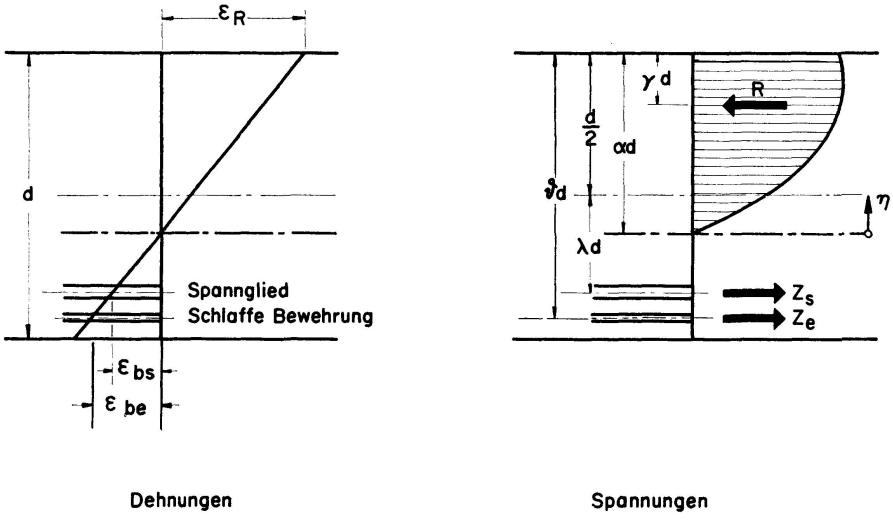


Fig. 5. Dehnungs- und Spannungsverteilung über den Querschnitt im Bereich der gerissenen Zugzone.

$$\gamma(x) = \frac{\frac{1}{2} + \lambda(x) + \frac{1}{6}\frac{\sigma_{bg}(x)}{\rho\,\sigma_v} - \frac{\mu_e\,\sigma_e(x)}{\rho\,\sigma_v}\vartheta}{1 - \frac{\mu_e\,\sigma_e(x)}{\rho\,\sigma_v}}. \tag{12}$$

Für gegebenes Spannungsdehnungsverhalten des Betons und der schlaffen Bewehrung läßt sich α durch γ ausdrücken. Mit

$$\epsilon_b = \epsilon_R \frac{\eta}{\alpha\, d} \tag{13}$$

lautet die Spannungsdehnungsbeziehung Gl. (3)

$$\sigma = E_b \frac{\epsilon_R}{\alpha\, d}\left(\eta + \frac{E_b}{4K}\frac{\epsilon_R}{\alpha\, d}\eta^2\right). \tag{14}$$

Die Druckresultierende ist dann

$$R = b\int_0^{\alpha d} \sigma\, d\eta = \frac{1}{2} E_b\, \alpha\, b\, d\, \epsilon_R\left(1 + \frac{1}{6}\frac{E_b}{K}\epsilon_R\right). \tag{15}$$

Das Moment der Druckspannungen um die Nullinie beträgt

$$R\,d\,(\alpha - \gamma) = b\int_0^{\alpha d} \eta\,\sigma\, d\eta = \frac{1}{3} E_b\, \alpha^2 d^2\, b\, \epsilon_R\left(1 + \frac{3}{16}\frac{E_b}{K}\epsilon_R\right). \tag{16}$$

Division von (16) durch (15) liefert eine Beziehung für die Randdehnung

$$\epsilon_R = -6\frac{K}{E_b}\frac{1 - \frac{1}{3}\frac{\alpha}{\gamma}}{1 - \frac{1}{4}\frac{\alpha}{\gamma}}. \tag{17}$$

Eine weitere folgt aus Gl. (15) unter Beachtung von

$$R = -Z_s - Z_e = +b\,d\,(\rho\,\sigma_v - \mu_e\,\sigma_e),$$

$$\epsilon_R^2 + 6\frac{K}{E_b}\epsilon_R - 12\frac{K}{E_b^2}\frac{1}{\alpha}(\rho\,\sigma_v - \mu_e\,\sigma_e) = 0. \tag{18}$$

Für die weitere Untersuchung muß nun unterschieden werden, ob die schlaffe Bewehrung noch im elastischen Bereich oder bereits im Fließbereich beansprucht ist.

5.2. Schlaffe Bewehrung fließt, $\sigma_e = \sigma_F$

Mit $\sigma_e = \sigma_F$ folgt die gesuchte Abhängigkeit der Lage der Nullinie von der Lage der resultierenden Druckkraft durch Einsetzen von Gl. (17) in Gl. (18) zu

$$\frac{1}{12}\,\frac{3\left(\frac{\alpha}{\gamma}\right)^2-\left(\frac{\alpha}{\gamma}\right)^3}{\left(1-\frac{1}{4}\,\frac{\alpha}{\gamma}\right)^2}=-\frac{1}{\gamma}\,\frac{\sigma_v}{K}\left(\rho-\frac{\mu_e\,\sigma_F}{\sigma_v}\right). \tag{19}$$

Mit γ nach Gl. (12), das für angenommenes ρ und gegebene Fließspannung σ_F der schlaffen Bewehrung bekannt ist, kann hieraus α punktweise für diskrete Abstände x bestimmt werden. Damit ist auch ϵ_R nach Gl. (17) bekannt, womit nach Gl. (10) die Betondehnungen ϵ_{bs} neben der Spanngliedachse angegeben und numerisch integriert werden können. Anhand der Dehnungen der schlaffen Einlagen ist dabei jeweils nachzuweisen, daß die Stahlspannungen die Fließgrenze auch tatsächlich erreicht haben,

$$\epsilon_{be}=-\frac{\vartheta-\alpha}{\alpha}\,\epsilon_R \geqq \frac{\sigma_F}{E_e}. \tag{20}$$

Gl. (19) ist in Fig. 6 in dem hier in Frage kommenden Bereich graphisch dargestellt. Die Lösungen α/γ können der Auftragung unmittelbar entnommen werden.

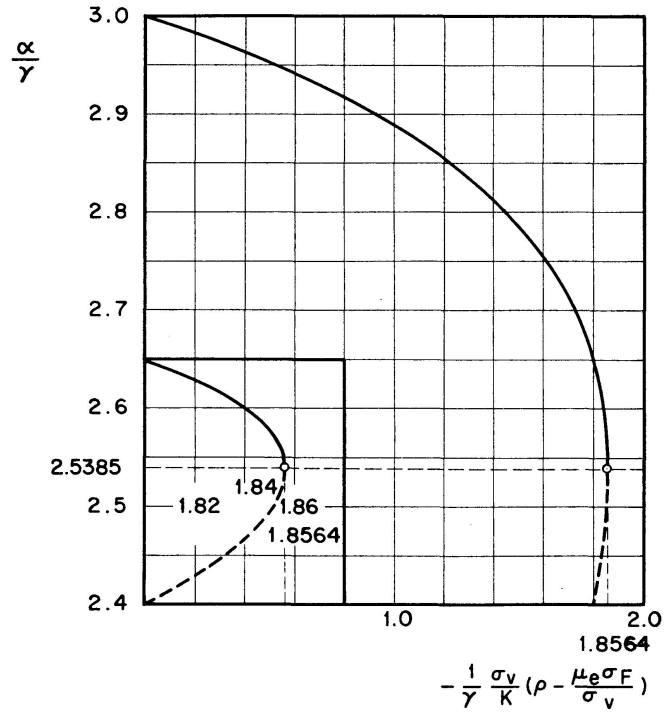


Fig. 6. Lösungskurve der Gl. (19).

5.3. Beanspruchung der schlaffen Bewehrung im elastischen Bereich, $\sigma_e < \sigma_F$

Befindet sich die Stahlspannung der schlaffen Bewehrung noch im elastischen Bereich, so ist die Zugkraft Z_e nicht mehr vorgegeben, sondern hängt von der Stabkrümmung, d. h. den Werten α und ϵ_R ab:

$$\sigma_e = E_e \epsilon_{be} = -E_e \frac{\vartheta - \alpha}{\alpha} \epsilon_R; \qquad \sigma_e < \sigma_F. \tag{21}$$

Damit kann γ nicht mehr wie im Falle des Fließens der schlaffen Bewehrung unabhängig von α vorweg angegeben werden. Beide Werte α und γ sind vielmehr als Lösungen zweier nichtlinearer algebraischer Gleichungen zu ermitteln. Die Bestimmungsgleichungen folgen aus Gl. (12) und aus Gl. (18), beide in Verbindung mit Gl. (17) und (21.).

Gl. (12) liefert:

$$\gamma - 6 \frac{\mu_e K}{\rho \sigma_v} \frac{E_e}{E_b} \left[\vartheta \left(1 + \frac{\gamma}{\alpha} \right) - \frac{1}{\gamma} \frac{\gamma}{\alpha} \vartheta^2 - \gamma \right] \frac{1 - \frac{1}{3} \frac{\alpha}{\gamma}}{1 - \frac{1}{4} \frac{\alpha}{\gamma}} = \frac{1}{2} + \lambda + \frac{\sigma_{bg}(x)}{6 \rho \sigma_v}. \tag{22}$$

Aus Gl. (18) folgt

$$\frac{1}{12} \frac{3 \left(\frac{\alpha}{\gamma} \right)^2 - \left(\frac{\alpha}{\gamma} \right)^3}{\left(1 - \frac{1}{4} \frac{\alpha}{\gamma} \right)^2} - 6 \frac{\mu_e}{\gamma^2} \frac{E_e}{E_b} \left(\frac{\vartheta}{\frac{\alpha}{\gamma}} - \gamma \right) \frac{1 - \frac{1}{3} \frac{\alpha}{\gamma}}{1 - \frac{1}{4} \frac{\alpha}{\gamma}} = -\frac{\rho \sigma_v}{\gamma K}. \tag{23}$$

5.4. Konstante Streckenlast und parabolische Spanngliedführung

Um die Integrationen zu vereinfachen, wird der Ursprung der Längskoordinate hier in die Mitte des Balkens verlegt, Fig. 3. Für die weitere praktische Durchführung der Rechnung ist es außerdem vorteilhaft, die Längskoordinate $\bar{x}$ auf den Integrationsbereich $\frac{l}{2}(1 - \bar{\beta})$ bezogen einzuführen:

$$\xi = \frac{\bar{x}}{\frac{l}{2}(1 - \bar{\beta})}.$$

Für den hier näher dargestellten Fall des symmetrischen Balkens mit parabolischer Spanngliedführung und gleichmäßig verteilter äußerer Last ergibt sich λ damit in der Form

$$\lambda(\xi) = \lambda_m - (\lambda_m - \lambda_0)(1 - \bar{\beta})^2 \xi^2 \tag{24}$$

und das Biegemoment zu

$$M(\xi) = M_m [1 - (1 - \bar{\beta})^2 \xi^2]. \tag{25}$$

Die Biegerandzugspannungen aus $M(\xi)$ sind dann

$$\sigma_{bg}(\xi) = \frac{6}{b d^2} M(\xi) = \sigma_{bg} [1 - (1 - \bar{\beta})^2 \xi^2]. \tag{25a}$$

Bei Fließen der schlaffen Bewehrung, $\sigma_e = \sigma_F$, ist dann die Lage der Druckresultierenden gemäß Gl. (12)

$$\gamma(\xi) = \frac{\frac{1}{2} + \lambda_m + \frac{\sigma_{bg}}{6\rho\sigma_v} - \left(\lambda_m - \lambda_0 + \frac{\sigma_{bg}}{6\rho\sigma_v}\right)(1-\bar{\beta})^2\xi^2 - \frac{\mu_e \sigma_F}{\rho\sigma_v}\vartheta}{1 - \frac{\mu_e\sigma_F}{\rho\sigma_v}}. \tag{26}$$

Die entsprechende Gleichung für den Fall $\sigma_e < \sigma_F$ lautet nach Gl. (22)

$$\gamma - 6\frac{\mu_e K}{\rho\sigma_v}\frac{E_e}{E_b}\left[\vartheta\left(1+\frac{\gamma}{\alpha}\right) - \frac{\gamma}{\alpha}\frac{1}{\gamma}\vartheta^2 - \gamma\right]\frac{1-\frac{1}{3}\frac{\alpha}{\gamma}}{1-\frac{1}{4}\frac{\alpha}{\gamma}} = \frac{1}{2} + \lambda_m + \frac{\sigma_{bg}}{6\rho\sigma_v} - \left(\lambda_m - \lambda_0 + \frac{\sigma_{bg}}{6\rho\sigma_v}\right)(1-\bar{\beta})^2\xi^2. \tag{27}$$

Mit den erhaltenen Lösungen für α/γ und γ werden die Betondehnungen ϵ_{bs} in Höhe der Spanngliedachse dann nach

$$\epsilon_{bs} = -\left\{\frac{1}{\gamma}\left[\tfrac{1}{2} + \lambda_m - (\lambda_m - \lambda_0)(1-\bar{\beta})^2\xi^2\right]\frac{\gamma}{\alpha} - 1\right\}\epsilon_R \tag{28}$$

bestimmt. Ist ϵ_{bs} für $n+1$ äquidistante Werte $\xi_0, \xi_1, \xi_2 \ldots \xi_n$ von 0 bis 1 ermittelt, so kann die Betonverlängerung im Bereich der gerissenen Zugzone durch numerische Integration, z. B. nach der Trapezregel bestimmt werden:

$$2\int_{x_1}^{l/2}\epsilon_{bs}\,dx = \delta_{b2} = 2\int_0^{(l/2)(1-\bar{\beta})}\epsilon_{bs}(\bar{x})\,d\bar{x} = 2\frac{l}{2}(1-\bar{\beta})\int_0^1\epsilon_{bs}(\xi)\,d\xi,$$

$$\delta_{b2} = \frac{l}{2}\frac{(1-\bar{\beta})}{n}\left[\epsilon_{bs}(\xi_0) + 2\,\epsilon_{bs}(\xi_1) + 2\,\epsilon_{bs}(\xi_2) + \cdots + \epsilon_{bs}(\xi_n)\right]. \tag{29}$$

6. Bruchbedingung, Bemerkungen zur praktischen Rechnung

Beim Spannbetonbalken ohne Verbund wird der Biegebruch i. a. durch primäres Versagen des Betons der Druckzone verursacht. Das Fehlen des Verbundes zwischen Spannglied und Beton bewirkt eine über die Länge gleichmäßige Dehnung des Spannstahls und damit sich stark öffnende, schnell fortschreitende Risse an der Zugseite, die die Betondruckzone schnell verkleinern.

Die Bruchbedingung folgt daher aus dem allein mit Hilfe der resultierenden Druckkraft der Biegedruckzone angeschriebenen Moment der inneren Kräfte, für das das Extremum zu bestimmen ist,

$$M = (h - \gamma d)\,R.$$

Darin ist h der Abstand der resultierenden Stahlzugkraft $Z_s + Z_e$ vom oberen Querschnittsrand. Im Bruchzustand wird die schlaffe Bewehrung am

Bruchquerschnitt die Streckgrenze immer erreicht haben. Nach Gl. (26) liegt damit der Wert γ bei gegebener äußerer Belastung fest. Das Moment der inneren Kräfte ist unter Einführung von Gl. (15) und Gl. (17) nur eine Funktion von α, oder, in der hier benutzten Schreibweise, des Verhältnisses α/γ. Die Bedingung für das Extremum lautet dann

$$\frac{d}{d\left(\frac{\alpha}{\gamma}\right)} \frac{3\left(\frac{\alpha}{\gamma}\right)^2 - \left(\frac{\alpha}{\gamma}\right)^3}{\left(1-\frac{1}{4}\frac{\alpha}{\gamma}\right)^2} = 0.$$

Der Bruch ist die linke Seite der Gl. (19), dargestellt in Fig. 6. Die Lösung ist $\frac{\alpha}{\gamma} = 2{,}5385$. Für kleinere Werte ist bei der hier eingeführten Verformungsbeziehung des Betons das Gleichgewicht nur bei wieder abnehmender äußerer Belastung möglich. Zur Vorausberechnung des Bruchmoments ist somit zu zeigen, daß das Verhältnis $\frac{\alpha}{\gamma}$ am höchst beanspruchten Querschnitt den Wert 2,5385 angenommen hat und daß dabei die Verträglichkeit der Verformungen des Spanngliedes und des Betons in Höhe der Spanngliedachse gewahrt ist.

Für die übliche Bemessungsaufgabe ist das Bruchmoment bekannt und es ist nachzuweisen, daß es mit den gewählten Querschnittsabmessungen aufgenommen werden kann.

Für den genannten Grenzwert $\frac{\alpha}{\gamma} = 2{,}5835$ kann das zugehörige Verhältnis ρ angegeben werden, das zweckmäßig zuerst bestimmt wird. Die zur Lösung der Aufgabe erforderliche Probierarbeit läßt sich hierdurch wesentlich herabsetzen bzw. ganz vermeiden.

Aus Fig. 6 geht hervor, daß der Ausdruck

$$-\frac{1}{\gamma}\frac{\sigma_v}{K}\left(\rho - \frac{\mu_e \sigma_F}{\sigma_v}\right) \leqq 1{,}8564$$

bleiben muß. Führt man diesen Grenzwert in die Gl. (26) für das kleinste, in Balkenmitte bei $\xi = 0$ vorliegende γ ein, so erhält man eine quadratische Gleichung für ρ mit der Lösung

$$\rho_{min} = -\left[0{,}9282\left(\tfrac{1}{2}+\lambda_m\right)\frac{K}{\sigma_v} - \frac{\mu_e \sigma_F}{\sigma_v}\right] \tag{31}$$
$$-\sqrt{\left[0{,}9282\left(\tfrac{1}{2}+\lambda_m\right)\frac{K}{\sigma_v} - \frac{\mu_e \sigma_F}{\sigma_v}\right]^2 - 0{,}3094\frac{\sigma_{bg} K}{\sigma_v^2} - \left(\frac{\mu_e \sigma_F}{\sigma_v}\right)^2 + 1{,}8564\frac{\mu_e \sigma_F}{\sigma_v^2}K\vartheta}.$$

Dieser Wert ist eine untere Schranke. Für kleinere Werte können die Gleichgewichtsbedingungen nicht mehr erfüllt werden. Mit diesem ρ_{min} wird man die erste Verformungsuntersuchung durchführen. Ergeben sich die Betonverformungen größer als die Verformungen des Spanngliedes, so ist damit die ausreichende Momententragfähigkeit bereits nachgewiesen. Durch Vergrößerung von ρ lassen sich die Spannstahldehnungen bei gleichzeitiger Ermäßigung

der Betonverformungen erhöhen, so daß die Verformungsbedingung (1a) immer erfüllt werden kann. Wiederholungsrechnungen mit größeren ρ sind nur dann erforderlich, wenn die zu dem vorgegebenen Biegemoment gehörende Spanngliedkraft genau bestimmt werden soll.

Soll dagegen das tatsächlich zu erwartende Biegemoment ermittelt werden, so wird man die Untersuchungen zunächst für ein geschätztes Biegemoment in derselben Weise durchführen. Bei nicht erfüllter Verformungsbedingung wird man jedoch hier das eingeführte Biegemoment ändern und die Untersuchung bei ρ_{min} beginnend wiederholen. Überwogen die Betonverformungen die Spannstahldehnungen, so ist für den nächsten Rechnungsgang das Moment zu erhöhen und umgekehrt.

7. Vergleich mit Versuchsergebnissen

Zur Überprüfung der Brauchbarkeit wurde das Rechenverfahren auf einige der in Heft 130 des DAfStB mitgeteilten Versuche angewendet. Diese Versuche umfaßten 6 Balken mit geraden, außerhalb des Betonquerschnitts liegenden Spanngliedern. Hiervon waren allerdings 2 unsymmetrisch belastet, so daß sie für den Vergleich nicht herangezogen werden konnten. Bei den symmetrisch beanspruchten war die Belastung durch 4 Einzellasten so aufgebracht worden, daß die Momentlinie etwa der Parabel für gleichmäßig verteilte Belastung entsprach. Weiterhin waren alle für die Rechnung benötigten Baustoffeigenschaften bestimmt worden.

Außerdem wurde noch ein von A. Páez, Madrid, geprüfter Balken mit parabolisch geführtem Spannglied untersucht, der ebenfalls in dem Bericht [1] erwähnt wird. Er war durch 6 Einzellasten beansprucht; die Momentenverteilung war dabei ebenfalls annähernd parabolisch. Hierzu waren allerdings die Betoneigenschaften nicht vollständig mitgeteilt. Die benötigten weiteren Werte wurden aus der bei Rüsch u. a. angegebenen Prismendruckfestigkeit zu $\sigma_R = 55\,\mathrm{kp/cm^2}$ und $E_b = 330\,\mathrm{Mp/cm^2}$ angenommen.

Mit Ausnahme des Balkens «München V» enthielten sie keine schlaffe Bewehrung. Bei «München V» waren oben 2, unten 4 schlaffe Einlagen St I $\varnothing$ 10 mm angeordnet.

Ein Zahlenbeispiel für die Durchführung der Rechnung ist in [3] für einen Balken ohne schlaffe Bewehrung angegeben.

In der Zahlentafel sind die rechnerisch ermittelten Bruchmomente M_U und Spanngliedkräfte Z_s den im Versuch bestimmten gegenübergestellt.

Für Balken «München II» waren dem Rechenverfahren zugrunde gelegte wesentliche Annahmen nicht mehr erfüllt. Es ergaben sich tatsächlich merkliche Abweichungen zwischen Versuch und Rechnung, die nicht mehr durch die übliche Streuung der Baustoffeigenschaften allein erklärt werden können. Der Balken war extrem hoch vorgespannt. Die mittlere Vorspannung betrug

Zahlentafel. Vergleich der Ergebnisse der Versuche und der Rechnung

Bezeichnung	$-\frac{\sigma_v}{K}$	$V(Mp)$	Versuch $Z_s(Mp)$	Versuch $M_U(Mpm)$	Rechnung $Z_s(Mp)$	Rechnung $M_U(Mpm)$
München I	0,131	23,3	~29	6,77	29,2	6,48
München II	0,293	18,5	24,3	5,18	21,7	4,22
München V*)	0,126	24,3	29,6	8,51	31,8	8,55
München VI	0,084	21,8	30,2	7,60	31,8	7,70
Madrid	0,132	38,3	—	12,6	45,7	12,72

*) mit zusätzlicher schlaffer Bewehrung

0,29 K, die Randspannung am unteren Rand 0,66 K. Für eine so hohe Beanspruchung ist der für den Bereich der ungerissenen Zugzone angenommene lineare Zusammenhang zwischen Spannungen und Verformungen des Betons nicht mehr gegeben. Tatsächlich hat auch für diesen Balken das von RÜSCH u. a. vorgeschlagene Verfahren, das nichtlineare Verformungsbeziehungen für den Beton über die gesamte Balkenlänge benutzt, eine bessere Übereinstimmung ergeben (Moment 5,05 Mpm, Spanngliedkraft 24,7 Mp). Das errechnete Bruchmoment liegt jedoch auf der sicheren Seite.

Bei den 4 anderen Balken, bei denen die Rechenannahmen gegeben waren, liefert der Vergleich dagegen eine überraschend genaue Übereinstimmung der errechneten mit den im Versuch bestimmten Werten. Die Abweichungen betragen beim Bruchmoment weniger als 5%. Sie sind damit allein aus den unvermeidlichen Streuungen der Baustoffeigenschaften gut erklärbar. Damit ist gezeigt worden, daß das Bruchmoment des rechteckigen Spannbetonbalkens ohne Verbund mit dem hier beschriebenen Verfahren im Rahmen der Unsicherheit der benutzten Ausgangsgrößen, insbesondere der Baustoffkennwerte, zutreffend vorhergesagt werden kann.

Bezeichnungen

E_b Elastizitätsmodul des Betons
E_e Elastizitätsmodul des schlaffen Bewehrungsstahls
E_s Elastizitätsmodul des Spannstahls
F_b Betonquerschnitt des Balkens
F_s Querschnitt des Spanngliedes
I_b Trägheitsmoment des vollen Betonquerschnitts
K Prismendruckfestigkeit des Betons
M Moment
N Normalkraft
x Längskoordinate mit Ursprung am Balkenende
$\bar{x}$ Längskoordinate mit Ursprung in Balkenmitte
V Spanngliedkraft nach Kriechen und Schwinden
Z_s Spanngliedkraft im Bruchzustand

Z_e Kraft der schlaffen Bewehrung
δ_{b1} Betonverformungen in der Faser der Spanngliedachse im ungerissenen Bereich
δ_{b2} dito im gerissenen Bereich
δ_s Verformung des Spanngliedes
ϵ_b Betondehnung
η bezogene Querschnittskoordinate
μ_e Querschnitt der schlaffen Bewehrung, bezogen auf den Betonquerschnitt (Bewehrungsverhältnis)
σ_e Spannung der schlaffen Bewehrung
σ_s Spannung des Spannstahls

Literatur

1. Rüsch, H., Kordina, K. und Zelger, C.: Bruchsicherheit bei Vorspannung ohne Verbund. Heft 130 DAfStB. Berlin 1959.
2. Rüsch, H.: Versuche zur Festigkeit der Biegedruckzone. Heft 120 DAfStB. Berlin 1958.
3. Plähn, J.: On the Ultimate Moment Analysis of Unbonded Prestressed Concrete Beams. Vorbericht Seminar "Problems of Prestressing" der indischen nationalen Gruppe der IVBH in Madras 1970, S. III/63.
4. Zerna, W.: Spannbeton. Eine Einführung in seine Theorie. Düsseldorf 1953.

Zusammenfassung

Die Vorausberechnung der Momententragfähigkeit des statisch bestimmt gelagerten Spannbetonbalkens ohne Verbund erfordert die Bestimmung des Spannungszustandes des 1fach innerlich statisch unbestimmten Systems unter Berücksichtigung nichtlinearer Verformungsbeziehungen für die Werkstoffe Beton und Stahl sowie der Veränderlichkeit der Querschnitte mit dem Biegemoment infolge des Aufreißens der Zugzone. Eine Lösung dieser Aufgabe wird für den Balken mit Rechteckquerschnitt unter gleichmäßig verteilter Belastung angegeben. Die Brauchbarkeit der Lösung wird durch Vergleich mit Versuchsergebnissen dargelegt.

Summary

In order to calculate the moment carrying capacity of an unbonded, simply supported, prestressed concrete beam it is necessary to determine the state of stress throughout this one-fold internally indeterminate system. The problem is complicated by non-linear material behaviour and variation in the cross section with moment due to cracking of the tension zone.

A solution to this problem is presented for the case of a beam with rectangular cross section subjected to a uniformly distributed loading. The applicability of the solution is demonstrated by comparison with test results.

Résumé

On calcule la limite de résistance en flexion d'une poutre isolée en béton précontraint et en appui statiquement déterminé. Ce calcul exige la détermination de l'état de tension du système intérieurement hyperstatique de seul degré en tenant compte des relations non linéaires de déformation pour les matériaux béton et acier ainsi que la variation de section avec le moment par suite des fissures dans la zone de traction. On donne une solution de ce problème pour une poutre de section rectangulaire soumise à une charge répartis. La validité de la solution est établie par comparaison avec les résultats des expériences.

Transverse Shear Deformation in Multicell Box Beam Bridges

Déformations latérales dues au cisaillement des poutres en caisson multicellulaire

Schubverformung in Querrichtung von mehrzelligen Kastenträger-Brücken

J. C. ROBERTSON
BSc, Research Assistant, University of Dundee

R. P. PAMA
PhD, Research Fellow, University of Dundee

A. R. CUSENS
PhD, Professor of Civil Engineering, University of Dundee

Notation

a	spacing of webs in box-beam section
b	half-width of bridge
c	position of load from the support
D_1	coupling rigidity per unit length of the bridge
D_2	coupling rigidity per unit width of the bridge
D_x	flexural rigidity per unit width of the bridge
D_y	flexural rigidity per unit length of the bridge
D_{xy}	torsional rigidity per unit width of the bridge
D_{yx}	torsional rigidity per unit length of the bridge
E	elastic modulus
G	shear modulus
h	overall depth of bridge
I	second moment of area
J	torsional second moment
$2H$	total torsional rigidity of the bridge
H_n	load function
L	span of bridge
M_x	longitudinal bending moment per unit width of the bridge
M_y	transverse bending moment per unit length of the bridge
M_{xy}	torsional moment per unit width of the bridge
M_{yx}	torsional moment per unit length of the bridge

n harmonic
R_x longitudinal reactive force per unit width of the bridge
R_y transverse reactive force per unit length of the bridge
S_B shear stiffness
V_x longitudinal shear per unit width of the bridge
V_y transverse shear per unit length of the bridge
w total vertical deflection
w_B deflection due to bending
w_S deflection due to shear
y_p distance of station from the load
α torsional parameter
α_s effective torsional parameter
α_n parameter dependent on the harmonic
η_1 dimensionless parameter defining the left hand edge of the bridge
η_2 dimensionless parameter defining the right hand edge of the bridge
θ flexural parameter
θ_S effective flexural parameter
γ shearing strain

Introduction

The box section beam is finding increasing application in bridge construction. The section is relatively light in weight but strong in torsion and flexure. A bridge deck which is composed of a multi-cell box section (six or more cells)

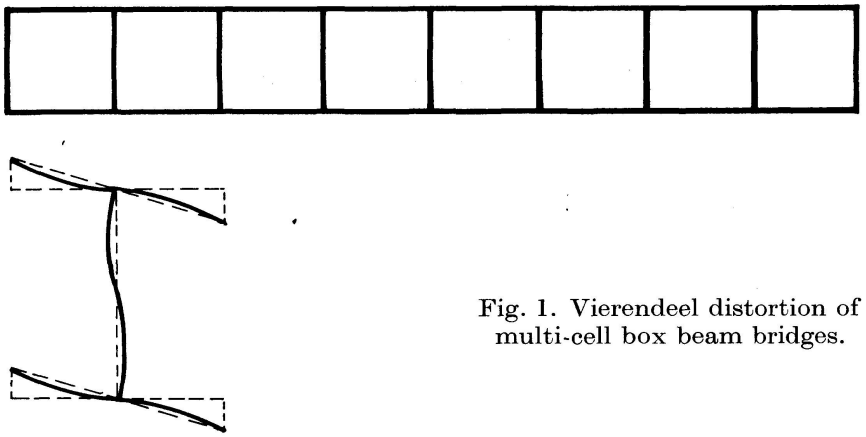


Fig. 1. Vierendeel distortion of multi-cell box beam bridges.

may be analysed as an orthotropic plate by conventional methods [1, 2, 3]. However if the webs or flanges of the box are slender, distortion of the cross-section is likely to occur in the absence of transverse diaphragms. Fig. 1 illustrates the deformation of the transverse cross-section in the manner of a vierendeel frame. Such vierendeel distortion will cause an increase in both deflection and longitudinal moment values in the proximity of concentrated

loads. MASSONNET and GANDOLFI [4] have drawn attention to this effect and showed that increases in deformation can be dramatic in the case of shear-weak sections. They also suggest a semi-empirical approach to the determination of deflection and moment in practical cases. More recently, SAWKO and COPE [5] have also considered shear distortion in box beams using a limited approach based on the assumption of a plane stress condition in the flanges of the box.

In a large proportion of practical designs of multi-cell box beam bridge decks significant shear distortion of the transverse cross-section will not occur but clearly neglect of this effect in all cases could have serious implications. In this paper the Huber orthotropic plate equation is modified by the introduction of an additional parameter to account for shear distortion. The resulting differential equations are solved by the use of half-range Fourier series and a general method of analysis is developed for the determination of deflections, moments and shears in a simply supported multi-cell box-section bridge deck under concentrated or line loads.

Theoretical Analysis

In addition to the customary assumptions made in the analysis of elastic plates, the following assumptions are made:

1. The total deflection of the deck is equal to the sum of the deflections due to bending and shear, i.e.

$$w = w_B + w_S, \tag{1}$$

where w is the total deflection; w_B and w_S are the deflections due to bending and shear respectively.

2. The transverse shear is equal to the product of the shear stiffness and the slope of the shear deformation in the transverse direction

$$V_y = S_B\left(\frac{\partial w_S}{\partial y}\right), \tag{2}$$

where S_B is the shear stiffness of the deck. The value of S_B is explained later in the section on elastic rigidities of the deck.

3. The curvature of the deck in the longitudinal direction is derived from the total deflection while for the transverse direction it is derived from the deflection due to bending only.

Thus,

$$\phi_x = \frac{\partial^2 w}{\partial x^2}, \tag{3}$$

$$\phi_y = \frac{\partial^2 w_B}{\partial y^2}. \tag{4}$$

It follows from this assumption that the longitudinal and transverse bending moments are

$$M_x = -\left[D_x \frac{\partial^2 w}{\partial x^2} + D_1 \frac{\partial^2 w_B}{\partial y^2}\right], \tag{5}$$

$$M_y = -\left[D_y \frac{\partial^2 w_B}{\partial y^2} + D_2 \frac{\partial^2 w}{\partial x^2}\right]. \tag{6}$$

The twisting moments in the two orthogonal directions x and y are obtained from the shearing strain

$$\gamma = \frac{\partial^2 w}{\partial x\, \partial y} - \frac{1}{S_B}\left(\frac{\partial V_y}{\partial x}\right). \tag{7}$$

From Eq. (2) this may be expressed as

$$\gamma = \left(\frac{\partial^2 w}{\partial x\, \partial y} - \frac{\partial^2 w_S}{\partial x\, \partial y}\right) = \frac{\partial^2 w_B}{\partial x\, \partial y}. \tag{8}$$

Hence the shearing strain is a function of the deformation due to bending only and the twisting moments become

$$M_{xy} = D_{xy}\gamma = D_{xy} \frac{\partial^2 w_B}{\partial x\, \partial y}, \tag{9}$$

$$M_{yx} = -D_{yx}\gamma = -D_{yx} \frac{\partial^2 w_B}{\partial x\, \partial y}. \tag{10}$$

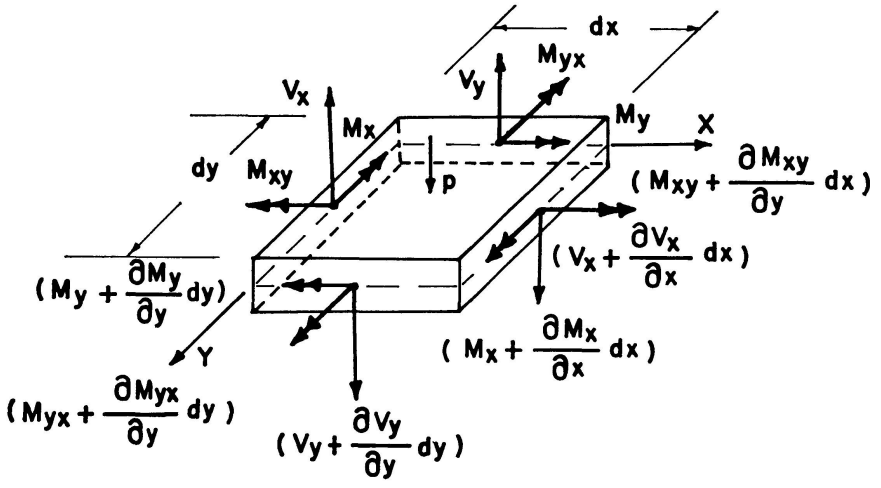


Fig. 2. Free-body diagram of an element of the deck.

From these moment-curvature relationships, the shearing and reactive forces (see Fig. 2) may be shown to be

$$V_x = \left(\frac{\partial M_x}{\partial x} + \frac{\partial M_{yx}}{\partial y}\right) = -\left[D_x \frac{\partial^3 w}{\partial x^3} + (D_{yx} + D_1) \frac{\partial^3 w_B}{\partial x\, \partial y^2}\right], \tag{11}$$

$$V_y = \left(\frac{\partial M_y}{\partial y} + \frac{\partial M_{xy}}{\partial x}\right) = -\left[D_y \frac{\partial^3 w_B}{\partial y^3} + D_2 \frac{\partial^3 w}{\partial x^2\, \partial y} + D_{xy} \frac{\partial^3 w_B}{\partial x^2\, \partial y}\right], \tag{12}$$

$$R_x = \left(V_x - \frac{\partial M_{xy}}{\partial y}\right) = -\left[D_x \frac{\partial^3 w}{\partial x^3} + (D_{xy} + D_{yx} + D_1) \frac{\partial^3 w_B}{\partial x \partial y^2}\right], \tag{13}$$

$$R_y = \left(V_y + \frac{\partial M_{yx}}{\partial x}\right) = -\left[D_y \frac{\partial^3 w_B}{\partial y^3} + D_2 \frac{\partial^3 w}{\partial x^2 \partial y} + (D_{xy} + D_{yx}) \frac{\partial^3 w_B}{\partial x^2 \partial y}\right]. \tag{14}$$

Consideration of the equilibrium of the vertical forces and the summation of moments in the two orthogonal directions leads to the usual equation for elastic plates

$$\frac{\partial^2 M_x}{\partial x^2} + \frac{\partial^2 M_y}{\partial y^2} + \frac{\partial^2 M_{yx}}{\partial x \partial y} - \frac{\partial^2 M_{xy}}{\partial x \partial y} = -p(x, y). \tag{15}$$

In terms of the deflections w and w_B this equation may be expressed as

$$D_x \frac{\partial^4 w}{\partial x^4} + (D_1 + D_{xy} + D_{yx}) \frac{\partial^4 w_B}{\partial x^2 \partial y^2} + D_2 \frac{\partial^4 w}{\partial x^2 \partial y^2} + D_y \frac{\partial^4 w_B}{\partial y^4} = p(x, y). \tag{16}$$

It is apparent from this expression that if $w_B = w$, the equation reduces to the HUBER orthotropic plate equation [6].

The slopes in the transverse direction may be expressed as

$$\frac{\partial w}{\partial y} = \frac{\partial w_B}{\partial y} + \frac{\partial w_S}{\partial y}. \tag{17}$$

From Eqs. (2) and (12),

$$\frac{\partial w}{\partial y} = \frac{\partial w_B}{\partial y} + \frac{V_y}{S_B} \tag{18}$$

or

$$\frac{\partial w}{\partial y} = \frac{\partial w_B}{\partial y} - \frac{1}{S_B}\left[D_y \frac{\partial^3 w_B}{\partial y^3} + D_2 \frac{\partial^3 w}{\partial x^2 \partial y} + D_{xy} \frac{\partial^3 w_B}{\partial x^2 \partial y}\right]. \tag{19}$$

The equation may be re-arranged into the form

$$S_B \frac{\partial w}{\partial y} - S_B \frac{\partial w_B}{\partial y} + D_y \frac{\partial^3 w_B}{\partial y^3} + D_2 \frac{\partial^3 w}{\partial x^2 \partial y} + D_{xy} \frac{\partial^3 w_B}{\partial x^2 \partial y} = 0. \tag{20}$$

Thus, the three original basic assumptions result in two simultaneous differential Eqs. (16) and (20) in w and w_B. If the load and deflections are expressed in half-range Fourier sine series, for the nth harmonic of the series the contributions to the total and bending deflections may be written as

$$w_n = W_n \sin \alpha_n x, \tag{21}$$

$$w_{Bn} = W_{Bn} \sin \alpha_n x, \tag{22}$$

where

$$\alpha_n = \frac{n\pi}{L}. \tag{23}$$

and L is the span of the deck.

The complete solution may be split into homogeneous and particular parts. For the homogeneous part, the following ordinary differential equations are

obtained if Eqs. (21) and (22) are substituted into Eqs. (16) and (20), with $p(x, y)$ set to zero:

$$\alpha_n^4 D_x W_n - \alpha_n^2 D_2 \frac{d^2 W_n}{dy^2} - \alpha_n^2 (D_1 + D_{xy} + D_{yx}) \frac{d^2 W_{Bn}}{dy^2} + D_y \frac{d^4 W_{Bn}}{dy^4} = 0, \quad (24)$$

$$S_B \frac{dW_n}{dy} - S_B \frac{dW_{Bn}}{dy} + D_y \frac{d^3 W_{Bn}}{dy^3} - \alpha_n^2 D_2 \frac{dW_n}{dy} - \alpha_n^2 D_{xy} \frac{dW_{Bn}}{dy} = 0. \quad (25)$$

Using the operator notation

$$D^m = \frac{d^m}{dy^m}, \quad (26)$$

these two equations may be expressed in matrix form as follows

$$\left[\begin{array}{c|c} \alpha_n^4 D_x - \alpha_n^2 D_2 D^2 & -\alpha_n^2 (D_1 + D_{xy} + D_{yx}) D^2 + D_y D^4 \\ \hline S_B D - \alpha_n^2 D_2 D & -(S_B + \alpha_n^2 D_{xy}) D + D_y D^3 \end{array}\right] \left[\begin{array}{c} W_n \\ \hline W_{Bn} \end{array}\right] = \left[\begin{array}{c} 0 \\ \hline 0 \end{array}\right]. \quad (27)$$

For a non-trivial solution, the determinant of Eq. (27) must be zero, hence

$$\{(-S_B D_y D^5) + [\alpha_n^4 D_x D_y + \alpha_n^2 D_2 S_B + \alpha_n^4 D_2 D_{xy} + \alpha_n^2 S_B (D_1 + D_{xy} + D_{yx}) - \alpha_n^4 D_2 (D_1 + D_{xy} + D_{yx})] D^3 + [-\alpha_n^4 D_x S_B - \alpha_n^6 D_x D_y] D\} \begin{bmatrix} W_n \\ W_{Bn} \end{bmatrix} = \begin{bmatrix} 0 \\ 0 \end{bmatrix}. \quad (28)$$

For simplicity, the following substitutions are made:

$$2H^* = (D_1 + D_{xy} + D_{yx}), \quad (29)$$

$$P_1 = -S_B D_y, \quad (30)$$

$$P_2 = S_B (D_2 + 2H^*) + \alpha_n^2 [D_x D_y - D_2 (D_1 + D_{yx})], \quad (31)$$

$$P_3 = -D_x (S_B + \alpha_n^2 D_{xy}) \quad (32)$$

and the operator equation may be written as

$$\{(P_1 D^5 + \alpha_n^2 P_2 D^3 + \alpha_n^4 P_3 D)\} \begin{bmatrix} W_n \\ W_{Bn} \end{bmatrix} = \begin{bmatrix} 0 \\ 0 \end{bmatrix}. \quad (33)$$

The absence of the term in D^0 implies that the total deflection function is of the form

$$w = w_B + w_S + c \ (= \text{constant}).$$

For this to be compatible with Eq. (1), the constant c must be zero which implies that the power of the operator equation may be reduced by one, thus

$$\{P_1 D^4 + \alpha_n^2 P_2 D^2 + \alpha_n^4 P_3\} \begin{bmatrix} W_n \\ W_{Bn} \end{bmatrix} = \begin{bmatrix} 0 \\ 0 \end{bmatrix}. \quad (34)$$

Consider now an ordinary differential equation of the type

$$P_1 \frac{d^4 W_n}{dy^4} + \alpha_n^2 P_2 \frac{d^2 W_n}{dy^2} + \alpha_n^4 P_3 W_n = 0 \quad (35)$$

and assume a solution of the form

$$W_n = A\, e^{(\alpha_n s)y}, \tag{36}$$

where A is an arbitrary constant. Upon substitution into Eq. (35), the characteristic equation is obtained as

$$P_1(\alpha_n s)^4 + \alpha_n^2 P_2(\alpha_n s)^2 + \alpha_n^4 P_3 = 0. \tag{37}$$

The roots may be evaluated by quadratic formula and the expression for the quantity s of the roots may be obtained as

$$s = \pm\sqrt{\left(\frac{-P_2}{2P_1}\right) \pm \sqrt{\left(\frac{-P_2}{2P_1}\right)^2 - \left(\frac{P_3}{P_1}\right)}}. \tag{38}$$

The four roots are $+(\alpha_n s_1)$, $+(\alpha_n s_2)$, $-(\alpha_n s_1)$ and $-(\alpha_n s_2)$. This may be generally represented as $\pm\alpha_n s_j$ so that j will have values of 1 and 2 only.

Introducing a parameter α_s such that

$$\alpha_s = \frac{(D_{xy} + D_{yx} + D_1 + D_2) + \frac{\alpha_n^2}{S_B}[D_x D_y - D_2(D_1 + D_{yx})]}{2\sqrt{D_x D_y\left(1 + \frac{\alpha_n^2 D_{xy}}{S_B}\right)}}, \tag{39}$$

the quantity s_j of the root may be simplified as

$$s_j = \sqrt[4]{\frac{D_x}{D_y}\left(1 + \frac{\alpha_n^2 D_{xy}}{S_B}\right)}\sqrt{\alpha_s \pm \sqrt{\alpha_s^2 - 1}}. \tag{40}$$

Upon inspection of Eq. (40) it becomes apparent that another parameter is identified as

$$\theta_s = \frac{b}{L}\sqrt[4]{\frac{D_x}{D_y}\left(1 + \frac{\alpha_n^2 D_{xy}}{S_B}\right)}. \tag{41}$$

These parameters α_s and θ_s are the equivalents of the torsional and flexural parameter α and θ originally by MASSONNET [2] for use in the conventional orthotropic plate theory. It follows that

$$\lim_{S_B \to \infty} \alpha_s = \frac{(D_{xy} + D_{yx} + D_1 + D_2)}{2\sqrt{D_x D_y}} = \alpha \tag{42}$$

and

$$\lim_{S_B \to \infty} \theta_s = \frac{b}{L}\sqrt[4]{\frac{D_x}{D_y}} = \theta. \tag{43}$$

Clearly the parameters α_s and θ_s vary with the harmonic hence a generalized notation will be employed in the solution.

Solution of the Orthotropic Plate Equation

Consider a bridge deck of span L and width $2b$ as an orthotropic plate simply supported along the ends $x = 0$ and $x = L$. The complete solution of the

non-homogeneous Eq. (16) may be obtained by adding the homogeneous and particular parts of the solution,

$$w = w^h + w^p . \tag{44}$$

The letters h and p will be used as superscript or subscript as appropriate to denote the quantities associated with the homogeneous and particular parts respectively. w^p is the particular part of the solution obtained by considering the effect of the loading. This does not in general satisfy all the boundary conditions. w^h, the homogeneous part is added to give the complete solution. The homogeneous part has to satisfy the equation without the lateral load $p(x, y)$ but with the boundary forces acting on it.

Homogeneous Solution

The roots of the characteristic equation may be real or complex and exist in pairs denoted by $+(\alpha_n s_j)$ and $-(\alpha_n s_j)$ where j has values 1 and 2. The amplitude of the deflection function may be written as

$$w^h = \sum_{j=1}^{2} (A_j^h e^{-\alpha_n s_j y_h} + A_{j+2}^h e^{+\alpha_n s_j y_h}), \tag{45}$$

$$w_B^h = \sum_{j=1}^{2} (B_j^h e^{-\alpha_n s_j y_h} + B_{j+2}^h e^{+\alpha_n s_j y_h}). \tag{46}$$

For the homogeneous solution, the distance of the reference station measured transversely from the longitudinal centre line of the deck is denoted by y_h. Stations to the right of the centre line are considered positive and those to the left as negative.

The relationships between the arbitrary constants in Eq. (45) and (46) may be established from the conditional Eq. (25) if these deflection functions are substituted into it, thus

$$\begin{aligned}(S_B - \alpha_n^2 D_2)(-\alpha_n s_j A_j^h e^{-\alpha_n s_j y_h}) + (S_B - \alpha_n^2 D_2)(\alpha_n s_j A_{j+2}^h e^{+\alpha_n s_j y_h}) \\ -[S_B - D_y \alpha_n^2 s_j^2 + \alpha_n^2 D_{xy}](-\alpha_n s_j B_j^h e^{-\alpha_n s_j y_h}) \\ -[S_B - D_y \alpha_n^2 s_j^2 + \alpha_n^2 D_{xy}](\alpha_n s_j B_{j+2}^h e^{+\alpha_n s_j y_h}) = 0 .\end{aligned} \tag{47}$$

Collecting all terms which are functions of $e^{-\alpha_n s_j y_h}$ and equating them to zero, an equation is obtained relating the arbitrary constants A_j^h and B_j^h,

$$B_j^h = A_j^h \frac{(S_B - \alpha_n^2 D_2)}{(S_B - D_y \alpha_n^2 s_j + \alpha_n^2 D_{xy})}. \tag{48}$$

The same relationship may be shown to exist between B_{j+2}^h and A_{j+2}^h if all terms containing $e^{+\alpha_n s_j y_h}$ are collected and equated to zero.

Setting

$$F W_j = \frac{B_j^h}{A_j^h} = \frac{B_{j+2}^h}{A_{j+2}^h} = \frac{(S_B - \alpha_n^2 D_2)}{(S_B - D_y \alpha_n^2 s_j + \alpha_n^2 D_{xy})} \tag{49}$$

the deflection functions for the homogeneous part may be written as follows:

$$w^h = \sum_{n=1}^{\infty} \sin \alpha_n x \sum_{j=1}^{2} (A_j^h e^{-\alpha_n s_j y_h} + A_{j+2}^h e^{+\alpha_n s_j y_h}), \tag{50}$$

$$w_B^h = \sum_{n=1}^{\infty} \sin \alpha_n x \sum_{j=1}^{2} F W_j (A_j^h e^{-\alpha_n s_j y_h} + A_{j+2}^h e^{+\alpha_n s_j y_h}). \tag{51}$$

It may be shown from Eq. (49) that the

$$\lim_{S_B \to \infty} F W_j = \frac{B_j^h}{A_j^h} = \frac{B_{j+2}^h}{A_{j+2}^h} = 1 \tag{52}$$

and the bending deflection is equal to the total deflection of the deck.

Particular Solution

An infinitely wide bridge deck, as seen in Fig. 3 under the action of a line load expressed in sinusoidal form, will be used in evaluating the deflection

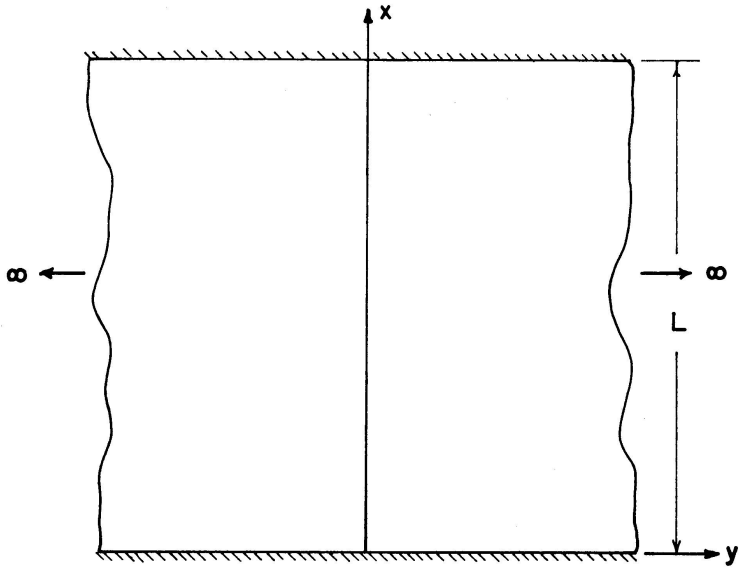


Fig. 3. Coordinate axis for infinitely wide bridge deck.

function w^p. For the particular part, the deflections may be expressed as

$$w^p = \sum_{n=1}^{\infty} \sin \alpha_n x \sum_{j=1}^{2} (A_j^p e^{-\alpha_n s_j y_p} + A_{j+2}^p e^{+\alpha_n s_j y_p}), \tag{53}$$

$$w_B^p = \sum_{n=1}^{\infty} \sin \alpha_n x \sum_{j=1}^{2} (B_j^p e^{-\alpha_n s_j y_p} + B_{j+2}^p e^{+\alpha_n s_j y_p}), \tag{54}$$

where the arbitrary constants are identified by the superscript p. The transverse distance of the station from the load is denoted by y_p. To preserve the symmetry of the system, an absolute value will be used for y_p thus an adjustment in sign is necessary for anti-symmetric quantities such as R_y for example. This will be fully explained later.

For the deflection function and its derivates to vanish at distances far from the load, the positive pairs of the roots $\alpha_n s_j$ will be discarded and the remaining expressions are simplified to the forms

$$w^p = \sum_{n=1}^{\infty} \sin \alpha_n x \sum_{j=1}^{2} A_j^p e^{-\alpha_n s_j y_p}, \tag{55}$$

$$w_B^p = \sum_{n=1}^{\infty} \sin \alpha_n x \sum_{j=1}^{2} B_j^p e^{-\alpha_n s_j y_p}. \tag{56}$$

Since the same conditional equation applies to the homogeneous and particular solutions, the arbitrary constants B_j^p and A_j^p are related in the same way as B_j^h and A_j^h, and hence the particular parts of the deflection functions may also be written in terms of the factor $F W_j$

$$w^p = \sum_{n=1}^{\infty} \sin \alpha_n x \sum_{j=1}^{2} A_j^p e^{-\alpha_p s_j y_p}, \tag{57}$$

$$w_B^p = \sum_{n=1}^{\infty} \sin \alpha_n x \sum_{j=1}^{2} F W_j A_j^p e^{-\alpha_n s_j y_p}. \tag{58}$$

The two arbitrary constants ($A_{j=1}^p$ and $A_{j=2}^p$) are obtained from the two boundary conditions under the load, namely:

1. For each harmonic, the slope of the bending deflection in the transverse direction is zero,

i. e.
$$\left(\frac{\partial w_B^p}{\partial y}\right)_{y_p=0} \tag{59}$$

and by substitution of Eq. (58)

$$\sum_{j=1}^{\infty} F W_j s_j A_j^p = 0. \tag{60}$$

2. The reactive force under the load is equal to half the load. If the applied load is expressed in half-range Fourier sine series, then for each harmonic

$$(R_y^p)_{y_p=0} = -\frac{H_n}{2} \sin \alpha_n x, \tag{61}$$

where H_n is a load function which may be derived for any form of load. This boundary condition may be expressed in terms of the deflection functions as follows:

$$-\left[D_y \frac{\partial^3 w^p}{\partial y^3} + (D_{xy} + D_{yx}) \frac{\partial^3 w^p}{\partial x^2 \partial y} + D_2 \frac{\partial^3 w^p}{\partial x^2 \partial y}\right] = -\frac{H_n}{2} \sin \alpha_n x \tag{62}$$

or
$$\sum_{j=1}^{2} A_j^p [D_y \alpha_n^3 s_j^3 F W_j - (D_{xy} + D_{yx}) \alpha_n^3 s_j F W_j - D_2 \alpha_n^3 s_j] = -\frac{H_n}{2}. \tag{63}$$

For simplicity, the term inside the bracket of Eq. (63) may be replaced by $F R_{yj}$, thus

$$F R_{yj} = [D_y \alpha_n^3 s_j^3 F W_j - (D_{xy} + D_{yx}) \alpha_n^3 s_j F W_j - D_2 \alpha_n^3 s_j] \tag{64}$$

and the two arbitrary constants are determined accordingly.

Complete Solution

The complete solutions for w and w_B are obtained by adding the homogeneous and particular solutions:

$$w = \sum_{n=1}^{\infty} \sin \alpha_n x \sum_{j=1}^{2} [A_j^p e^{-\alpha_n s_j y_p} + A_j^h e^{-\alpha_n s_j y_h} + A_{j+2}^h e^{+\alpha_n s_j y_h}], \tag{65}$$

$$w_B = \sum_{n=1}^{\infty} \sin \alpha_n x \sum_{j=1}^{2} F W_j [A_j^p e^{-\alpha_n s_j y_p} + A_j^h e^{-\alpha_n s_j y_h} + A_{j+2}^h e^{+\alpha_n s_j y_h}]. \tag{66}$$

Both deflection functions are symmetrical and it is therefore convenient to use the notation $S Y_j$ for the function inside the bracket of Eqs. (65) and (66), so that

$$S Y_j = (A_j^p e^{-\alpha_n s_j y_p} + A_j^h e^{-\alpha_n s_j y_h} + A_{j+2}^h e^{+\alpha_n s_j y_h}). \tag{67}$$

It must be emphasized here that the term $S Y_j$ is a function of the number of the harmonic, the value of j and also the transverse positions of both the load and the reference station. The deflection functions may be simply written as

$$w = \sum_{n=1}^{\infty} \sin \alpha_n x \sum_{j=1}^{2} S Y_j, \tag{68}$$

$$w_B = \sum_{n=1}^{\infty} \sin \alpha_n x \sum_{j=1}^{2} F W_j S Y_j. \tag{69}$$

The distance y_p of the station from the load is an absolute value as already mentioned in the derivation of the particular solution. This means that for a symmetrical function such as w, the contribution of the particular part $A_j^p e^{-\alpha_n s_j y_p}$ requires no change of sign. However, for antisymmetrical functions such as M_{xy}, M_{yx}, V_y and R_y, it is necessary to consider the particular part as

$$K A_j^p e^{-\alpha_n s_j y_p},$$

where K has the value of $+1$ if the station is to the right of the load and -1 if it is situated to the left.

Consider the anti-symmetric reactive force R_y such that

$$\begin{aligned} R_y = \sum_{n=1}^{\infty} \sin \alpha_n x \sum_{j=1}^{2} (&F R_{yj} K A_j^p e^{-\alpha_n s_j y_p} \\ &+ F R_{yj} A_j^h e^{-\alpha_n s_j y_h} + F R_{yj+2} A_{j+2}^h e^{+\alpha_n s_j y_h}). \end{aligned} \tag{70}$$

The quantity $F R_{yj+2}$ may be obtained from the expression for $F R_{yj}$ by replacing s_j by $-s_j$. It then becomes apparent that

$$F R_{yj+2} = -F R_{yj}. \tag{71}$$

This change of sign is consistent for all anti-symmetric functions mentioned earlier on since each is dependent on an odd power of the root $\alpha_n s_j$. Thus, the

term inside the bracket of Eq. (70) may be replaced by a simple notation $A\,S\,Y_j$ so that

$$A\,S\,Y_j = F\,R_{yj}\,(K\,A_j^p\,e^{-\alpha_n s_j y_p} + A_j^h\,e^{-\alpha_n s_j y_p} - A_{j+2}^h\,e^{+\alpha_n s_j y_p}). \tag{72}$$

With these notations $S\,Y_j$ and $A\,S\,Y_j$, the deflections, moments, twists, shears and reactive forces may be expressed in an abbreviated form.

Boundary Conditions

The four arbitrary constants of the homogeneous solution are obtained from the boundary conditions at the edges of the deck. If the deck is elastically

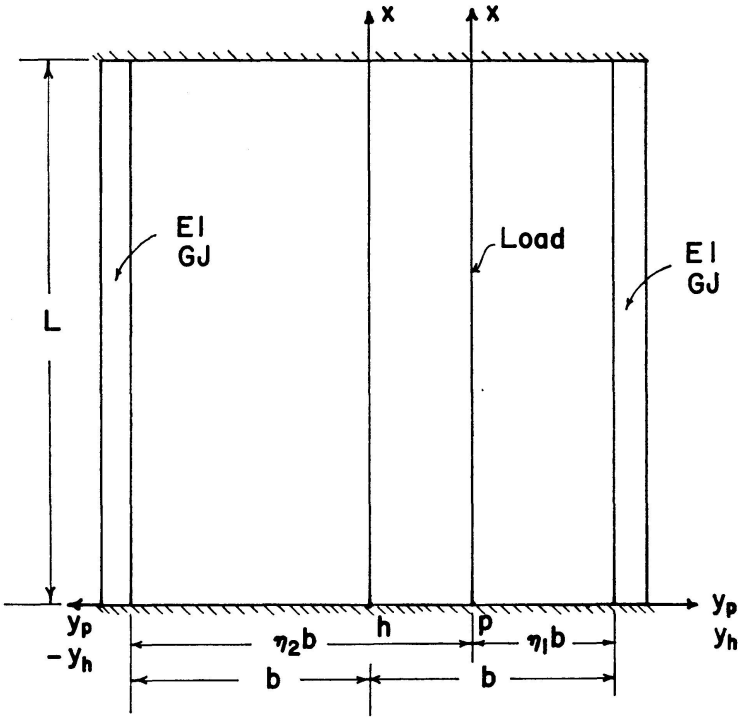


Fig. 4. Coordinate axes.

restrained by edge beams of flexural rigidity $E\,I$ and torsional rigidity $G\,J$ as shown in Fig. 4, the boundary conditions may be written as

$$(R_y^p)_{y_p=\eta_1 b} + (R_y^h)_{y_h=b} = -E\,I\left[\left(\frac{\partial^4 w^p}{\partial x^4}\right)_{y_p=\eta_1 b} + \left(\frac{\partial^4 w^h}{\partial x^4}\right)_{y_h=b}\right], \tag{73}$$

$$(R_y^p)_{y_p=\eta_2 b} + (R_y^h)_{y_h=-b} = +E\,I\left[\left(\frac{\partial^4 w^p}{\partial x^4}\right)_{y_p=\eta_2 b} + \left(\frac{\partial^4 w^h}{\partial x^4}\right)_{y_h=-b}\right], \tag{74}$$

$$(M_y^p)_{y_p=\eta_1 b} + (M_y^h)_{y_h=b} = +G\,J\left[\left(\frac{\partial^3 w^p}{\partial x^2\,\partial y}\right)_{y_p=\eta_1 b} + \left(\frac{\partial^3 w^h}{\partial x^2\,\partial y}\right)_{y_h=b}\right], \tag{75}$$

$$(M_y^p)_{y_p=\eta_2 b} + (M_y^h)_{y_h=-b} = -G\,J\left[\left(\frac{\partial^3 w^p}{\partial x^2\,\partial y}\right)_{y_p=\eta_2 b} + \left(\frac{\partial^3 w^h}{\partial x^2\,\partial y}\right)_{y_h=-b}\right], \tag{76}$$

$$\sum_{j=1}^{2}\{(F\,R_{yj}+\alpha_n^4\,E\,I)\;\;[A_j^p\,e^{-\eta_1\beta_j}+A_j^h\,e^{-\beta_j}]\;\;-(F\,R_{yj}-\alpha_n^4\,E\,I)\,A_{j+2}^h\,e^{\beta_j}\}\;\;=0\,,\quad(77)$$

$$\sum_{j=1}^{2}\{(F\,R_{yj}+\alpha_n^4\,E\,I)\;\;[A_j^p\,e^{-\eta_2\beta_j}+A_{j+2}^h\,e^{-\beta_j}]-(F\,R_{yj}-\alpha_n^4\,E\,I)\,A_j^h\,e^{\beta_j}\}\;\;=0\,,\quad(78)$$

$$\sum_{j=1}^{2}\{(F\,M_{yj}-\alpha_n^3\,s_j\,G\,J)[A_j^p\,e^{-\eta_1\beta_j}+A_j^h\,e^{-\beta_j}]\;\;+(F\,M_{yj}+\alpha_n^3\,s_j\,G\,J)\,A_{j+2}^h\,e^{\beta_j}\}=0\,,\quad(79)$$

$$\sum_{j=1}^{2}\{(F\,M_{yj}-\alpha_n^3\,s_j\,G\,J)[A_j^p\,e^{-\eta_2\beta_j}+A_{j+2}^h\,e^{-\beta_j}]+(F\,M_{yj}+\alpha_n^3\,s_j\,G\,J)\,A_j^h\,e^{\beta_j}\}\;\;=0\,,\quad(80)$$

where
$$\beta_j=\alpha_n\,s_j\,b \tag{81}$$

and
$$F\,M_{yj}=(D_2\,\alpha_n^2-D_y\,\alpha_n^2\,s_j^2\,F\,W_j)\,. \tag{82}$$

Thus the four arbitrary constants are determined by solving these four equations simultaneously. With the deflections w and w_B known, the bending and twisting moments, shearing and reactive forces are determined by successive differentiation. These are summarized as follows:

Deflection

Total:
$$w\;\;=\sum_{n=1}^{\infty}\sin\alpha_n\,x\sum_{j=1}^{2}S\,Y_j\,. \tag{83}$$

Bending:
$$w_B\;=\sum_{n=1}^{\infty}\sin\alpha_n\,x\sum_{j=1}^{2}F\,W_j\,(S\,Y_j)\,. \tag{84}$$

Longitudinal Bending Moment:
$$M_x\;=\sum_{n=1}^{\infty}\sin\alpha_n\,x\sum_{j=1}^{2}F\,M_{xj}\,S\,Y_j\,. \tag{85}$$

Transverse Bending Moment:
$$M_y\;=\sum_{n=1}^{\infty}\sin\alpha_n\,x\sum_{j=1}^{2}F\,M_{yj}\,S\,Y_j\,. \tag{86}$$

Transverse Twisting Moment:
$$M_{xy}=\sum_{n=1}^{\infty}\cos\alpha_n\,x\sum_{j=1}^{2}F\,M_{xyj}\,A\,S\,Y_j\,. \tag{87}$$

Longitudinal Twisting Moment:
$$M_{yx}=\sum_{n=1}^{\infty}\cos\alpha_n\,x\sum_{j=1}^{2}F\,M_{yxj}\,A\,S\,Y_j\,. \tag{88}$$

Longitudinal Shearing Force:
$$V_x\;\;=\sum_{n=1}^{\infty}\cos\alpha_n\,x\sum_{j=1}^{2}F\,V_{xy}\,S\,Y_j\,. \tag{89}$$

Transverse Shearing Force:
$$V_y\;\;=\sum_{n=1}^{\infty}\sin\alpha_n\,x\sum_{j=1}^{2}F\,V_{yj}\,A\,S\,Y_j\,. \tag{90}$$

Longitudinal Reactive Force:

$$R_x = \sum_{n=1}^{\infty} \cos \alpha_n x \sum_{j=1}^{2} F R_{xj} S Y_j . \tag{91}$$

Transverse Reactive Force:

$$R_y = \sum_{n=1}^{\infty} \sin \alpha_n x \sum_{j=1}^{2} F R_{yj} A S Y_j . \tag{92}$$

The quantities $F R_{yj}$ and $F M_{yj}$ have been defined earlier and the rest are given as follows:

$$F M_{xj} = (\alpha_n^2 D_x - \alpha_n^2 s_j^2 D_1 F W_j), \tag{93}$$

$$F M_{xyj} = -D_{xy} \alpha_n^2 s_j F W_j , \tag{94}$$

$$F M_{yxj} = D_{yx} \alpha_n^2 s_j F W_j , \tag{95}$$

$$F V_{xj} = D_x \alpha_n^3 - (D_1 + D_{yx}) \alpha_n^3 s_j^2 F W_j , \tag{96}$$

$$F R_{xj} = D_x \alpha_n^3 - (D_1 + D_{xy} + D_{yx}) \alpha_n^3 s_j^2 F W_j , \tag{97}$$

$$F V_{yj} = (D_y s_j^3 - D_{xy} s_j) \alpha_n^3 F W_j - D_2 \alpha_n^3 s_j . \tag{98}$$

Elastic Rigidities of the Deck

Considering a multicell box-beam bridge deck without intermediate diaphragms (see Fig. 6), the flexural rigidities, D_x and D_y in the longitudinal and transverse directions respectively, may be defined in terms of moment per unit curvature and are independent of the value of the shearing rigidity S_B. For the calculation of D_x, the second moment of area of the longitudinal section is taken in the usual way. This value is expressed per unit width and then multiplied by the value of Young's modulus to give the flexural rigidity D_x. The corresponding flexural rigidity in the transverse direction is obtained from the top and bottom flanges of the deck.

The torsional rigidity D_{xy} is obtained by considering the shear flow in the multicell structure. For decks where webs and flanges are relatively small as compared with the dimensions of the deck, Wittrick's equation [7] may be used. For decks with six or more cells, the torsional rigidity may be obtained by neglecting the net shear flow through the internal webs since these are generally small; the effective shear flow is taken along the flanges and outermost webs. Thus Bredt's single-cell formula [8] may be used. The torsional rigidity is expressed per unit width and D_{xy} is taken as one-half of this quantity. If the deck is closed at the ends by diaphragms, then a similar approach may be used to calculate D_{yx} in the longitudinal direction.

The coupling rigidities D_1 and D_2 are both taken as Poisson's ratio times the contribution to D_y from the flanges.

The shear stiffness S_B may be obtained by considering a transverse slice of the deck of unit width subjected to equal and opposite shearing forces V_{y1} and V_{y2} at the ends as shown in Fig. 5. This isolated slice may be considered as a frame with points of contraflexure in the flanges midway between the

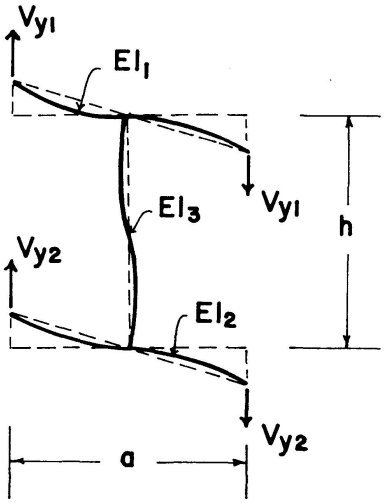


Fig. 5. Assumed frame deformation (Holmberg).

webs. HOLMBERG [9] has shown that for such a frame the shear stiffness S_B may be simplified to the form

$$S_B = \frac{1}{\frac{a\,h}{12\,E\,I_3} + \frac{a^2\,[3\,h\,(I_1+I_2)+a\,I_3]}{12\,E\,[12\,h\,I_1\,I_2+a\,I_3\,(I_1+I_2)]}}.$$

It will be appreciated that the assumptions involved in Holmberg's analysis are not completely realistic. However, in comparisons with more accurate analyses involving the use of computer programs for vierendeel frameworks, Holmberg's method has been found to give safe values for a range of web and flange dimensions. It is adopted here as a simple and conservative procedure for assessing shear stiffness.

Discussion of Results

In order to show the effect of vierendeel distortion on the load distribution characteristics of the deck, a twelve cell box-beam bridge deck is taken as an example. The dimensions are shown in Fig. 6 and the elastic rigidities in flexure, torsion and shear are calculated in the appendix.

The results are expressed in terms of distribution coefficients for deflection and moment. These coefficients were obtained by dividing individual values of deflection or longitudinal moment by their mean value as obtained from simple beam theory. For convenience the transverse bending moment is expressed in terms of the mean longitudinal moment. Using these elastic rigidities, the deck was analyzed with and without shear deformation and the

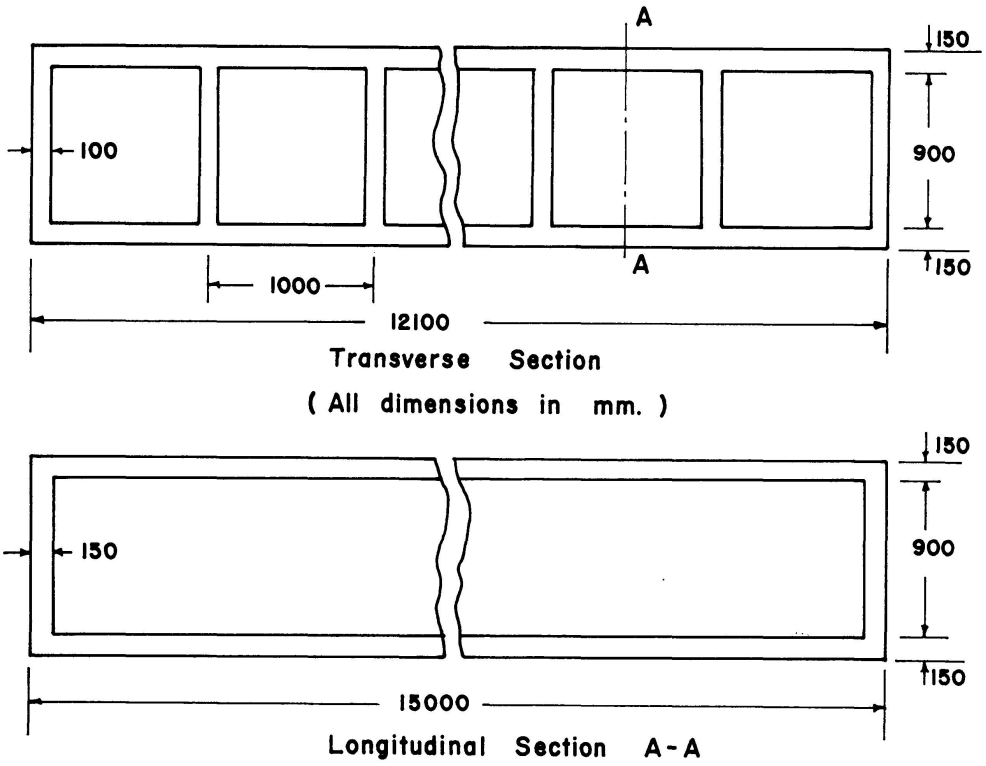


Fig. 6. Design example.

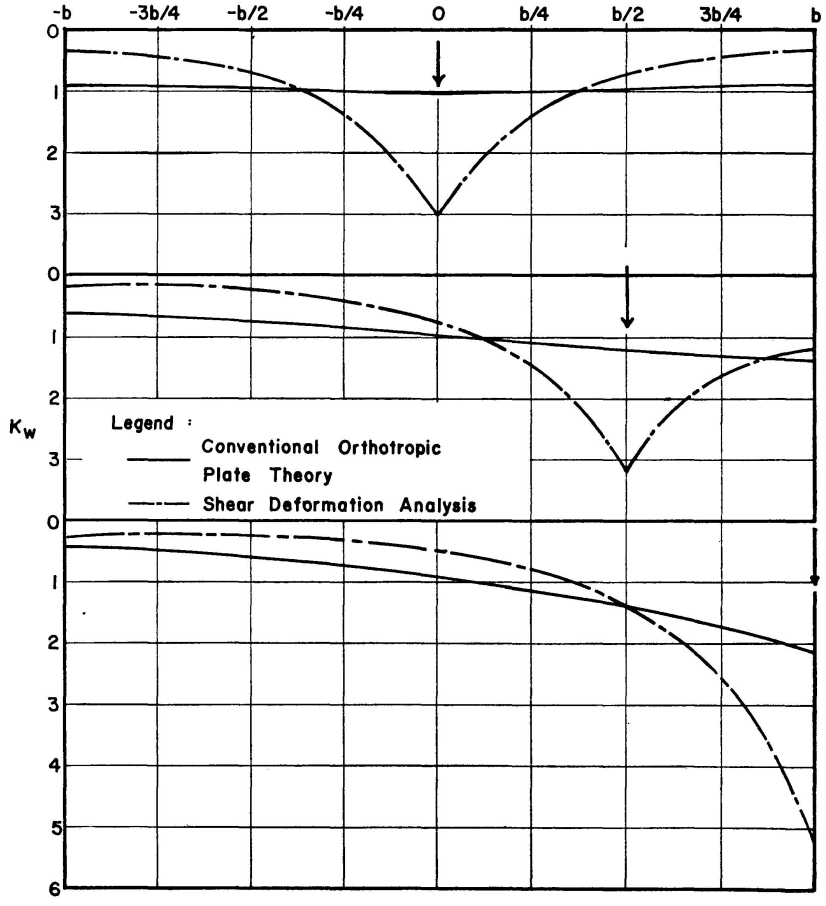


Fig. 7. Distribution coefficients for deflection.

results for central and two eccentric positions of concentrated load at midspan are shown in Figs. 7, 8 and 9. The values of deflection, longitudinal and transverse bending moment were computed using nine harmonics of the series. For the shear stiffness S_B, Holmberg's equation was used. From these figures

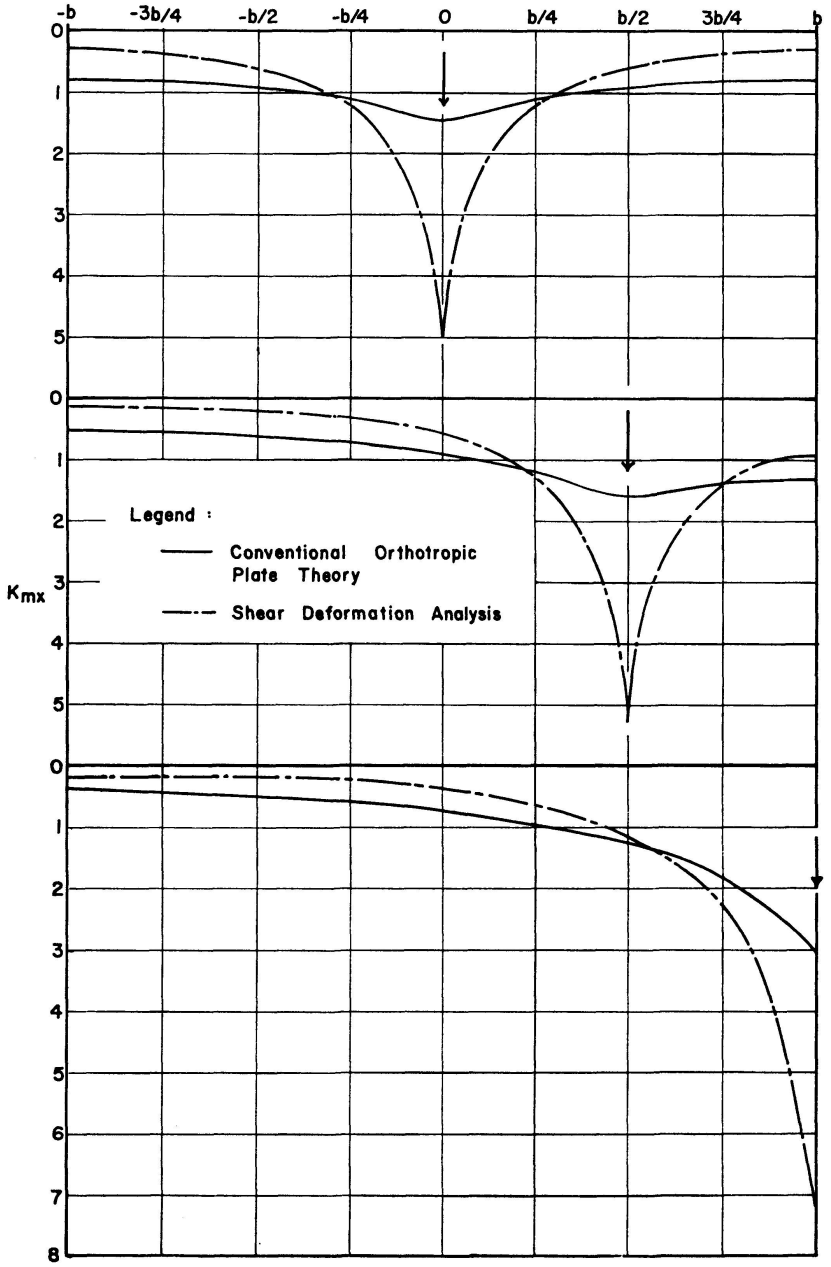


Fig. 8. Distribution coefficients for longitudinal moment.

it is apparent that the effect of vierendeel distortion on the deck is highly localized under the load. The peak values of the distribution coefficients for longitudinal moment vary from two to three times the corresponding values obtained using the conventional orthotropic plate theory, depending on the eccentricity of the load. A more realistic comparison may be made by con-

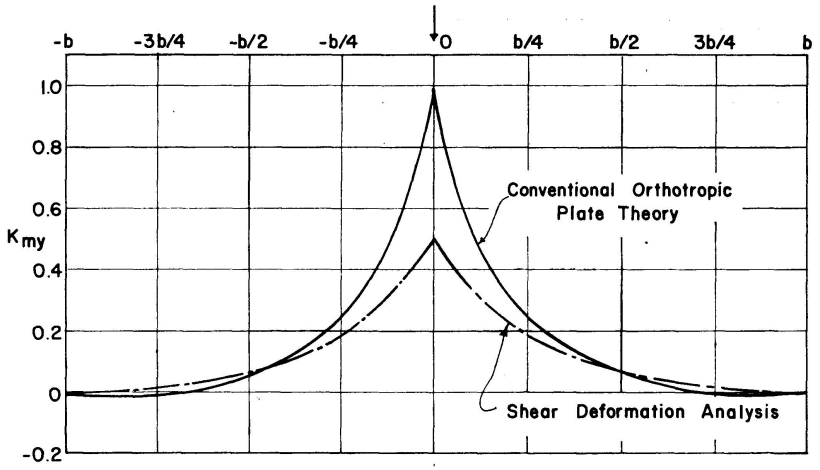


Fig. 9. Distribution coefficients for transverse moment.

sidering the areas under the curves. With the load at stations 0, $b/2$ and b, the percentage increases in the moment carried by the beams under these loads with the inclusion of the shear correction are 150, 126 and 86% respectively. This indicates the magnitude of the shear deformation effect and the necessity for taking account of it in design, especially when the webs of the multi-cell box beam bridge deck are fairly thin.

The presence of shear deformation decreases the peak value of transverse moment as shown in Fig. 9. This is to be expected as the shear stiffness S_B has the effect of reducing the overall rigidity of the deck in the transverse direction leading to a decrease of transverse moment.

The effect of shear stiffness on the load distribution characteristics of the

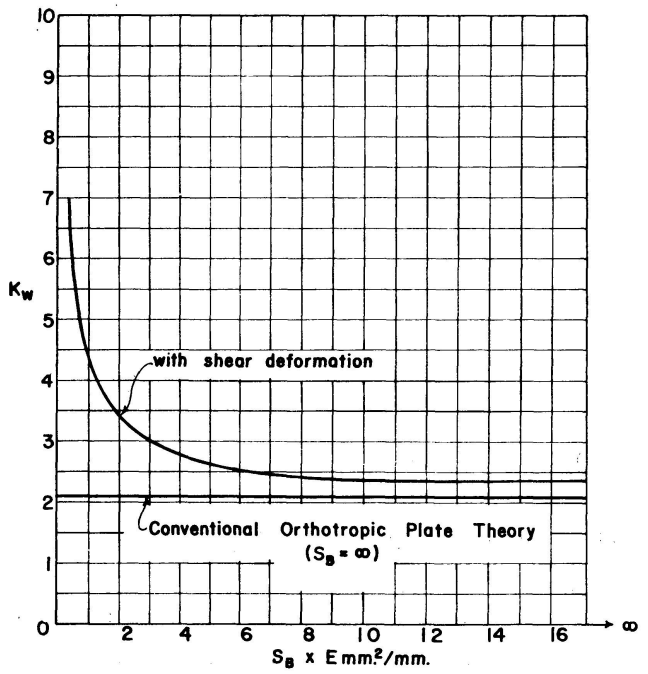


Fig. 10. Relation between peak value of distribution coefficient and shear stiffness.

deck is shown in Fig. 10. To illustrate this effect on the example bridge deck, values of S_B are plotted against the distribution coefficients for deflection. The load is placed at the edge to produce the peak value of distribution coefficient. For convenience the first harmonic only was considered. From this figure it appears that rapid increases in the value of $K_{w\,max}$ occur at low values of S_B. As the shear stiffness is increased the distribution coefficient approaches the value obtained from conventional orthotropic plate theory.

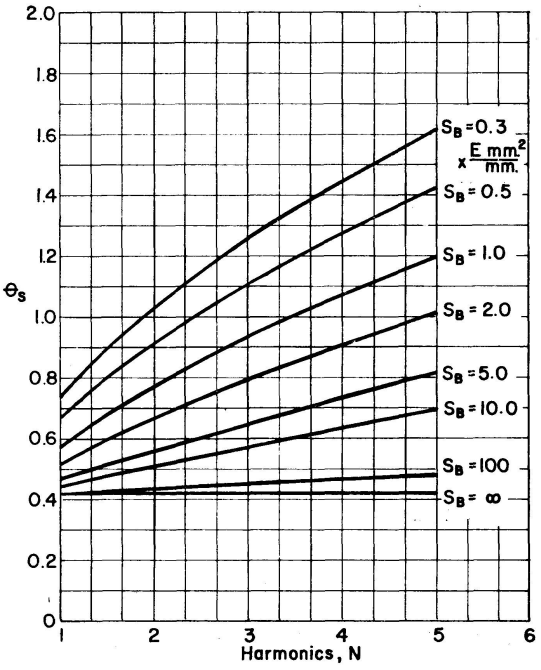


Fig. 11. Variation of flexural parameter θ_s with the harmonic.

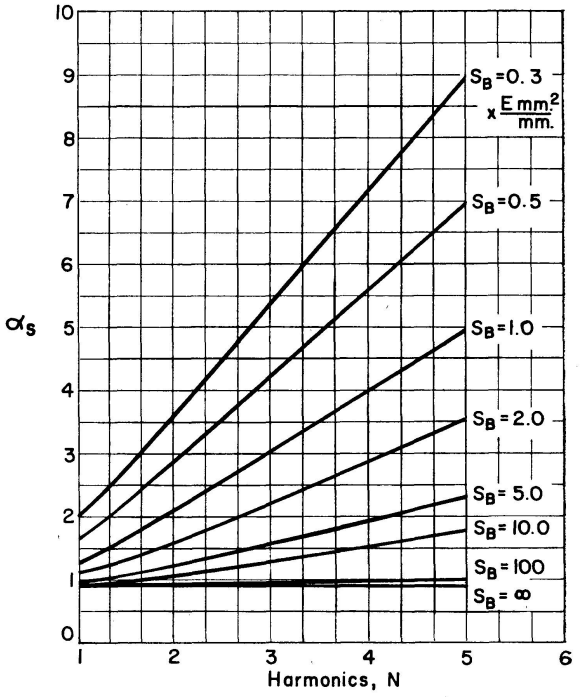


Fig. 12. Variation of torsional parameter α_s with the harmonic.

Figs. 11 and 12 are included to illustrate the effect of the number of harmonics on the values of the flexural and torsional parameters θ_s and α_s (Eqs. (39) and (41)). It is shown in the theoretical analysis that the parameters α_s and θ_s are functions of the harmonics. This makes it a difficult, if not impossible, task to reproduce the results in the form of design curves for the benefit of designers who do not have ready access to a digital computer. This can only be a practical proposition if distribution coefficients are obtained from the first harmonic of the series only. Experience has shown that up to nine harmonics are required in order to obtain accurate results with an analysis including shear deformation, especially for the values of moments and shears.

Conclusions

A theoretical analysis has been presented for determining the effect of vierendeel distortion on the load distribution characteristics of multicell box

beam bridges. It has been shown that this effect is somewhat localized in the vicinity of the load. Large increases in the peak values of longitudinal moment occur under the load as a direct consequence of vierendeel distortion, with an accompanying decrease in the transverse bending moment of the deck. Approximately, the increases in the peak values of deflection and longitudinal moment are inversely proportional to the shear stiffness of the deck. When S_B is infinitely large the values correspond with results from conventional orthotropic plate theory.

The flexural and torsional parameters have each been shown to be a function of the harmonics. The use of a digital computer is imperative for an accurate solution.

Acknowledgement

This work was carried out as an integral part of a research project on multibeam concrete bridge decks sponsored by the Construction Industry Research and Information Association. The authors are grateful to the Association for permission to publish these results in this form.

Appendix: Illustrative Example

The dimensions of the bridge deck are shown in Fig. 6. For the purpose of calculating the elastic rigidities of the deck in flexure and torsion, the value of Poisson's Ratio is taken as 0.15. The elastic rigidities are determined as follows:

$$D_x = \frac{1}{12}\left(1200^3 - \frac{900}{1000}\times 900^3\right) E = 89.325\times 10^6\, E \text{ mm}^4/\text{mm},$$

$$D_y = \frac{1}{12}(1200^3 - 900^3)\, E = 83.25\times 10^6\, E \text{ mm}^4/\text{mm},$$

$$D_1 = D_2 = \nu D_y = 0.15\times 83.25\times 10^6\, E = 12.49\times 10^6\, E \text{ mm}^4/\text{mm},$$

$$D_{xy} = \frac{1}{2}\times\frac{G\,4A^2}{b\oint\frac{ds}{t}} = \frac{G\times 4\,(12\,000\times 1050)^2}{2\times 12\,100\left(\frac{12\,000}{150}\times 2+\frac{1050}{100}\times 2\right)} = 63.06\times 10^6\, E \text{ mm}^4/\text{mm},$$

$$D_{yx} = \frac{G\times 4\,(14\,850\times 1050)^2}{2\times 15\,000\left(\frac{14\,850}{150}\times 2+\frac{1050}{150}\times 2\right)} = 66.50\times 10^6\, E \text{ mm}^4/\text{mm},$$

$$2H = (D_{xy}+D_{yx}+D_1+D_2) = 154.54\times 10^6\, E \text{ mm}^4/\text{mm}.$$

Using Holmberg's formula, the shear stiffness is obtained as

$$S_B = 0.834\, E \text{ mm}^2/\text{mm}.$$

For the conventional orthotropic plate theory the parameters α and θ are as follows:

$$\alpha = \frac{H}{\sqrt{D_x D_y}} = \frac{154.54}{2\sqrt{89.325 \times 83.25}} = 0.896,$$

$$\theta = \frac{b}{L}\sqrt[4]{\frac{D_x}{D_y}} = \frac{12100}{2 \times 15000}\sqrt[4]{\frac{89.325}{83.25}} = 0.410.$$

References

1. Y. GUYON: Calcul des ponts larges à poutres multiples solidarisées par des entretoises. Annales des Ponts et Chaussées, Vol. 24, No. 5, Sept.-Oct. 1946, p. 553.
2. C. MASSONNET: Méthode de calcul des ponts à poutres multiples tenant compte de leur résistance à la torsion. Publications, International Association for Bridge and Structural Engineering, Vol. 10, 1950, p. 147.
3. A. R. CUSENS, and R. P. PAMA: Distribution of concentrated loads on orthotropic bridge decks. The Structural Engineer, Vol. 47, No. 9, September 1969, p. 377–385.
4. C. MASSONNET, and A. GANDOLFI: Des cas exceptionnels dans la théorie des ponts à poutres multiples. Publications, International Association for Bridge and Structural Engineering, Vol. 27, 1967, p. 73–94.
5. F. SAWKO, and R. J. COPE: Analysis of multi-cell bridges without transverse diaphragms – a finite element approach. The Structural Engineer, Vol. 47, No. 11, November 1969, p. 455–460.
6. W. H. HUBER: Die Theorie der kreuzweise bewehrten Eisenbetonplatte nebst Anwendungen auf mehrere bautechnisch wichtige Aufgaben über rechteckige Platten. Bauingenieur, Vol. 4, 1923, p. 354.
7. W. H. WITTRICK: Torsion of a multi-webbed rectangular tube. Aircraft Engineering, Vol. 25, No. 298, Dec. 1963, p. 372.
8. R. BREDT: Torsion of tubular members. Z. Ver. Deut. Ing., Vol. 40, 1896, p. 815.
9. A. HOLMBERG: Shear-weak beams on elastic foundations. Publications, International Association for Bridge and Structural Engineering, Vol. 10, 1950, p. 69–85.

Summary

A theoretical analysis is presented for the analysis of multicell rectangular box beam bridges, without intermediate diaphragms, which considers the effect of Vierendeel distortion of the deck. The solution is expressed in Fourier Half-Range Sine Series and as such it is limited to simply supported bridge decks. The edges may be free or elastically restrained by edge beams of known elastic rigidities in flexure and torsion. The equations for deflection, moments and shears are derived and an illustrative example is included to show the effect of Vierendeel distortion on the load distribution characteristics of the deck. Comparison is made with conventional orthotropic plate theory.

Résumé

On présente une analyse théorique applicable au calcul des ponts en caisson multicellulaire sans entretoises, avec l'influence de l'effet de Vierendeel sur la chaussée. La solution est donnée sous forme de séries de Fourier et elle est limitée au cas des plaques simplement supportées. Les bords peuvent être libres, ou partiellement encastrés par des entretoises extrêmes de rigidités flexionnelle et torsionnelle connues. On établit les équations pour les flèches, les moments et les efforts tranchants; à l'aide d'un exemple, on montre l'effet de Vierendeel sur la répartition des charges sur la chaussée. On compare les résultats avec la théorie conventionnelle des plaques orthotropes.

Zusammenfassung

Es wird eine theoretische Analyse für die Berechnung mehrzelliger Kastenträger-Brücken, ohne Querscheiben, unter Beachtung der Vierendeelwirkung der Fahrbahn durchgeführt. Die Lösung wird in Fourier-Reihen ausgedrückt und ist auf einfach gelagerte Fahrbahnplatten begrenzt. Die Ränder können frei oder durch Endträger von bekannter Steifigkeit hinsichtlich Biegung und Torsion eingespannt sein. Die Gleichungen für Durchbiegung, Momente und Schub werden abgeleitet, und an einem Beispiel wird die Vierendeelwirkung auf die Lastverteilungscharakteristiken der Fahrbahn gezeigt. Zudem wird ein Vergleich mit der konventionellen orthotropen Plattentheorie angestellt.

Finite Element Analysis of Skew, Curved Box-Girder Bridge

Calcul à l'aide des éléments finis des ponts courbes, biais à section en caisson

Berechnung von schiefen, gekrümmten Brücken mit Kastenquerschnitt mit der Methode der finiten Elemente

R. G. SISODIYA
M. Sc., Graduate Student, Dept. of Civil Engineering, University of Calgary, Calgary, Alberta, Canada

Y. K. CHEUNG
Ph.D., MICE, Professor of Civil Engineering, University of Calgary

A. GHALI
Ph.D., Professor of Civil Engineering, University of Calgary

Introduction

In modern highways, many skew bridges are built, and very often these bridges are curved in plan. The box section has been favoured by many designers because of its aesthetic appearance and because of its high torsional rigidity.

In the past curved box-girders has been treated one-dimensionally as a curved beam, thus ignoring the distortions of the cross-section, and in many cases the skew effect as well.

CHEUNG et al. [1] use the finite strip method to analyse curved box-girder bridges. In this method, the curved plates should be circular and of constant width and the bridge should be ended by two radial cross sections. If all these conditions are satisfied, the finite strip method provides a solution which can be conveniently used in practical design, because it requires relatively short computer time and small computer storage.

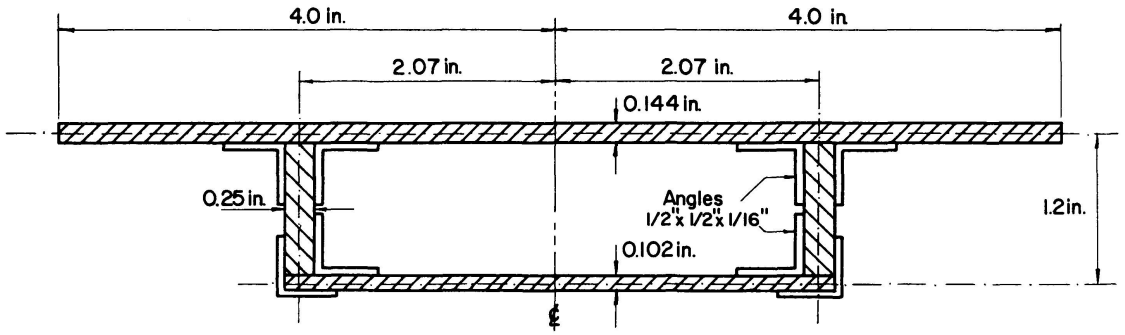
The present paper deals with finite element analysis of single box-girder skew bridges curved in any shape. The bridge may be of varying width and of any support conditions.

The procedure of the analysis and the types of the finite elements used to idealize the bridge deck is presented in a separate paper [2] which is limited to skew straight bridges. Results of the analysis of a curved bridge are presented here and they are compared with the results of experiments on a model 3.

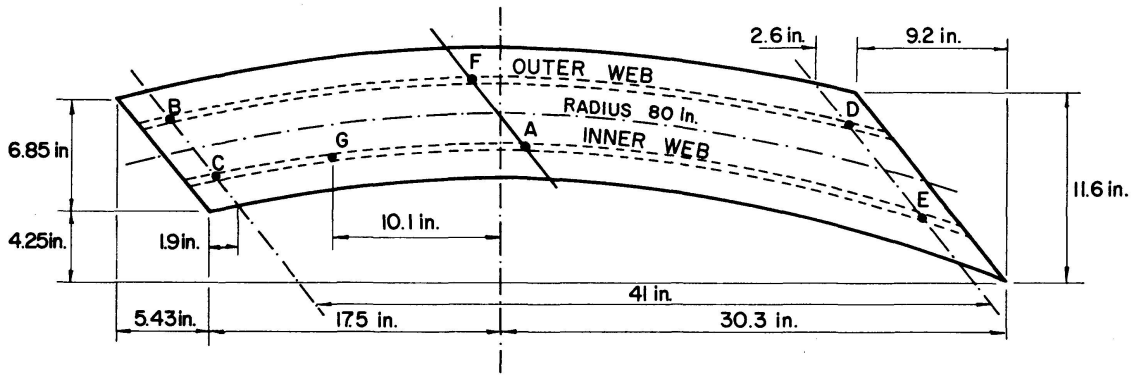
In the earlier paper [2] we recommended that the webs of the box be divided into rectangular elements. Here we will show how the ratio of the sides of the rectangular elements can affect the accuracy of the results.

Finite Element Analysis and Test Results

The general principles of the finite element method and the detailed formulation of the elements used in this paper can be found in a text by ZIENLIEWICZ and CHEUNG [4], and shall not be discussed here.



a) Cross-section.

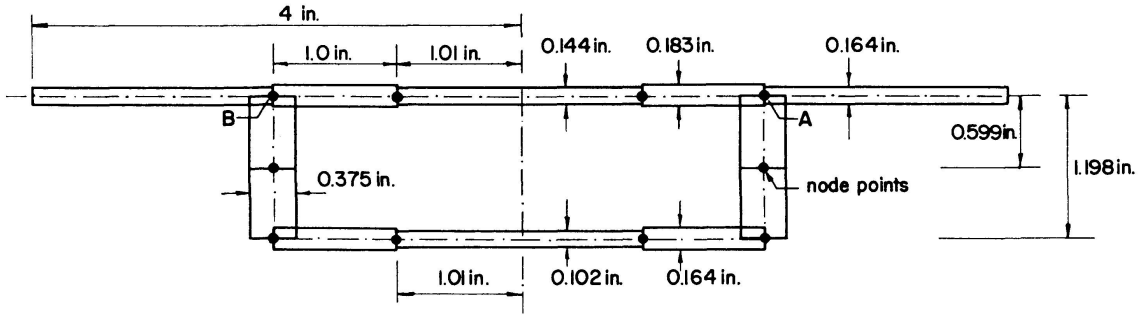


b) Plan.

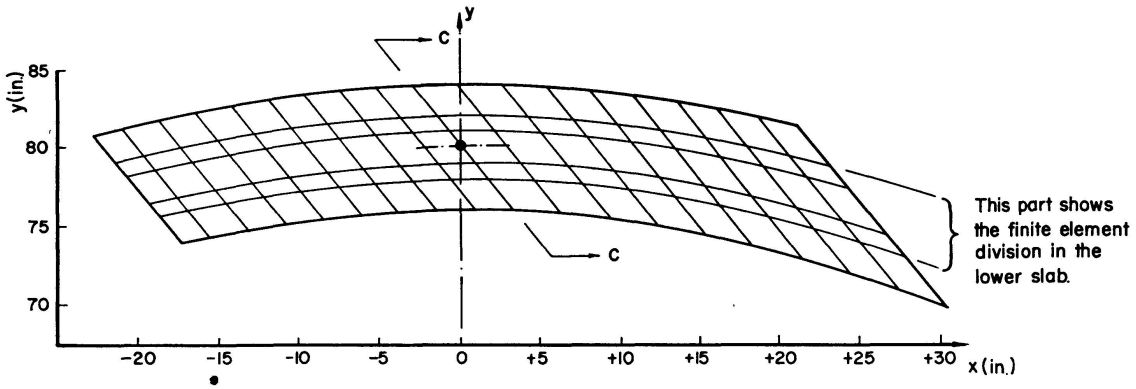
Fig. 1. Curved box-section bridge model.

Fig. 1a and b show the plan and the cross section of a bridge model made of aluminum alloy*) which was analysed by finite elements and tested for various loading cases. Fig. 2a and b show the finite element idealization used for the analysis, in which rectangular elements are used for the webs while the top and bottom slabs are divided into parallelogram elements. As an alternative the top and bottom slabs may be divided into triangles as shown in Fig. 2c. Both idealizations gave identical results and the computer time was shorter with the triangular elements. However the parallelogram element offers

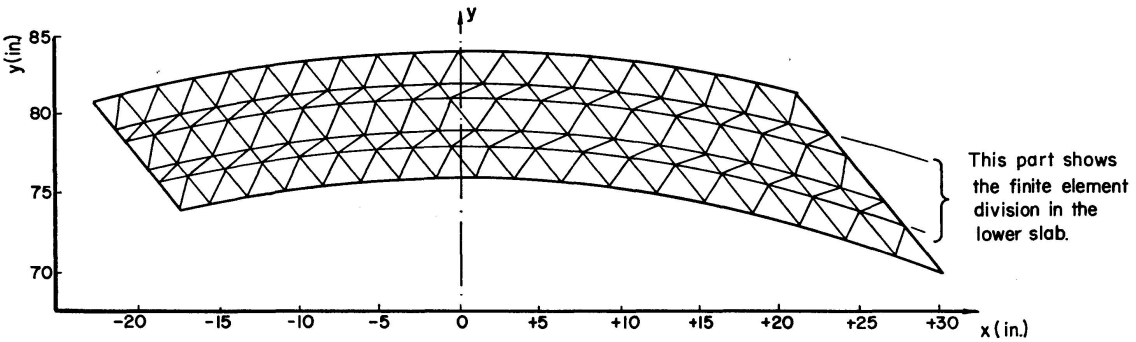
*) For details of testing procedure see Ref. 3.



a) Cross-section.

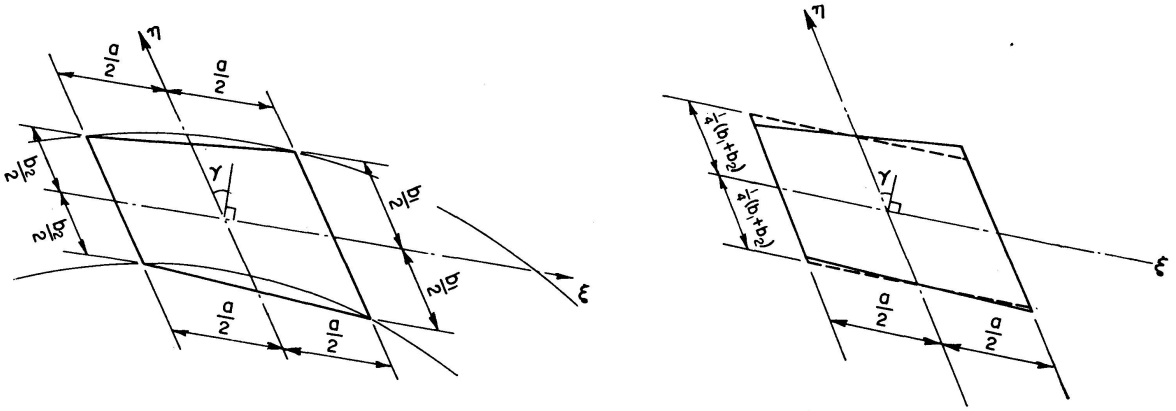


b) Use of parallelogram elements for top slab.



c) Use of triangular element for top slab.

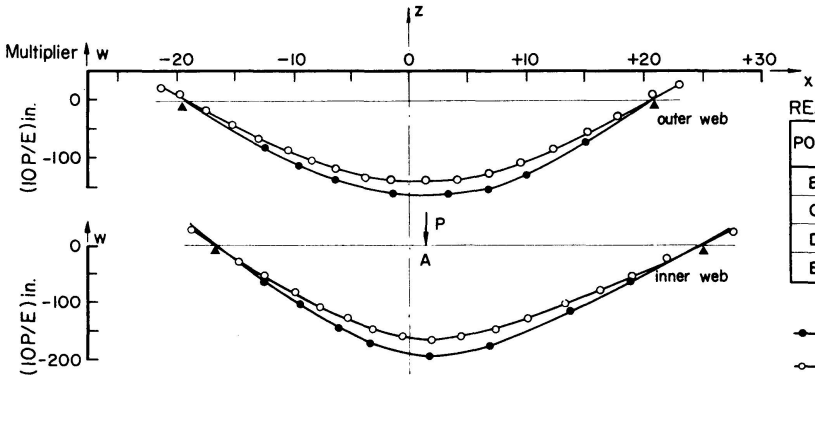
Fig. 2. Finite element idealization.



a) Quadrilateral defined by 2 arcs of circles with same centre and two parallel lines.

b) Parallelogram approximation of quadrilateral in a).

Fig. 3. Parallelogram approximations of the elements in top and bottom slabs (Fig. 2b).



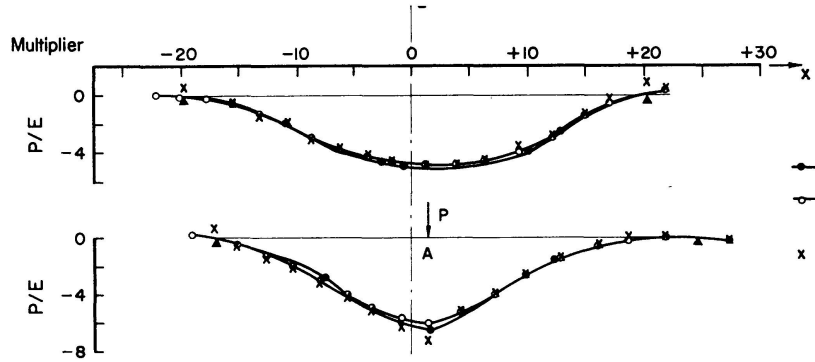
REACTIONS (Multiplier : P)

POINT	EXPERIMENTAL	ANALYTICAL	
		Coarse Mesh	Fine Mesh
B	− 0.131	− 0.169	− 0.169
C	+ 0.606	+ 0.669	+ 0.669
D	+ 0.657	+ 0.647	+ 0.647
E	− 0.127	− 0.147	− 0.147

Experimental

F.E. using parallelogram with a coarse mesh. The finer mesh gave almost identical deflections.

a) Vertical deflections of the webs.

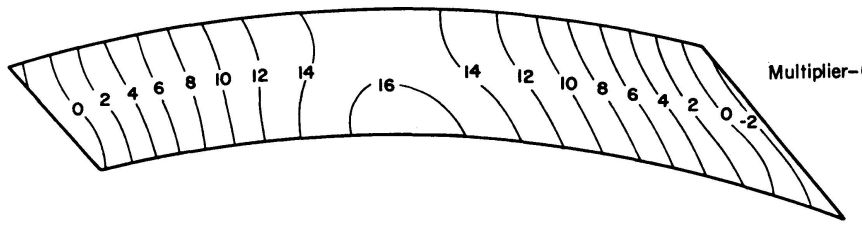


Experimental

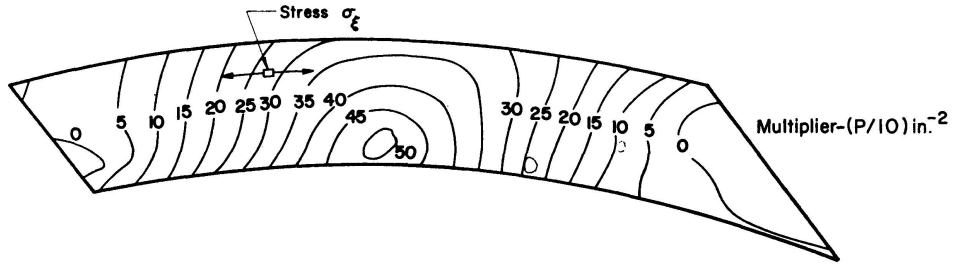
F.E. using parallelograms with a coarse mesh.

x x F.E. using parallelograms with a fine mesh. The plotted values are only those which are significantly different from the coarse mesh results

b) Tangential strains at upper surface of the top slab.



c) Conturs of the vertical deflections of the top slab.



d) Lines of equal circumferential stress σ_ξ at the middle of the top slab.

Fig. 4. Deflections, reactions, strains, and stresses due to vertical load P at point A for one span bridge model (Fig. 1).

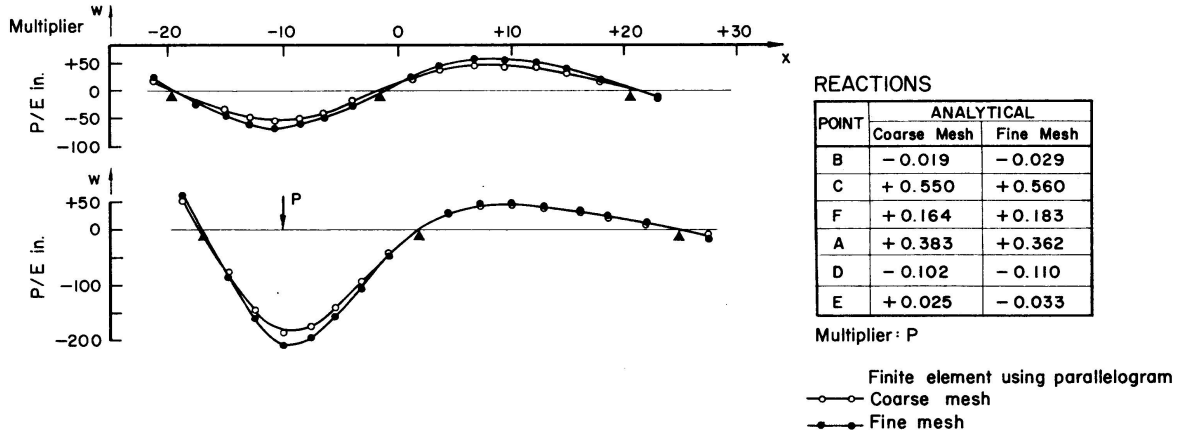
The deck is supported at four points B, C, D and E (Fig. 1 b), and the reactions are assumed to have vertical component only.

some advantage in the interpretation of the results since the stresses as well as displacements are computed at the same nodal points.

It is obvious that the top and bottom slabs cannot be divided into elements which are perfect parallelograms, and thus some approximation is necessary. The lines of division in Fig. 2b are actually straight lines parallel to the lines of supports, and in the other direction they are in fact polygonal lines joining points on circular arcs. In the calculation of the stiffness matrix and the stresses in an element such as that in Fig. 3a, it is approximated into a perfect parallelogram element as in Fig. 3b.

Some of the results of the analysis and experiment are given in Fig. 4, which represent the effects of a unit vertical load applied at point A (Fig. 1b).

In Fig. 4a the variation of the vertical deflection and the strains are plotted along the centre line of the web, together with a table giving te reactions at the supports. Two different finite element mesh divisions are used in the analysis; a coarse mesh corresponding to the idealization shown in Fig. 2a and b, and a fine mesh obtained by subdividing into two all the elements of the coarse one in the span direction (except for the elements adjacent to the end cross-sections). The deflections obtained for the two different meshes are practically identical. The experimental values for the deflections are somewhat



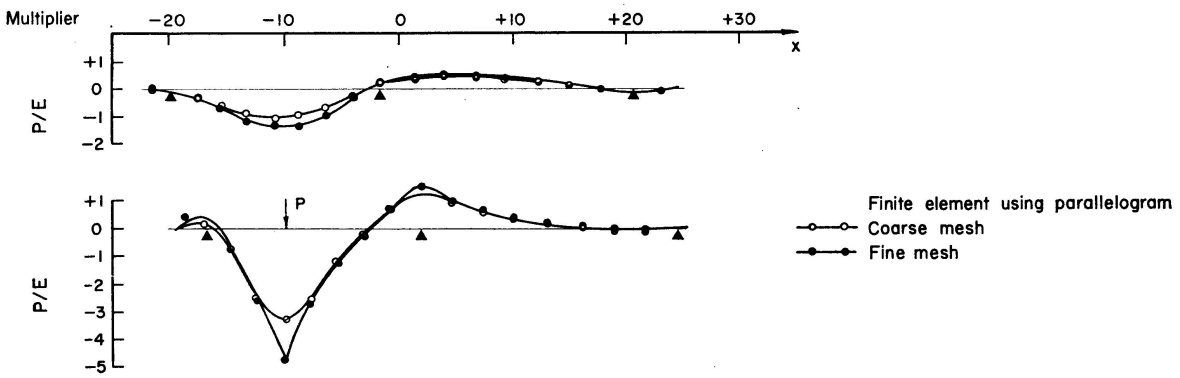
REACTIONS

POINT	ANALYTICAL	
	Coarse Mesh	Fine Mesh
B	−0.019	−0.029
C	+0.550	+0.560
F	+0.164	+0.183
A	+0.383	+0.362
D	−0.102	−0.110
E	+0.025	−0.033

Multiplier: P

Finite element using parallelogram
Coarse mesh
Fine mesh

a) Vertical deflections of the webs.



b) Tangential strains ϵ_{ξ} at points A and B in Fig. 2a.

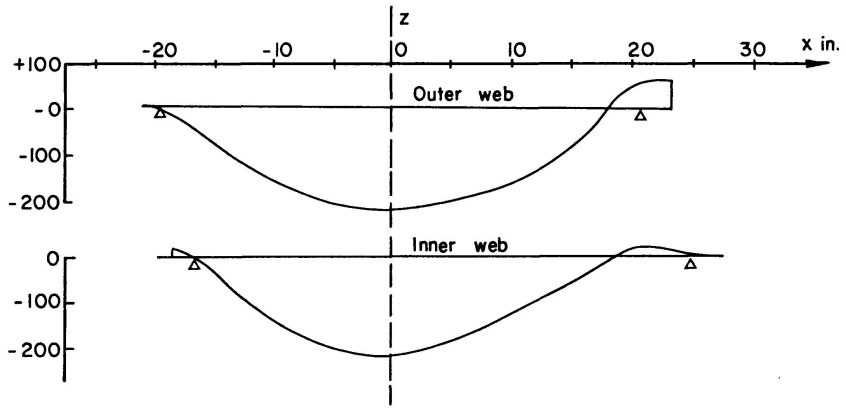
Fig. 5. Deflections, reactions and strains due to vertical load P at point G for two span bridge model (Fig. 1).

higher on the whole and this has been attributed to the fact that the stiffness of the model beam has been reduced by the imperfect epoxy bond between the web and flanges. The contours for the circumferential stress σ_ξ is shown in Fig. 4d.

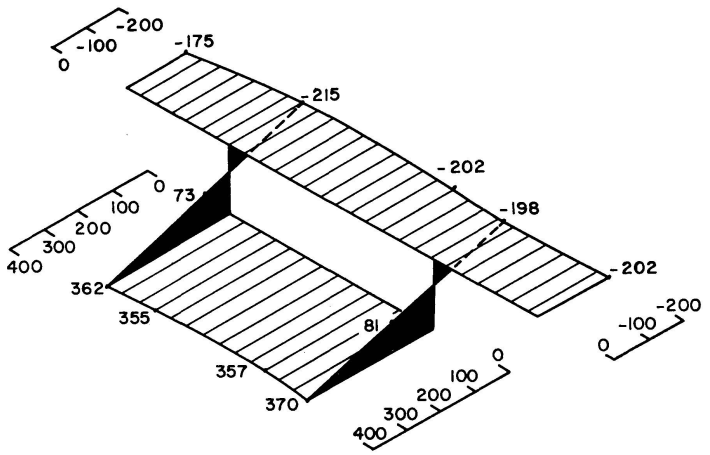
The same model was analysed as a continuous bridge over two spans by introducing the supports at A and F and applying a vertical concentrated load at G (Fig. 1b). The vertical deflections, strains and reactions are plotted in Fig. 5 for the coarse and fine meshes described above.

The number of node points in the idealized structure in Fig. 2 is 228 requiring the solution of $6 \times 228 = 1368$ equations. The time taken by an IBM 360-50 computer was 24 minutes to calculate the displacements, the reactions and the stresses due to one loading case, and the time is increased by 2 minutes for each additional case.

When the finer mesh described above was used, the number of node points and equations became 420 and 2520 respectively. Because of the large number of equations and the short word length (32 bits) of the computer, double precision had to be used in the equation solving routines.



a) Along span of the bridge at points A and B in Fig. 2a.



b) At section C-C in Fig. 2b.

Fig. 6. Variation of stress σ_ξ (lb./in.^{2}) as defined in Fig. 4d due to self weight of specific weight of 1 lb./in.^{3}.

To analyse the bridge model for load representing its own weight, the weight of each element is distributed equally to the four corner nodes (Fig. 2b). The variation of stress σ_ξ along the span of the beam at the intersection of the web and the top slab (points A and B in Fig. 2a) are shown in Fig. 6a. In Fig. 6b, we give the variation of σ_ξ on Section C-C (see Fig. 2b).

Accuracy of In-Plane Rectangular Element for Beam Problems

As previously mentioned, the agreement between the experimental and analytical deflections in Fig. 4a is not entirely satisfactory, and originally the discrepancies were suspected to be due to the mesh division used for the web, which has a 1 : 4 aspect ratio for the elements used in the coarse mesh, and a 1 : 2 aspect ratio in the fine mesh.

In order to obtain further information on the adequacy of the mesh divisions, the simply-supported beam in Fig. 7a was analysed using rectangular elements (Fig. 7b) with $b = a$, $2a$ and $4a$ respectively for three different cases.

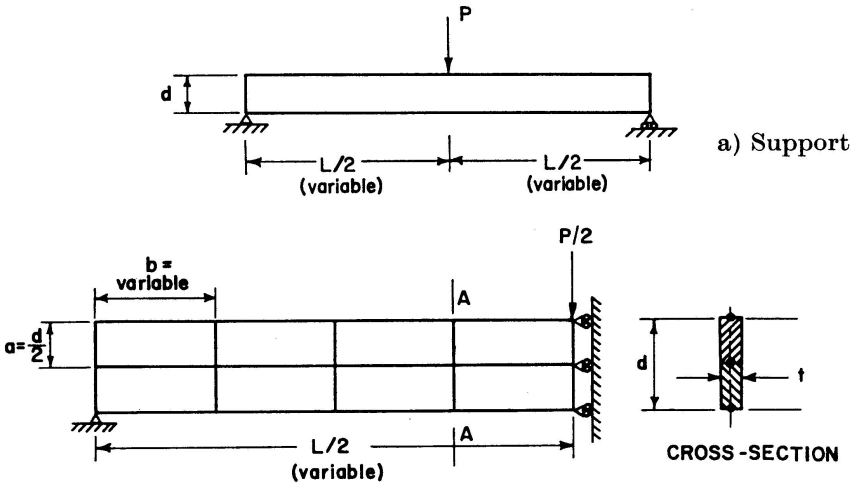


Fig. 7. Simply supported beam.

The deflection at centre and stresses at Section A-A in Fig. 7 are compared with known values from beam theory (including shear deformation for Poisson's ratio = 0) in Table 1.

It is indeed surprising to note that the rectangular element which has been widely used in two-dimensional elasticity problems gives such poor results in beam analysis when the ratio of the sides a/b is smaller than unity, and that the deterioration in accuracy when the aspect ratio changes from 1 : 1 to 1 : 4 can be so drastic.

However, the above drawback of the in-plane rectangular element does not have such an important effect on the analysis of box sections, since the longi-

Table 1. Central Deflection and Maximum Stresses in a Test Problem (See Fig. 7)

Half Span Length $L/2$	Ratio $a:b$	Deflection at Mid-Span in terms of P/Et			Maximum Stresses at Section A-A in terms of $P/t\,d$		
		F.E.M.	Beam Theory Including Shear Deformation [5]	F.E.M. Results as a Percentage of the Beam Theory Result	F.E.M.	Beam Theory	F.E.M. Results as a Percentage of the Beam Theory Result
$2\,d$	1 : 1	16.62	18.19	91.4 %	4.00	4.5	88.7 %
$4\,d$	1 : 2	88.38	132.59	66.7 %	6.00	9	66.7 %
$8\,d$	1 : 4	340.58	1033.29	33.0 %	5.94	18	33.0 %

tudinal forces are mainly resisted by the top and bottom slabs. This is confirmed by only a small improvement of the results achieved by the use of the finer mesh described earlier (see Fig. 4a and b) for the curved box-girder bridge.

Conclusion

The finite element method can be economically used to replace model testing for the analysis of curved skew box-girder bridges. More research is needed to develop elements which permit the use of smaller number of equations and to reduce computing time and programming effort, before the method can be widely accepted by bridge designers.

It is suggest that rectangular elements be used for the webs and either parallelogram or triangular element for the top and bottom slabs. In practice, the support of a skew bridge lie on parallel lines, and curved bridges have large radii of curvature such that it is often possible to approximate the top and bottom slabs as assemblage of parallelograms. The triangular element can be used in any general case.

Acknowledgement

This project was supported by grants from the National Research Council of Canada, which is gratefully acknowledged.

Notation

E Young's Modulus
L span length
P load
R reaction

a, b sides of a rectangular element
d depth of a beam
t thickness of an element
w vertical deflection
ξ, η skew coordinates for a parallelogram element
σ stresses
ϵ strains
x, y, z axes

References

1. M. S. Cheung, and Y. K. Cheung: Analysis of Curved Box-Girder Bridges by Finite Strip Method. In preparation.
2. R. G. Sisodiya, A. Ghali, and Y. K. Cheung: Finite Element Analysis of Skew Box-Girder Bridges. Submitted for publication.
3. R. G. Sisodiya: Analysis of Box-Girder Bridges by the Finite Element Method. M.Sc. Thesis, University of Calgary, 1969.
4. O. C. Zienkiewicz, and Y. K. Cheung: Finite Element Methods in Structural and Continuum Mechanics. McGraw-Hill Book Co., 1967.

Summary

Box-girder bridges having one or two spans and with curved layout and skew supports are analysed by the finite element method. The results of analysis is verified by tests on an aluminum bridge model.

The type of elements used to idealize the bridge are described and the effect of their choice on the accuracy of the analysis is discussed.

Résumé

On présente le calcul par la méthode des éléments finis des ponts à une ou deux travées, présentant un axe courbe et des appuis biais, avec une section en caisson fermé. On a vérifié les résultats du calcul à l'aide d'essais sur des modèles de ponts en aluminium.

Le présent article décrit le type des éléments utilisés et étudie l'incidence du choix de la forme des éléments sur l'exactitude du calcul.

Zusammenfassung

Kastenförmige Brücken über eine oder zwei Spannweiten mit gekrümmter Achse und schiefer Lagerung werden mittels der Methode der finiten Elemente gerechnet. Die Ergebnisse der Berechnung werden durch Versuche an einem Aluminium-Brückenmodell bestätigt.

Die Art der verwendeten Elemente zur Idealisierung der Brücke werden beschrieben und die Auswirkung ihrer Wahl auf die Genauigkeit der Rechnung diskutiert.

Leere Seite
Blank page
Page vide